Identification of Structural Damage, Ground Motion Response, and the Benefits of Dense Seismic Instrumentation

Thesis by

Filippos Filippitzis

In Partial Fulfillment of the Requirements for the degree of

Doctor of Philosophy

CALIFORNIA INSTITUTE OF TECHNOLOGY
Pasadena, California

2021
Defended September 30th, 2020

Filippos Filippitzis
ORCID: 0000-0001-8377-4914

ACKNOWLEDGMENTS

First and foremost, I would like to thank my advisors, Professors Tom Heaton and Monica Kohler, for their guidance and support throughout my graduate studies. Their enthusiasm and the freedom they granted to me to pursue various research topics have always been an inspiration for me.

Many thanks to the members of my thesis committee, Professors Domniki Asimaki and Rob Clayton, for the time they dedicated to my thesis and research progress. Their insightful observations and advice are greatly appreciated.

Special gratitude goes to my interim advisor Professor Ares Rosakis for his mentoring and his support during my first years at Caltech. I am very grateful to the Community Seismic Network team, Professor K. Mani Chandy, Dr. Richard Guy, and Dr. Julian Bunn, for our close collaboration and their exceptional feedback in many research projects. I would also like to thank the U.S. Geological Survey and particularly Dr. Robert Graves for our collaboration and their insightful discussions and comments. Many thanks to Professors John Hall and Michael Mello for their academic guidance and the opportunity to work as a teaching assistant.

I would like to thank the California Institute of Technology for the outstanding education it has provided to me and its generous financial support. I would also like to thank the faculty, staff, officemates, and friends from Gates-Thomas for the stimulating conversations and memorable experiences we shared. I especially wish to acknowledge the current and past members of my research group, Becky Roh, Dr. Kenny Buyco, and Dr. Anthony Massari, for their irreplaceable feedback and many contributions in all aspects of my research work.

I specifically want to thank Dr. Kenny Buyco for his help by producing the data response time histories that were used in order to test the proposed methodologies of Chapter 2 of this thesis, through conducting the Frame-2D finite element analyses. I also want to specifically acknowledge

Dr. Robert Graves, who performed the 3D finite difference ground motion simulations for the M7.1 Ridgecrest event, which are used and presented in Chapter 4 of this thesis.

Finally, I would like to thank my family and friends outside of work. This thesis is dedicated to my parents: Venia and Konstantinos. I am forever grateful for their unconditional love, patience, and encouragement.

ABSTRACT

This study explores the problems of identifying structural damage in steel frame buildings, through the use of dense instrumentation over the height of the building, and of characterizing the ground motion response in urban Los Angeles following the 2019 Ridgecrest earthquakes, through the use of dense instrumentation from available seismic networks, including the very dense Community Seismic Network.

First we explore the possibility of tracing possible nonlinear behavior of a structure by updating an equivalent linear system model in short time segments of the earthquake-induced excitation and response time histories, using a moving time window approach. The stiffness and damping related parameters of the equivalent linear model are estimated by minimizing a measure of fit between the measured and model predicted response time histories for each time window. We explore the effectiveness of the methodology for two example applications, a single-story and a six-story steel moment frame building. For the single-story building, the methodology is shown to be very effective in tracing the nonlinearities, while the six-story building is designed to also reveal the limitations of the methodology, mainly arising from the different types of model errors manifested in the formulation.

Next, we investigate the problem of structural damage identification through the use of sparse Bayesian learning (SBL) techniques. This is based on the premise that damage in a structure appears only in a limited number of locations. SBL methods that had been previously applied for structural damage identification used measurements related to modal properties and were thus limited to linear models. Here we present a methodology that allows for the application of SBL in non-linear models, using time history measurements recorded from a dense network of sensors installed along the building height. We develop a two-step optimization algorithm in which the most probable values of the structural model parameters and the hyper-parameters are iteratively obtained. An equivalent single-objective minimization problem that results in the most probable model parameter values is also derived. We consider the example problem of identifying damage

in the form of weld fractures in a 15-story moment resisting steel frame building, using a nonlinear finite element model and simulated acceleration data. Fiber elements and a bilinear material model are used in order to account for the change of local stiffness when cracks at the welds are subjected to tension and the model parameters characterize the loss of stiffness as the crack opens under tension. The damage identification results demonstrate the effectiveness and robustness of the proposed methodology in identifying the existence, location, and severity of damage for a variety of different damage scenarios, and degrees of model and measurement errors. The results show the great promise of the SBL methodology for damage identification by integrating nonlinear finite element models and response time history measurements.

The final part of the thesis involves studying the ground motion response in urban Los Angeles during the two largest events (M7.1 and M6.4) of the 2019 Ridgecrest earthquake sequence using recordings from multiple regional seismic networks as well as a subset of 350 stations from the much denser Community Seismic Network. The response spectral (pseudo) accelerations for a selection of periods of engineering significance are calculated. Significant spectral acceleration amplification is present and reproducible between the two events. For the longer periods, coherent spectral acceleration patterns are visible throughout the Los Angeles Basin, while for the shorter periods, the motions are less spatially coherent. The dense Community Seismic Network instrumentation allows us to observe smaller-scale coherence even for these shorter periods. Examining possible correlations of the computed response spectral accelerations with basement depth and Vs30, we find the correlations to be stronger for the longer periods. Furthermore, we study the performance of two state-of-the-art methods for estimating ground motions for the largest event of the Ridgecrest earthquake sequence, namely 3D finite difference simulations and ground motion prediction equations. For the simulations, we are interested in the performance of the two Southern California Earthquake Center 3D Community Velocity Models (CVM-S and CVM-H). For the ground motion prediction equations, we consider four of the 2014 Next Generation Attenuation-West2 Project equations. For some cases, the methods match the observations reasonably well; however, neither approach is able to reproduce the specific locations of the maximum response spectral accelerations, or match the details of the observed amplification patterns.

PUBLISHED CONTENT AND CONTRIBUTIONS

[1] Filippitzis, F., Kohler, M. D., & Heaton, T. H. (2019). “Identification of Sparse Damage in Steel-Frame Buildings Using Dense Seismic Array Measurements.” *Structural Health Monitoring 2019: Enabling Intelligent Life-cycle Health Management for Industry Internet of Things (IIOT)*. Vol.2. Destech Publications, Lancaster, PA. ISBN 978-1-60595-601-5. DOI: 10.12783/shm2019/32398.

F. F. participated in the conception of the project, developed the damage identification methodology and software, constructed the finite element models, collected the data, carried out the computations, created the figures, and wrote the draft manuscript.

[2] Kohler, M. D., Filippitzis, F., Heaton, T. H., Clayton, R. W., Guy, R. G., Bunn, J. J., & Chandy K. M. (2020). “2019 Ridgecrest Earthquake Reveals Areas of Los Angeles that Amplify Shaking of High-Rises.” *Seismological Research Letters*, DOI: 10.1785/ 0220200170.

F. F. participated in the conception of the project, did the data processing, carried out the computations, created the figures, and helped write the manuscript.

[3] Filippitzis, F., Kohler, M. D., Heaton, T. H., Graves, R. W., Clayton, R. W., Guy, R. G., Bunn, J. J., & Chandy, K. M. “Ground Motion Response in Urban Los Angeles from the 2019 Ridgecrest Earthquake Sequence.” *Earthquake Spectra*. [Under Review].

F. F. participated in the conception of the project, did the data processing, carried out the computations, created the figures, and wrote the draft manuscript.

TABLE OF CONTENTS

LIST OF ILLUSTRATIONS

LIST OF TABLES

Chapter 1

INTRODUCTION

1.1. Dense Seismic Networks in Urban Los Angeles

Measurements are valuable in all fields of science and engineering for validating models of a physical system, as well as for long-term monitoring of the performance and state of the system or important subsystems comprising the system. Such measurements are usually provided from sensor networks installed on the system. In this thesis measurements consist of ground and civil infrastructure (e.g., buildings, bridges, storage tanks) motion (e.g., acceleration) data, collected by sensor networks, during shaking caused by seismic activity. The collection of these strong motion measurements is essential to earthquake engineering as well as to seismology, since they are needed in order to validate models of the built infrastructure, to trace the health of infrastructure components, as well as to study ground motion response and validate models of geological regions.

The collection of such measurements is achieved using seismic networks that consist of accelerometers spread though a structure or a region. A great example is the area of Los Angeles, California, that has been instrumented with numerous arrays of sensors that go as far back as the 1920's (Caltech, 1926; Hutton, et al., 2010). Urban Los Angeles is one of the most densely instrumented areas in the world with multiple seismic networks permanently installed in the area. In the last decade the Community Seismic Network (CSN) (Clayton, et al., 2011; 2015), a dense seismic network, was installed in order to monitor both the ground motion in the urban Los Angeles area as well as the civil infrastructure. Following the recent expansion of the network with the deployment of accelerometers on campuses of the Los Angeles Unified School District (LAUSD) (Clayton, et al., 2019), CSN has a total of over 700 deployed active stations set up in locations provided by its numerous community hosts. The network utilizes ground stations, as well as stations along the height of mid-rise and high-rise buildings. This dissertation presents work

associated with two aspects of the CSN: A) dense instrumentation over the height of a building and B) dense instrumentation over a geographic region.

As a part of the CSN project a number of high-rise buildings have dense instrumentation along the height of the building, with one or more deployed triaxial stations per floor. Apart from the CSN deployments, instrumentation along the height of the building is generally increasing with more cities issuing structural monitoring regulations with a minimum number of sensors assigned for mid- and high-rise building, for example, for Los Angeles as described in the Information Bulletin P/BC 2017-117 (LADBS, 2017). Such instrumentation is vital for high resolution structural health monitoring. The ability to monitor the health of a structure, identify damage and prognose its safety has been receiving continuously increasing attention in the civil, mechanical, and aerospace communities. Damage is defined as changes to the material and/or geometric properties of a system, including changes to the boundary conditions and system connectivity, which adversely affect the system's performance. The goals of damage identification are the detection, localization, and quantification of damage following a potentially damaging event. The first part of this dissertation is concerned with the development and implementation of damage identification methodologies in civil infrastructure.

The recent CSN deployments (Clayton, et al., 2019) have led to unprecedented station numbers and density in urban Los Angeles. The CSN network spans an approximately 30 km by 30 km area with an average station spacing of about 0.5 km. For specific host locations such as the Jet Propulsion Laboratory (JPL) campus, the station density is even higher than that, with the average station spacing at JPL stations being about 50m. This spatial density is valuable for comprehending the ground motion response in urban Los Angeles and for examining the accuracy of model predicted ground motion intensity measures. The recent July 2019 Ridgecrest earthquake sequence, well-recorded by numerous Southern California seismic arrays and CSN, offered a unique opportunity for such a study. As a result the second part of the dissertation is focused on studying the recorded ground motion response that occurred in urban Los Angeles during the two largest events (M7.1 and M6.4) of the sequence, its correlation with site parameters, and the performance of model ground motion intensity measure predictions.

1.2 Structural Damage Identification Methodologies

The field of structural damage identification has been a subject of continuous research over the past few decades. As a result, there exists a vast amount of alternative damage identification methodologies. Here we will focus on vibration-based damage identification techniques for which the fundamental idea is to get damage information about the structure from its dynamic response to either natural (seismic, wind, ambient) or artificial (driven by mechanical exciters attached on the structure) loads (Rytter, 1993). The methods can be classified into model-based, which make use of models to simulate the structure behavior, and non-model-based, which are based on changes in the measured data.

Additionally, the model-based approaches can also be classified with respect to the type of model used into physics-based model approaches and non-physics-based model approaches. In particular, physics-based model techniques utilize the laws of physics to build the governing equations of motion that describe the behavior of the structure. For most practical situations physics-based models are linear or non-linear finite element models. This dissertation focuses on vibration-based damage identification techniques that make use of parametric finite element models. In these techniques, parameterized models are used in order to simulate the behavior of the real system and damage is identified as a change in the model parameters. In order to be able to reflect damage, the parameters of the finite element model are usually associated with local stiffness or geometrical properties of the structure. Thus, the damage identification problem is effectively the inverse problem of estimating the model parameters using the data, also referred to as model calibration or model updating (Beck, 1979; Mottershead & Friswell, 1993; Friswell & Mottershead, 1995). The nominal model is calibrated using vibration measurements from the initial (undamaged) state of the structure and the values of the parameters are monitored by processing vibration measurements from a permanently installed sensor network, before, during, or after a severe loading event such as an earthquake. Changes in the parameters of the finite element model from their nominal values are used in order to capture the existence of damage, its location, and severity.

Once these changes are identified, the updated finite element model can be used to reconstruct the response and update the safety of the structure based on its new condition.

A large number of studies have assumed that the structure behaves linearly for the vibration levels examined and thus use the modal properties (usually modal frequencies and modeshapes at the measured degrees of freedom) to update a linear finite element model of the structure. This is actually the second stage of a two-stage model updating approach, in which the first stage applies modal identification techniques to estimate the modal properties (modal frequencies and damping ratios, modeshapes at measured degrees of freedom, and modal participation factors) of the structure. One focus of this thesis is to perform the parameter estimation of a finite element model and the damping ratios in a single stage using the response time histories (e.g., acceleration, velocity, or displacement) and avoiding the intermediate estimation of the modal properties.

The literature of vibration-based damage identification is vast and there are a number of extensive literature reviews. Some exemplary reviews include those by Doebling, et al. (1996), categorizing the different methods based on the analysis technique and application, as well as its follow-up update by Sohn et al. (2003). Carden & Fanning (2004) provide state-of-the-art literature reviews. Fan & Qiao (2011) provide reviews and comparisons for the different methods and categories. An et al. (2019) summarizes progress made in the last decade being more targeted for bridge structure applications.

Despite the long development of damage identification methodologies, damage identification of full-scale civil infrastructure is still at a development phase, with many of the techniques being challenging to implement effectively in practice. The major limiting factor is the presence of model errors, i.e. the chosen class of models is unable to reproduce the exact behavior of the structure. Causes of model errors can be the incomplete or insufficient knowledge of the structure, (e.g., material properties, building practices, material deterioration, undocumented changes); modeling simplifications, assumptions and approximations (e.g., use of rigid diaphragms, point masses, beam theories, simplified material laws); and incomplete knowledge or understanding of systems and environmental variabilities (e.g., changes in structural properties due to thermal variations or

moisture, environmental noise). The model uncertainties are further magnified by measurement errors, i.e. errors associated with the data measurements (e.g., sensor noise, data processing errors). An additional challenge is the effective selection of the parameters to be included for updating. The choice of parameters is often a difficult task since damage locations are not known a-priori. Including a smaller number of parameters can lead to model error since the model is not flexible enough to track the damaged system's behavior, while on the other hand high-dimensional model parameter spaces may add difficulty in the inversion.

The presence of the model and measurement errors, in combination with the high-dimensional model parameter spaces, limited number of sensors available, and sub-optimal sensor placement, lead to the measurement data often being insufficient and can cause the damage identification inverse problems to be ill-conditioned and/or non-unique (Beck & Katafygiotis, 1998; Katafygiotis & Beck, 1998). This has motivated many researchers to tackle the problem of damage identification from a probabilistic perspective (Beck, 1989; Beck & Katafygiotis, 1998). The different approaches can be divided into those based on modal properties and those based on time histories. The methods based on modal properties can be implemented for linear models only, and some example papers include the ones by Vanik, et al. (2000) and Kuok & Yuen (2012). On the other hand, the methods based on time histories can be implemented both for linear and nonlinear model, and some example papers include Beck (Beck, 2010), Green, et al. (2015), and Ebrahimian, et al. (2017). A book discussing the Bayesian inference methods in structural dynamics is offered by Yuen (2010). Huang at al., (2019b) offers a state-of-the-art review of different Bayesian methodologies.

The task of model updating involves two levels of inference: model fitting and model comparison (MacKay, 1992). Under the Bayesian view (Jeffreys, 1939; Cox, 1946; Jaynes, 2003) probability represents a degree of plausibility of an uncertain proposition taking into account the given information. Thus, for the first level of inference, rather than looking for the optimal parameter vector, the predictive posterior distribution of the parameter vector can be used in order to quantify the degree of plausibility of each model within a proposed set of models. In the second level of inference different model classes can be compared and ranked in light of the data. This Bayesian

model comparison embodies Occam's razor, penalizing complex models (Gull, 1988; Jefferys & Berger, 1992; MacKay, 1996; Beck & Yuen, 2004).

The issues of ill-posedness and ill-conditioning can be further addressed by accounting for some prior information available for the problem. In the deterministic approach this prior information can be applied in the form of a regularization (Hansen, 1998; Neumaier, 1998; Titurus & Friswell, 2008), while in the Bayesian approach it is accounted in the selection of the prior distribution. For the problem of structural damage identification, damage in steel moment frame buildings, that is not severe enough to bring the building in a collapse condition, is expected to occur at a limited number of locations. For such cases, the damage possesses sparsity when compared with the numerous elements of the entire structure. This concept of sparsity is prior information that is commonly used in order to tackle the problem.

Sparse Bayesian learning (SBL) is a Bayesian probabilistic sparse recovery technique that is gaining increasing attention over the past few years. SBL was introduced by Tipping (Tipping, 2001) for obtaining sparse solutions to regression and classification problems (Faul & Tipping, 2002; Bishop, 2006). SBL promotes sparsity in the solution through the use of the automatic relevance determination (ARD) prior (MacKay, 1996). The ARD prior embodies the concept of relevance, practically “switching-off” of parameters deemed to be irrelevant resulting in simpler models (sparse solutions). SBL has been found to provide robust solutions for structural damage identification problems, with some example studies being the series of papers introducing and improving the SBL theory for structural identification from Huang, Beck and Li (Huang & Beck, 2015; Huang, et al., 2017a; Huang, et al., 2017b; Huang & Beck, 2018); the multitask SBL methodology from Huang, et al. (Huang, et al., 2019a); the SBL methodology developed making use of the Expectation–Maximization Technique by Hou et al. (Hou, et al., 2019); as well as the recent application of the method for identification under varying temperature conditions (Hou, et al., 2020). The aforementioned SBL methods are developed for linear models of systems using experimentally identified modal properties. Another focus of this thesis is to extend the SBL method to handle nonlinear models and more general parameterizations using directly the recorder input-output acceleration time histories.

1.3 Ground Motion Response Studies in Urban Los Angeles

The existence of interesting geological features such as sedimentary basins and faults, the strong presence of the oil/gas structures and other critical infrastructure (e.g., ports and airports), and the high population in combination with the observed seismic activity have made the area of urban Los Angeles the focus of numerous ground motion response studies. These ground motion response studies can be divided into two categories: those studying recorded data and using it in order to calculate response spectral quantities and other intensity measures, and those estimating the intensity measures through model predictions involving full waveform simulation or ground motion prediction equations (GMPEs).

Some example studies based on recorded ground motions are the following. Campbell (1976) using damage records from the 1933 Long Beach Earthquake exhibited how damage to Type III buildings (predominantly masonry buildings less than five stories) was greater in recent alluvium cites than older alluvium cites. Rogers et al. (1979) using ground motion records from nuclear events at the Nevada Test Site (NTS) as well as from the 1971 San Fernando earthquake found spectral amplification factors as high as 11 in Long Beach stations in the period band from 0.2 to 6 s. Rogers et al. (1979; 1984; 1985) compared the mean spectral levels of response over different period bands with geologic factors. The depth to basement rock and sediment thickness were found to be controlling factors for periods longer than 0.5 s. Liu and Heaton (1984) studying records from the 1971 San Fernando earthquake demonstrated the striking differences in amplitudes and duration between stations located in hard-rock sites versus those located in the sedimentary basins. In addition to that, they showed how the structure interaction on the waveforms is minimal. Saikia et al. (1994) studying records from several NTS explosions among other conclusions also found that the long period ground motions and the duration of significant shaking were amplified in the Los Angeles basin relative to sites outside the basin. Gao, et al. (1996) studied ground motion amplifications in the Santa Monica area during the 1994 Northridge earthquake. Hartzell et al. (1996; 1998) using ground motion records from the 1971 San Fernando, 1987 Whittier Narrows, 1991 Sierra Madre, and the 1994 Northridge mainshocks and Northridge aftershocks calculated

the site response over different period bands and presented site spectral amplification maps for the Los Angeles area. Harmsen (1997) presented analogous maps and discussed the correlation of the above records with top 30m average shear-wave velocity (VS30) and basin depth. Hatayama and Kalkan (2011), using recordings from the 2010 El Mayor-Cucapah earthquake also presented maps of the spectral amplification factors for the Los Angeles region, for different periods. The largest amplification factor was reported to be 10 at a period of 6 s, in the Western part of the Los Angeles basin. Furthermore, they discuss the importance of considering the detailed velocity profile of a site, rather than just the depth to the basin basement or the thickness of sediment.

In addition to using measured data, other studies attempt to simulate the ground motions or provide intensity measure estimates through model predictions. Some examples include calculations of finite-difference seismograms for the 1971 San Fernando earthquake from Vidale & Helmberger (1988) and the use of 2D finite-difference ground-motion simulations for the 1994 Northridge earthquake from Graves, et al. (1998). In later years 3D numerical simulations saw increasing use. Some examples include studies of the 1994 Northridge earthquake (Olsen, et al., 2003), the Landers earthquake (Wald & Graves, 1998), the 2001 Hollywood and the 2002 Yorba Linda earthquakes (Komatitsch, et al., 2004), or scenario earthquakes (Olsen, et al., 1995). State-of-the-art simulations model now wave propagation using realistic rupture, attenuation, and 3D material models. Some examples of recent studies include work on source complexity (Shi & Day, 2013; Graves & Pitarka, 2016; Rodgers, et al., 2018) and fault zone plasticity (Roten, et al., 2017; Wollherr, et al., 2018), as well as work on attenuation models (Withers, et al., 2015; 2019). The most commonly used regional seismic velocity models for this purpose are the two Southern California Earthquake Center (SCEC) Community Velocity Models (CVMs): CVM-S (Magistrale, et al., 2000; Kohler, et al., 2003; Lee, et al., 2014) and CVM-H (Süss & Shaw, 2003; Shaw, et al., 2015). The differences in the two CVMs lead to different simulation results and performance (Lee, et al., 2014; Taborda & Bielak, 2013; 2014; Taborda, et al., 2016).

GMPEs are empirical equations frequently used in seismic hazard applications to provide estimates of the response spectral acceleration, peak ground acceleration and peak ground velocity as a function of predictor variables such as earthquake magnitude, site-to-source distance, and site

parameters (Petersen, et al., 2008). The most frequently used GMPEs, in the Western U.S., are the five that were developed as part of the Next Generation Attenuation-West2 (NGA-West2) project (Bozorgnia, et al., 2014). Similar to the CVMs, the different model derivations result in broad differences in the GMPE predictions (Gregor, et al., 2014).

The last focus of this thesis is to explore the seismic network recordings from two largest events of the 2019 Ridgecrest earthquake sequence in order to investigate the response characteristics in urban Los Angeles, the correlation of the response spectral acceleration with site parameters and the capabilities of 3D simulations and GMPEs in making reliable spectral acceleration predictions.

1.4 Summary of this Thesis

As discussed above, the thesis is organized in two main parts. The first (Chapters 2 and 3) is concerned with the development and implementation of damage identification methodologies, and the second (Chapter 4) is concerned with a study of the recorded and model predicted ground motions in urban Los Angeles for the July 2019 Ridgecrest earthquake sequence. The contents of the remaining chapters (Chapters 2-5) of this dissertation are as follows.

In Chapter 2 we apply a deterministic structural identification approach, and we explore the possibility of tracing possible nonlinear behavior by updating the stiffness and damping ratios of an equivalent linear system model in short time segments of the earthquake-induced excitation and response time histories. In order to achieve this, we combine a linear finite element model updating framework with a moving time window approach. For each time window, the estimation of the model parameters is accomplished in a single stage by minimizing a measure of fit between the measured and model-predicted response time histories. Predictions of the response are obtained using modal analysis for solving the system equations of motion. Details of the implementation of the finite element model updating methodology are presented. We explore the effectiveness of the methodology for two example steel moment frame applications, a single-story and a six-story building. In both models the materials follow a nonlinear softening behavior. For the single story building the methodology is shown to be very effective in tracing the nonlinearities using an

equivalent linear finite element model. The six-story building is designed to reveal also the limitations of the methodology, mainly arising from the different types of model errors manifested in the formulation. These sources of model errors include the discrepancy between the model used to generate the simulated data and the model used for parameter estimation, the stiffness parameterization which constrains the flexibility of the model to fit the simulated data, and the number of contributing modes. In particular, the number of contributing modes is kept fixed and reasonably low over the different time segments in order to avoid ill-conditioning in time segments that do not contain sufficient information to identify higher-order modes. This modal truncation introduces model error in time segments where the non-considered modes are contributing.

In Chapter 3 we adopt and further extend the SBL methodology for structural damage identification in order to handle model nonlinearities, by formulating the problem fully in the time domain using response time history measurements. The available SBL techniques for structural damage identification, discussed in Section 1.2, rely on processing measurements related to modal properties and are thus limited to linear models. The possibility of using nonlinear models allows for higher fidelity finite element models as well as for more accurate representation of the damage in the structure, ultimately reducing model error. We develop a two-step optimization algorithm in which the most probable values of the structural model parameters and the hyper-parameters (related to prediction error and automatic relevance determination prior) are obtained using a two-step iterative approach. It is shown for the first time that the two-step iterative algorithm can be replaced by an equivalent single-objective minimization problem that results in the most probable structural model parameter values. The effectiveness of the methodology is explored for the example problem of identifying damage in the form of weld fractures in a 15-story moment resisting steel frame building, using a nonlinear finite element model and simulated acceleration data. Fiber elements and a bilinear material model are used in order to account for the change of local stiffness when cracks at the welds are subjected to tension and the model parameters characterize the loss of stiffness as the crack opens under tension. The damage identification results demonstrate the effectiveness and robustness of the proposed methodology in identifying the existence, location, and severity of damage for a variety of different damage scenarios and degrees of model and measurement errors.

In Chapter 4 we study the ground motion response in urban LA during two largest events (M7.1 and M6.4) of the July 2019 Ridgecrest earthquake sequence, using recordings from multiple regional seismic networks as well as from the much denser CSN. We calculate and present maps of the response spectral (pseudo) acceleration for a selection of periods of engineering significance. Significant spectral acceleration amplification is present and reproducible between the two events. For the longer periods coherent patterns are visible throughout the whole Los Angeles Basin, while for the shorter periods the high network density was able to capture a smaller scale coherence. Furthermore, we examine possible correlations of the computed spectral accelerations with two site parameters: basement depth and Vs30. Following that, we test the performance of two state-of-the-art methods for estimating ground motions for the largest event (M7.1) of the Ridgecrest earthquake sequence, namely 3D finite difference simulations and ground motion prediction equations. For the simulations, we were interested in the performance of the two Southern California Earthquake Center 3D Community Velocity Models (CVM-S and CVM-H), while for the Ground Motion Prediction Equations, we consider four of the 2014 Next Generation Attenuation-West2 Project equations. We present and discuss maps of the predicted spectral accelerations, as well as comparisons with spectral accelerations calculated from the data in the form of tables and figures.

Chapter 5 discusses conclusions and directions for future work.

Chapter 2

UPDATING EQUIVALENT LINEAR MODELS USING RESPONSE TIME HISTORIES FOR TRACING NONLINEARITIES

This chapter presents a methodology for estimating the condition of a steel moment resisting frame structure and tracing possible nonlinear behavior activated due to an earthquake excitation. Linear finite element model updating is used to track the possible nonlinear behavior of the structure, by using moving time windows and fitting an equivalent linear finite element model within each window. We update the model parameters of the equivalent linear finite element model so that the model predictions match the measured data obtained from the structure within each window. The model parameters correspond to the equivalent stiffness properties as well as to the damping ratios (percent of critical damping) of the contributing modes. The initial conditions for each time window are considered unknown and are added as extra parameters. It is expected that the softening behavior of the structure activated during the strong motion part of the earthquake excitation will result in a decrease of the equivalent linear stiffness. Moreover, the hysteretic loop, associated with energy dissipation, will introduce extra damping which will be manifested as an increase in the modal damping ratios of the equivalent linear finite element model.

This study investigates the effectiveness of the equivalent linear finite element model to detect the nonlinearities activated in the structure during an earthquake excitation. The measurements consist of response time histories, usually accelerations obtained from sensor networks such as the Community Seismic Network (CSN) (Clayton, et al., 2011) on buildings. The matching between the recorded response time histories (here simulated response time histories are generated) and the response time histories predicted by an equivalent linear structural model are obtained by minimizing a misfit function that depends on the model parameters. Implementation details as well as possible ill-conditioning issues are discussed.

Section 2.1 presents the model updating framework, i.e.: the way the equations of motion of the finite element model are solved, the parameterization of the model, and the selected measure-of-fit. Section 2.2 demonstrates four example applications used in order to test the effectiveness of the methodology. Two steel moment frame buildings are used: a single-story and a six-story structure. We discuss the way the data are simulated, the method implementation details, and the results for four example cases. Section 2.3 summarizes the conclusions.

2.1 Model Updating Framework

We consider response time history measurements recorded from a sensor network (such as CSN) that is employed in a structure. The structural type under consideration is a multi-story steel moment frame building. The measurements are collected during a seismic event and consist of earthquake excitations at the base of the building and response time histories at the levels of the different building floors. We assume that the seismic excitation at the base is such that the building model nonlinearities may be activated. Such nonlinearities are mainly associated to the stress-strain hysteretic behavior manifested at the material level of the beam and column elements in the building. The objective is to fit an equivalent linear finite element model of the structure to the available measured data in order to trace possible nonlinear behavior and identify the level of the hysteretic nonlinearities activated during the earthquake excitation. A deterministic finite element model updating method based on input-output response time history measurements is used in this chapter. Since the level of nonlinearities activated during the duration of the excitation varies in time, we use a moving time window approach to associate the activated nonlinearities with the parameters of an equivalent finite element model of the structure for each time window. The variations of the model parameters with respect to time provide insight on the nonlinear behavior of the building during the duration of the earthquake excitation. This chapter investigates the performance of equivalent finite element models identified over each time window for tracing the softening nonlinearities (identify nonlinearities and strength of nonlinear activation) during an earthquake excitation.

To calculate the response time histories using the parameterized linear finite element model, one has to set up the equation of motions and the relation between the response and the stiffness, damping and mass properties. The following Sections 2.1.1 and 2.1.2 present the details of the equations of motion and the solution strategy which is carried out in the time domain using state space analysis. The state space system can be conveniently solved using Matlab in order to predict the responses of linear systems to the input (herein earthquake base) excitations. The equivalent linear finite element model is parameterized with parameters related to stiffness, damping and mass. Details are provided in Section 2.1.3. To estimate these parameters within a time window, one has to introduce a measure of fit between the measured response time histories and the response time histories predicted by the equivalent finite element model. The measure of fit depends on the stiffness properties, the modal damping ratios and the initial conditions of each mode contributing to the response. This is discussed in Section 2.1.4. The last Section 2.1.5 provides implementation details for conveniently reformulating the measure of fit with respect to stiffness properties and modal damping ratios only.

2.1.1 Linear Equations of Motion

For a linear finite element model of a structure subject to earthquake ground motion, the equations of motion are given by the linear system of second order equations

$$\boldsymbol{M}\ddot{\boldsymbol{u}}(t) + \boldsymbol{C}\dot{\boldsymbol{u}}(t) + \boldsymbol{K}\boldsymbol{u}(t) = \boldsymbol{f}_{eff}(t) \tag{2.1}$$

with initial conditions $\boldsymbol{u}(0) = \boldsymbol{u_0}$ and $\dot{\boldsymbol{u}}(0) = \boldsymbol{v_0}$, where $\boldsymbol{u}\epsilon\mathcal{R}^n$ is the displacement, $\dot{\boldsymbol{u}}\epsilon\mathcal{R}^n$ is the velocity, and $\ddot{\boldsymbol{u}}\epsilon\mathcal{R}^n$ is the acceleration of the finite element model degrees of freedom (DOF), with n being the number of the system DOF (these are the DOF of the superstructure and do not include the support/base DOF). The matrices $\boldsymbol{M}\epsilon\mathcal{R}^{n\times n}$, $\boldsymbol{C}\epsilon\mathcal{R}^{n\times n}$, and $\boldsymbol{K}\epsilon\mathcal{R}^{n\times n}$ are the mass, damping, and stiffness matrices respectively. For earthquake excitations at the base of the structure and assuming identical motion for all support/base DOF in a horizontal direction, the vector of effective earthquake forces $\boldsymbol{f}_{eff}(t)\epsilon\mathcal{R}^n$ is equal to

$$\boldsymbol{f}_{eff}(t) = -\boldsymbol{M}\boldsymbol{L}\ddot{\boldsymbol{w}}(t) \tag{2.2}$$

where the influence or correspondence matrix $\boldsymbol{L}\epsilon\mathcal{R}^{n\times N_f}$ is a matrix usually of zeros and ones that associates the set of independent ground accelerations $\ddot{\boldsymbol{w}}(t)\epsilon\mathcal{R}^{N_f}$ to the DOF of the structure. This correspondence is usually restricted to the translational DOF since these are the only components recorded during earthquakes (Chopra, 2011). The independent ground accelerations in $\ddot{\boldsymbol{w}}(t)$ are usually the two horizontal acceleration components recoded by a base sensor. Note that in the case of identical motion for all support/base DOF in the horizontal directions, the translational components of the vector $\boldsymbol{u}$ denote the displacements relative to the base motion (relative displacement). For cases of multiple support excitation, the vector of effective earthquake forces can have a more complicated form but for many practical applications it can be simplified in the form displayed in Eq. (2.2) (Chopra, 2011).

Since the number of system DOF is usually very large, rather than directly solving the equations of motion, we use modal analysis. The modal frequencies ω_r and mass normalized modeshapes $\boldsymbol{\varphi}_r$, with $r = 1, \dots, n$, satisfying $\boldsymbol{\varphi}_r^T\boldsymbol{M}\boldsymbol{\varphi}_r = 1$, are calculated by solving the eigenvalue problem

$$[\boldsymbol{K} - \omega_r^2\boldsymbol{M}]\boldsymbol{\varphi}_r = \boldsymbol{0}\,. \tag{2.3}$$

We keep the lower m contributing modes. Usually $m \ll n$ which helps reduce the dimension of the system considerably. Thus, the response is obtained from the modal expansion

$$\boldsymbol{u}(t) = \sum_{r=1}^{m} \xi_r(t)\boldsymbol{\varphi}_r = \boldsymbol{\Phi}\boldsymbol{\xi}(t) \tag{2.4}$$

where $\boldsymbol{\Phi} = [\boldsymbol{\varphi}_1\ \boldsymbol{\varphi}_2 \dots \boldsymbol{\varphi}_m]\epsilon\mathcal{R}^{n\times m}$ is the matrix of modeshapes, $\xi_r(t)$ with $r = 1, \dots, m$ are the modal coordinates and $\boldsymbol{\xi}(t) = [\xi_1(t)\ \xi_2(t) \dots\ \xi_m(t)]^T$ is the modal vector. Assuming a classically damped system (Caughey & O'Kelly, 1965) one ends up with the modal vector $\boldsymbol{\xi}(t)$ satisfying the system of uncoupled modal equations

$$\ddot{\boldsymbol{\xi}}(t) + \boldsymbol{Z}\dot{\boldsymbol{\xi}}(t) + \boldsymbol{\Lambda}\boldsymbol{\xi}(t) = -\boldsymbol{\Phi}^T\boldsymbol{M}\boldsymbol{L}\ddot{\boldsymbol{w}}(t) \tag{2.5}$$

with initial conditions

$$\boldsymbol{\xi}(0) = \boldsymbol{\Phi}^T\boldsymbol{M}\boldsymbol{u_0} \quad \text{and} \quad \dot{\boldsymbol{\xi}}(0) = \boldsymbol{\Phi}^T\boldsymbol{M}\boldsymbol{v_0} \tag{2.6}$$

and

$$\boldsymbol{\Lambda} = \begin{bmatrix} \omega_1^2 & 0 & 0 \\ 0 & \ddots & 0 \\ 0 & 0 & \omega_m^2 \end{bmatrix} \quad \text{and} \quad \boldsymbol{Z} = \begin{bmatrix} 2\zeta_1\omega_1 & 0 & 0 \\ 0 & \ddots & 0 \\ 0 & 0 & 2\zeta_m\omega_m \end{bmatrix} \tag{2.7}$$

where ω_r^2 are the modal frequencies and ζ_r are the modal damping ratios (percent of critical damping). The equations are uncoupled and each modal coordinate $\xi_r(t)$ satisfies the modal equations

$$\ddot{\xi}_r(t) + 2\zeta_r\omega_r\dot{\xi}_r(t) + \omega_r^2\xi_r(t) = -\boldsymbol{\varphi}_r^T\boldsymbol{M}\boldsymbol{L}\ddot{\boldsymbol{w}}(t), \;\; r = 1, \dots, m \tag{2.8}$$

with initial conditions

$$\xi_r(0) = \boldsymbol{\varphi}_r^T\boldsymbol{M}\boldsymbol{u_0} \quad \text{and} \quad \dot{\xi}_r(0) = \boldsymbol{\varphi}_r^T\boldsymbol{M}v_{\boldsymbol{0}} \, . \tag{2.9}$$

It should be pointed out that in order to simulate the response time history using modal analysis (using Eqs. (2.4) and (2.8) with initial conditions from Eq. (2.9)), one needs to know the stiffness and mass matrices of the structure, the modal damping ratios for the contributing modes, and the initial conditions $\xi_r(0)$ and $\dot{\xi}_r(0)$. In particular, using the stiffness and mass matrices, the eigenvalue problem (2.3) can be solved to obtained the modal frequencies and modeshape components required in the modal equations.

2.1.2 State Space Formulation

In order to solve the second-order system of differential equations (Eq. 2.5), we convert it to its state space form (Antsaklis & Michel, 2007; Friedland, 2012). Introducing the state space vector

$$\boldsymbol{x}(t) = \begin{pmatrix} \boldsymbol{\xi}(t) \\ \dot{\boldsymbol{\xi}}(t) \end{pmatrix} \tag{2.10}$$

the m second-order modal differential equations can be written in the form of a system of $2m$ first order differential equations

$$\dot{\boldsymbol{x}}(t) = \boldsymbol{A}\boldsymbol{x}(t) + \boldsymbol{B}\boldsymbol{p}(t) \tag{2.11}$$

where the matrices $\boldsymbol{A}\epsilon\mathcal{R}^{2m\times 2m}$ and $\boldsymbol{B}\epsilon\mathcal{R}^{2m\times N_f}$ are

$$\boldsymbol{A} = \begin{bmatrix} \boldsymbol{0} & \boldsymbol{I} \\ -\boldsymbol{\Lambda} & -\boldsymbol{Z} \end{bmatrix} \quad \text{and} \quad \boldsymbol{B} = \begin{bmatrix} \boldsymbol{0} \\ \boldsymbol{\Phi^T}\boldsymbol{M}\boldsymbol{L} \end{bmatrix} \tag{2.12}$$

and $\boldsymbol{p}(t) = \ddot{\boldsymbol{w}}(t) \epsilon \mathcal{R}^{N_f}$, with $\boldsymbol{I} \epsilon \mathcal{R}^{m \times m}$ being the identity matrix. The output quantities of interest (QOI) $\boldsymbol{y}(t) \epsilon \mathcal{R}^{n_y}$, which may consist of displacements, velocities, acceleration, strains, etc., depend on the state vector $\boldsymbol{x}$ and the forcing vector $\boldsymbol{p}$. They can be written in the general form

$$\boldsymbol{y}(t) = \boldsymbol{D}\boldsymbol{x}(t) + \boldsymbol{E}\boldsymbol{p}(t) \, . \tag{2.13}$$

As one example to illustrate the selection of $\boldsymbol{D}$ and $\boldsymbol{E}$, consider the case where the output QOI consists of components of the acceleration $\ddot{\boldsymbol{u}}(t)$ at some "measured" DOF. For this case one has

$$\boldsymbol{y}(t) = \boldsymbol{H}\ddot{\boldsymbol{u}}(t) \tag{2.14}$$

where $\boldsymbol{y}(t) \epsilon \mathcal{R}^{n_o}$, with n_o being the number of measured/observed degrees of freedom, and $\boldsymbol{H} \epsilon \mathcal{R}^{n_o \times n}$ is a matrix of zeros and ones that associates the n DOF of the model to the n_o DOF that are measured. Then, using Eqs. (2.4) and (2.5) and solving with respect to $\ddot{\boldsymbol{u}}(t)$, one has

$$\begin{aligned} \boldsymbol{y}(t) = \boldsymbol{H}\ddot{\boldsymbol{u}}(t) = \boldsymbol{H}\boldsymbol{\Phi}\ddot{\boldsymbol{\xi}}(t) = \boldsymbol{H}\boldsymbol{\Phi}\left(-\boldsymbol{Z}\dot{\boldsymbol{\xi}}(t) - \boldsymbol{\Lambda}\boldsymbol{\xi}(t) + \boldsymbol{\Phi}^T\boldsymbol{M}\boldsymbol{L}\ddot{\boldsymbol{w}}(t)\right) \\ = \left[-\boldsymbol{H}\boldsymbol{\Phi}\boldsymbol{\Lambda} \quad -\boldsymbol{H}\boldsymbol{\Phi}\boldsymbol{Z}\right]\begin{pmatrix}\boldsymbol{\xi}(t)\\ \dot{\boldsymbol{\xi}}(t)\end{pmatrix} + \boldsymbol{H}\boldsymbol{\Phi}\,\boldsymbol{\Phi}^T\boldsymbol{M}\boldsymbol{L}\ddot{\boldsymbol{w}}(t) \, . \end{aligned} \tag{2.15}$$

Thus Eq. (2.15) can be written in the form of Eq. (2.13) with

$$\boldsymbol{D} = \left[-\boldsymbol{H}\boldsymbol{\Phi}\boldsymbol{\Lambda} \quad -\boldsymbol{H}\boldsymbol{\Phi}\boldsymbol{Z}\right] \quad \text{and} \quad \boldsymbol{E} = \boldsymbol{H}\boldsymbol{\Phi}\boldsymbol{\Phi}^T\boldsymbol{M}\boldsymbol{L} \, . \tag{2.16}$$

As a second example, consider the case where the output QOI consists of the velocity $\dot{\boldsymbol{u}}(t)$ at some "measured" DOF. For this case one has

$$\boldsymbol{y}(t) = \boldsymbol{H}\dot{\boldsymbol{u}}(t) \tag{2.17}$$

where again $\boldsymbol{y}(t) \epsilon \mathcal{R}^{n_o}$, with n_o being the number of measured/observed degrees of freedom, and $\boldsymbol{H} \epsilon \mathcal{R}^{n_o \times n}$ is a matrix of zeros and ones that associates the n DOF of the model to the n_o DOF that are measured. Then using Eq. (2.4) one has

$$\boldsymbol{y}(t) = \boldsymbol{H}\dot{\boldsymbol{u}}(t) = \boldsymbol{H}\boldsymbol{\Phi}\dot{\boldsymbol{\xi}}(t) \, . \tag{2.18}$$

Thus Eq. (2.15) can be written in the form of Eq. (2.13) with

$$\boldsymbol{D} = \left[\boldsymbol{0} \quad \boldsymbol{H}\boldsymbol{\Phi}\right] \quad \text{and} \quad \boldsymbol{E} = \boldsymbol{0} \, . \tag{2.19}$$

The numerical solution of the equations of motion in modal space is carried out using Matlab software tools based on the state space analysis. One can use one of the many available methods to solve the linear first-order system. Herein, the system is discretized assuming zero-order hold for the input (Antsaklis & Michel, 2007).

Next we derive analytical formulas for the response using state space formulation. The analysis that follows is required in simplifying the measure of fit introduced in Section 2.5 in terms of a reduced number of parameters. The solution (Friedland, 2012) of Eq. (2.11) is

$$\boldsymbol{x}(t) = e^{\boldsymbol{A}t}\boldsymbol{x}(0) + \int_0^t e^{\boldsymbol{A}(t-\tau)}\boldsymbol{B}\boldsymbol{p}(\tau)d\tau \tag{2.20}$$

and the solution of Eq. (2.13) is given by

$$\boldsymbol{y}(t) = \boldsymbol{D}e^{\boldsymbol{A}t}\boldsymbol{x}(0) + \boldsymbol{D}\int_0^t e^{\boldsymbol{A}(t-\tau)}\boldsymbol{B}\boldsymbol{p}(\tau)d\tau + \boldsymbol{E}\boldsymbol{p}(t)\,. \tag{2.21}$$

Introducing $\boldsymbol{\Psi}(t) = \boldsymbol{D}e^{\boldsymbol{A}t}$, we have

$$\boldsymbol{y}(t) = \boldsymbol{\Psi}(t)\boldsymbol{x}(0) + \boldsymbol{y}_0(t) \tag{2.22}$$

where

$$\boldsymbol{y}_0(t) = \boldsymbol{D}\int_0^t e^{\boldsymbol{A}(t-\tau)}\boldsymbol{B}\boldsymbol{p}(\tau)d\tau + \boldsymbol{E}\boldsymbol{p}(t)\,. \tag{2.23}$$

The total solution is the superposition of two terms. The second term corresponds to the solution $\boldsymbol{y}_0(t)$, for zero initial conditions $\boldsymbol{x}(0)$ and non-zero force $\boldsymbol{p}(t)$, while the first term corresponds to the solution $\boldsymbol{\Psi}(t)\boldsymbol{x}(0)$ for non-zero initial conditions $\boldsymbol{x}(0)$ and zero force $\boldsymbol{p}(t)$. We can also write the solution as

$$\boldsymbol{y}(t) = [\boldsymbol{\psi}_1(t), \dots, \boldsymbol{\psi}_{2m}(t)]\boldsymbol{x}(0) + \boldsymbol{y}_0(t) \tag{2.24}$$

where $\boldsymbol{\psi}_i(t)$ are the columns of the matrix $\boldsymbol{\Psi}(t) = [\boldsymbol{\psi}_1(t), \dots, \boldsymbol{\psi}_{2m}(t)]$. It should be noted that the columns $\boldsymbol{\psi}_i(t)$ can be obtained by solving the linear system with zero force $\boldsymbol{p}(t) = \boldsymbol{0}$ and initial condition $\boldsymbol{x}(0) = \boldsymbol{\delta}_i$, where $\boldsymbol{\delta}_i$ is a vector with one at the i-th element and zero at all other

elements. Using the modal equations (2.8) with initial conditions (2.9), one can develop analytical expressions for the column vectors $\boldsymbol{\psi}_r(t)$ or $\boldsymbol{\psi}_{r+m}(t)$ with respect to the modal frequencies ω_r, modal damping ratios ζ_r and the initial conditions $(\xi_r(0), \dot{\xi}_r(0)) = (1,0)$ or $(\xi_r(0), \dot{\xi}_r(0)) = (0,1)$.

2.1.3 Parameterization

In order to achieve our goal of tracing nonlinear behavior by updating a linear model with a moving time window, several types of parameters can be introduced in our modeling. In this study the model parameters include stiffness-related parameters and damping-related parameters. The stiffness and damping are expected to vary as the model goes through nonlinear behavior. The nonlinearities occurring within a time window, will be manifested as changes in the model parameter values, with the amount of change in the parameters reflecting the size of nonlinearity activated during the earthquake. Furthermore, due to the use of a moving time window, the initial conditions for each time window are treated as extra parameters to be estimated in the model updating formulation.

More specifically, the model updating process involves a set of parameters $\boldsymbol{\theta} \epsilon \mathcal{R}^{N_\theta}$ of the finite element model, also referred to as model parameters. We consider two types of model parameters: stiffness related parameters ($\boldsymbol{\theta}_K$) and damping related parameters ($\boldsymbol{\theta}_\zeta$). Thus it holds that $\boldsymbol{\theta} = \left[\boldsymbol{\theta}_K^T, \boldsymbol{\theta}_\zeta^T\right]^T$. The finite elements of the model are grouped into substructures. Let N_S be the number of substructures. A convenient parameterization for the stiffness and mass matrices is (Simoen, et al., 2015)

$$\boldsymbol{K}(\boldsymbol{\theta}) = \boldsymbol{K_0} + \sum_{j=1}^{N_S} \boldsymbol{K_j} \theta_{K,j} \tag{2.25}$$

where each $\boldsymbol{K_j}$ are the nominal contributions to the global stiffness matrix from substructure j. These nominal substructure contributions can be calculated from a finite element model of the undamaged structure. The nominal stiffness matrix is $\boldsymbol{K}(\boldsymbol{\theta_0})$ where $\boldsymbol{\theta_0} = [1,1,\dots,1]^T$. Here, the

number of stiffness related parameters equals the number of substructures, i.e. $\boldsymbol{\theta}_K \epsilon \mathcal{R}^{Ns}$. The substructures are selected in order to achieve the desired parameterization with every substructure j being assigned a stiffness related ($\theta_{K,j}$) parameter.

The mass matrix ($\boldsymbol{M}$) could also be parameterized using mass related parameters and a substructuring approach similar to what is done for the stiffness matrix ($\boldsymbol{K}$) in Eq. (2.25) can be derived. However, for our problem of tracing nonlinear behavior we will assume that the mass matrix is known and remains constant. Parameterizing the mass matrix can be of interest for damage identification (in cases where the change of mass is non-negligible) and for fitting the nominal finite element model (e.g., when the mass calculated from structural drawings is not sufficient or precise).

This parameterization is by no means exhaustive but is very convenient since the interfacing of the finite element software (e.g., SAP2000, or OpenSEES) with the optimization process (e.g., using Matlab optimizers) can be completely avoided. Before the optimization, the model can be efficiently parameterized in the finite element software and the information for the stiffness and mass properties of the different substructures are passed (offline) to the optimization process.

The other type of model parameters are damping related parameters, and more specifically the percent critical damping for each contributing mode. Assuming classically damped modes, the number of such parameters is equal to the number of contributing modes. For Rayleigh damping, the number of parameters is 2. However, Rayleigh damping is not used in this study. Assigning an independent modal damping ratio for each mode gives more freedom to fit the data. This may result in ill-conditioning if one or more of the considered modes do not contribute to the response. Nonlinearities due to the plastic (hysteresis loop) energy dissipation within a time window are expected to be manifested as a decrease in the equivalent stiffness of the linear finite element model and as an increase in the equivalent percent critical damping of the viscous damping model.

Finally, the third type of parameters needed, since we are using a moving window approach, are the initial conditions. When using a moving time window approach at the start of each window, the initial conditions are non-zero and unknown, so they are left to be selected by the model updating methodology in order to provide the best fit to the measured data within the window. Let $\boldsymbol{\gamma} \epsilon \mathcal{R}^{N_\gamma}$ denote the unknown initial conditions. The initial conditions augment the unknown parameter set $\boldsymbol{\theta}$, to the new parameter set $(\boldsymbol{\theta}, \boldsymbol{\gamma})$. Since we perform modal analysis to estimate the response, the initial conditions are required at the modal level, and the number of unknown initial conditions will be equal to the dimension of the state vector, i.e. $N_\gamma = 2m$. Thus the total number of unknown parameters to be estimated is $N_\theta + 2m$ (where m is the number of considered modes).

The procedure for calculating the response given the values of the model parameters is as follows. Given the values of the stiffness related parameters $\boldsymbol{\theta}_K$, one can conveniently obtain the stiffness matrix of the model using the expansion presented in Eq. (2.25). The eigenvalue problem in Eq. (2.3) is then solved to estimate the modal frequencies ω_r and modeshapes $\boldsymbol{\varphi}_r$. Using also the modal damping ratio parameters ζ_r in $\boldsymbol{\theta}_\zeta$ and the initial conditions in $\boldsymbol{\gamma}$, the predictions of the response time histories are obtained by solving the modal equations (2.8) and applying the modal expansion Eq. (2.4).

Depending on the number of considered modes m, including the unknown initial conditions in the parameter space can increase drastically the number of unknown parameters as it can often be that $2m \gg N_\theta$. However, as we will see in Section 2.1.4, the measure-of-fit that we minimize depends quadratically on the initial conditions $\boldsymbol{\gamma}$. This allows us to simplify considerably the formulation and express $\boldsymbol{\gamma}$ analytically with respect to $\boldsymbol{\theta}$, thus reducing to N_θ the number of the unknown parameters involved in the measure-of-fit.

2.1.4 Measure-of-fit

The selected measure-of-fit function (also referred to as misfit function) is based on response time histories. Let $\hat{\boldsymbol{y}}(k) \equiv \hat{\boldsymbol{y}}(t_k)$ denote the measured response time histories (e.g., accelerations or

velocities) available from sensors placed in the structure, where $t_k = k\Delta t$, $k = 1, \ldots, N_d$, Δt is the sampling/discretization time and N_d is the number of time data points. Let also $\boldsymbol{y}(k;\boldsymbol{\theta},\boldsymbol{\gamma}) \equiv \boldsymbol{y}(t_k;\boldsymbol{\theta},\boldsymbol{\gamma})$ denote the corresponding predictions from the finite element model of the structure. These predictions depend on the model parameters $\boldsymbol{\theta}$ and the initial conditions $\boldsymbol{\gamma}$ which are assumed unknown and have to be estimated simultaneously with the model parameters $\boldsymbol{\theta}$.

The measure-of-fit represents the misfit between these measured response time histories $\hat{\boldsymbol{y}}(k) \epsilon \mathcal{R}^{n_o}$ and the finite element model predicted response time histories $\boldsymbol{y}(k;\boldsymbol{\theta},\boldsymbol{\gamma}) \epsilon \mathcal{R}^{n_o}$, where n_o is the number of measured/observed degrees of freedom. The measure-of-fit (the objective function) to be minimized for estimating the model parameters and the initial conditions is defined as

$$J(\boldsymbol{\theta},\boldsymbol{\gamma}) = \frac{\tilde{J}(\boldsymbol{\theta},\boldsymbol{\gamma})}{\sum_{k=1}^{N_d} \|\hat{\boldsymbol{y}}(k)\|^2} \tag{2.26}$$

with $\tilde{J}(\boldsymbol{\theta},\boldsymbol{\gamma})$ being the least squares error between the model predicted and the data response time histories

$$\tilde{J}(\boldsymbol{\theta},\boldsymbol{\gamma}) = \sum_{k=1}^{N_d} \|\boldsymbol{y}(k;\boldsymbol{\theta},\boldsymbol{\gamma}) - \hat{\boldsymbol{y}}(k)\|^2 \tag{2.27}$$

and the normalizing constant $\sum_{k=1}^{N_d} \|\hat{\boldsymbol{y}}(k)\|^2$, the the sum of squares of the response time histories, is used to provide a normalized measure of the misfit. Thus the objective function represents a normalized least squares error between the model-predicted and the measured response time histories. The optimal values of the parameters $(\boldsymbol{\theta},\boldsymbol{\gamma})$ are obtained by minimizing the measure of fit with respect to $\boldsymbol{\theta}$ and $\boldsymbol{\gamma}$.

The responses $\boldsymbol{y}(t;\boldsymbol{\theta},\boldsymbol{\gamma})$ denote the solution $\boldsymbol{y}(t)$ presented in Section 2.3 that depends on the values of the parameters $(\boldsymbol{\theta},\boldsymbol{\gamma})$. From Eq. (2.24) the total solution is obtained as

$$\boldsymbol{y}(t;\boldsymbol{\theta},\boldsymbol{\gamma}) = [\boldsymbol{\psi}_1(t;\boldsymbol{\theta}), \ldots, \boldsymbol{\psi}_{2m}(t;\boldsymbol{\theta})]\boldsymbol{\gamma} + \boldsymbol{y}_0(t;\boldsymbol{\theta}) \,. \tag{2.28}$$

From the above equation one can see that the response $\boldsymbol{y}(t)$ depends linearly on the parameters $\boldsymbol{\gamma}$ and nonlinearly on the parameters $\boldsymbol{\theta}$. Thus the objective function in (2.27) is quadratic in the

parameters $\boldsymbol{\gamma}$. In the next section (Section 2.1.5) this particular structure of the response and the objective function will be used to simplify the parameter estimation problem using a measure-of-fit that is based on response time histories. This simplification amounts to computing $\boldsymbol{\gamma}$ with respect to $\boldsymbol{\theta}$ and thus reducing the parameters to be estimated to those involved in $\boldsymbol{\theta}$ in the formulation for the measure of fit.

2.1.5 Reformulation of measure-of-fit with respect to θ

Making use of Eq. (2.28), the least squares error $\tilde{J}(\boldsymbol{\theta},\boldsymbol{\gamma})$ in Eq. (2.27) can be written as

$$\tilde{J}(\boldsymbol{\theta},\boldsymbol{\gamma}) = \sum_{k=1}^{N_d} \|[\boldsymbol{\psi}_1(k;\boldsymbol{\theta}),\dots,\boldsymbol{\psi}_{2m}(k;\boldsymbol{\theta})]\boldsymbol{\gamma} + \boldsymbol{y}_0(k;\boldsymbol{\theta}) - \hat{\boldsymbol{y}}(k)\|^2 \tag{2.29}$$

which gives

$$\tilde{J}(\boldsymbol{\theta},\boldsymbol{\gamma}) = \sum_{k=1}^{N_d} [\gamma_1\boldsymbol{\psi}_1(k;\boldsymbol{\theta}) + \cdots + \gamma_{2m}\boldsymbol{\psi}_{2m}(k;\boldsymbol{\theta}) + \boldsymbol{y}_0(k;\boldsymbol{\theta}) - \hat{\boldsymbol{y}}(\mathrm{k})]^T [\gamma_1\boldsymbol{\psi}_1(k;\boldsymbol{\theta}) + \cdots + \gamma_{2m}\boldsymbol{\psi}_{2m}(k;\boldsymbol{\theta}) + \boldsymbol{y}_0(k;\boldsymbol{\theta}) - \hat{\boldsymbol{y}}(k)] .$$

One can explore the fact that the objective function $\tilde{J}(\boldsymbol{\theta},\boldsymbol{\gamma})$ is quadratic in $\boldsymbol{\gamma}$ in order to write an explicit relation between the optimal value $\hat{\boldsymbol{\gamma}}(\boldsymbol{\theta})$ conditioned on the value of $\boldsymbol{\theta}$ and then write the least squares error function $\tilde{J}\big(\boldsymbol{\theta},\hat{\boldsymbol{\gamma}}(\boldsymbol{\theta})\big) = \tilde{\mathcal{J}}(\boldsymbol{\theta})$ and the measure-of-fit function $J\big(\boldsymbol{\theta},\hat{\boldsymbol{\gamma}}(\boldsymbol{\theta})\big) = \mathcal{J}(\boldsymbol{\theta})$ with respect to the parameter set $\boldsymbol{\theta}$ only. This reduces the number of parameters to be estimated, often accelerating the computation and also avoiding ill-conditioning of the parameter estimation problem arising from the large number of parameters involved. The relation $\hat{\boldsymbol{\gamma}}(\boldsymbol{\theta})$ is obtained by considering the condition at the minimum which is

$$\frac{\partial\tilde{J}(\boldsymbol{\theta},\boldsymbol{\gamma})}{\partial\gamma_j} = 0, \qquad j = 1,\dots,2m \tag{2.30}$$

and exploiting the quadratic relation between the objective function $\tilde{J}(\boldsymbol{\theta},\boldsymbol{\gamma})$ and the parameters $\boldsymbol{\gamma}$ to analytically solve for the optimal value $\hat{\boldsymbol{\gamma}}(\boldsymbol{\theta})$ given the value of $\boldsymbol{\theta}$. Specifically, the derivative in the left-hand side of Eq. (2.30) is

$$\begin{aligned}\frac{\partial \tilde{J}(\boldsymbol{\theta},\boldsymbol{\gamma})}{\partial \gamma_j} &= \sum_{k=1}^{N_d} 2[\gamma_1\boldsymbol{\psi}_1(k;\boldsymbol{\theta})+\cdots+\gamma_{2m}\boldsymbol{\psi}_{2m}(k;\boldsymbol{\theta})+\boldsymbol{y}_0(k;\boldsymbol{\theta})-\hat{\boldsymbol{y}}(k)]^T\frac{\partial}{\partial\gamma_j}[\gamma_1\boldsymbol{\psi}_1(k;\boldsymbol{\theta})+\cdots+\gamma_{2m}\boldsymbol{\psi}_{2m}(k;\boldsymbol{\theta}) \\ &\qquad +\boldsymbol{y}_0(k;\boldsymbol{\theta})-\hat{\boldsymbol{y}}(k)] \\ &= \sum_{k=1}^{N_d} 2[\gamma_1\boldsymbol{\psi}_1(k;\boldsymbol{\theta})+\cdots+\gamma_{2m}\boldsymbol{\psi}_{2m}(k;\boldsymbol{\theta})+\boldsymbol{y}_0(k;\boldsymbol{\theta})-\hat{\boldsymbol{y}}(k)]^T\boldsymbol{\psi}_j(k;\boldsymbol{\theta}) \\ &= \sum_{k=1}^{N_d} 2\big[\gamma_1\boldsymbol{\psi}_1^T(k;\boldsymbol{\theta})\boldsymbol{\psi}_j(k;\boldsymbol{\theta})+\cdots+\gamma_{2m}\boldsymbol{\psi}_{2m}^T(k;\boldsymbol{\theta})\boldsymbol{\psi}_j(k;\boldsymbol{\theta})+\{\hat{\boldsymbol{y}}(k)-\boldsymbol{y}_0(k;\boldsymbol{\theta})\}^T\boldsymbol{\psi}_j(k;\boldsymbol{\theta})\big]\end{aligned} \tag{2.31}$$

which when introduced in the stationarity conditions (Eqs. (2.30)) one derives

$$\gamma_1\sum_{k=1}^{N_d}\big[\boldsymbol{\psi}_1^T(k;\boldsymbol{\theta})\boldsymbol{\psi}_j(k;\boldsymbol{\theta})\big]+\cdots+\gamma_{2m}\sum_{k=1}^{N_d}\big[\boldsymbol{\psi}_{2m}^T(k;\boldsymbol{\theta})\boldsymbol{\psi}_j(k;\boldsymbol{\theta})\big]=\sum_{k=1}^{N_d}\big[\{\hat{\boldsymbol{y}}(k)-\boldsymbol{y}_0(k;\boldsymbol{\theta})\}^T\boldsymbol{\psi}_j(k;\boldsymbol{\theta})\big] \tag{2.32}$$

for $j=1,\ldots,2m$. Introducing the quantities

$$\Delta_{ij}=\sum_{k=1}^{N_d}\big[\boldsymbol{\psi}_i^T(k;\boldsymbol{\theta})\boldsymbol{\psi}_j(k;\boldsymbol{\theta})\big] \tag{2.33}$$

and

$$d_j=\sum_{k=1}^{N_d}\big[\{\hat{\boldsymbol{y}}(k)-\boldsymbol{y}_0(k;\boldsymbol{\theta})\}^T\boldsymbol{\psi}_j(k;\boldsymbol{\theta})\big] \tag{2.34}$$

and noting that $\boldsymbol{\Delta}(\boldsymbol{\theta})\epsilon\mathcal{R}^{2m\times 2m}$ with elements Δ_{ij} is a matrix of dimension $2m\times 2m$ and $\boldsymbol{d}(\boldsymbol{\theta})\epsilon\mathcal{R}^{2m}$ with elements d_j is a vector of dimension $2m$, a system of $2m$ equations arises from Eq. (2.30) which can be written in matrix form as

$$\boldsymbol{\Delta}(\boldsymbol{\theta})\boldsymbol{\gamma}=\boldsymbol{d}(\boldsymbol{\theta}) \tag{2.35}$$

The solution of (2.35) is $\hat{\boldsymbol{\gamma}}=\hat{\boldsymbol{\gamma}}(\boldsymbol{\theta})$ given by

$$\hat{\boldsymbol{\gamma}}(\boldsymbol{\theta})=[\boldsymbol{\Delta}(\boldsymbol{\theta})]^{-1}\boldsymbol{d}(\boldsymbol{\theta})\,. \tag{2.36}$$

Introducing the value of $\hat{\boldsymbol{\gamma}}(\boldsymbol{\theta})$ in the least squares error equation (2.27), one derives that

$$\begin{aligned}\tilde{J}(\boldsymbol{\theta}) &= \tilde{J}\big(\boldsymbol{\theta}, \hat{\boldsymbol{\gamma}}(\boldsymbol{\theta})\big) \\ &= \sum_{k=1}^{N_d} \|\boldsymbol{\Psi}(k;\boldsymbol{\theta})\hat{\boldsymbol{\gamma}}(\boldsymbol{\theta}) + \boldsymbol{y}_0(k;\boldsymbol{\theta}) - \hat{\boldsymbol{y}}(k)\|^2\end{aligned} \tag{2.37}$$

where $\hat{\boldsymbol{\gamma}}(\boldsymbol{\theta})$ is given by (2.36). Substituting (2.36) into (2.37) gives

$$\tilde{J}(\boldsymbol{\theta}) = \sum_{k=1}^{N_d} \left\|\boldsymbol{\Psi}(k;\boldsymbol{\theta})[\boldsymbol{\Delta}(\boldsymbol{\theta})]^{-1}\boldsymbol{d}(\boldsymbol{\theta}) + \boldsymbol{y}_0(k;\boldsymbol{\theta}) - \hat{\boldsymbol{y}}(k)\right\|^2 . \tag{2.38}$$

It should be noted that the first term in the right-hand side (RHS) of Eq. (2.38) takes into account that the initial conditions are unknown and non-zero. This first term in the RHS will disappear if the initial conditions are assumed to be zero.

From (2.26) the measure-of-fit $\mathcal{J}(\boldsymbol{\theta}) = J\big(\boldsymbol{\theta}, \hat{\boldsymbol{\gamma}}(\boldsymbol{\theta})\big)$ is a function of $\boldsymbol{\theta}$ only

$$\mathcal{J}(\boldsymbol{\theta}) = \frac{\tilde{J}(\boldsymbol{\theta})}{\sum_{k=1}^{N_d} \|\hat{\boldsymbol{y}}(k)\|^2} \tag{2.39}$$

with $\tilde{J}(\boldsymbol{\theta})$ given from Eq. (2.38). Thus the optimization problem is converted to minimizing $\mathcal{J}(\boldsymbol{\theta})$ with respect to $\boldsymbol{\theta}$.

Finally, the Hessian matrix of the objective function $\mathcal{J}(\boldsymbol{\theta})$ computed at the optimal value of the model parameters contains useful information about the accuracy of the estimates of the model parameters and the possible ill-conditioning of the estimation problem. Specifically, an eigenvalue of the Hessian matrix gives an estimate of the accuracy of the parameters along the direction in the parameter space defined by the corresponding eigenvector. Large eigenvalues of the Hessian correspond to strong curvatures of the objective function and relate to good localization or estimation of the parameter value, while small eigenvalues correspond to weak curvatures and relate to high uncertainty in the parameter value or low estimation accuracy. The condition number of the Hessian matrix, defined as the ratio of the maximum to the minimum eigenvalue, provides a quantitative measure of the ill-conditioning in the estimation of the model parameters. In this

study, in addition to the optimal values of the model parameters that minimize the measure of fit, the Hessian of the measure of fit at the optimal parameter values is computed numerically and an estimate of the condition number is reported.

2.2 Example Applications

We apply the presented methodology to four example cases in order to test the capabilities and effectiveness of the proposed structural identification framework in tracking the change in the model parameters as the system moves from linear to non-linear behavior. The four example cases involve two example steel moment frame buildings: a single-story and a six-story. In the absence of experimental data, we simulate data using a nonlinear model of the structures, while a linear model is used for the updating. For simulating the data, we consider two excitation types: an impulse and an earthquake excitation. For the measure-of-fit, we consider two different QOI (y): acceleration or velocity time histories.

The four example cases being presented in this section are as follows:

- Case 1: One-story structure - Impulse excitation - Fitting acceleration time histories
- Case 2: One-story structure - Earthquake excitation - Fitting acceleration time histories
- Case 3: Six-story structure - Earthquake excitation - Fitting acceleration time histories
- Case 4: Six-story structure - Earthquake excitation - Fitting velocity time histories

2.2.1 Simulating the data

In the absence of experimental data, simulated data are generated for the two building models by subjecting them to specified ground acceleration. In the examples presented we consider two types of ground excitation: A) an impulse excitation, and B) an earthquake excitation.

The impulse excitation was selected for its simplicity. Using the excitation input and the simpler one-story structure it is clear to demonstrate the effectiveness of the methodology. The impulse

consists of a ramp up and then a decrease, as is shown in Figure 2.1A. For the rest of the presented cases, a more realistic input is used. The structure is subjected to scaled versions of the Nishi-Akashi station ground acceleration, recorded during the 1995 M6.9 Kobe Japan earthquake, shown in Figure 2.1B.

In order to study the transition to the nonlinear regime, we considered three different time-domain amplitude scales for both ground acceleration inputs. The scales for the ground acceleration inputs were selected so that for the lower scaling the structure behaves linearly, while for the higher scales nonlinear mechanisms due to softening behavior of the steel beams and columns are activated.

For the impulse excitation, the analyses were repeated for the three different scales: x1.0 (nonlinearities are not activated – response is linear), x15.0 (nonlinearities are activated), and x30.0 (stronger nonlinearities are activated). For the earthquake, the analyses were similarly repeated for the three different scales: x0.2 (nonlinearities are not activated – response is linear), x1.0 (nonlinearities are activated), and x2.0 (stronger nonlinearities are activated).

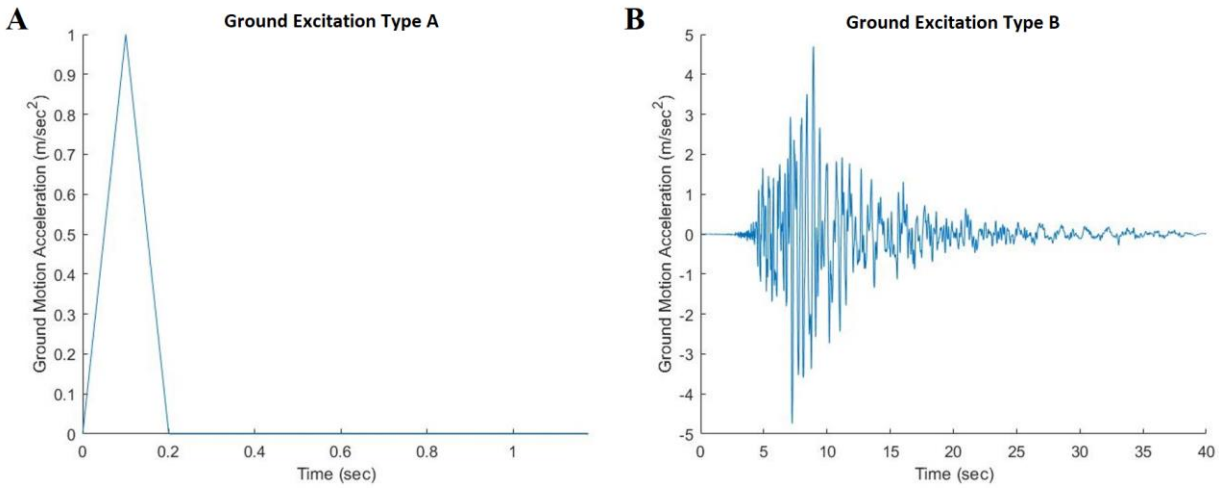

Figure 2.1. The two ground acceleration inputs considered. (A) The impulse excitation, unscaled – x1.0. (B) The earthquake excitation (1995 Kobe Japan Nishi-Akashi station record), unscaled – x1.0.

2.2.2 Implementation Details

While the data is simulated through the use of a nonlinear model, a linear model is fitted to the data in every time window. Linear model updating is performed in each time window by minimizing the measure-of-fit, shown in Eq. (2.38). The length of the time window and the time step the time window is being shifted in the moving window approach are defined by the user. Different QOI or even weighted combinations of QOI can be used in the measure-of-fit. For the results presented here we assume to have one sensor at every floor and the measured QOI considered in the analysis will be either acceleration or velocity time histories.

The choice of the window length should be longer than the fundamental period of the equivalent model of the structure so that the time series (e.g., acceleration) signal within the window length contains sufficient information to identify the lowest modal frequencies of the equivalent linear model. Also, the window length should be short enough so that one can trace the variation in the nonlinearities (type and strength) activated during the earthquake. A very long window length will average the time varying nonlinear characteristics activated in the structure during the excitation. The value of the shift of the center of the window length in the moving window approach affects the smoothing of the time varying curves that demonstrate the mechanical characteristics (stiffness, damping ratio, modal frequencies, etc.) of the equivalent linear system. Note that the time windows may overlap.

As part of this thesis work, the structural identification framework presented in Section 2.1 has been fully implemented in Matlab. In order to minimize the measure-of-fit, optimization algorithms native to Matlab are used. Specifically, the *fminunc* Broyden–Fletcher–Goldfarb–Shanno (BFGS) algorithm (MATLAB, 2019; Broyden, 1970), an unconstrained gradient-based optimization is used. The stiffness and mass information (the stiffness submatrices appearing in the expansion (2.25) and the mass matrix) are calculated using models created in commercial finite element software (e.g. SAP2000 is used for the examples presented here) and is passed (offline) in Matlab. The gradients of the objective function with respect to the model parameters are estimated numerically in the Matlab optimization toolbox.

Even though the modulus of elasticity of the material does not change, a convenient way to introduce the desired stiffness parameterization, as seen in Eq. (2.25), is by specifying the modulus of elasticity of the elements belonging to the substructure to be proportional to the stiffness-related parameters $\boldsymbol{\theta}_K$. Thus, the stiffness of the substructure is parameterized by selecting the modulus of elasticity of all finite elements (columns and beams) comprising the substructure to be proportional to a parameter, with proportionality constant defined by their nominal modulus of elasticity values. Specifically, if E denotes the modulus of elasticity of an element belonging to the j substructure, then $E = \theta_{K,j} E_{nom}$, where E_{nom} is the nominal value of the modulus of elasticity of the element (Simoen, et al., 2015). Selecting the value of the parameter to be equal to 1 corresponds to the nominal values of the substructure of the finite element model.

2.2.3 Building Models Considered

Two example buildings, a single-story and a six-story building, are considered. The two buildings are shown in Figure 2.2.

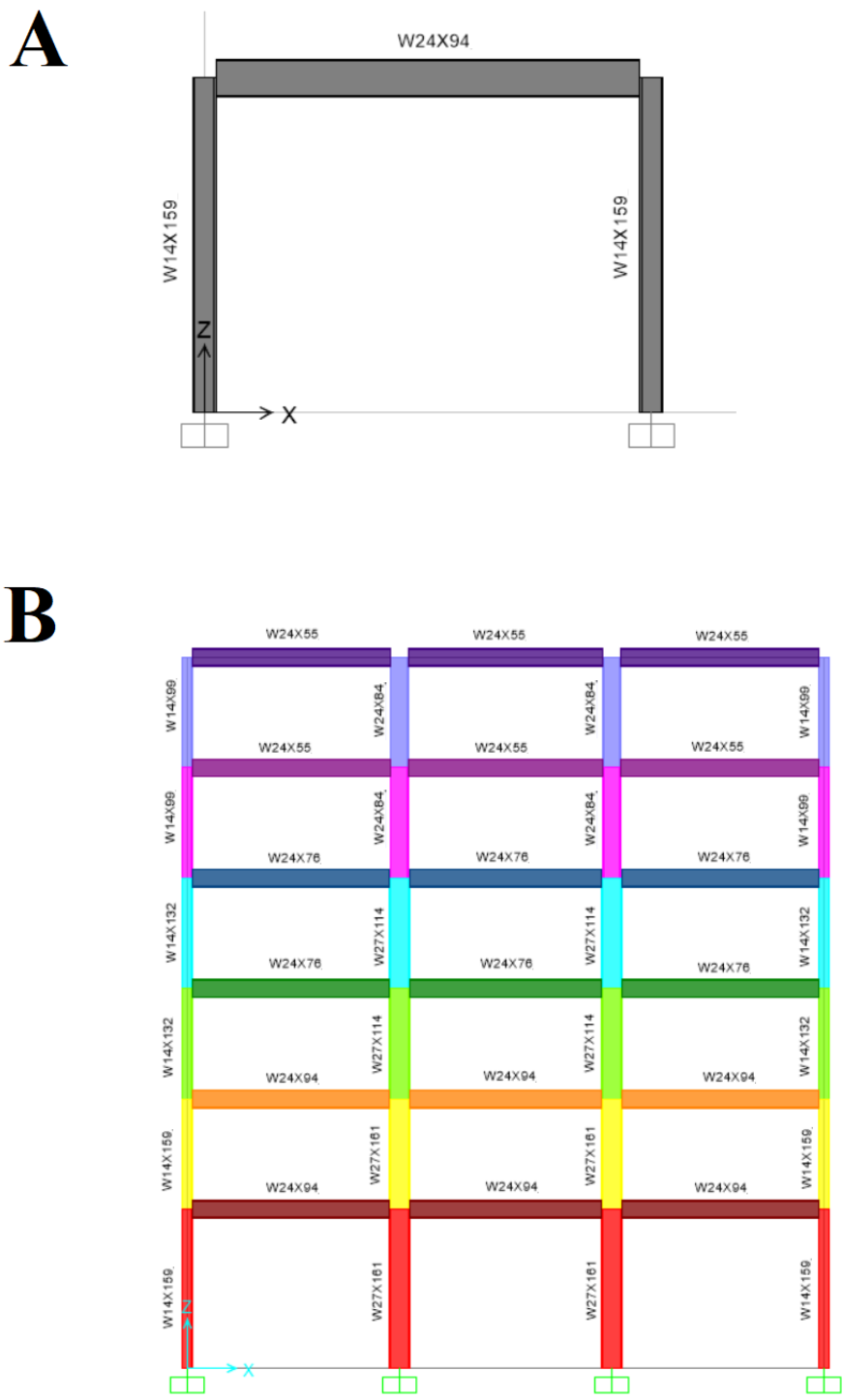

Figure 2.2 The two steel moment frame structures (plotted using the SAP2000 interface) (A) One-story Steel Frame Model. (B) Six-story Steel Frame Model. The I-beam sections assigned to each element are also displayed.

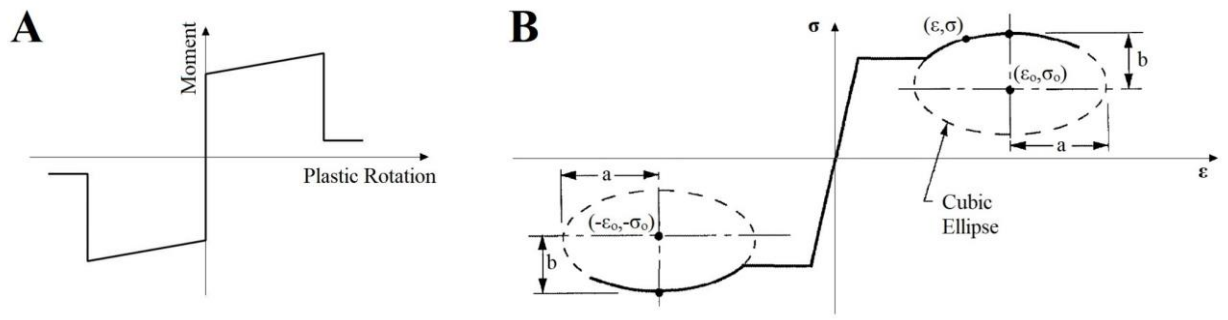

Figure 2.3. Material nonlinearities in the two models. (A) Hinge moment-plastic rotation curve. (B) Axial stress-strain curve for beam and column fibers. Figure is modified from Challa (1992).

2.2.3.1 Structure 1: One-story Steel Moment Frame Building

The first example building considered is a simple, one-story, steel frame structure. The structure is composed of 2 columns and 1 horizontal beam. The structure and the selected I-beam frame sections can be seen in Figure 2.2A. The material used is A36 steel.

A 2D model of the structure was constructed in SAP2000 (CSI, 1999). All connections are moment connections. Additionally, we assume fixed constraints for the nodes at the base, motion only in the x (horizontal) direction, and rigid diaphragm constraints for the first floor nodes. A hinge at the bottom of the columns is introduced to model a nonlinear softening moment-rotation relationship. The hinge represents concentrated post-yield behavior in one or more degrees of freedom (here for the rotational degree of freedom) (CSI, 1999). The shape of the moment-plastic rotation curve followed is shown in Figure 2.3A. The nonlinear analysis was run using SAP2000 and was repeated for the different scaled excitations in order to generate the simulated response time histories. We assigned 1% modal damping ratio to the first mode. Additional damping is expected to appear due to the material hysteretic behavior. The analysis output comes in the form of a (relative) acceleration time history (in the horizontal direction), measured in one of the nodes of the first floor.

The model updating is performed using an equivalent linear finite element model developed in SAP2000 assuming linear moment-rotation relationship. The mass and stiffness matrices were exported from SAP2000 (offline) and passed onto Matlab where the updating framework is implemented. All elements of the structure were selected to belong to one substructure. Thus, there is one stiffness-related parameter corresponding to the stiffness of all beams and columns. Furthermore, the structure has only one mode due to its constraints and as a result there is one modal damping parameter. Thus, there is a total of two model parameters to be updated, the stiffness parameter and the modal damping ratio. The nominal values of the modal period (first mode) is: $T_1 = 0.73s$ (modal frequency: $f_1 = 1.37Hz$).

2.2.3.2 Structure 2: Six-story Steel Moment Frame Building

The second structure considered is a six-story steel moment frame building. The basis behind this structure is a building designed according to the 1994 Uniform building code, as described by J. Hall (Hall, 1998). The structure and the selected I-beam frame sections can be seen in Figure 2.2B. The material used is A36 steel.

A simplified 2D model of the building was developed in Frame-2D (Buyco, 2018). Frame-2D, also known as STEEL, is a computer program developed at Caltech with the goal of providing detailed analysis of steel structures (Challa, 1992; Challa & Hall, 1994; Hall & Challa, 1995; Hall, 1995; Bjornsson, 2014). A Frame-2D model consists of a planar arrangement of beam, column and brace elements that connect into panel zone elements. The beam, column, and brace elements are divided into segments along their length and each element is further discretized along its cross-section into fibers. Each steel fiber has a hysteretic axial stress-strain relationship, equipped with a yield plateau and strain-hardening/softening region (Hall, 1998; Buyco, 2018). The shape of this axial stress-strain relationship is shown in Figure 2.3B. Geometric nonlinearities (e.g. P-Δ) are also accounted for. Rayleigh damping was considered with 1% of critical damping assigned in the first and third modes. The nonlinear analysis was also performed in Frame-2D (Buyco, 2018) for the three different scaled excitations to simulate the artificial response time histories. The analysis output comes in the form of displacement time histories (measured in one node per floor, in the

horizontal direction). The time histories were differentiated and filtered in order to produce the velocity and acceleration data used in the model updating. Here, measurement error is possibly introduced, due to the data processing that was performed in order to obtain the velocity and acceleration time histories from displacement time histories.

The linear finite element model to be used for model updating was created in SAP2000. There is a large number of possible substructures one can consider for such a structure. For the cases presented here we are considering two substructures: the first one includes the beams and columns of the first and second floor, while the second one includes the beams and columns of the third and fourth floor. This is instigated by the fact that nonlinearity or damage is usually located at the lower floors. Selecting more parameters/substructures would accentuate the ill-conditioning of the problem. Only the first three modes are used to obtain results from the linear finite element model and thus there are three extra model parameters corresponding to the damping ratios of these three modes. As a result, the number of total model parameters is five. The nominal values of the modal periods of the first three modes are: $T_1 = 1.84s$, $T_2 = 0.64s$, and $T_3 = 0.36s$ (modal frequencies: $f_1 = 0.54Hz$, $f_2 = 1.55Hz$, and $f_3 = 2.78Hz$).

It should be noted that increasing the number of modes introduces the modal damping ratios of each mode as extra parameters to be updated. The increase in the number of modes is desirable to improve the fit, in the case that the added modes contribute to the response. If the contribution of extra modes is negligible then there is no information in the data to estimate the modal damping ratios of the added modes and the identification problem becomes ill-conditioned. Thus, there is trade-off between the number of modes to be included to improve the fit and the ill-conditioning arising from the fact that the introduced higher modes do not significantly contribute to the response. It is not easy to automate the procedure so that the optimal number of modes is used. This automation should be implemented for every time segment in the moving time window approach because different number of modes contribute in different time segments. For example, for windows toward the end of the excitation, only one mode significantly contributes, while the addition of extra modes does not significantly improve the fit. As a result, ill-conditioning arises during estimation of the model parameters.

Model error arises from the fact that the model used in the updating is not an exact representation of the behavior of the system. For the one-story structure since the finite element model used to generate the data is the same as the model used for predictions, model error is introduced from the fact that the model being updated is linear, while the measured (simulated data) are generated from a potentially nonlinear finite element model. If nonlinearities are not activated when generating the artificial data, then there is no model error and the model used to estimate the parameters should be capable of exactly fitting the simulated response time histories. For the six-story structure, additional model error is introduced due to the fact that the two models are different even in the linear regime. Specifically, for low intensity excitations for which the nonlinearities are not activated in the Frame-2D model, there is model error introduced due to the different software (Frame-2D and SAP2000) used to generate the artificial measurements and simulate the behavior of the structure in the model updating procedure. These differences are due to the modeling assumptions used in each software to build the model and simulate the response, despite the attempt to create a SAP2000 model as close to the Frame-2D model as possible.

The parameterization also introduces additional model error due to the constraints imposed in the model updating when a number of structural elements are grouped together in order to limit the number of parameters to be identified. Introducing these model errors allows us to study the performance of the method under more realistic conditions encountered in practical applications.

For the case of the six-story building further model error is introduced due to the fact that we neglect higher modes when the equations of motion of the linear model are solved using modal analysis. Model error is introduced also from the assumptions in the damping matrix. For the six-story frame structure, Rayleigh damping is used in Frame-2D, while modal damping is assigned in the linear model developed in SAP2000 used for the finite element model updating.

2.2.4 Case 1: One-story Building, Impulse Excitation

For case 1, the one-story steel moment frame structure is subjected to the impulse ground excitation. The data are simulated by running the nonlinear model of the structure. The data consist of the acceleration time history of one of the first-floor nodes. Figure 2.4 shows an example of the response and the nonlinear hinge behavior under the x15.0 input scaling. Linear model updating is performed in each time window by using the accelerations as our QOI and minimizing the measure-of-fit, shown in Eq. (2.38). The time window length is 1.0 s and the time window is shifted by 0.5 s at each step.

The identification results are shown in Figure 2.5. The different line colors correspond to the three different scales of the earthquake ground acceleration input. The horizonal axes are time and they correspond to the center of the moving time window. Figure 2.5A displays the hinge plastic rotation versus time. Horizontal lines in the curves indicate that the structure behaves linearly (zero plastic rotation rate). It can be seen that for scaling of x1.0 the response always remains linear, while nonlinearities are activated in the beginning of the excitation (for less than approximately 2 s) for scaling of x15.0 and x30.0. Figure 2.5B displays the measure-of-fit ($\tilde{J}$) values following the model updating at each time window. Figure 2.5C shows the values of the stiffness related parameter and Figure 2.5D shows the values of the modal damping ratio (percent critical damping). Figure 2.5E depicts the equivalent linear modal frequency. Figure 2.5F shows the condition number, which is the ratio of the maximum to the minimum eigenvalue of the Hessian matrix of the measure-of-fit ($\tilde{J}$).

Case 1 is the simpler of the presented cases and it demonstrates clearly the effectiveness of the methodology in tracing nonlinearities activated during an excitation event. By studying the hinge moment or plastic rotation curves, one can pinpoint the time windows where nonlinear behavior occurs and the results demonstrate that these windows were identified successfully. More specifically, when nonlinearities occur the measure-of-fit ($\tilde{J}$) is no longer zero, since it is impossible for the linear model to give a perfect fit to the acceleration time history when nonlinearities are activated. As can be seen in Figure 2.5 for less than 2 s, the stronger the nonlinearities, the worse the fit. Furthermore, as expected when nonlinearities take place, the

equivalent stiffness parameter and the equivalent linear modal frequencies decrease due to the softening nonlinearity, while the equivalent modal damping ratio increases due to energy dissipation. The length and overlaps of the time windows affect the shape of the curves, with larger time window lengths producing smoother results but also possibly resulting in missing some shorter time transitions to linear/nonlinear behavior.

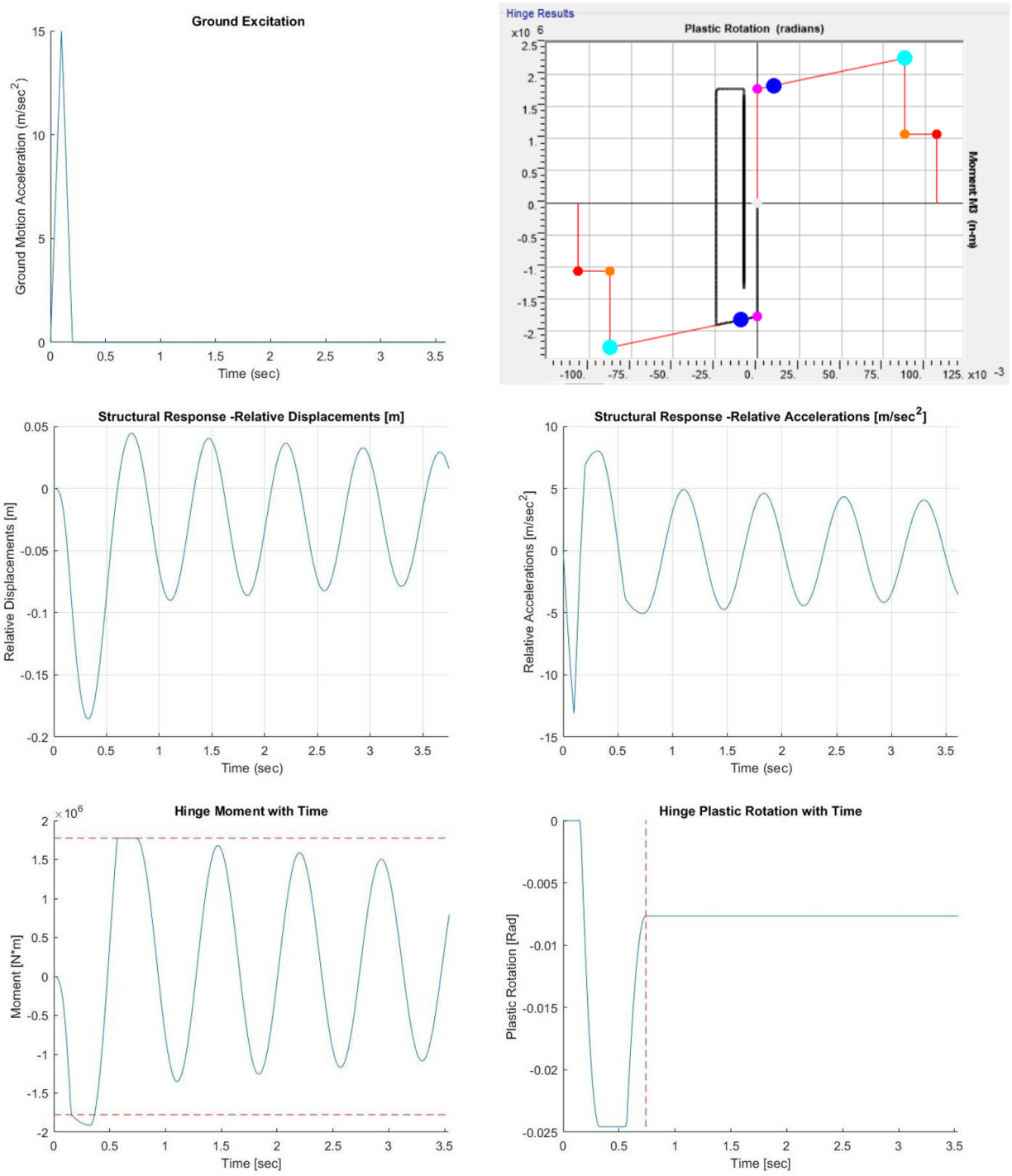

Figure 2.4. Response and hinge moment-plastic rotation plot simulated from the nonlinear 1-story building model using the impulse ground excitation – scaled x15.0.

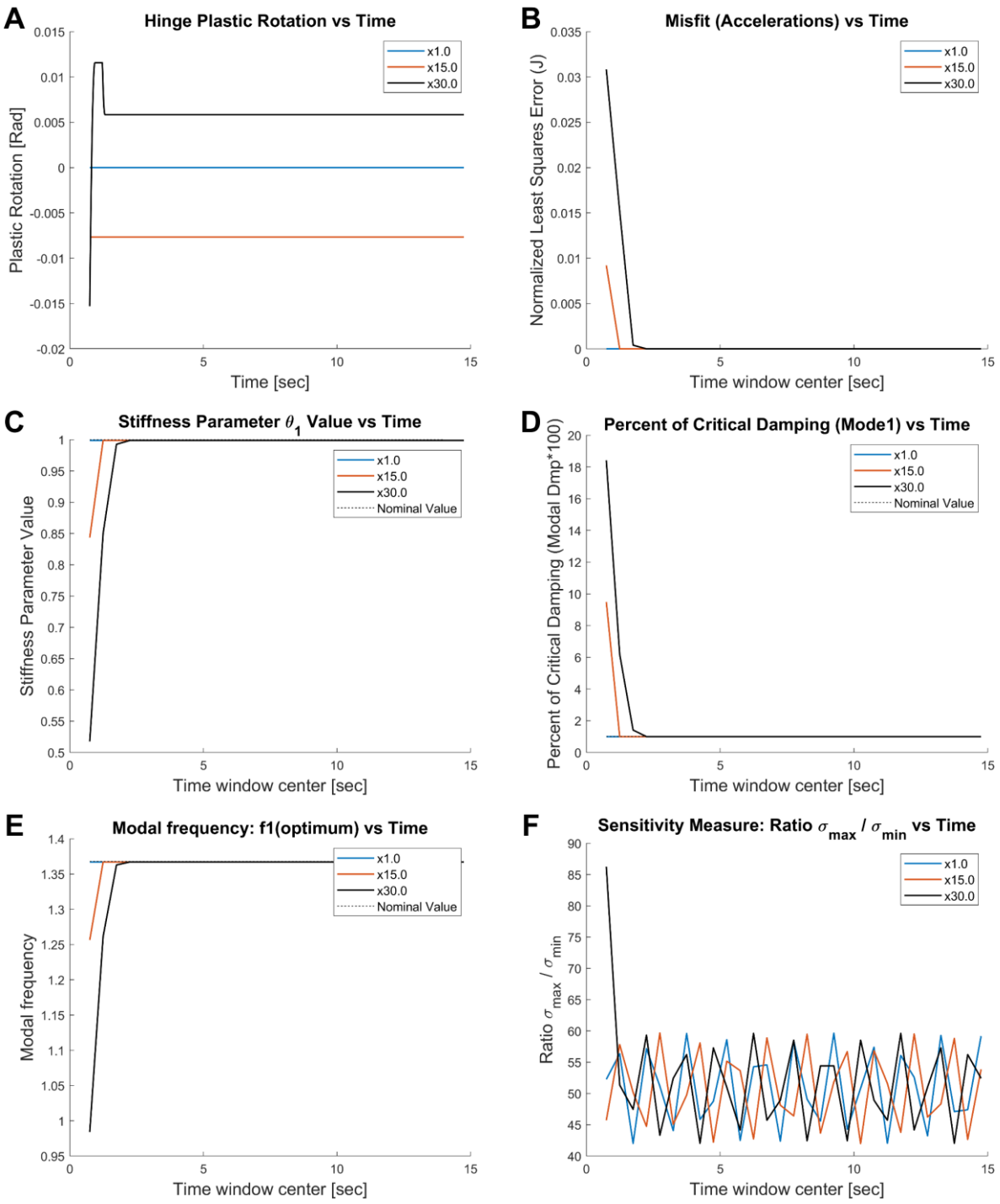

Figure 2.5. Estimated parameters and properties of the equivalent linear model for the single-story building, using impulse excitation (case 1).

2.2.5 Case 2: One-story Building, Earthquake Excitation

For the second case the one-story steel moment frame structure is subjected to the earthquake (1995 Kobe Japan Nishi-Akashi station record) ground excitation. The measured data are acceleration response time histories of one of the first-floor nodes, simulated by running the nonlinear model of the structure. The simulated acceleration time history data are shown in Figure 2.6, for the three different scales (x0.2, x1.0, and x2.0). Linear model updating is performed in each time window by using the accelerations as our QOI and minimizing the measure-of-fit, shown in Eq. (2.38). The time window length is 1.5 s, and the window is shifted by 0.5 s.

The case 2 results are shown in Figure 2.7. The different line colors correspond to the three different scales of the earthquake ground acceleration input. The horizonal axes are time and they correspond to the center of the moving time window. Figure 2.7A displays the hinge plastic rotation versus time. This information is output from the finite element software (SAP2000) and clearly indicates the time instances when transitions to nonlinear behavior of the structure take place. Horizontal lines in the curves indicate that the structure behaves linearly (zero plastic rotation rate). It can be seen that for scaling of x0.2 the response is linear, while nonlinearities are activated for scaling of x1.0 and x2.0. Figure 2.7B displays the measure-of-fit ($\tilde{J}$) values following the model updating at each time window. It can be seen that when the response is linear (x0.2 scaling) there is a perfect fit ($\tilde{J} = 0$). On the other hand, when nonlinearities are activated, the measure-of-fit $\tilde{J}$ is non-zero, as expected, since it is impossible for the linear model to give a perfect fit to the acceleration data in these cases. Furthermore, as the nonlinearities get stronger, the fit worsens, as indicated by the higher $\tilde{J}$ values. Figure 2.7C shows the values of the identified stiffness-related model parameter at each time window, while Figure 2.7D and E depict the equivalent linear modal frequency and modal damping ratio (percent critical damping) respectively. When softening nonlinearities take place, the equivalent stiffness parameter values and the equivalent modal frequency are expected to decrease, while the equivalent damping ratio is expected to increase due to energy dissipation arising from the hysteretic nonlinearity. Figure 2.7F shows the condition number of the Hessian matrix of the measure-of-fit ($\tilde{J}$). The condition number is monitored because it may indicate possible ill-conditioning of the structural identification framework. When this ratio is higher, the ill-conditioning is worse. We can see a

spike of the condition number for the x2.0 scaling and for a time window that corresponds to the strongest nonlinearities.

For the case of the single-story building, the expected behaviors following a transition to the non-linear regime are clearly visible. Specifically, the following conclusions can be made based on the results displayed in Figure 2.7:

- For the x0.2 excitation case, the nonlinearities are not activated and the identification yields the initial nominal values of the model parameters, modal frequencies and percent critical damping. The misfit is extremely small, with the predicted response perfectly fitting the measured data. This is due to the fact that the linear model represents exactly the behavior of the structure.
- For the x1.0 and x2.0 excitation cases the framework can detect the transition to the nonlinear regime through fitting an equivalent linear model to the data using a moving time window approach. In the cases where non-linearities take place along the moving window, a decrease in the equivalent stiffness is evident at the corresponding time windows, together with an increase in the modal damping ratios, and a drop in the modal frequencies, which is consistent with what is expected. The stronger the excitation, the higher the change from the nominal values of the stiffness, modal frequencies and percent critical damping values. Moreover, the stronger the excitation, the higher the misfit values due to the fact that a linear model is less appropriate to exactly represent the manifested nonlinear behavior.
- It is also worth noting that in the nonlinear regime between 5 to 20 s there is sudden drop at some time instances of the identified properties of the equivalent linear model to their initial values. These times correspond to cases where the nonlinearities over the window length considered are not activated, as is evident from the flat (horizontal) lines in the rotation vs time curves. For example, this is evident in the windows centered at approximate time instances of 12-13 s and 17-18 s.

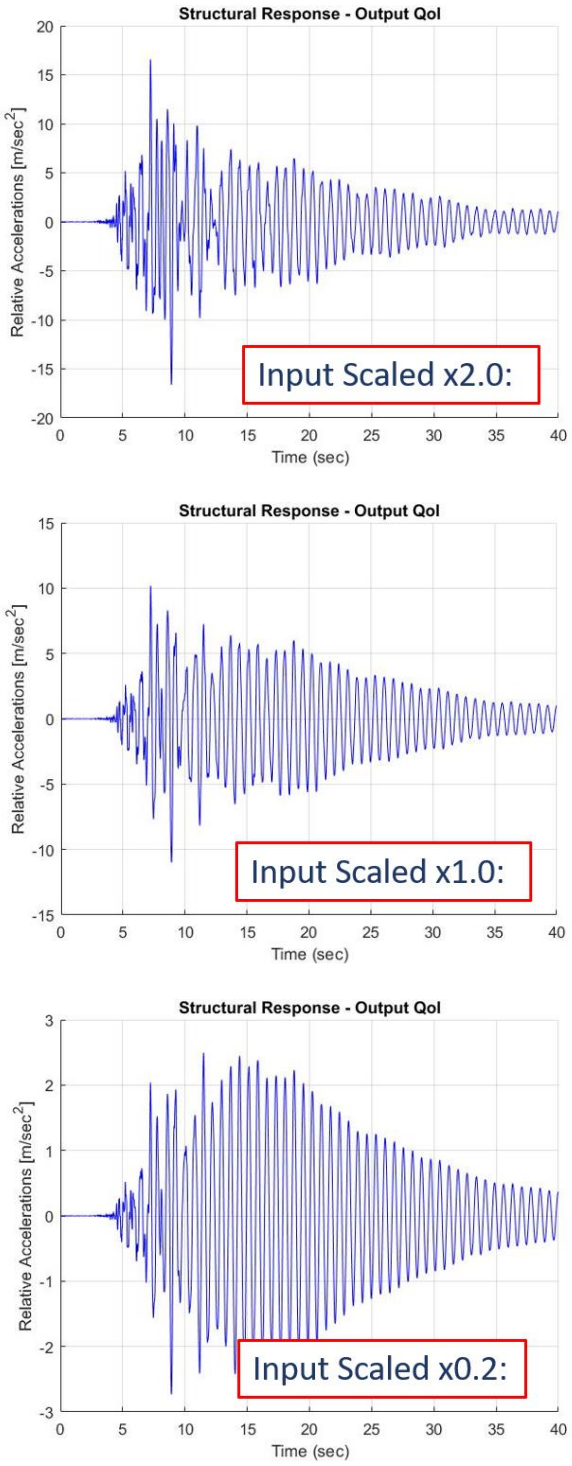

Figure 2.6. The acceleration time history data used in case 2, simulated from the nonlinear 1-story building model using the 1995 Kobe Japan earthquake (Nishi-Akashi station) ground excitation.

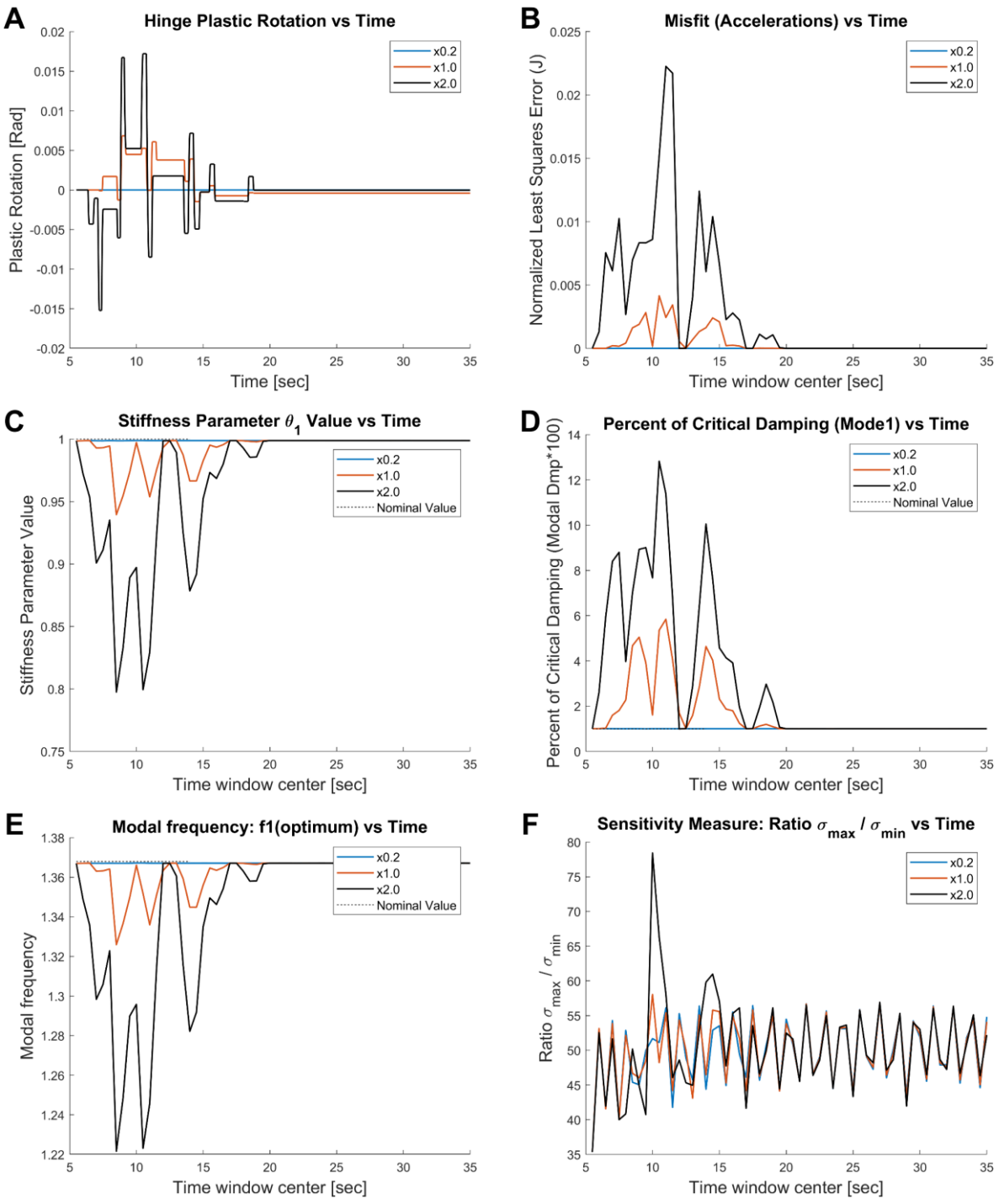

Figure 2.7. Estimated parameters and properties of the equivalent linear model for the single-story building, using earthquake excitation (case 2).

2.2.6 Case 3: Six-story Building, Earthquake Excitation

The third case considered involves the six-story steel moment frame structure subjected to the 1995 Kobe Japan earthquake (Nishi-Akashi station) ground excitation. The QOI used for the model updating are acceleration time history data (one time series per floor). The acceleration time history data recorded at the six floors are shown in Figure 2.8, for the three different scales (x0.2, x1.0, and x2.0). Linear model updating is performed in each time window by minimizing the measure-of-fit, Eq. (2.38). The length of the time window is 5.0 s and the window is shifted by 1.0 s at each step. The first window center is at 7.0 s and the last is at 50.0 s. Thus, there is a total of 44 overlapping time windows.

The identification results using the three different excitation scales are shown in Figure 2.9 and Figure 2.10. Here again the different line colors correspond to the different scales of the earthquake ground acceleration input, and the different properties are presented as a function of time (plotted against the moving time window center). Figure 2.9 presents the identified model parameters (stiffness related parameters and damping ratios), while Figure 2.10 displays the measure-of-fit, condition number, and modal frequency results.

Observing the excitation and response time histories, we expect the non-linear behavior (for the x1.0 and x2.0 scales) to take place from 0 to approximately 20 s. It should be noted that the scale x0.2 corresponding to linear behavior give values of the model parameters that differ from the nominal values of the initial linear finite element model used to generate the simulated data. This is due to the model error resulting from the fact that the nonlinear Frame-2D model used to generate the simulated measurements and the linear modal model (we keep 3 modes) used for performing the model updating are not exactly the same. Additional model error is introduced from the assumed model (stiffness) parameterization that introduces constraints in fitting the data by varying the two stiffness parameters, as well as from the fact that only three modes are included in the model predictions. The type and strength of each source of model error vary in the different time segments along the time history. Due to these sources of model error, the stiffness parameter associated with the first two floors has values that are approximately 10% lower than the nominal values, while the stiffness parameter associated with the third and fourth floors has values of

approximately 40% higher than the nominal value. Similar discrepancies between the estimated and nominal values for the linear case (scale x0.2) are observed for the modal damping ratios and modal frequencies.

We thus identify the transition into nonlinear behavior by comparing the higher scale curves (x1.0 and x2.0) to the x0.2 scale curve, rather than comparing to the nominal values. Keeping this in mind, one can identify the expected behaviors following a transition to the non-linear regime. More specifically, in the time interval from 5 to 20 s, as the excitation level increases (scales x1.0 and 2.0), the values of the two stiffness related parameters decrease (Figure 2.9A-B), the values of the modal damping ratios increase (Figure 2.9C-E), the measure-of-fit values increase (Figure 2.10A) and the values of the modal frequencies decrease (Figure 2.10C-E) in relation to the corresponding values identified for the linear case (scale x0.2). The higher the excitation, the higher the change of these properties. The changes observed as a function of time are similar to those observed for the one-story building, although due to model error the expected decrease or increase in these model properties is not as evident as in the one-story building. Similar behaviors of the properties of the equivalent linear system are also observed in the time interval from approximately 25 to 35 seconds where, as can be seen in Figure 2.8, the acceleration response time histories show an intensity that increases as the scale of the earthquake increases from x0.2 to x1.0 and eventually to x2.0.

For the time interval from approximately 20 s to 25 s, an unexpected behavior of the properties of the equivalent linear system is observed which can be attributed to the fact that the response time histories in Figure 2.8 are relatively small and the nonlinearities may not have been activated. Specifically, for the scale of x1.0 and x2.0 earthquake input the responses in Figure 2.8 barely reach the value of 1 to 2 m/s^2 which is of the same order of magnitude as the strong motion part of the scale of x0.2 earthquake input for which the structure behaves linearly. In this time interval (from 20 to 25 s), the nonlinearities are probably not activated and thus the observed time variation of the properties of the equivalent linear system is reasonable. The observed variability of the modal properties for the three different scales (x0.2, x1.0 and x2.0) is expected and is likely due to model error.

The condition number indicates that the estimation is well-posed for most window segments with centers ranging from 5 to approximately 35 s. For window segments centered after 35 s, the condition number increases dramatically which may indicate an ill-posed estimation problem. This may be due to the fact that less than three modes participate in the response at later times (after 35 seconds). Thus a number of model parameters, such as the percent of critical damping for the third and possibly also the second mode cannot be identified from the measured response time histories, giving rise to the ill-conditioning. This ill-conditioning is also confirmed by the unreasonably high damping ratio values estimated from approximately 40 to 50 s for the third mode in Figure 2.9E. The results in Figures 2.9 and 2.10 suggest that the estimates, especially for the modal damping ratio for the third mode, should be ignored due to ill-conditioning.

For the latest time interval from 40 s to 50 s, the measure-of-fit value is very close to zero for all excitation levels, indicating that the equivalent linear system can adequately fit the response time histories and that nonlinearities are not activated due to low amplitude response levels. The two stiffness parameters of the linear model and the modal frequencies of the three modes approach the corresponding stiffness values and the modal frequencies of the nominal model used to generate the simulated data. Differences from the nominal values and for the values obtained for the three different excitation levels are due to the model error. This is expected since the response time histories are different, and the ill-conditioning arising from the fact that one or more modes might not contribute to the response. Model error due to modal truncation is not an issue here since less than three modes are contributing to the response. In addition, the fact that less than three modes contribute to the response provides higher flexibility for the finite element model predictions to fit the data by changing the values of the two stiffness parameters and the damping ratios of the contributing modes, reducing the size of model error. This reduced model error may also explain the fact that the values of the model properties (two stiffness parameters and modal frequencies) are closer to the properties corresponding to the nominal values used to generate the simulated data.

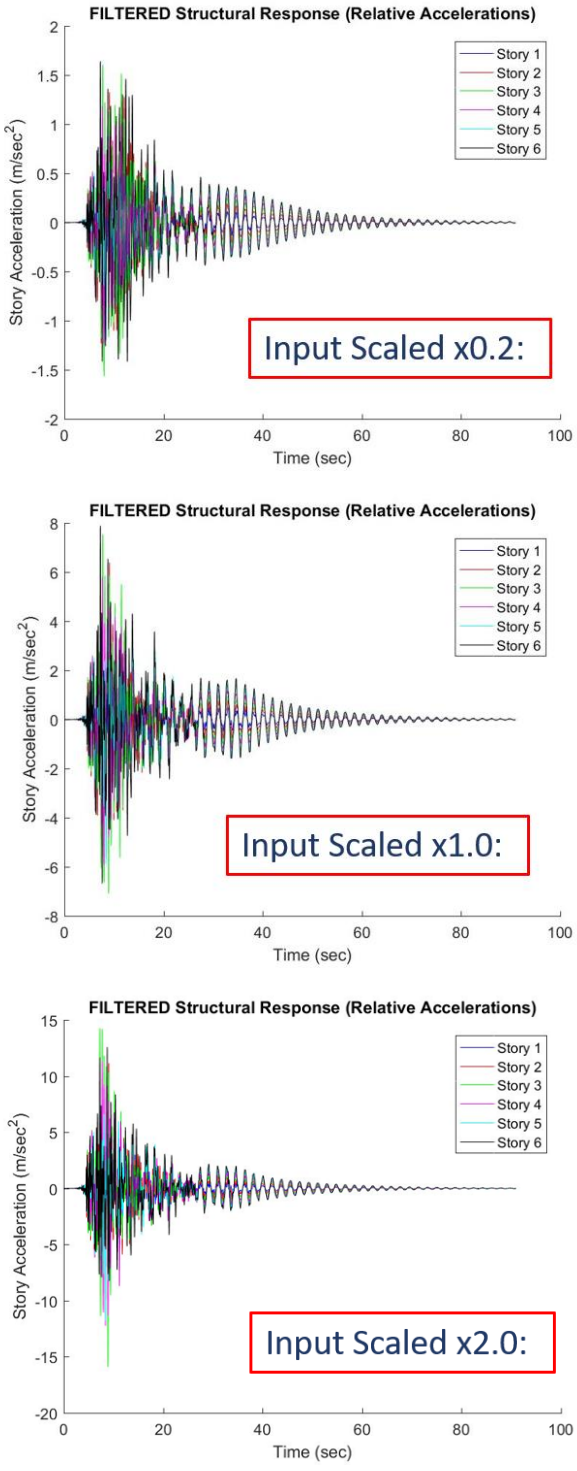

Figure 2.8. The acceleration time history data used in case 3, simulated from the nonlinear 6-story building model using the 1995 Kobe Japan earthquake (Nishi-Akashi station) ground excitation.

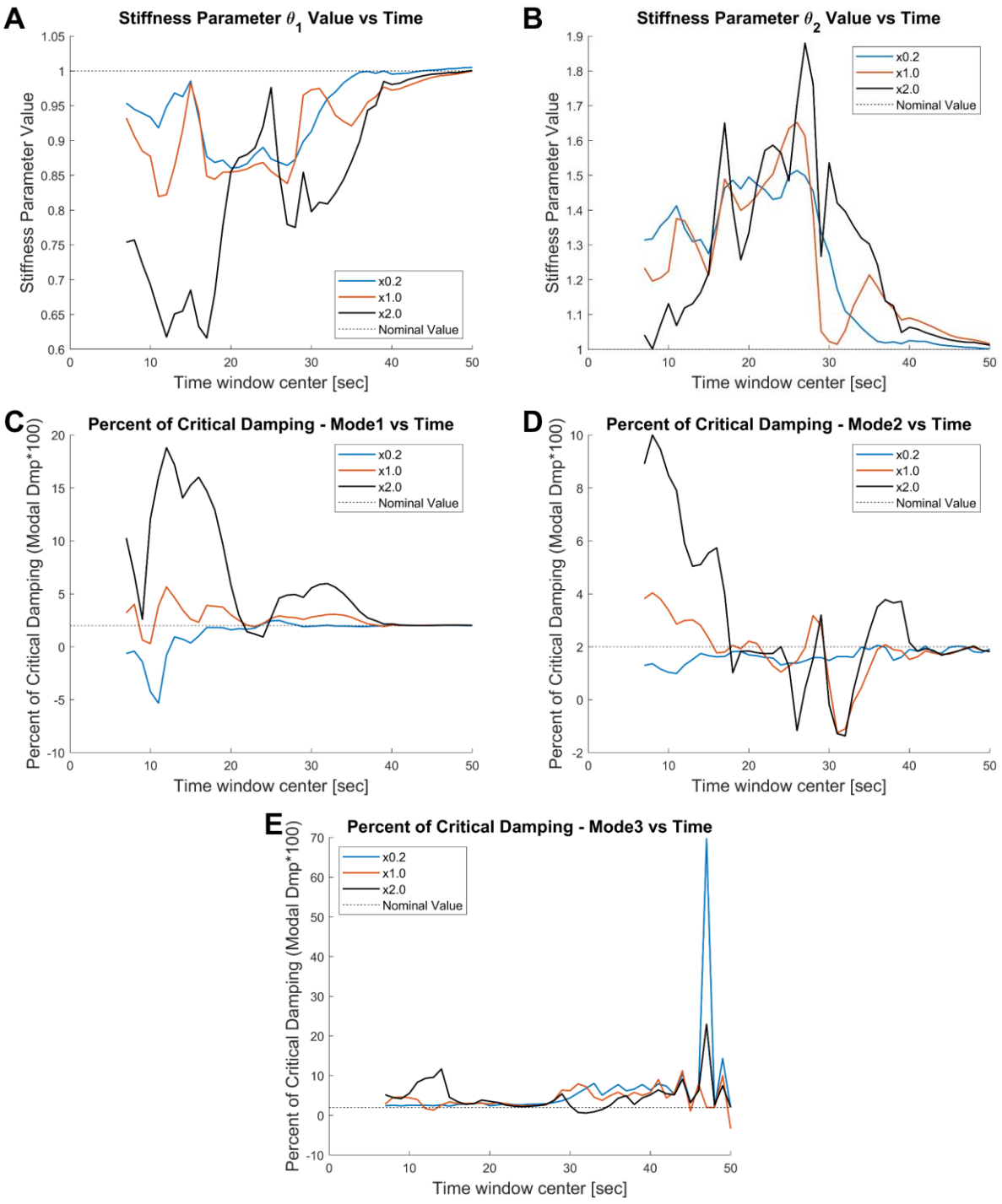

Figure 2.9. Estimated parameters of the equivalent linear model for the six-story building, using acceleration measurements (case 3).

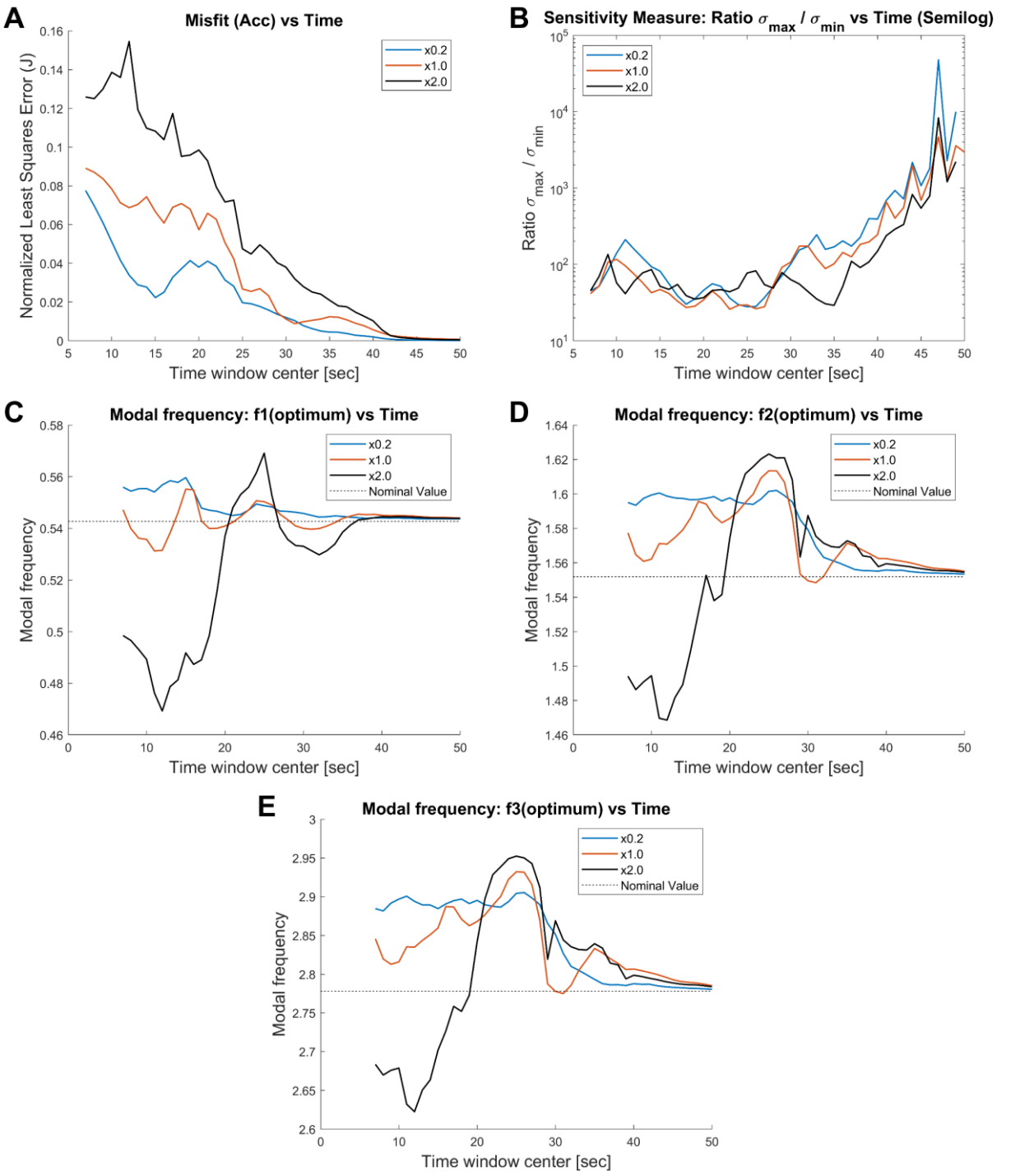

Figure 2.10. Estimated properties of the equivalent linear model for the six-story building, using acceleration measurements (case 3).

2.2.7 Case 4: Six-story Building, Earthquake Excitation, Velocity Measurements

For the fourth case, the six-story steel moment frame structure is subjected to the 1995 Kobe Japan (Nishi-Akashi station) ground excitation, but this time velocity time history data (one time series per floor) is used for the model updating. The velocity time history data are shown in Figure 2.11, for the three different scales (x0.2, x1.0, and x2.0). Linear model updating is performed in each time window by minimizing the measure-of-fit, shown in Eq. (2.38). The time window length is 5.0 s and at each step it is being shifted by is 1.0 s. We use velocity instead of acceleration time history data, in order to evaluate whether or not the different type of measured time histories has an effect on the results obtained in the third case.

The identified model parameters (stiffness related parameters and damping ratios) are shown in Figure 2.12, and the measure-of-fit, condition number, and modal frequency results are shown in Figure 2.13. The results obtained for the variation of the properties (stiffness related parameters, modal frequencies and modal damping ratios) of the equivalent linear model as a function of time are qualitatively similar to those obtained for the third case using acceleration time history data. This shows that the identification framework works equally well when using velocity time history data. In particular, some of the results obtained using velocity time history data, especially in the time range from 0 s to 20 s, demonstrate more clearly the change in the properties of the equivalent linear system that is expected to occur due to activation of nonlinearities along the time history and due to the higher intensity earthquake events.

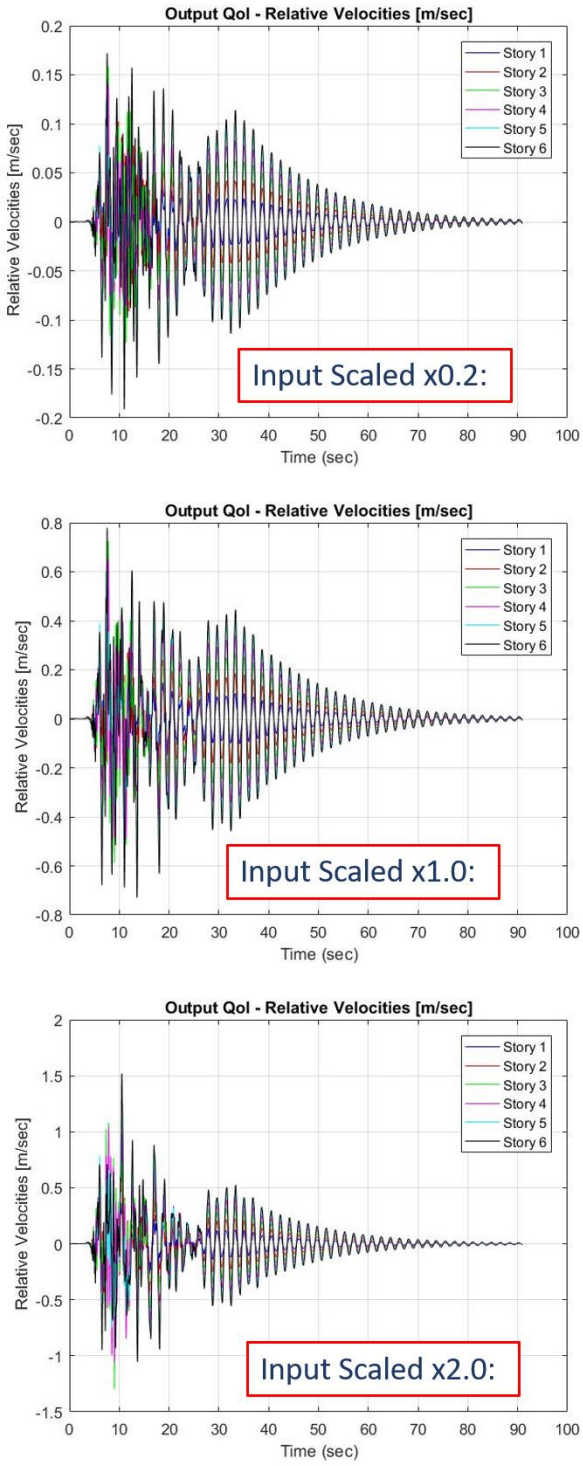

Figure 2.11. The velocity time history data used in case 4, simulated from the nonlinear 6-story building model using the using the 1995 Kobe Japan earthquake (Nishi-Akashi station) ground excitation.

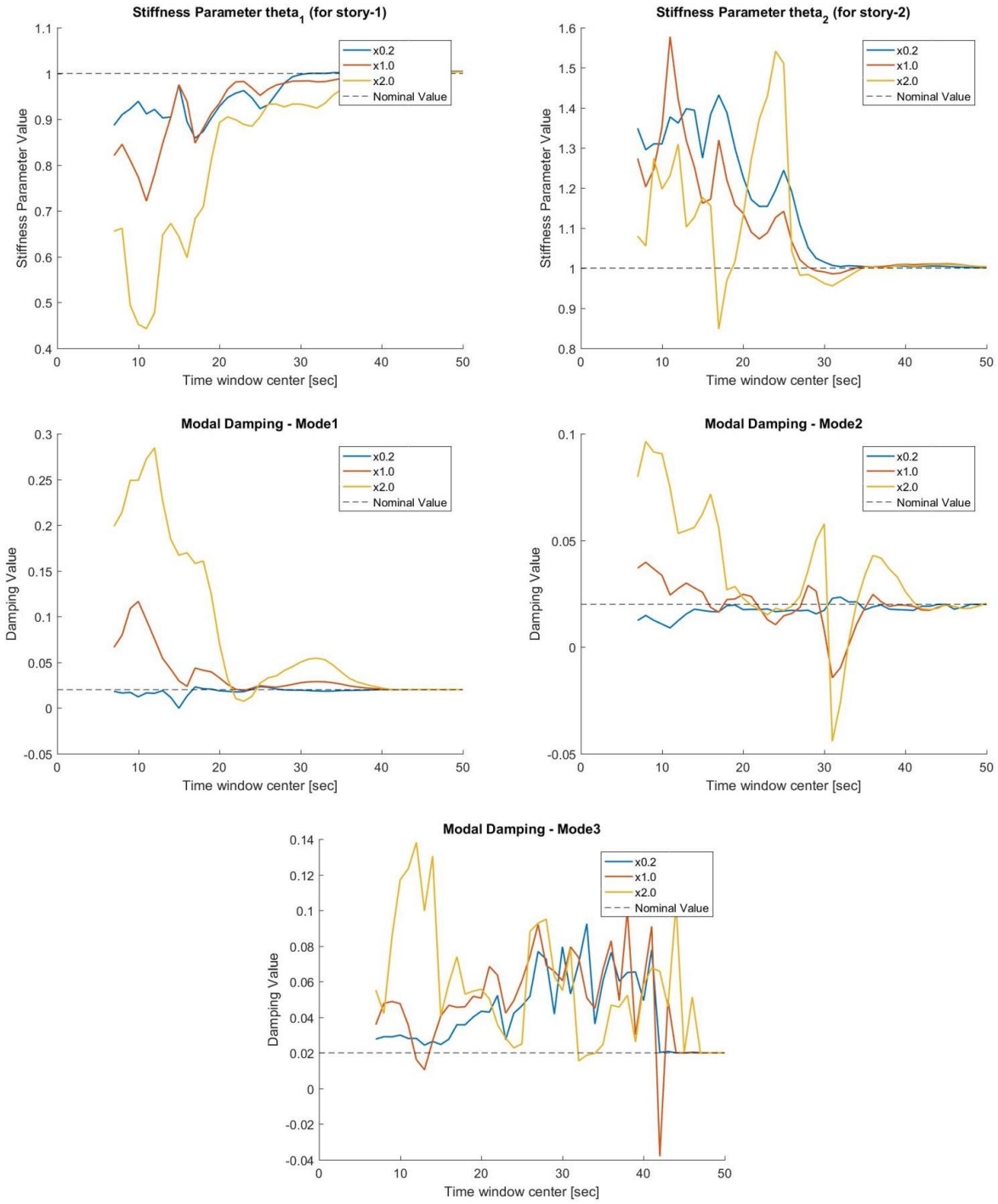

Figure 2.12. Estimated parameters of the equivalent linear model for the six-story building, using acceleration measurements (case 4).

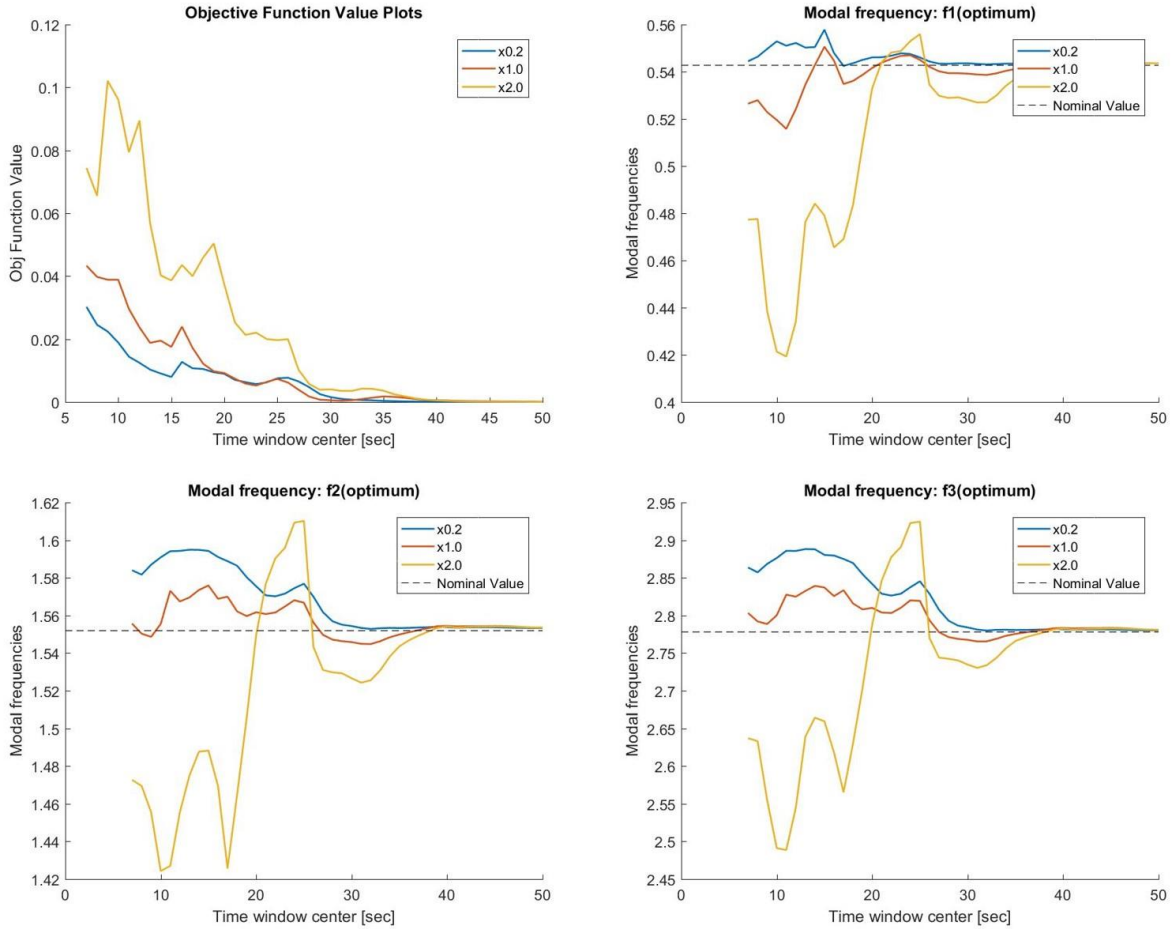

Figure 2.13. Estimated properties of the equivalent linear model for the six-story building, using acceleration measurements (case 4).

2.3 Conclusions

We developed a methodology and software framework for tracing the nonlinear behavior of a building using response time histories recorded during an earthquake. This was achieved by using a moving time window approach and updating an equivalent linear model using the response time history data within each window. The model predictions were obtained using modal analysis and the parameters that were updated include stiffness properties and modal damping ratios. The update was based on the least squares fit between the measured and model predicted response time histories. Results have been obtained for two different example cases, a one-story building and a six-story building. The effectiveness of the methodology to identify the transition in the plastic

regime as a function of time during a strong intensity earthquake event and under various sources of model error manifested in the analysis was demonstrated using simulated data.

Overall, the methodology does a reasonable job of identifying the transition in the plastic regime and tracing the nonlinear behavior with time. The results for the single-story building display clearly the expected behavior as the ground acceleration intensity increases and the nonlinearities get stronger. The results for the six-story building demonstrate that the proposed methodology can identify reasonably well the nonlinearities and the extent of nonlinearities activated during an earthquake, although the expected behavior of the identified structural and modal properties is not as clear as in the single-story building due to the various sources of model error manifested in the analysis performed. More specifically:

- As the equivalent linear model tries to fit strongly non-linear behavior, the result for the fit between the simulated response time histories and the model predicted response time histories worsen. Thus, higher misfit values are identified, as expected, for larger scale levels of the excitation that progressively activate nonlinearities.
- Because of softening nonlinearities, the equivalent stiffness parameter values drop and the equivalent modal frequencies decrease as compared to the stiffness parameter values and the modal frequency values corresponding to excitations that do not activate nonlinear phenomena.
- The plastic (hysteresis loop) energy dissipation raises, as expected, the values of the percent critical damping identified using the equivalent linear viscous model.

Although results are shown for four representative cases, a number of additional cases have been considered and demonstrate that the framework is promising for identifying the nonlinearities with time during an earthquake by fitting an equivalent linear finite element model to different time windows using a moving time window approach. One can use the framework with different inputs, stiffness parameter selections, number of modes, time windows, as well as measures-of-fit functions to perform the structural identification.

The method presented in this chapter is a single-stage approach for directly estimating stiffness-related model parameters and modal damping ratios of an equivalent linear finite element model of a structure using measured response time histories. Using the estimated model parameters, the equivalent linear finite element model can be used to compute the modal frequencies and the modeshapes of the structure. Using a moving time window approach, the proposed method traces the model properties along each window.

The proposed method should be contrasted to the previously published two-stage linear finite element model updating methods. In the first stage the modal properties (modal frequencies, modal damping ratios and modeshape components at the measured DOF) are identified using input-output response time histories (e.g. accelerations) (Beck, 1979; Beck & Jennings, 1980). Using a moving window approach, the first stage is useful to detect damage or even the nonlinearities activated in each time window by tracing the change in global properties of the structure, such as modal frequencies, modal damping ratios and modeshapes. However, the first stage is not sufficient to map the changes in the modal properties to changes in the stiffness characteristics of the structure. This is achieved in the second stage where the stiffness-related properties of the finite element model are estimated using the modal frequencies and modeshapes identified in the first stage. Finite element model updating techniques based on modal properties has been developed and widely used since the early work by Friswell and Mottershead (Mottershead & Friswell, 1993; Friswell & Mottershead, 1995). A review can also be found in Moaveni (2007) for deterministic methods and Huang et al. (2019b) for probabilistic methods. In particular, Moaveni et al. (2010; 2011) have applied linear finite element model updating based on modal properties on a reduced-scale 7-story concrete building to trace the identified stiffness changes of the equivalent linear model from the damage distribution in building floors during progressively stronger excitation levels.

The two-stage method is applicable to linear systems, since it involves modal properties defined only for linear models. In the present approach a single-stage model updating method is used based on response time histories. The single-stage approach presented here is based directly on response time histories and not the modal features; it is thus more general since it can be extended to update

nonlinear finite element models as well. The two approaches (single stage and two-stage) are not expected to give exactly the same results but they are expected to give similar results for the identified stiffness properties as well as modal properties. The first step in the two-stage approach has certain advantages since the change in the modal properties can be sufficient for providing the necessary information about the system nonlinearities and the strength of nonlinearities or for tracing these nonlinearities over the different time windows. However, in order to associate the modal property changes to changes in the equivalent stiffness properties, one needs to use the second stage as well.

Chapter 3

SPARSE BAYESIAN LEARNING FOR DAMAGE IDENTIFICATION USING NONLINEAR MODELS

This chapter presents a sparse Bayesian learning (SBL) methodology for identifying the existence, location, and severity of structural damage. SBL is a well-established technique used for tackling supervised learning problems, while taking advantage of the prior knowledge that the expected solution is sparse. Based on the premise that initial damage in a structure appears only in a limited number of locations, SBL has been explored for identifying structural damage, showing promising results. A literature review of SBL methods for structural damage identification is available in the introduction chapter in Section 1.2. Existing SBL methods applied for structural damage identification use measurements related to modal properties and are thus limited to linear models. In this chapter we present a methodology that allows for application of SBL in non-linear models, using time history measurements obtained from dense sensor networks, such as the Community Seismic Network (CSN), installed in buildings.

Using SBL, we develop a two-step optimization algorithm in which the most probable values of the structural model parameters, indicative of the location and size of structural damage, are iteratively obtained. An equivalent single-objective minimization problem that results in the most probable model parameter values is also derived. In order to demonstrate the effectiveness and robustness of the proposed methodology, we consider the example problem of identifying damage in the form of weld fractures in a three-dimensional, 15-story, moment resisting steel frame building, using a nonlinear finite element model and simulated acceleration data. Fiber elements and a bilinear material model are used in order to account for the change of local stiffness when cracks at the welds are subjected to tension and the model parameters characterize the loss of stiffness as the crack opens under tension. In the cases presented, various damage scenarios and

different parameterizations are considered, as well as different degrees of model and measurement error.

In Section 3.1 we present the developed SBL framework that allows for damage identification based on time history measurements. Section 3.2 demonstrates an example application considered in order to test the effectiveness of the methodology. Four different studies are considered through which we examine different damage scenarios, degrees of model and measurement errors, parameterization and instrumentation density, and their effects on the damage identification results. Section 3.3 presents the conclusions of this investigation.

3.1 Sparse Bayesian Learning Framework

Let $D = \{\hat{\boldsymbol{x}}(k) \in \mathcal{R}^{N_o},\ k = 1, \dots, N_D\}$ be the measured response time histories (e.g., acceleration, velocity, displacement, or strain time histories), at N_o measured (observed) degrees of freedom (DOF), where N_D is the number of the sampled data at time instances $t_k = k\Delta t$, corresponding to a sampling rate Δt. A parameterized finite element model is introduced to simulate the behavior of the structure. Let $\boldsymbol{\theta} \epsilon \mathcal{R}^{N_\theta}$ be the set of the free structural model parameters. These model parameters are associated with local properties (e.g., stiffness of an element or substructure) of the finite element model. Changes in the values of the model parameters will be indicative of damage in the structure. The structural model is parameterized so that the undamaged state corresponds to $\boldsymbol{\theta} = \mathbf{0}$, while damage corresponds to negative values of $\boldsymbol{\theta}$. Thus, identifying the value of the model parameter set $\boldsymbol{\theta}$ accomplishes the damage identification goals, i.e. determining the existence, location, and severity of damage. To cover all possible damage scenarios, the number of parameters may be relatively large compared to the information contained in the data. Taking advantage of the prior information about the expected sparsity of damage will help alleviate the ill-conditioning of the problem. Let $\{\boldsymbol{x}(k;\boldsymbol{\theta}) \in \mathcal{R}^{N_o},\ k = 1, \dots, N_D\}$ be the model-predicted response time histories at the measured DOF, obtained for a particular value of the parameter set $\boldsymbol{\theta}$.

To formulate the likelihood function in the Bayesian inference, the prediction error equation is introduced. The prediction errors measure the discrepancy between the measured and the model-predicted response. Specifically, the prediction error $e_j(k)$ between the measured response time histories and the corresponding response time histories predicted from a model that corresponds to a particular value of the parameter set $\boldsymbol{\theta}$, for the jth measured DOF and the kth sampled data point, satisfies the prediction error equation

$$\hat{x}_j(k) = x_j(k, \boldsymbol{\theta}) + e_j(k) \tag{3.1}$$

where $j = 1, \dots, N_o$ and $k = 1, \dots, N_D$. The prediction error accounts for the model and measurement errors.

Following Beck and Katafygiotis (1998), the prediction errors at different time instants are modeled by i.i.d. (independent identically distributed) zero-mean Gaussian vector variables, i.e. $\varepsilon_j(k) \sim N\left(0, \hat{s}_j^2 \sigma_j^2\right)$, based on the principle of maximum information entropy (Jaynes, 1983; 2003), with $\hat{s}_j^2$ being the mean-square response of the jth measured time history, given by

$$\hat{s}_j^2 = \frac{1}{N_D} \sum_{k=1}^{N_D} \hat{x}_j^2(k) \tag{3.2}$$

and σ_j^2 being the normalized variance. The prediction error parameters $\sigma_j \epsilon \mathcal{R}$, for $j = 1, \dots, N_o$ represent the fractional difference between the measured and the model-predicted response at a time instant and comprise the prediction error parameter set $\boldsymbol{\sigma} \epsilon \mathcal{R}^{N_o}$. Assuming also that the prediction errors for different DOF are independent, we show in Appendix 3.A.1 that the likelihood function, given the values of the model parameters $\boldsymbol{\theta}$ and $\boldsymbol{\sigma}$, takes the form

$$p(D|\boldsymbol{\theta}, \boldsymbol{\sigma}) = \frac{1}{\left(\sqrt{2\pi}\right)^{N_D N_o} \prod_{j=1}^{N_o} \hat{s}_j^{N_D} \sigma_j^{N_D}} \exp\left\{-\frac{N_D N_o}{2} \mathcal{J}(\boldsymbol{\theta}; \boldsymbol{\sigma})\right\} \tag{3.3}$$

with $\mathcal{J}(\boldsymbol{\theta}; \boldsymbol{\sigma})$ being a measure-of-fit between the measured and model-predicted response time histories, equal to

$$\mathcal{J}(\boldsymbol{\theta};\boldsymbol{\sigma}) = \frac{1}{N_o}\sum_{j=1}^{N_o}\frac{1}{\sigma_j^2}J_j(\boldsymbol{\theta}) \tag{3.4}$$

where

$$J_j(\boldsymbol{\theta}) = \frac{\sum_{k=1}^{N_D}\left[\hat{x}_j(k) - x_j(k,\boldsymbol{\theta})\right]^2}{\sum_{k=1}^{N_D}\left[\hat{x}_j(k)\right]^2}. \tag{3.5}$$

The likelihood function quantifies the probability of observing the data given the values of the model parameters $\boldsymbol{\theta}$ and $\boldsymbol{\sigma}$. The functions $J_j(\boldsymbol{\theta})$ represent the measure of fit between the measured and the model-predicted response time history for the jth DOF. Similarly, the function $\mathcal{J}(\boldsymbol{\theta})$ in Eq. (3.4) is the average measure of fit over all DOFs.

Note that for the presented example applications, we are considering the special case of $\sigma_j = \sigma \epsilon \mathcal{R}$, $\forall j$. For this case, we have $\varepsilon_j(k) \sim N\left(0, \hat{s}_j^2\sigma^2\right)$ and the likelihood function given in equation (3.3) can be written in the form

$$p(D|\boldsymbol{\theta},\sigma) = \frac{1}{\left(\sqrt{2\pi}\right)^{N_D N_o}\prod_{j=1}^{N_o}\hat{s}_j^{N_D}\,\sigma^{N_D N_o}}\exp\left\{-\frac{N_D N_o}{2\sigma^2}J(\boldsymbol{\theta})\right\} \tag{3.6}$$

where $J(\boldsymbol{\theta}) = \sigma^2\mathcal{J}(\boldsymbol{\theta};\sigma)$ is the measure-of-fit between the measured and model-predicted response time histories for the special case of $\sigma_j = \sigma,\ \forall j$, equal to

$$J(\boldsymbol{\theta}) = \frac{1}{N_o}\sum_{j=1}^{N_o}J_j(\boldsymbol{\theta}) \tag{3.7}$$

with $J_j(\boldsymbol{\theta})$ from Eq. (3.5).

Similar to Tipping (2001), in order to promote sparsity in the model parameters, we consider the case of an automatic relevance determination (ARD) prior (MacKay, 1996) probability density function (PDF)

$$p(\boldsymbol{\theta}|\boldsymbol{\alpha}) = \frac{1}{(2\pi)^{N_\theta/2}} \prod_{i=1}^{N_\theta} \alpha_i^{1/2} \, exp\left[-\frac{1}{2} \sum_{i=1}^{N_\theta} \alpha_i \theta_i^2 \right] \tag{3.8}$$

which is Gaussian for the model parameters $\boldsymbol{\theta}$ with the variance of each parameter θ_i being $1/\alpha_i$. The hyper-parameters α_i are unknown parameters to be estimated using the available measurements. Let $\boldsymbol{\alpha} \in \mathcal{R}^{N_\theta}$ be the prior hyper-parameter set. The hyperparameters effectively control the weights associated with each dimension of the model parameter vector. The ARD model embodies the concept of relevance and allows the "switching-off" of certain model parameters (the corresponding α_i values going to infinity). Since the Bayesian model comparison embodies Occam's razor, in practice most of the hyperparameters do indeed go to infinity deeming the corresponding model parameters irrelevant, resulting in a sparse solution and therefore a simpler model.

Applying the Bayes theorem to infer the posterior PDF of the structural model parameters $\boldsymbol{\theta}$ given $\boldsymbol{\sigma}$ and $\boldsymbol{\alpha}$, one has

$$p(\boldsymbol{\theta}|D, \boldsymbol{\sigma}, \boldsymbol{\alpha}) = \frac{p(D|\boldsymbol{\theta}, \boldsymbol{\sigma}, \boldsymbol{\alpha}) p(\boldsymbol{\theta}|\boldsymbol{\sigma}, \boldsymbol{\alpha})}{p(D|\boldsymbol{\sigma}, \boldsymbol{\alpha})}. \tag{3.9}$$

Taking into account the independence of the likelihood function $p(D|\boldsymbol{\theta}, \boldsymbol{\sigma}, \boldsymbol{\alpha})$ on $\boldsymbol{\alpha}$ and the independence of the prior PDF $p(\boldsymbol{\theta}|\boldsymbol{\sigma}, \boldsymbol{\alpha})$ on $\boldsymbol{\sigma}$, one has

$$p(\boldsymbol{\theta}|D, \boldsymbol{\sigma}, \boldsymbol{\alpha}) = \frac{p(D|\boldsymbol{\theta}, \boldsymbol{\sigma}) p(\boldsymbol{\theta}|\boldsymbol{\alpha})}{p(D|\boldsymbol{\sigma}, \boldsymbol{\alpha})}. \tag{3.10}$$

Substituting Eq. (3.3) and Eq. (3.8) into Eq. (3.10), the posterior PDF takes the form

$$p(\boldsymbol{\theta}|D, \boldsymbol{\sigma}, \boldsymbol{\alpha}) = \frac{c \prod_{j=1}^{N_o} \sigma_j^{-N_D} \prod_{i=1}^{N_\theta} \alpha_i^{1/2}}{\left(\sqrt{2\pi}\right)^{N_D N_o + N_\theta} \prod_{j=1}^{N_o} \hat{s}_j^{N_D}} \exp\left\{ -\frac{N_D N_o}{2} \mathcal{J}(\boldsymbol{\theta}; \boldsymbol{\sigma}) - \frac{1}{2} \sum_{i=1}^{N_\theta} \alpha_i \theta_i^2 \right\} \tag{3.11}$$

with the evidence $c^{-1} = p(D|\boldsymbol{\sigma}, \boldsymbol{\alpha})$ being independent of $\boldsymbol{\theta}$.

The optimal value $\widehat{\boldsymbol{\theta}} = \widehat{\boldsymbol{\theta}}(\boldsymbol{\sigma}, \boldsymbol{\alpha})$, of the model parameters $\boldsymbol{\theta}$ for given $\boldsymbol{\sigma}$ and $\boldsymbol{\alpha}$, corresponds to the most probable model maximizing the updated PDF $p(\boldsymbol{\theta}|D, \boldsymbol{\sigma}, \boldsymbol{\alpha})$ or, equivalently, minimizing

$-\ln[p(\boldsymbol{\theta}|D,\boldsymbol{\sigma},\boldsymbol{\alpha})]$. The optimal value $\widehat{\boldsymbol{\theta}}$ is also referred to as the most probable value, or maximum a posteriori (MAP) estimate, and is given by

$$\widehat{\boldsymbol{\theta}}(\boldsymbol{\sigma},\boldsymbol{\alpha}) = argmin_{\boldsymbol{\theta}}\left[N_D N_o \mathcal{J}(\boldsymbol{\theta};\boldsymbol{\sigma}) + \sum_{i=1}^{N_\theta}\alpha_i\theta_i^2\right]. \tag{3.12}$$

The optimal value of the model parameters $\boldsymbol{\theta}$ depends on the values of the prediction error parameter set $\boldsymbol{\sigma}$ and the prior hyperparameters $\boldsymbol{\alpha}$.

Note that for the special case of $\sigma_j = \sigma,\ \forall j$, the posterior PDF can be written in the form

$$p(\boldsymbol{\theta}|D,\sigma,\boldsymbol{\alpha}) = \frac{c\sigma^{-N_D N_o}\prod_{i=1}^{N_\theta}\alpha_i^{1/2}}{\left(\sqrt{2\pi}\right)^{N_D N_o + N_\theta}\prod_{j=1}^{N_o}\hat{s}_j^{N_D}}\exp\left\{-\frac{N_D N_o}{2\sigma^2}J(\boldsymbol{\theta}) - \frac{1}{2}\sum_{i=1}^{N_\theta}\alpha_i\theta_i^2\right\} \tag{3.13}$$

and similarly to Eq. (3.12), the optimal value $\widehat{\boldsymbol{\theta}}$ is given by

$$\widehat{\boldsymbol{\theta}}(\sigma,\boldsymbol{\alpha}) = argmin_{\boldsymbol{\theta}}\left[\frac{N_D N_o}{\sigma^2}J(\boldsymbol{\theta}) + \sum_{i=1}^{N_\theta}\alpha_i\theta_i^2\right]. \tag{3.14}$$

Thus, the optimal values of the model parameters $\boldsymbol{\theta}$ depend on the values of the prediction error parameter σ and the prior hyperparameters $\boldsymbol{\alpha}$.

The selection of the optimal values of these parameters is formulated as a model selection problem. Specifically, using Bayesian inference, the posterior PDF of the hyperparameter set $(\boldsymbol{\sigma},\boldsymbol{\alpha})$, given the data D, takes the form

$$p(\boldsymbol{\sigma},\boldsymbol{\alpha}|D) = \frac{p(D|\boldsymbol{\sigma},\boldsymbol{\alpha})p(\boldsymbol{\sigma},\boldsymbol{\alpha})}{p(D)} \tag{3.15}$$

where $p(D|\boldsymbol{\sigma},\boldsymbol{\alpha})$ is the evidence appearing in the denominator of Eq. (3.10) and $p(\boldsymbol{\sigma},\boldsymbol{\alpha})$ is the prior PDF of the hyperparameter set $(\boldsymbol{\sigma},\boldsymbol{\alpha})$. For simplicity, a uniform prior PDF is assumed for the hyperparameter set $(\boldsymbol{\sigma},\boldsymbol{\alpha})$. Thus, following the Bayesian model selection, among all values of $\boldsymbol{\sigma}$ and $\boldsymbol{\alpha}$, the most preferred values are the ones that maximize the posterior PDF $p(\boldsymbol{\sigma},\boldsymbol{\alpha}|D)$ or, equivalently, maximize the evidence $p(D|\boldsymbol{\sigma},\boldsymbol{\alpha})$, given from Eq. (3.10) by

$$p(D|\boldsymbol{\sigma},\boldsymbol{\alpha}) = \int_{\Theta} p(D|\boldsymbol{\theta},\boldsymbol{\sigma})p(\boldsymbol{\theta}|\boldsymbol{\alpha})d\boldsymbol{\theta} \tag{3.16}$$

with Θ being the domain in the parameter space of the possible values of $\boldsymbol{\theta}$.

The optimal values, $\hat{\boldsymbol{\sigma}}$ and $\hat{\boldsymbol{\alpha}}$ that maximize the evidence of the model must satisfy the stationarity conditions

$$\left.\frac{\partial p(D|\boldsymbol{\sigma},\boldsymbol{\alpha})}{\partial \sigma_j}\right|_{\substack{\boldsymbol{\sigma}=\hat{\boldsymbol{\sigma}}\\ \boldsymbol{\alpha}=\hat{\boldsymbol{\alpha}}}} = \int_{\Theta} \frac{\partial p(D|\boldsymbol{\theta},\boldsymbol{\sigma})}{\partial \sigma_j} p(\boldsymbol{\theta}|\boldsymbol{\alpha})d\boldsymbol{\theta}\Bigg|_{\substack{\boldsymbol{\sigma}=\hat{\boldsymbol{\sigma}}\\ \boldsymbol{\alpha}=\hat{\boldsymbol{\alpha}}}} = 0 \tag{3.17}$$

for $j = 1, \dots, N_o$ and

$$\left.\frac{\partial p(D|\boldsymbol{\sigma},\boldsymbol{\alpha})}{\partial \alpha_i}\right|_{\substack{\sigma=\hat{\sigma}\\ \boldsymbol{\alpha}=\hat{\boldsymbol{\alpha}}}} = \int_{\Theta} p(D|\boldsymbol{\theta},\sigma) \frac{\partial p(\boldsymbol{\theta}|\boldsymbol{\alpha})}{\partial \alpha_i} d\boldsymbol{\theta}\Bigg|_{\substack{\sigma=\hat{\sigma}\\ \boldsymbol{\alpha}=\hat{\boldsymbol{\alpha}}}} = 0 \tag{3.18}$$

for $i = 1, \dots, N_\theta$.

It is shown in Appendix 3.A.2 that from Eqs. (3.17) and (3.18) one can readily get

$$\hat{\sigma}_j^2 = \int_{\Theta} J_j(\boldsymbol{\theta}) p(\boldsymbol{\theta}|D,\hat{\boldsymbol{\sigma}},\hat{\boldsymbol{\alpha}})d\boldsymbol{\theta} \tag{3.19}$$

and

$$\hat{\alpha}_i = \frac{1}{\int_{\Theta} \theta_i^2 p(\boldsymbol{\theta}|D,\hat{\boldsymbol{\sigma}},\hat{\boldsymbol{\alpha}})d\boldsymbol{\theta}}. \tag{3.20}$$

The above integrals are high dimensional and the numerical integration is intractable. They can be computed using sampling methods which are computationally very costly (Ching & Chen, 2007). Here we use a Laplace asymptotic approximation for the integrals (Beck & Katafygiotis, 1998), based on the fact that one has a large number of data. In this case the uncertainty in the posterior distribution concentrates in the neighborhood of the most probable value. The size of the uncertainty region is inversely proportional to the square root of the number of data, and thus decreases as the number of data increases. The posterior distribution can be asymptotically

approximated by a delta function located at the most probable value $\widehat{\boldsymbol{\theta}} = \widehat{\boldsymbol{\theta}}(\widehat{\boldsymbol{\sigma}}, \widehat{\boldsymbol{\alpha}})$ in the parameter space. In this case the expressions in Eq. (3.19) and Eq. (3.20) for the most preferred values $\widehat{\boldsymbol{\sigma}}$ and $\widehat{\boldsymbol{\alpha}}$ become

$$\hat{\sigma}_j^2 \sim J\left(\widehat{\boldsymbol{\theta}}(\widehat{\boldsymbol{\sigma}}, \widehat{\boldsymbol{\alpha}})\right) \tag{3.21}$$

for $j = 1, \dots, N_o$ and

$$\hat{\alpha}_i \sim \frac{1}{\hat{\theta}_i^2(\widehat{\boldsymbol{\sigma}}, \widehat{\boldsymbol{\alpha}})} \tag{3.22}$$

for $i = 1, \dots, N_\theta$.

Note that for the special case of $\sigma_j = \sigma, \ \forall j$, as shown in Appendix 3.A.2, in place of Eq. (3.19) one gets

$$\hat{\sigma}^2 = \int_{\Theta} J(\boldsymbol{\theta}) p(\boldsymbol{\theta}|D, \hat{\sigma}, \widehat{\boldsymbol{\alpha}}) d\boldsymbol{\theta} \,. \tag{3.23}$$

By asymptotically approximating the posterior distribution by a delta function located at the most probable value $\widehat{\boldsymbol{\theta}} = \widehat{\boldsymbol{\theta}}(\hat{\sigma}, \widehat{\boldsymbol{\alpha}})$, in place of Eq. (3.21) one gets

$$\hat{\sigma}^2 \sim J\left(\widehat{\boldsymbol{\theta}}(\hat{\sigma}, \widehat{\boldsymbol{\alpha}})\right). \tag{3.24}$$

In order to get a solution, one requires the estimation of $\widehat{\boldsymbol{\theta}}(\widehat{\boldsymbol{\sigma}}, \widehat{\boldsymbol{\alpha}})$, obtained by minimizing Eq. (3.12) with values of $\boldsymbol{\sigma}$ and $\boldsymbol{\alpha}$ given by the most preferred values $\widehat{\boldsymbol{\sigma}}$ and $\widehat{\boldsymbol{\alpha}}$. The structure of Eqs. (3.12), (3.21) and (3.22) can be used to solve this problem in an iterative manner as follows. Let m be the counter of the iterations. Select starting values $\widehat{\boldsymbol{\theta}}^{(0)}$ for the model parameters and estimate the prediction error parameter $\widehat{\boldsymbol{\sigma}}^{(0)}$ and the hyperparameters $\widehat{\boldsymbol{\alpha}}^{(0)}$ from Eqs. (3.21) and (3.22) respectively. Iterate over m until convergence is achieved, by performing the following two steps to update the current values of $\widehat{\boldsymbol{\theta}}^{(m-1)}$, $\widehat{\boldsymbol{\sigma}}^{(m-1)}$ and $\widehat{\boldsymbol{\alpha}}^{(m-1)}$:

1) Use Eq. (3.12) to estimate $\widehat{\boldsymbol{\theta}}^{(m)} = \widehat{\boldsymbol{\theta}}\left(\hat{\sigma}^{(m-1)}, \widehat{\boldsymbol{\alpha}}^{(m-1)}\right)$.

2) Update the values $\widehat{\boldsymbol{\sigma}}^{(m)}$ and $\widehat{\boldsymbol{\alpha}}^{(m)}$ using Eqs. (3.21) and (3.22) with $\widehat{\boldsymbol{\theta}}$ replaced by the current $\widehat{\boldsymbol{\theta}}^{(m)}$.

We terminate the iterations over m when the norm of the difference between two consecutive values in the iteration is less than a tolerance value ε. For example

$$\left\|\widehat{\boldsymbol{\theta}}^{(m)} - \widehat{\boldsymbol{\theta}}^{(m-1)}\right\|_{\infty} \leq \varepsilon \tag{3.25}$$

where $\|\boldsymbol{\theta}\|_{\infty} = \max|\theta_i|$ is the infinity norm.

It can be shown that the above two-step minimization algorithm is equivalent to the following single-objective minimization problem

$$\widehat{\boldsymbol{\theta}} = argmin_{\boldsymbol{\theta}} \left[N_D \sum_{j=1}^{N_o} ln\left(J_j(\boldsymbol{\theta})\right) + \sum_{i=1}^{N_\theta} ln(\theta_i^2) \right]. \tag{3.26}$$

For the special case of $\sigma_j = \sigma,\ \forall j$, one instead ends up with

$$\widehat{\boldsymbol{\theta}} = argmin_{\boldsymbol{\theta}} \left[N_D N_o ln\big(J(\boldsymbol{\theta})\big) + \sum_{i=1}^{N_\theta} ln(\theta_i^2) \right]. \tag{3.27}$$

The proofs of Eqs. (3.26) and (3.27) are given in Appendix 3.A.3.

3.2 Example Applications

3.2.1 Problem description

We demonstrate the methodology by considering an example of a three-dimensional, single-bay, 15-story steel moment frame structure, shown in Figure 3.1A. Damage in steel moment frame buildings is most often manifested in the form of cracks in the beam-column connections (e.g., Miller, 1998; Roeder, 2000). The presence of a crack causes a reduction of the local stiffness when the crack is under tension. However, the ability to bear compressive loads is unaltered when the crack closes under compression. Guided by these observations, we consider the damage to the structure to be in the form of reduction of the stiffness in tension at the beams ends.

The finite element model of the structure is developed in OpenSEES (Mazzoni, et al., 2006). In order to be able to model the realistic behavior associated with the opening and closing of the cracks, we make use of fiber elements for the beams (Taucer, et al., 1991). In order to monitor the local stiffness reduction in the beam-column connections, the beams parallel to the horizontal x-direction are divided into segments along their length. The ends of each beam structural element are separate elements, as displayed in Figure 3.1B, which we refer to as "beam end elements." Each element is further discretized along its cross-section into a number of fibers, similar to what is displayed in Figure 3.1C, with the uniaxial material used for the fibers having a bilinear stress-strain behavior, as shown in Figure 3.1D. The lowest five modal frequencies of the building using the nominal values of the material properties are: $f_1 = 0.34Hz$ (1st translational mode in the y-direction), $f_2 = 0.40Hz$ (1st translational mode in the x-direction), $f_3 = 0.41Hz$ (1st torsional mode), $f_4 = 1.04Hz$ (2nd translational mode in the y-direction) and $f_5 = 1.24Hz$ (2nd translational mode in the x-direction).

There are many possible ways of parameterizing the structure so that the parameters are associated with structural damage. Choosing the most appropriate parameterization can always be viewed as a model selection problem – second level of inference (MacKay, 1992). For our examples we will be considering damage to the beams oriented along the x horizontal direction. The beam end elements are grouped into substructures and each substructure is associated with a parameter. For the initial damage scenarios we parameterize the model using one parameter per story. This allows us to determine the location of the damage in a story-by-story level. As shown in Figure 3.1A all beam end elements of every floor belong to the same substructure and get associated to the same parameter. For our 15-story building, the number of model parameters is 15.

More specifically, each model parameter accounts for the change of stiffness in tension of the beam end elements. This fractional change is assumed to be the same for all beam ends of a story. Thus, the components θ_i of the model parameters $\boldsymbol{\theta}$ used for parameterizing the stiffness of the substructure are defined as follows:

$$\theta_i = \frac{\psi_i - \psi_i^{nom}}{\psi_i^{nom}} \tag{3.28}$$

where ψ_i is the stiffness in tension of the elements at the new state and ψ_i^{nom} is the nominal (undamaged) stiffness in tension. We define our "Damage index" to be equal to the MAP value ($\widehat{\boldsymbol{\theta}}$) of the model parameters $\boldsymbol{\theta}$. Thus, the damage index monitors the change of stiffness in tension of the beam end elements. The undamaged state corresponds to $\boldsymbol{\theta} = \mathbf{0}$, while damage (loss of stiffness in tension) corresponds to negative values of $\boldsymbol{\theta}$.

For any undamaged elements, the uniaxial material stress-strain relationship is linear, having the same nominal modulus of elasticity (E^{nom}) in both compression and tension. The nominal material modulus of elasticity is assumed to be known, since it can be estimated from model calibration prior to the damaging event. Even though the modulus of elasticity of the material does not change, a way to introduce the desired stiffness reduction in tension is through a bilinear material stress-strain constitutive relation. Using this modeling, the model parameters $\boldsymbol{\theta}$ are associated with the fiber uniaxial material modulus of elasticity in tension, as depicted in Figure 3.1D. The modulus of elasticity in compression remains unaltered and equal to the nominal value (E^{nom}).

The nonlinearities due to the crack opening are activated during low, moderate and severe earthquake events as well as ambient vibrations. For this example problem, we consider no material nonlinearities and will be using excitations small enough for the materials to remain in the elastic regime. However, since the methodology relies on time history measurements, the proposed damage identification framework can be used for any finite element model, and a model with material hysteretic behavior can be used in the same way.

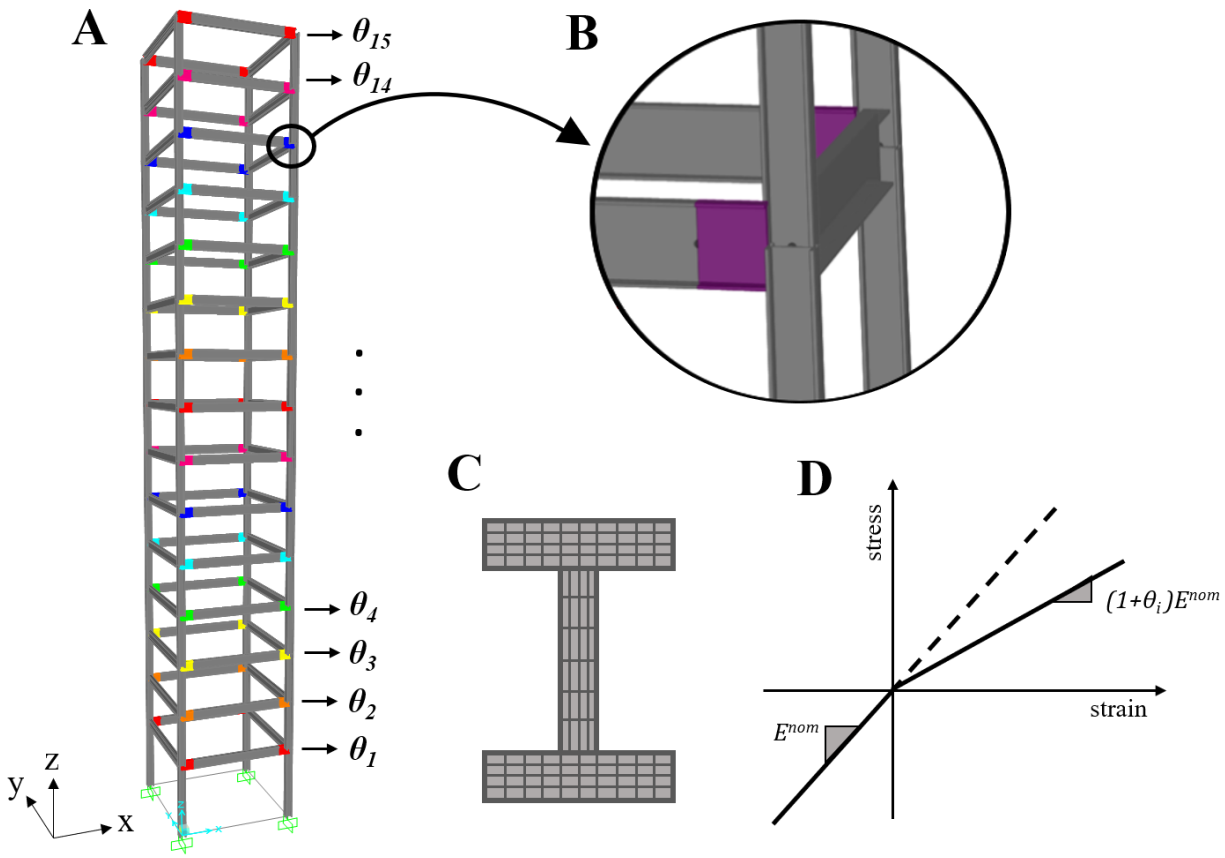

Figure 3.1. (A) The 15-story steel moment frame structure considered. Different colors denote the elements corresponding to the different substructures (here parameterization case A is shown). Each substructure is allocated a different parameter (θ_i). (B) Detail: the beam end elements are colored in purple. (C) Cross-section of an example fiber element. (D) The uniaxial material stress-strain curve – the model parameter θ_i characterizes the loss of stiffness in tension.

3.2.2 Damage scenarios and application details

We introduce damage by applying a 50% reduction in the stiffness in tension at the beam end elements. We consider the following 8 damage scenarios. Damage is introduced in:

A) all the beam ends of the 1st floor (corresponding to distributed weld damage in the 1st floor);

B) all the beam ends of the 1st and 5th floors (corresponding to distributed weld damage in the 1st and 5th floors);

C) all the beam ends of the 14th floor (corresponding to distributed weld damage in the 14th floor);

D) all the beam ends every 3rd floor (corresponding to distributed weld damage in floors 1, 4, 7, 10, and 13);

E) the left half of the beam ends of the 1st floor (corresponding to weld damage on one side of the beam elements of the 1st floor);

F) the front beam of the 1st floor; (corresponding to weld damage on both sides of one of the beams of the 1st floor);

G) the front beam ends of the floors 1 and 2 & the back beam ends of floors 4 and 5 (corresponding to weld damage on both sides of a beam in floors 1, 2, 4, and 5);

H) the left-side end elements of the front beams in floors 1, 2, and 3 (corresponding to weld damage on one side of a beam in floors 1, 2, and 3).

The elements damaged for each case are shown in Figure 3.2 (marked in red).

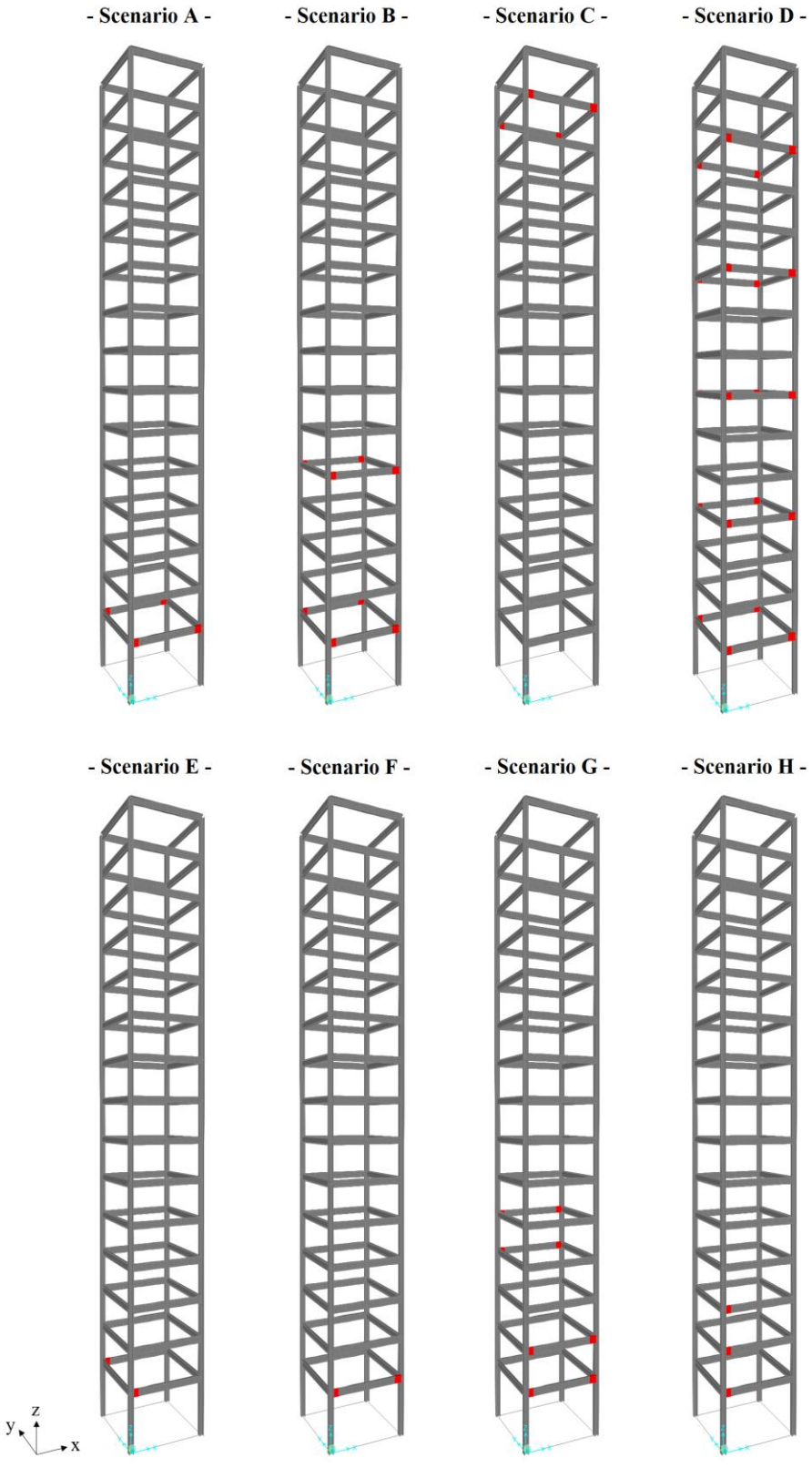

Figure 3.2. The damage scenarios considered.

The data is simulated by running an excitation through the damaged structural model. The identification is done based on low amplitude vibrations (e.g. vibrations from aftershocks) so that material nonlinearities throughout the structure are not activated. In our example the simulated data are generated by subjecting the building to a scaled version (x0.2) of the north-south component of the 1995 Kobe Japan earthquake (M6.9) recorded at the Nishi-Akashi station, displayed in Figure 3.3. The excitation is applied in all ground (fixed) nodes in both horizontal directions.

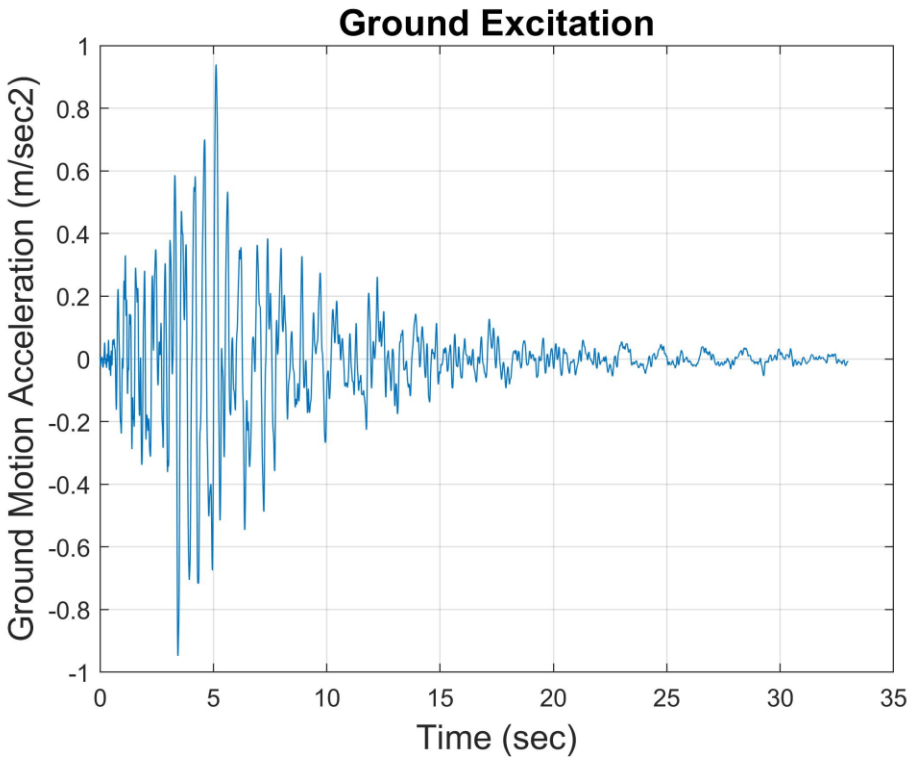

Figure 3.3. The applied ground acceleration –1995 Kobe Japan earthquake (Nishi-Akashi station) record, scaled (x0.2).

Floor-by-floor measurement data is assumed to be available for the structure. This is consistent with the density of the CSN network which has dense sensors deployments present in multiple buildings. We consider the bottom left corner of each story to be instrumented with one tri-axial

accelerometer per floor. The acceleration recordings in the two horizontal directions are used in the analysis.

Additional model error is considered by perturbing the stiffness properties of the model used to simulate the measurements. For model error level e_α, the stiffness values of all beam and column elements in the structure are independently perturbed using a Gaussian distribution with mean equal to the nominal stiffness value and standard deviation equal to e_α multiplied by the nominal stiffness value. For some cases, measurement error is also considered. For measurement error level e_β, the simulated time history responses are perturbed by adding zero-mean Gaussian white noise with standard deviation equal to e_β multiplied by the response intensity.

Regarding the additional model error, we consider four different model error cases corresponding to $e_\alpha = 0$ (no added model error), $e_\alpha = 1\%$ and 2% (small to moderate added model error) and $e_\alpha = 5\%$ (large added model error). The 5% model error case corresponds to a large model error since the stiffness values of all beam and column elements in the structure are being independently perturbed using a Gaussian distribution with standard deviation equal to 5% of their nominal stiffness value. For a Gaussian distribution, 31.73% of the samples are expected to be further than one standard deviation away, while 4.55% of the samples can be further than two standard deviations away. For example, for our 15-story model that has 180 elements, this corresponds to about 57 elements with nominal stiffness ψ_i^{nom} having stiffness less than $0.95\,\psi_i^{nom}$ or greater than $1.05\,\psi_i^{nom}$, and about 8 elements having stiffness less than $0.9\,\psi_i^{nom}$ or greater than $1.1\,\psi_i^{nom}$. Depending on the distribution of these elements in the structure this can severely alter the structure's properties.

The finite element analysis in OpenSEES is fully integrated with MATLAB where the formulations discussed in the previous section (Section 3.1) are implemented. For the optimizations, the *fmincon* Interior Point Algorithm (MATLAB, 2019; Byrd, et al., 2000), a bounded gradient-based optimization is used. For convenience, to allow for a non-intrusive modeling when integrating the SBL algorithm with the OpenSEES finite element model, the derivatives of the objective function are numerically computed. The $\hat{\theta}_i$ values are bounded within

$[-0.9, 0.01]$, based on the fact that we expect neither a total loss, nor an increase of the stiffness in tension at the beam ends. The initial values of the model parameters are assigned $\hat{\theta}_i^{(0)} = -0.05$, for $i = 1, \dots, N_\theta$, i.e. close to the values corresponding to the initial (undamaged) state of the structure. Solving the single-objective minimization problem is generally much more efficient than the iterative one. However for our application where we use a gradient-based algorithm with the derivatives being numerically computed, the logarithms in Eq. (3.27) can cause convergence issues. Thus, for our example problem, the two-step optimization algorithm is used. The initial values for $\hat{\sigma}^{(0)}$ and $\widehat{\boldsymbol{\alpha}}^{(0)}$ are calculated from Eqs. (3.24) and (3.22) using the selected $\widehat{\boldsymbol{\theta}}^{(0)}$.

3.2.3 Study I: Damage Identification under Varying Model and Measurement Error Levels

In study I, we examine the first five damage scenarios (scenarios A-E in Figure 3.2). We have a floor-by-floor parameterization (as shown in Figure 3.1A), and assume one sensor per floor. Overall, the SBL identification successfully yields distinct non-zero values for the damage indices at the damaged floors, for all damage scenarios and degrees of model and measurement error assumed. For all scenarios when there is no model and measurement error, we get the exact solution, i.e. the model parameter values used for simulating the data. This also demonstrates that the optimization algorithm using numerically evaluated derivatives works well.

For damage scenario A (damage in floor 1) we consider four different model error cases corresponding to $e_\alpha = 0$ (no model error), $e_\alpha = 1\%$ and 2% (small to moderate model error) and $e_\alpha = 5\%$ (large model error). The damage indices obtained as a function of the floor level for different model errors are presented in Figure 3.4. The damage identification is pretty good, even for the higher model error cases. The two-step optimization algorithm converges within 2-3 iterations over m. The existence of damage is recognized for all model error cases. For the low-medium model error cases, the location and degree of damage is identified almost perfectly. The 2%-5% false damage estimated in floors 2 to 6 is due to the model error. The damage at floor 1 is slightly overestimated at 52-55% instead of 50%, which is the actual inflicted damage. For the large model error case, the false alarms of around 15% in floors 2-6 are evident. However, the actual damage location and the magnitude of damage are adequately identified.

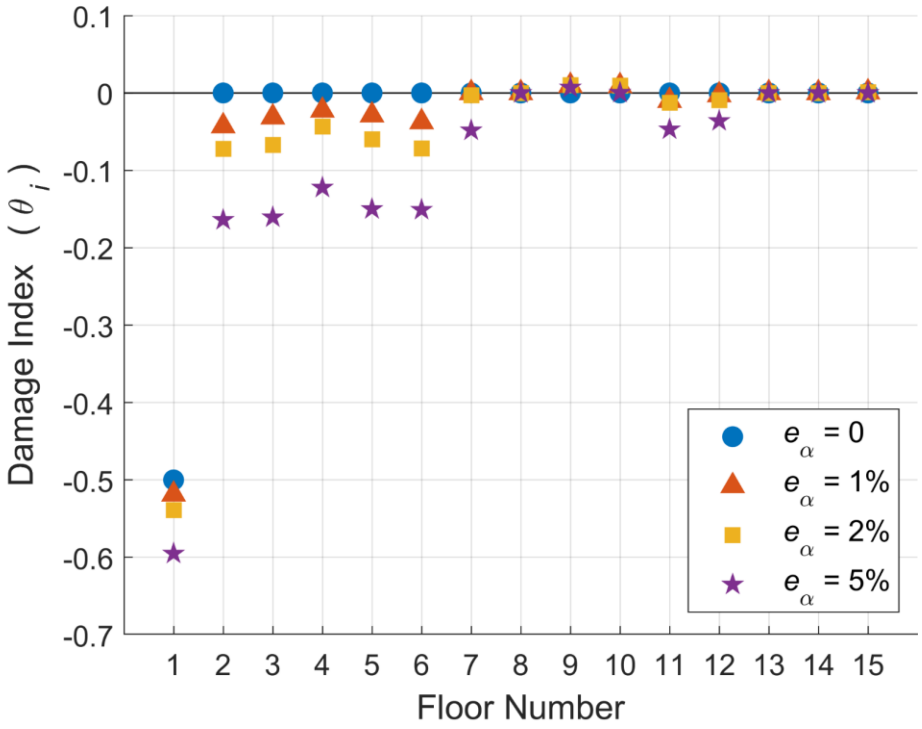

Figure 3.4. Damage indices for scenario A (damage in floor 1) for varying model error (e_α) levels.

For damage scenario B (damage in floors 1 and 5) we consider the effectiveness of the method for different model errors, as well as different measurement errors. Figure 3.5 displays the identification results for different sizes of model error, ranging from 0% to 5%. Like in the previous scenario, the existence of damage is successfully recognized for all model error cases. The location and extent of damage are also determined to a satisfying degree. For low to moderate model error, damage is slightly overestimated in floor 1 and slightly underestimated in floor 5, while floors neighboring the damaged ones demonstrate false damage of small magnitude not exceeding 9% for $e_\alpha = 1\%$ magnitude of model error and 15% for $e_\alpha = 2\%$ magnitude of model error. For the higher model error case, we again get a successful identification of the two damaged floors, but false alarms of up to 25% also emerge for floors 2, 3, 4, and 6.

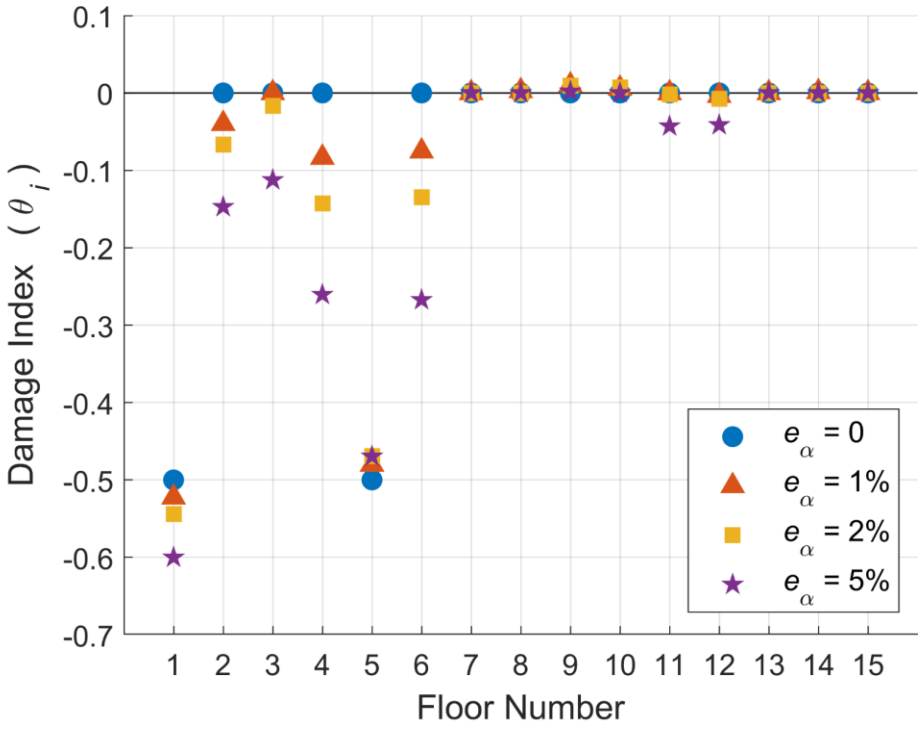

Figure 3.5. Damage indices for scenario B (damage in floors 1 and 5) for varying model error (e_α) levels.

Figure 3.6 shows the identification results for damage scenario B, for different degrees of measurement error, ranging from 0% to as high as 80%. The identification is almost perfect independent of measurement error. Adding white noise measurement error to data simulated by the nominal damage model, a procedure that has been widely used in the literature when simulating data, does not really affect the effectiveness of the method for identifying the location and magnitude of damage. It seems that such a procedure of adding white measurement noise, ignoring model error, should be avoided or considered with care when testing a damage identification method for its effectiveness using simulated data.

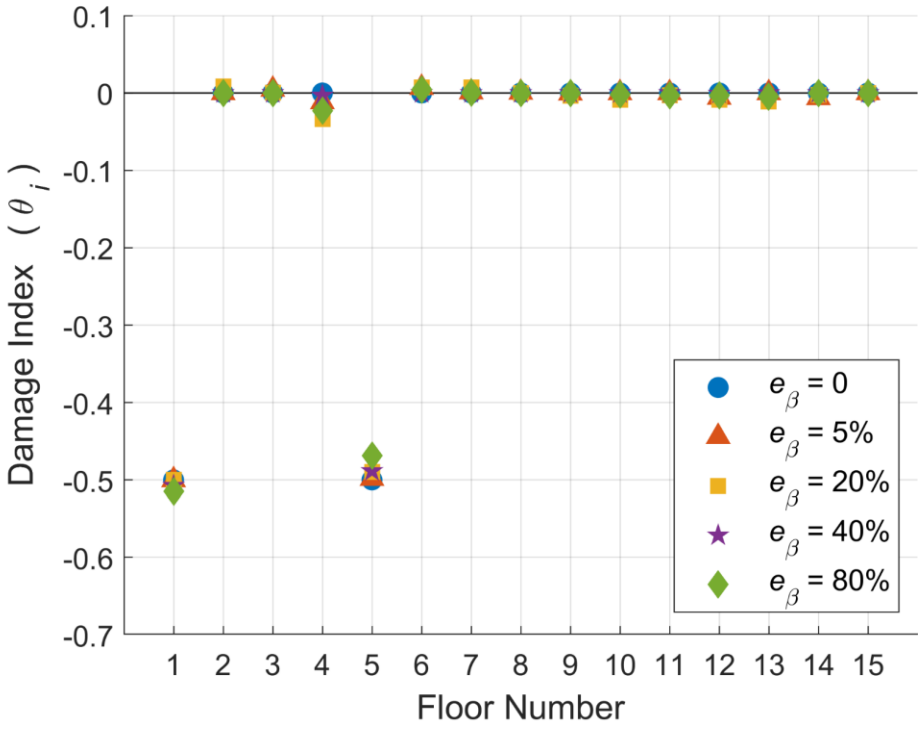

Figure 3.6. Damage indices for scenario B (damage in floors 1 and 5) for varying measurement error (e_β) levels.

In all cases considered, the two-step optimization algorithm converges rapidly, usually within 2-4 iterations over m. In Figures 3.7 and 3.8 we show for two example cases the behavior of the MAP θ_i values, the σ, and select α_i values, for each iteration over m. Figure 3.7 displays the variation during the iterative process for the case of damage scenario B with model error $e_\alpha = 2\%$, and Figure 3.8 for the case of damage scenario B with measurement error $e_\beta = 40\%$. For brevity we plot only two of the hyperparameters. We chose to plot α_5 and α_{10} in order to capture both behaviors of a hyperparameter. The hyperparameter α_5 corresponds to the "relevant" parameter θ_5 and its value decreases as a consequence. On the other hand, hyperparameter α_{10} corresponds to the "irrelevant" parameter θ_{10} and its value goes to infinity, effectively "shutting-off" the corresponding parameter, implementing Occam's razor. Starting from all damage indices being non-zero, most of them go to zero and the damage gets decently localized within 1-2 iterations. For both cases, a hyperparameter value $\alpha_{10} > 10^4$ leads to the damage index for the corresponding

model parameter θ_{10} being zero. The prediction error parameter σ changes during the first iteration, but remains relatively constant after that.

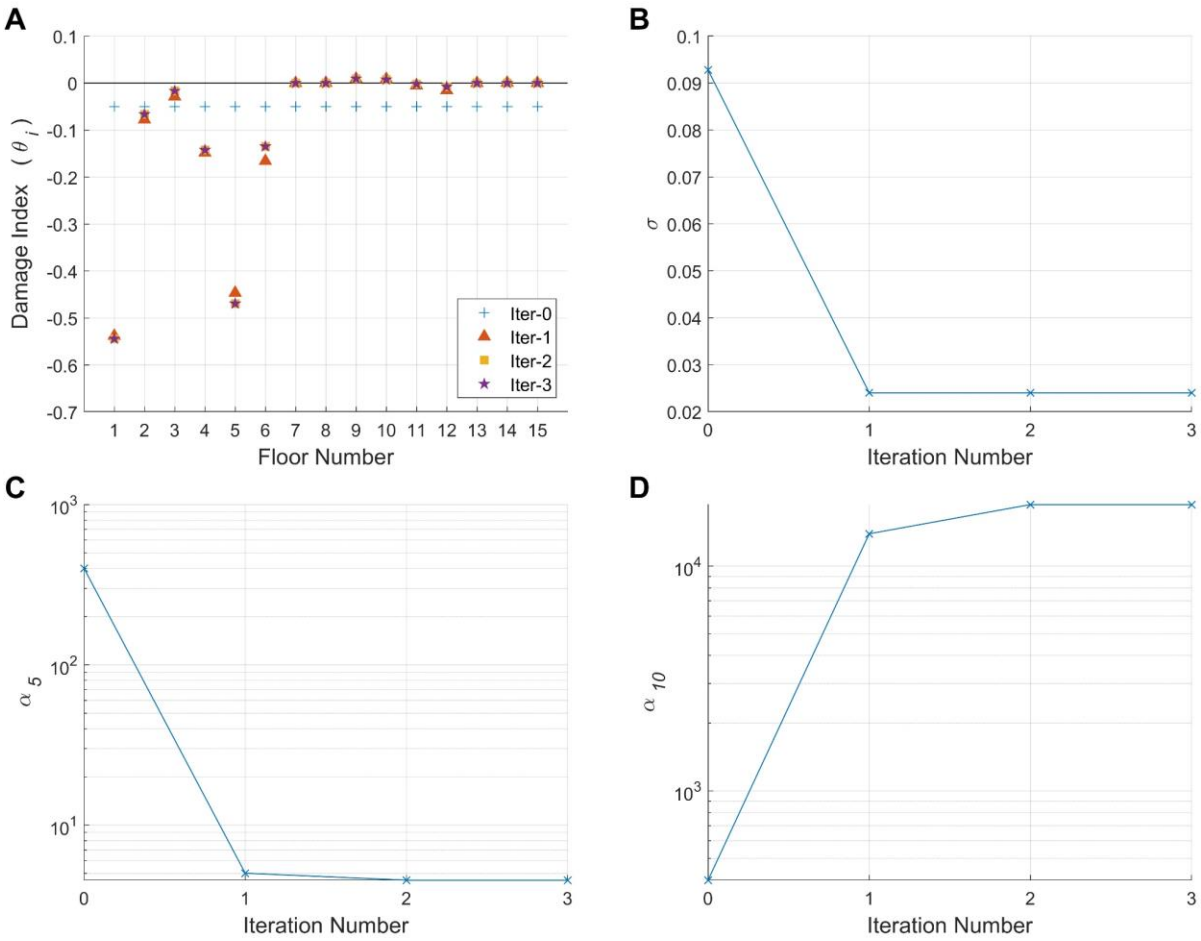

Figure 3.7. Evolution with iterations. Scenario B (damage in floors 1 and 5) with e_α = 2% model error. (A) Damage indices. (B) Prediction error parameter σ. (C) Hyperparameter α_5. (D) Hyperparameter α_{10}.

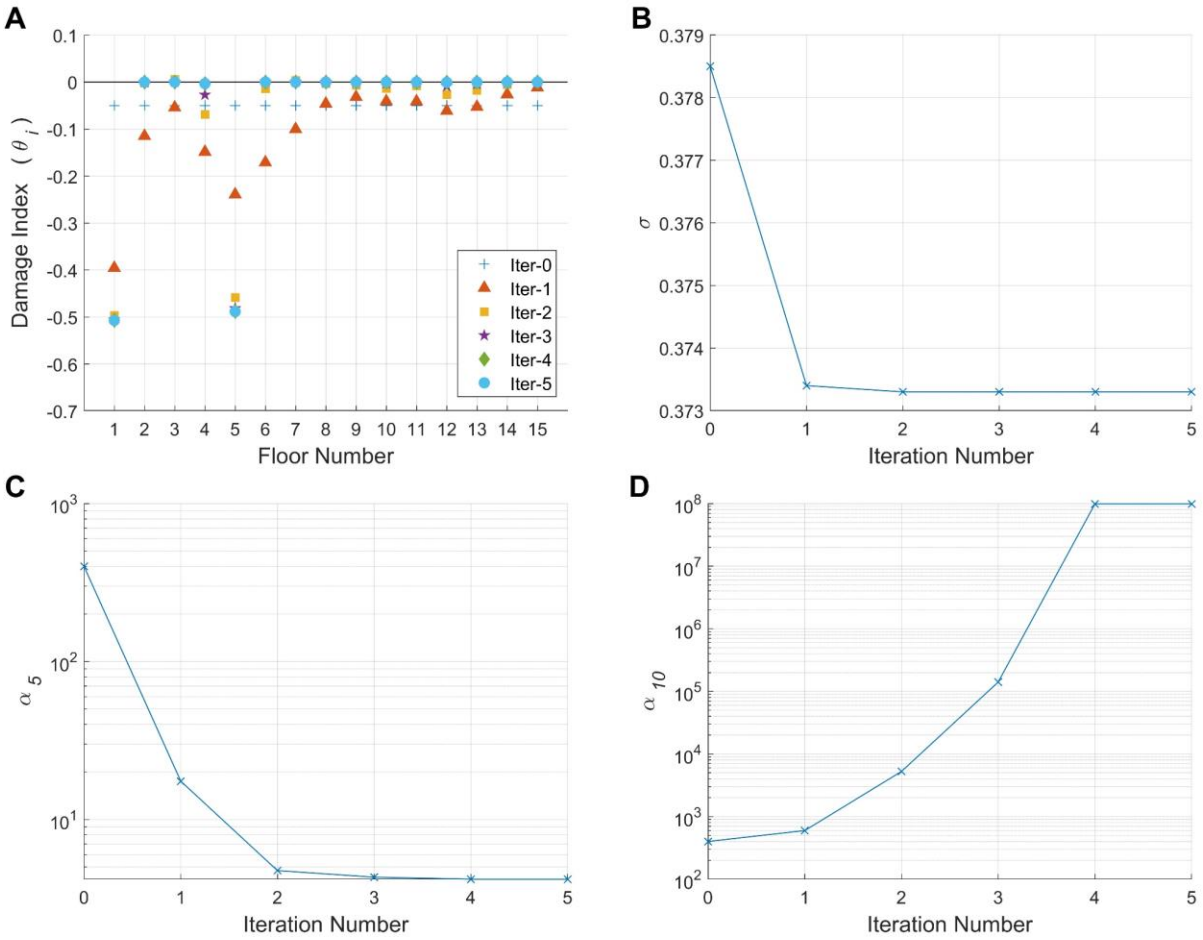

Figure 3.8. Evolution with iterations. Scenario B (damage in floors 1 and 5) with e_β = 40% measurement error. (A) Damage indices. (B) Prediction error parameter σ. (C) Hyperparameter α_5. (D) Hyperparameter α_{10}.

Figure 3.9 displays the identification results for damage scenario C (damage in floor 14). Here we again consider four different model error cases corresponding to $e_\alpha = 0$ (no model error), $e_\alpha =$ 1% and 2% (small to moderate model error) and $e_\alpha = 5\%$ (large model error). This is expected to be a rare damage scenario, since damage in a steel moment frame structure is usually observed in the lower floors. Compared to the previous scenarios where the damage was located at the lower floor, the identification of the damage at the higher floors (floor 14) is more challenging. The identification is perfect, as expected, for no model error. For low and moderate model errors, the damage at floor 14 is still identified, but as 40% instead of the inflicted 50% extent of damage. However, there are possible false alarms on floors 1, 3, 5, 6, 13, and 15 with extent of damage of

15%, 11%, 5%, 10%, 6%, and 20%, respectively. For the larger model error case it is harder to reliably identify the damage at floor 14 since false alarms with extent of damage of similar or higher level than the one identified in floor 14 is reported in floors 1, 3, 6, and 13. Identification of damage in the top few floors is challenging, due to the fact that the model predictions are insensitive to changes of stiffness in the higher floors, i.e. the changes in the response are very small when the higher floor parameters change.

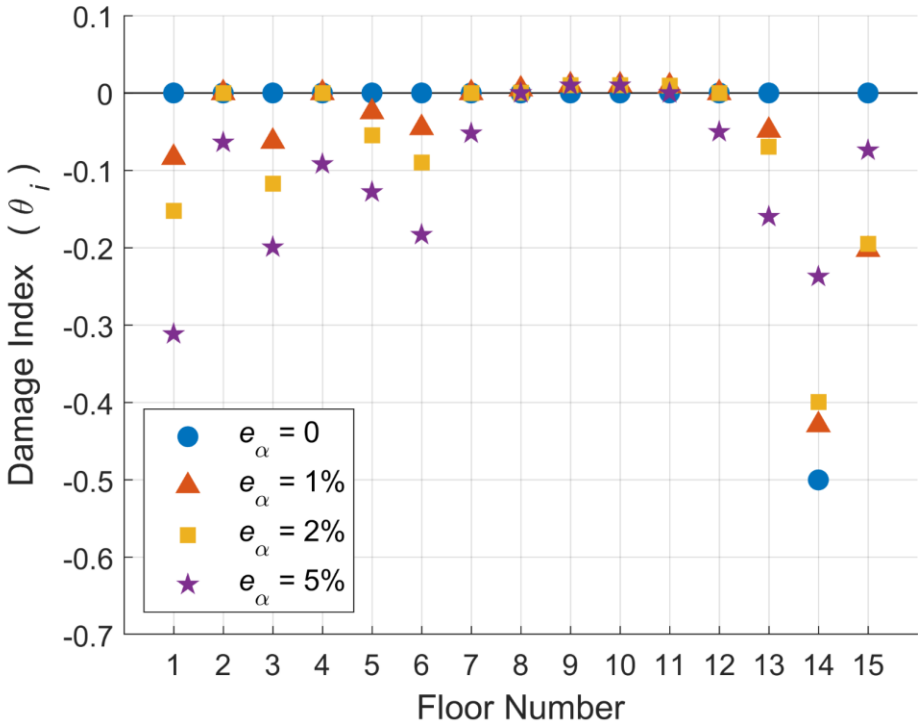

Figure 3.9. Damage indices for scenario C (damage in floor 14) for varying model error (e_α) levels.

For damage scenario D (damage in floors 1, 4, 7, 10, and 13), the identification results are shown in Figure 3.10. We again consider four different model error cases ranging from 0% to 5%. Damage identification for this scenario is expected to be challenging since the damage pattern has less sparsity, but also there is damage at the higher floors. This damage scenario is also expected to be rare since damage in a steel moment frame structure is usually found to be sparse and is observed in the lower floors. For low and moderate model errors, the identification of the location

and extent of damage is still pretty good with the appearance of the previously observed spread of the identified damage to floors neighboring the damaged ones. The extent of damage in the floors neighboring those that are damaged is not higher than 15%. For high model error, the damaged floors are still identified but there is a high number of false alarms. Specifically, the identification of the damage at the higher floors (e.g., at floor 13) is difficult. This is, as discussed previously, due to the fact that the model predictions are insensitive to changes of stiffness in the higher floors.

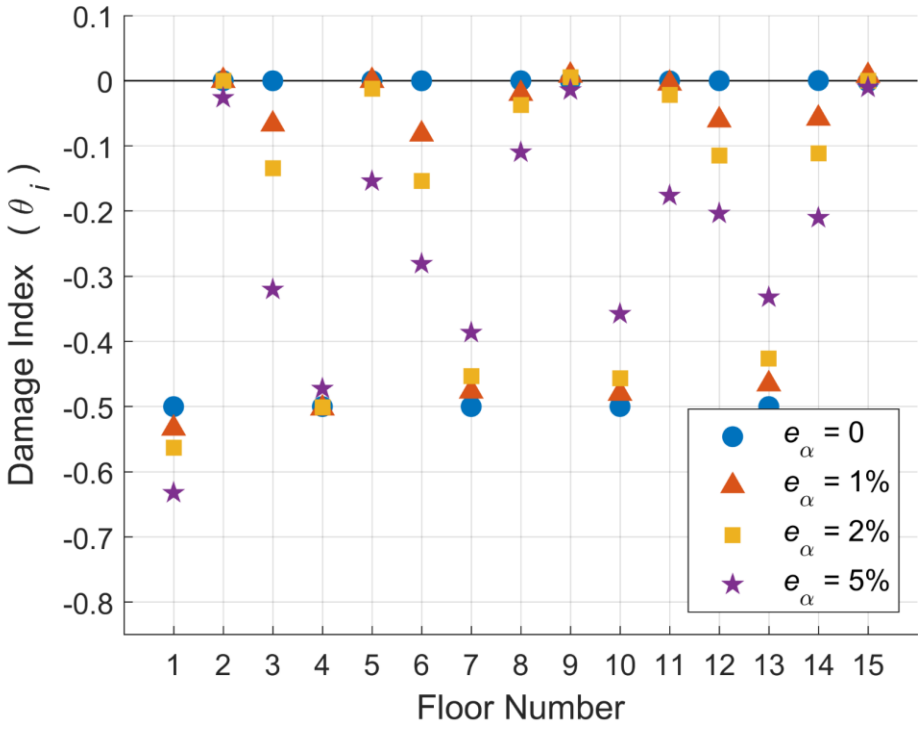

Figure 3.10. Damage indices for scenario D (damage in floors 1, 4, 7, 10, and 13) for varying model error (e_α) levels.

For damage scenario E (damage only in the left side beam end elements of floor 1), there is significant model error added since there is no possible solution from the parameterized model that will exactly predict the simulated data even for $e_\alpha = 0$. The results are shown in Figure 3.11, for 4 different levels of additional model error, with e_α ranging from 0% to 5%. Considering the existence of model error even for $e_\alpha = 0$, the identification of the damage is successful. For low to moderate model error ($e_\alpha = 0\%$, 1% and 2%), the extent of damage is estimated to be 32% to

40%, lower than the inflicted damage of 50%. The estimated extent of damage is reasonable considering that damage was inflicted at one end of the beams while the model parameters change at both ends. The observations as the model error increases are similar to the previous damage scenarios. The damaged floors are always identified but there is also a number of false alarms occurring for high model error.

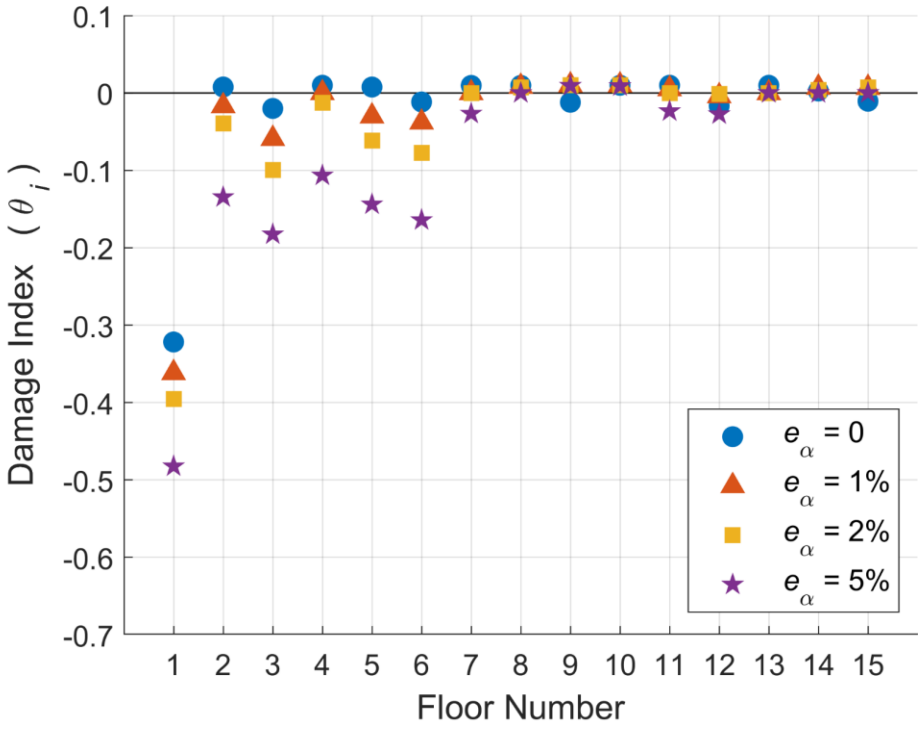

Figure 3.11. Damage indices for scenario E (damage in half of the beam end elements of floor 1) for varying model error (e_α) levels.

3.2.4. Study II: Exploring Alternative Parameterizations

In the second study we investigate the performance of the damage identification methodology that was developed in this thesis for different parameterizations. In addition to the initial parameterization where we parameterize the model using one parameter per story (parameterization case A – Figure 3.12A), we will consider three additional parameterizations, shown in Figure 3.12. For the parameterization case B, we parameterize the model using two

parameters per floor (Figure 3.12B) for the first five floors. Case C is similar but extended to the first seven floors (Figure 3.12C). Case D is the extreme case where each beam end belongs to a separate substructure and has its own parameter (Figure 3.12D). Thus, for case D we have four parameters per floor, for the first four floors. These denser parameterizations are limited to the first few floors in order to keep the model parameters at a reasonable number and to avoid excessive computational cost due to the large number of parameters. This parameterization of the lower floors is also guided by observations that damage in steel moment frame buildings is concentrated at the lower floors.

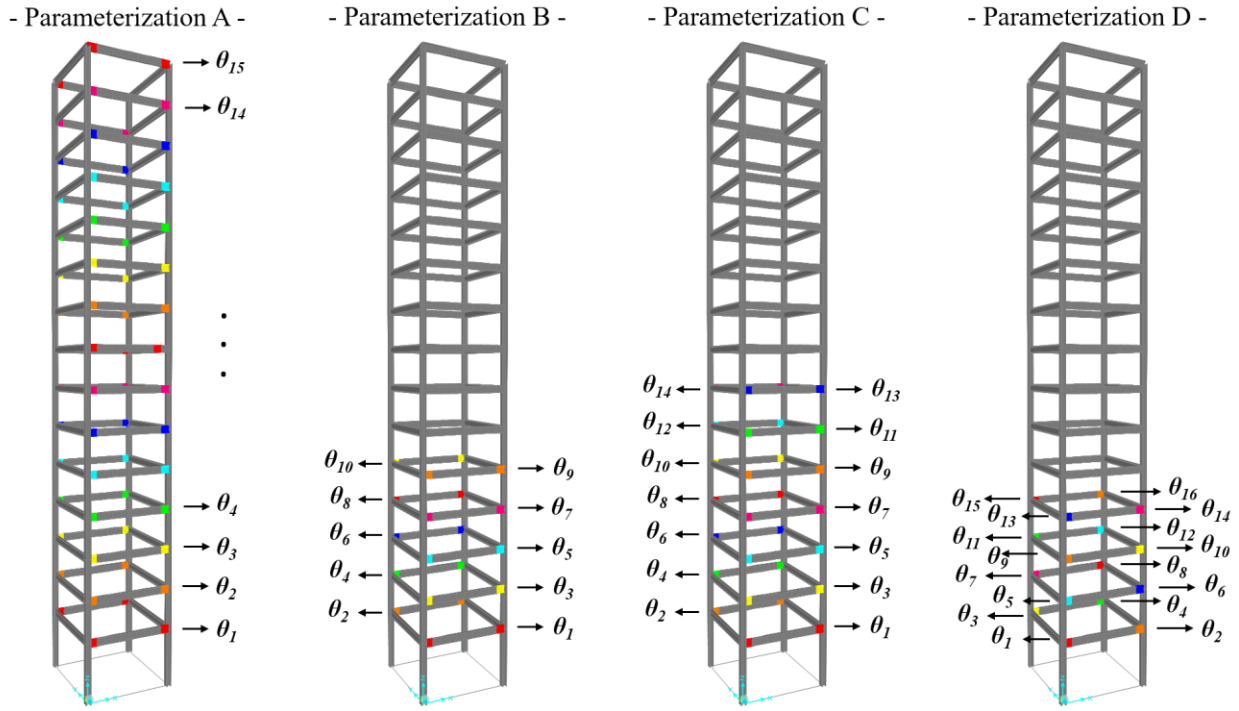

Figure 3.12. The parameterization cases considered.

In study 2 we consider the damage scenarios F, G, and H. For these three scenarios, the damage pattern is no longer symmetric and the torsional mode of the structure will also be excited. Furthermore, by studying the modes of the structure, one can see that the former translational modes (for the undamaged structure) now also contain a small torsional contribution after the damage is introduced to the structure. This can be viewed in Figure 3.13, where we plot the modeshapes based on the initial tensile stiffness of the damaged model, for damage scenario H.

When damage is introduced in the left beam ends of floors 1-3, the 3rd mode which is torsional now contributes to the motion, and the previously purely translational in the x-direction 2nd mode also contains some torsional contribution, as it can be seen in Figure 3.13B. The change in the modal frequencies of the building from the undamaged to the damaged state is extremely low. The largest decrease is near 1% for the 2nd mode (from $f_2 = 0.4Hz$ to $f_2 = 0.395Hz$).

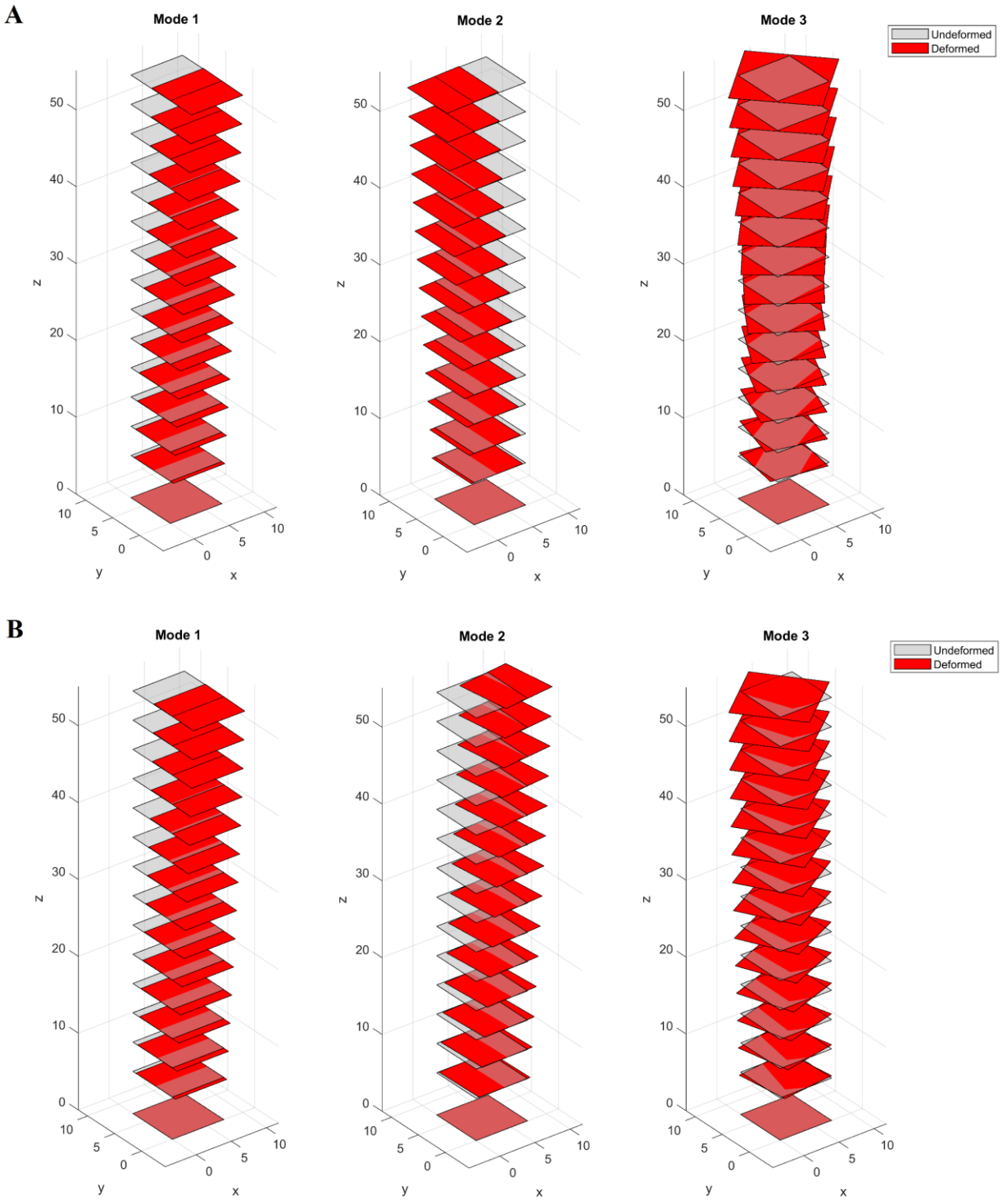

Figure 3.13. The first 3 modeshapes of the structure. (A) For the undamaged structure. (B) For the damaged structure (damage scenario H).

Note that if the original floor-by-floor parameterization (case A) was used for identifying damage scenarios F-H, then model error would be introduced in the analysis due to the parameterization. This is because there will be no values of the model parameters that will predict the artificial data simulated by the damaged model in the zero model error case ($e_\alpha = 0$), similar to what we had for case E.

It should be noted that up to now the damage scenarios involved simultaneous damage in both opposing sides (here termed front and back sides) of a floor. In contrast, the damage scenarios F, G and H involve damage on one side of the floor. The case B and C parameterizations shown in Figure 3.12 are introduced to pinpoint damage at one or both sides (front and/or back sides) of a floor. These parameterizations are used to test the effectiveness of our SBL technique to identify the damaged side (front or back) of a floor, instead of the damaged floor as was done with the study I. Moreover, parameterization case D is more detailed, and is used to identify damage at one of the two ends of the floor beam located at the front or back side.

For the damage scenario F (damage in the front beam of the 1st floor – Figure 3.2), with the two parameters per floor (parameterization case B - Figure 3.12B), we consider the same four model error cases: $e_\alpha = 0$ (no model error), $e_\alpha = 1\%$ and 2% (small to moderate model error) and $e_\alpha = 5\%$ (large model error). The damage indices obtained as a function of the parameter number (now 10 total parameters) for different model errors are presented in Figure 3.14. For this higher resolution (using two parameters per floor), the damage identification is again successful, even for the higher model error cases. The two-step optimization algorithm converges within 3-5 iterations over m. The existence of damage is recognized for all model error cases. For zero model error we get the exact solution. For the low-medium model error cases, the location and extent of damage is identified successfully at the front side of the 1st floor, although some false alarms at the back side of the 1st floor and the front side of the 2nd, 3rd and 5th floors corresponding to a small extent of damage of 10% in lower floors to 20% in the 5th floor is also identified. For the large model error, the presence of damage in the front side of the first floor is clearly identified with 60%, instead of the inflicted 50%, extent of damage. A few false detections at the lower floors are also

possible with extent of damage as high as 30% for the lower floors and 40% for the 5th floor. In summary, for moderate model error the identification of damage is successful, while for large model error there is a number of false alarms at non-damaged sides of the other floors.

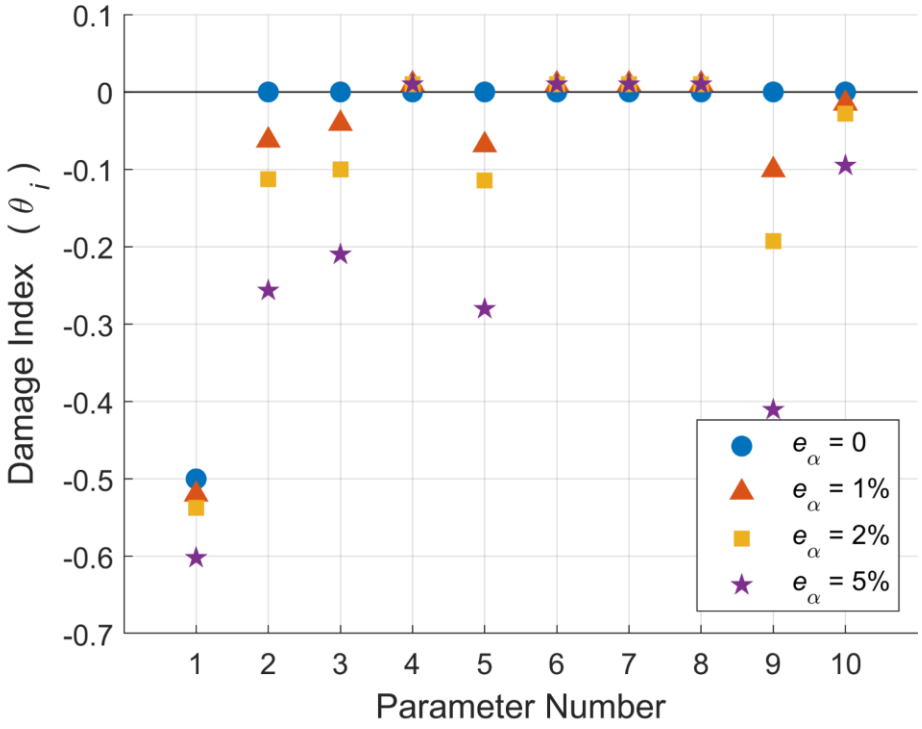

Figure 3.14. Damage indices for scenario F (damage in the front beam end elements of floor 1) for varying model error levels (e_α). Two parameters per floor (parameterization B).

For scenario G, we introduce damage in floors 1 and 2 at the front beam and in floors 4 and 5 at the beam in the back (Figure 3.2). The two parameters per floor parameterization is extended to the first 7 floors (parameterization case C - Figure 3.12C), so there are 14 total model parameters. The identification results are shown in Figure 3.15, for no model error and moderate model error (2%). For no model error, the exact solution is found, as expected. For moderate model error the damage locations and magnitudes are again adequately identified. The magnitudes of the damage in floors 1, 2, and 4 (parameters θ_1, θ_3, and θ_8) are found pretty successfully, with the error between the predicted and the inflicted damage being less than 5%. The identification gets more challenging for the higher floor (floor 5 – parameter θ_8) where the damage is underestimated, with

the error between the predicted and the inflicted damage to be around 20%. Similar to the previous moderate model error examples, a few false alarms with extend of damage less than 20% appear in undamaged floors. Using the damage results in Figure 3.14 (damage scenario F) and Figure 3.15 (damage scenario G), it can be concluded that the SBL technique, with the appropriate parameterization, can identify not only the damaged floor but also the side that is damaged in a floor.

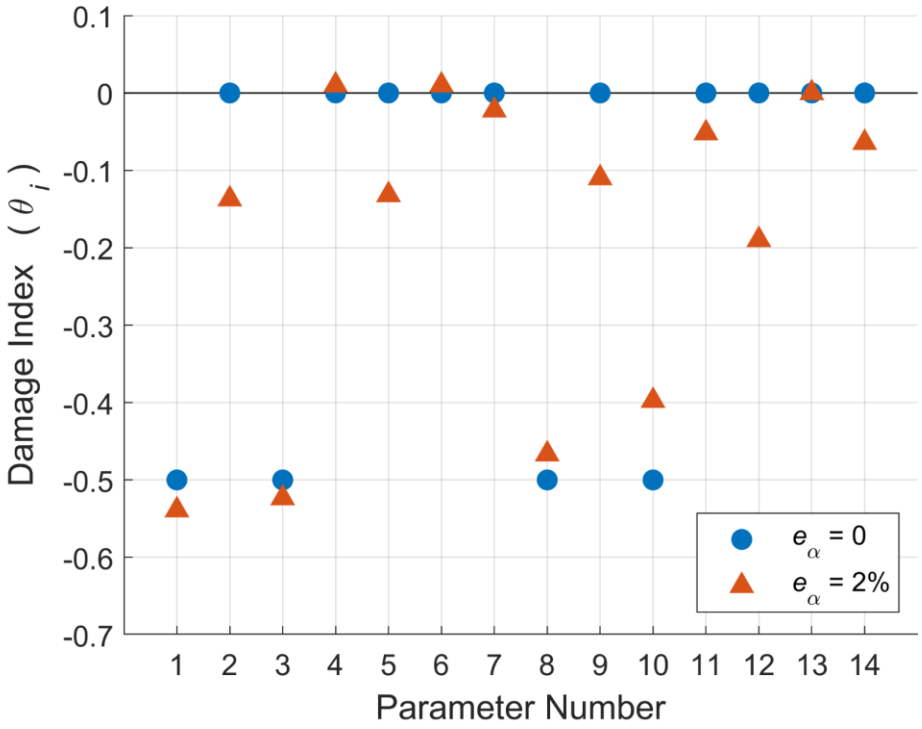

Figure 3.15. Damage indices for scenario G (damage in the front beam ends of the floors 1 and 2 & the back beam ends of floors 4 and 5) for varying model error levels (e_α). Two parameters per floor (parameterization B).

In scenario H, damage is introduced at one side (the left side) of the beam end elements of the front beams in floors 1, 2, and 3 (Figure 3.2). Figure 3.16 presents the identification results using two parameters per floor (parameterization B), for no model error and moderate model error (2%). Note that when using parameterization B for identifying damage scenario H, there is inherent model error arising from the parameterization, since parameterization B simultaneously changes

the stiffness properties of both the left and the right beam end elements, while the damage is at the left beam end element only. Despite the model parameterization error, under no additional model error ($e_\alpha = 0$), the identification of the damage locations is ideal with only the three damaged beams (θ_1, θ_3, and θ_5) having a damage index that is significant different than zero. Furthermore, the fact that the magnitude is almost the same for the three locations is encouraging. Under moderate model error ($e_\alpha = 2\%$) the three damage locations are correctly identified, and false alarms appear in floors 2 and 9 predicting damage indices of around 10% and 20%.

For scenario H we also experiment with an even denser parameterization in an effort to locate the end of the beam that is damaged in a specific floor. Figure 3.17 displays the identification results using four parameters per floor (parameterization D). Using this parameterization there is no longer inherent model error due to parameterization, since in this case there exist parameter values that will give predictions that match the simulated data. The case $e_\alpha = 0\%$ (no model error) should be able to identify the location and size of damage exactly. The exact damage index values are shown in blue in Figure 3.17. This is the expected solution under no model error. From the identified results shown in Figure 3.17 it can be seen that it is impossible to distinguish the damage between the two beam ends of the same element. Nonetheless, the algorithm does a great job of identifying which beam is damaged, as well as the magnitude of the damage. For example, under no model error the algorithm correctly finds the front beam of the 1st floor to be damaged, even though it identifies the right end beam to be the one damaged rather than the left one. Similarly for the 2nd and 3rd floors, the damage is successfully located at the front beam. The results are similar for the moderate (2%) model error case with the addition of the few expected low magnitude false alarms. Specifically, the extent of damage is missed in the third floor, while a false alarm is obtained indicating damage in the neighboring fourth floor. It seems that one set of measurements per floor in the two horizontal directions is not adequate to identify the end point of the beam where damage occurs. Also, this detailed parameterization per floor should be considered with care since the extra parameters seem to be redundant and have an effect of deteriorating the performance of the SBL methodology.

Based on the results obtained and the fact that a damage scenario to be predicted by the zero model error case is not the one that is inflicted, one can conclude that the solution is non-unique. There is more than one global solution to the problem with each one of them identifying damage at the left or right end of the damaged beam. The search for these multiple solutions was not pursued further due to the computational cost. However, one way to identify them is to run the optimization algorithm several times and use different starting values for each run.

These results reveal the good performance of the method for identifying damage with higher spatial resolution. For our example application, the SBL methodology presented here is able to identify damage in a beam-by-beam level.

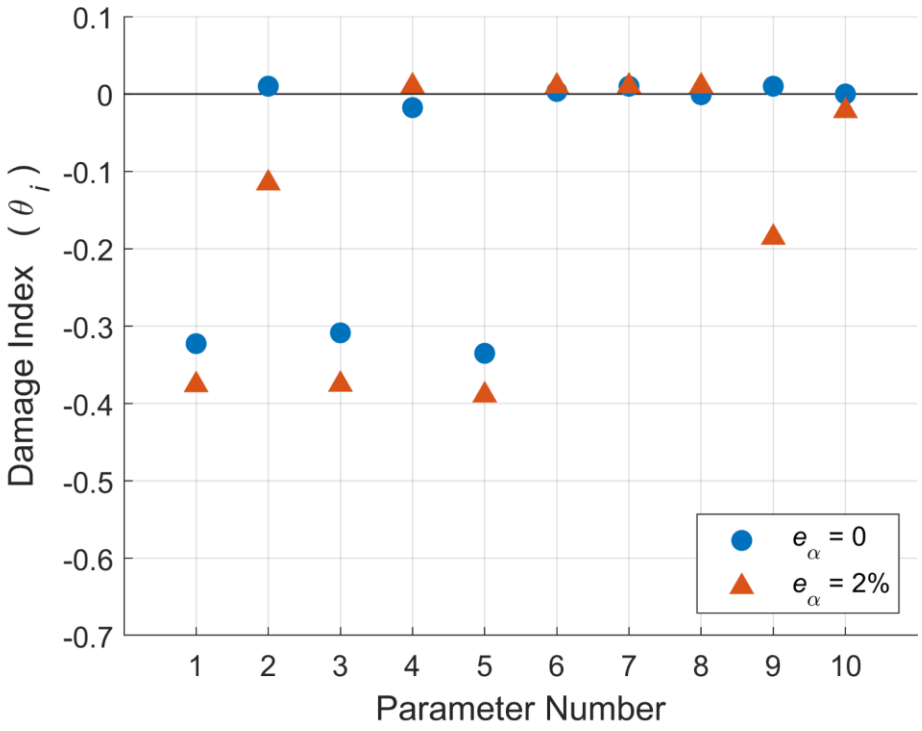

Figure 3.16. Damage indices for scenario H (left-side end elements of the front beams in floors 1, 2, and 3) for varying model error levels (e_o). Two parameters per floor (parameterization B).

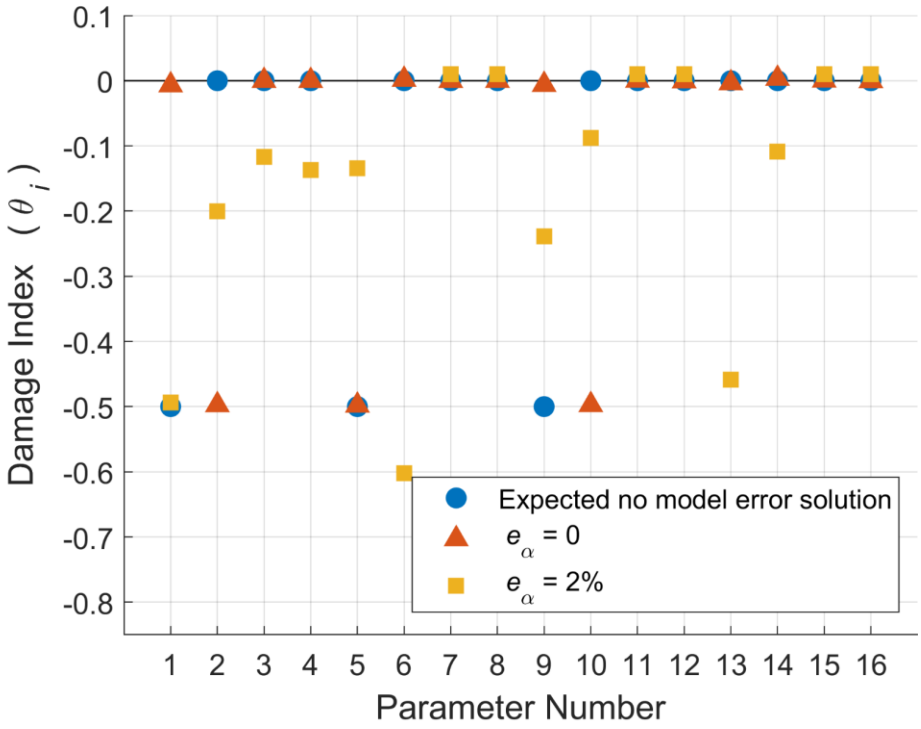

Figure 3.17. Damage indices for scenario H (left-side end elements of the front beams in floors 1, 2, and 3) for varying model error levels (e_α). Four parameters per floor (parameterization D). The expected solution under no model error is marked in blue.

3.2.4 Study III: Updating of a Linear Model

We next present an additional illustrative example case where we examine the effect of using a linear model, instead of the nonlinear model, for the updating while the data is still simulated using the original nonlinear model. For the linear model updating, the stiffnesses in both tension and compression at the beam ends are considered to be the same. The model parameters are selected to be the stiffnesses in both tension and compression of the beam ends. We parameterize the model using one parameter per story and the same substructures are used (parameterization A). This is another case with inherent model error due to the parameterization since there are no parameter values of the linear model that will give predictions that match those simulated from the nonlinear model. We consider damage scenario B, i.e. 50% stiffness reduction in tension for all the beam ends of the 1st and 5th floors, with no additional model error.

The results are shown in Figure 3.18. As we saw previously, when using the nonlinear model with no additional model error we get the exact solution. When using the linear model for the updating, we still get decent identification of the damage but the performance is greatly reduced. The location of damage is correctly identified to be at the 1st and 5th floors but the size of damage is significantly underestimated to be 30% and 20%, respectively, instead of the inflicted damage of 50%. The results are quite similar with what we were getting when applying additional model error (Figure 3.5), with regards to the errors related to the magnitude of the damage and possible false alarms in floors neighboring the damaged ones. This case clearly suggests that using the right model structure and the right parameterization (here a nonlinear model and parameters related to nonlinear behavior) is important, since the methodology can be much more effective in identifying damage than when using approximate model structures (e.g. linear models) and parameters that are non-consistent with the damage pattern.

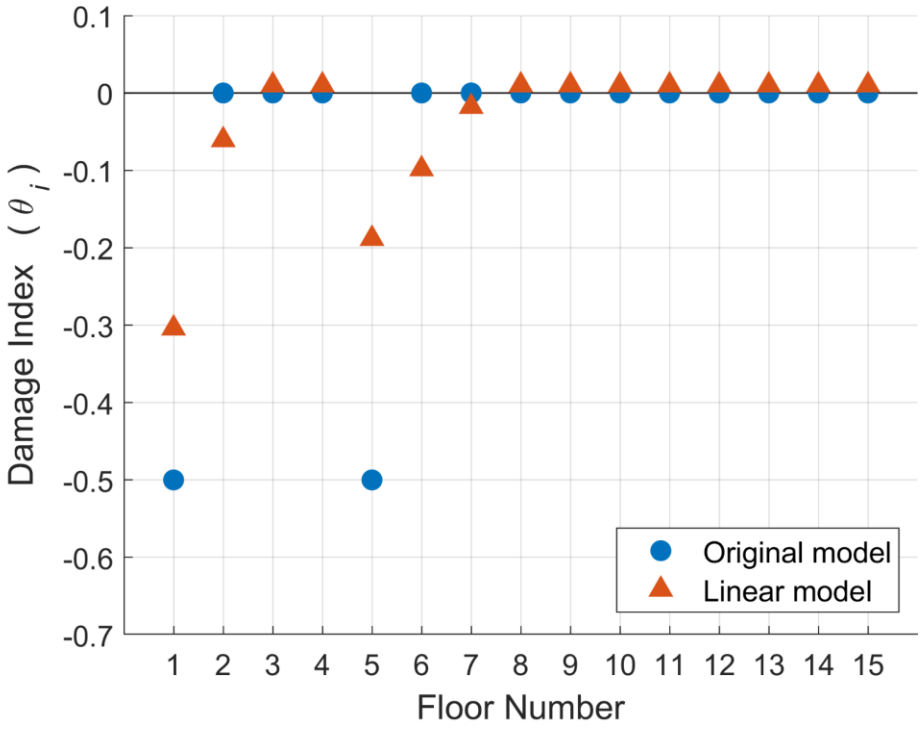

Figure 3.18. Resulting damage indices comparison when updating a nonlinear versus a linear model, for scenario B (damage in floors 1 and 5). The data were simulated using the nonlinear model.

3.2.5 Study IV: Exploring Denser Instrumentation

For the fourth study we consider damage scenarios B, G, and H. We examine the effect of denser instrumentation, considering measurements in two locations per floor instead of the previous one location per floor. The two instrumentation types are shown in Figure 3.19. For instrumentation case A we assume the bottom left corner of each floor to be instrumented; this is the instrumentation used so far. For instrumentation case B we consider the two diagonally opposite corners of every floor to be instrumented and measured.

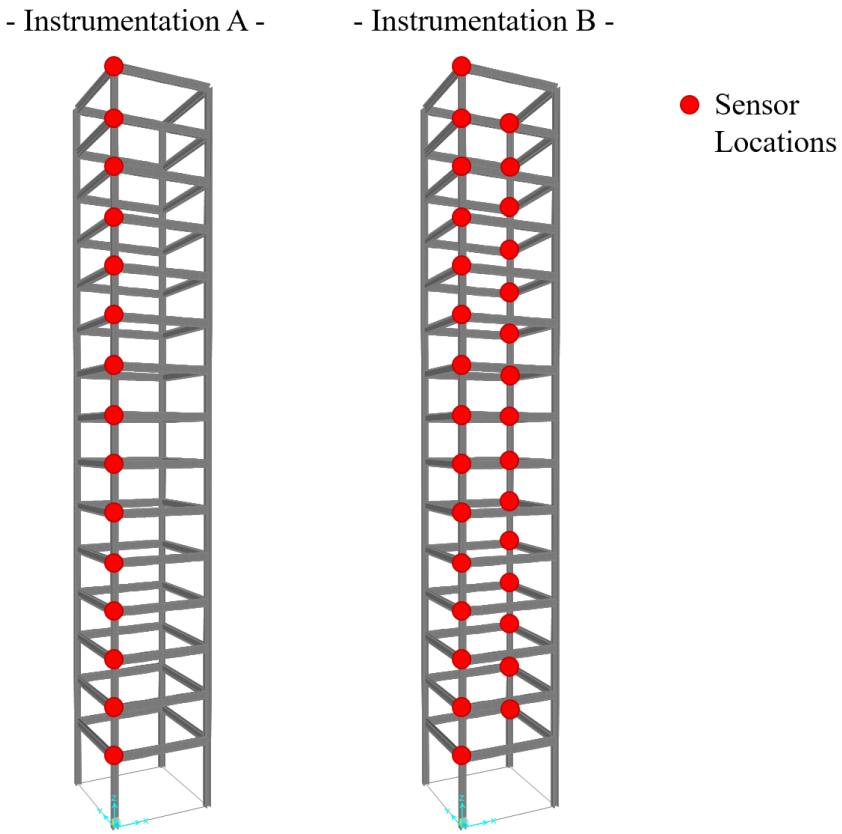

Figure 3.19. The instrumentation cases considered.

We consider damage scenario B (50% stiffness reduction in tension in all the beam ends of the 1st and 5th floors) with $e_\alpha = 2\%$ model error. The parameterization is case A with one parameter per

floor. Figure 3.20 displays the identification results when using two sensors per floor compared with the previous results using one sensor per floor. The performance of the method is the same for the damaged floors and slightly worse for some of the undamaged floors. The extra measurement data seem to include no additional information and thus do not improve the performance. On the contrary, the use of twice as many acceleration time histories to identify damage slightly deteriorates the results obtained in the undamaged floors, mainly due to the model error.

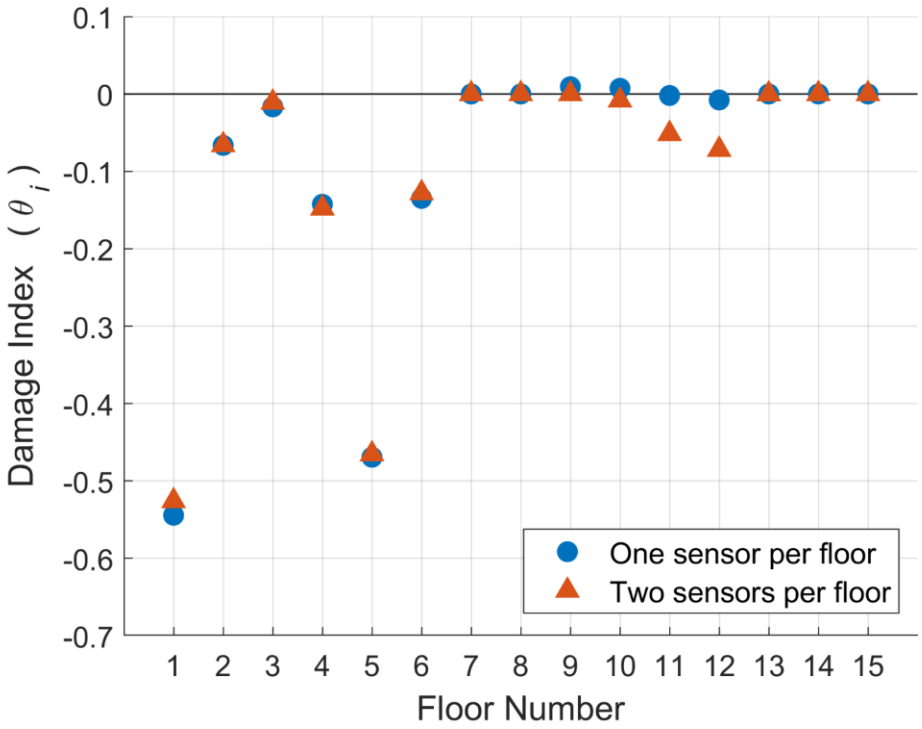

Figure 3.20. Resulting damage indices comparison when having instrumentation in 1 versus 2 locations per floor, for scenario B (damage in floors 1 and 5) with e_α = 2% model error.

Considering the denser parameterization cases, Figure 3.21 displays the identification results when using two sensors per floor compared with the previous one sensor per floor for damage scenario G considering two parameters per floor (parameterization case C) and $e_\alpha = 2\%$ model error. Figure 3.22 displays the identification results for damage scenario H considering four parameters per floor (parameterization case D) for both the $e_\alpha = 0\%$ and the $e_\alpha = 2\%$ model error cases. The

performance of the method for the $e_\alpha = 2\%$ model error case is the same. In both cases, there is no clear evidence that adding two sensors per floor improves the damage identification results. Some slight improvement at the damage floors is observed in Figure 3.21 but such improvement is not clear in Figure 3.22. Finally, note from the results in Figure 3.22 that for the zero model error case, one or two sensors per floor identifies the beam location and size of damage reliably.

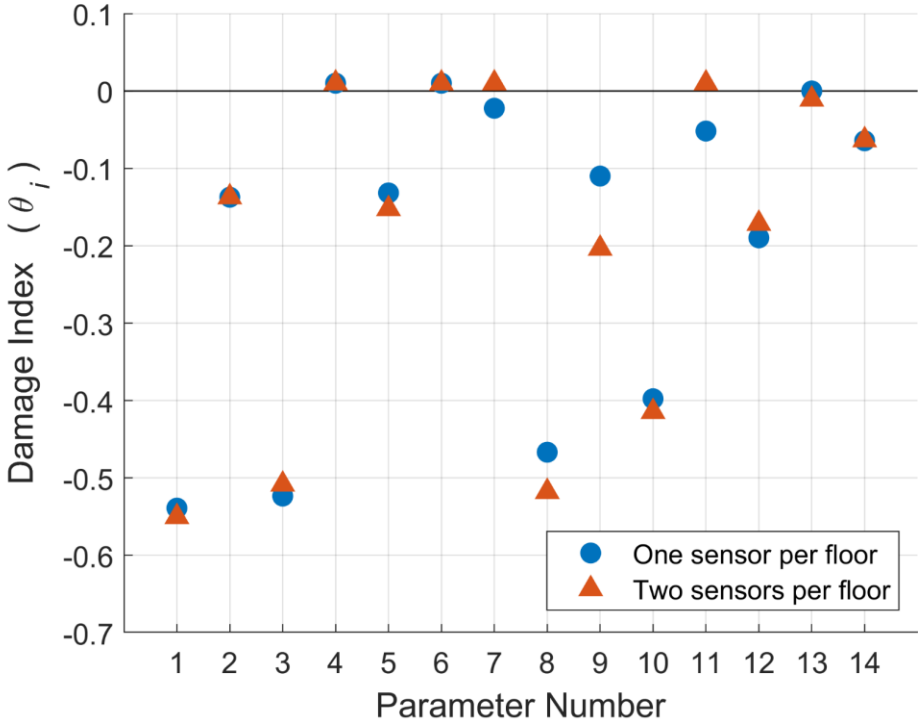

Figure 3.21. Resulting damage indices comparison when having instrumentation in 1 versus 2 locations per floor, for scenario G (damage in the front beam ends of the floors 1 and 2 & the back beam ends of floors 4 and 5) with e_α = 2% model error. Two parameters per floor (parameterization B).

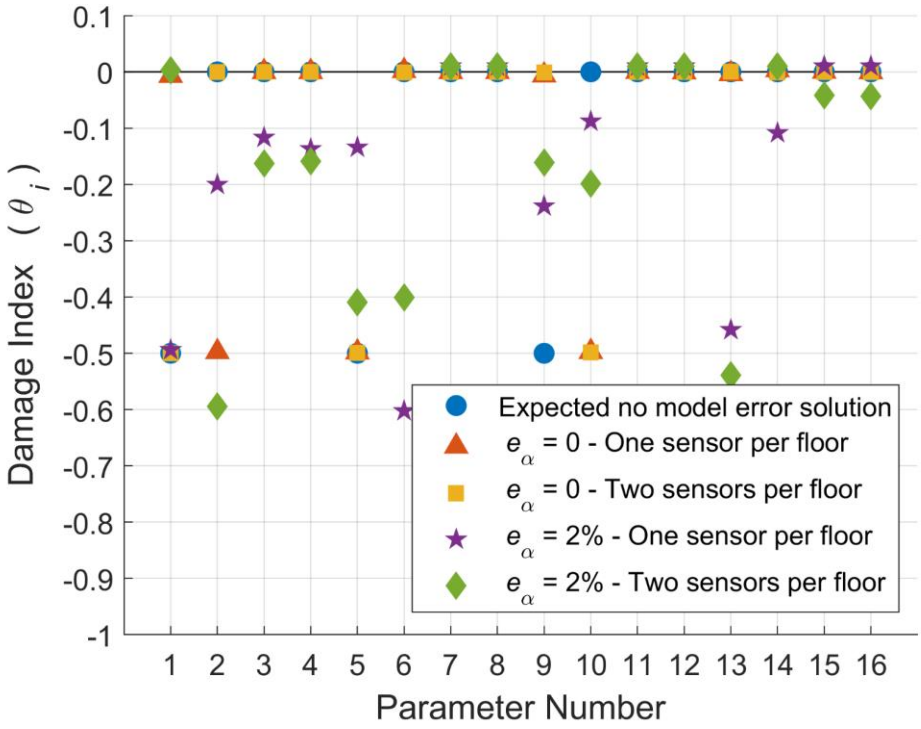

Figure 3.22. Damage indices for scenario H (left-side end elements of the front beams in floors 1, 2, and 3). Zero and e_α = 2% model error levels are shown. Four parameters per floor (parameterization D). The expected solution under no model error is marked in blue.

3.3. Conclusions

An SBL methodology is developed and tested for its effectiveness in identifying structural damage. The method uses time history measurements and, as a result, can be applied with non-linear finite element models. The proposed SBL methodology is potentially applicable to any system (e.g., high-rise buildings, bridges) and also for any type of model nonlinearities (e.g., hysteretic material models). The damage identification is accomplished by evaluating the model parameter set $\boldsymbol{\theta}$ with each component in the parameter set being associated with a damage location and severity. Through the Bayesian model selection embodying Occam's razor and the ability of the ARD prior PDF to deem certain parameters irrelevant, sparsity in the resulting model parameters is promoted.

Considering a three-dimensional, single-bay, 15-story steel moment frame structure, the effectiveness of the method is illustrated under different inflicted damage scenarios associated with weld fractures in the beam ends. For all damage scenarios and sizes of model and measurement errors considered, distinct non-zero damage index values were acquired at the damaged floors. For small to moderate model error, the identification of the existence, location and degree of damage is successful. Under large model error the identification of the damage gets more difficult with false alarms appearing in floors neighboring the damaged ones. In most damage cases considered, the location and extent of damage is correctly identified. False alarms at non-damaged locations with lesser extent of damage may also be produced. However, the identification of the damaged locations is promising.

The computational effort for damage identification using the SBL algorithm depends on the time that it takes to run one simulation for the system model and the number of iterations involved in the SBL algorithm. The time to run a system simulation depends on the complexity of the model, the nonlinearities activated and the solution strategies employed to solve the equation of motion. The number of iterations required for convergence depends on the number of model parameters and on the sparsity of the damage. For the 15-story, three-dimensional, steel frame building used in this study, the time-to-solution ranges from 4 hours to a couple of days on a personal computer (using a i7-6700HQ 4-core processor and parallel CPU computing with Matlab). The time-to-solution also depends on the damage scenarios considered, the parameterization used to identify damage, and the number of sensors. The computational effort can substantially increase for high-rise buildings and for the cases where hysteretic behavior is activated during strong ground motion.

3.A Appendices

3.A.1 Likelihood Derivation

In this appendix we derive Eq. (3.3) for the likelihood function given the values of the model parameters $\boldsymbol{\theta}$ and $\boldsymbol{\sigma}$. The probability of observing the data given $\boldsymbol{\theta}$ and $\boldsymbol{\sigma}$ is given by

$$\begin{aligned} p(D|\boldsymbol{\theta},\boldsymbol{\sigma}) &= p(\{\hat{\boldsymbol{x}}(k) \in \mathcal{R}^{N_o}, k = 1,\dots,N_D\}|\boldsymbol{\theta},\boldsymbol{\sigma}) \\ &= p\left(\{\hat{x}_1(k),\dots,\hat{x}_{N_o}(k), k = 1,\dots,N_D\}|\boldsymbol{\theta},\boldsymbol{\sigma}\right). \end{aligned} \tag{3.29}$$

Assuming independence for the prediction errors between different response time histories, equation (3.29) can, from probability theory, be equivalently written as

$$p(D|\boldsymbol{\theta},\boldsymbol{\sigma}) = \prod_{j=1}^{N_o} p\left(\{\hat{x}_j(k), k = 1,\dots,N_D\}|\boldsymbol{\theta},\boldsymbol{\sigma}\right). \tag{3.30}$$

Further assuming that the prediction errors for a response time history are independent at different time instants, one obtains

$$p(D|\boldsymbol{\theta},\boldsymbol{\sigma}) = \prod_{j=1}^{N_o}\prod_{k=1}^{N_D} p\left(\hat{x}_j(k)|\boldsymbol{\theta},\boldsymbol{\sigma}\right). \tag{3.31}$$

Also, assuming that the predictions errors at different time instants are modeled by i.i.d. zero-mean Gaussian variables, i.e. $\varepsilon_j(k) \sim N\left(0, \hat{s}_j^2\sigma_j^2\right)$, the measured time histories $\hat{x}_j(k)$ are from the prediction error equation (3.1) also implied to be Gaussian variables, that is, $\hat{x}_j(k) \sim N\left(x_j(k,\boldsymbol{\theta}), \hat{s}_j^2\sigma_j^2\right)$, with mean $x_j(k,\boldsymbol{\theta})$ and variance $\hat{s}_j^2\sigma_j^2$. Therefore, the PDF of $\hat{x}_j(k)$, given the values of $\boldsymbol{\theta}$ and $\boldsymbol{\sigma}$, is given by

$$p\left(\hat{x}_j(k)|\boldsymbol{\theta},\boldsymbol{\sigma}\right) = \frac{1}{\sqrt{2\pi}\hat{s}_j\sigma_j} exp\left\{-\frac{1}{2\hat{s}_j^2\sigma_j^2}\left[\hat{x}_j(k) - x_j(k,\boldsymbol{\theta})\right]^2\right\}. \tag{3.32}$$

Substituting Eq. (3.32) into Eq. (3.31), one obtains

$$p(D|\boldsymbol{\theta},\boldsymbol{\sigma}) = \prod_{j=1}^{N_o}\prod_{k=1}^{N_D} \frac{1}{\sqrt{2\pi}\hat{s}_j\sigma_j} exp\left\{-\frac{1}{2\hat{s}_j^2\sigma_j^2}\left[\hat{x}_j(k) - x_j(k,\boldsymbol{\theta})\right]^2\right\} \tag{3.33}$$

which is equivalent with the target Eq. (3.3).

3.A.2 Derivation of Equations (3.19) and (3.20)

In this appendix we use the stationarity conditions (3.17) and (3.18) in order to derive Eqs. (3.19) and (3.20), as well as Eq. (3.23) for the special case of $\sigma_j = \sigma,\ \forall j$.

Using the likelihood defined in Eq. (3.3) one has

$$\begin{aligned}\frac{\partial p(D|\boldsymbol{\theta},\boldsymbol{\sigma})}{\partial \sigma_j} &= \frac{\partial}{\partial \sigma_j}\left\{\frac{1}{\left(\sqrt{2\pi}\right)^{N_D N_o}\prod_{\mathrm{m}=1}^{N_o}\hat{s}_m^{N_D}\sigma_m^{N_D}}\exp\left\{-\frac{N_D N_o}{2}\mathcal{J}(\boldsymbol{\theta};\boldsymbol{\sigma})\right\}\right\} \\ &= N_D p(D|\boldsymbol{\theta},\boldsymbol{\sigma})\left[-\frac{1}{\sigma_j}+\frac{1}{\sigma_j^3}J_j(\boldsymbol{\theta})\right].\end{aligned} \tag{3.34}$$

Substituting Eq. (3.34) into the stationarity condition (3.17) we get

$$\int_{\Theta} N_D p(D|\boldsymbol{\theta},\widehat{\boldsymbol{\sigma}})\left[-\frac{1}{\hat{\sigma}_j}+\frac{1}{\hat{\sigma}_j^3}J_j(\boldsymbol{\theta})\right]p(\boldsymbol{\theta}|\widehat{\boldsymbol{\alpha}})d\boldsymbol{\theta} = 0\,. \tag{3.35}$$

Rearranging terms, one derives that

$$\hat{\sigma}_j^2 = \frac{\int_{\Theta} J_j(\boldsymbol{\theta})p(D|\boldsymbol{\theta},\widehat{\boldsymbol{\sigma}})p(\boldsymbol{\theta}|\widehat{\boldsymbol{\alpha}})d\boldsymbol{\theta}}{\int_{\Theta} p(D|\boldsymbol{\theta},\widehat{\boldsymbol{\sigma}})p(\boldsymbol{\theta}|\widehat{\boldsymbol{\alpha}})d\boldsymbol{\theta}}\,. \tag{3.36}$$

Using Bayes theorem (Eq. (3.10)), one has that

$$p(D|\boldsymbol{\theta},\widehat{\boldsymbol{\sigma}})p(\boldsymbol{\theta}|\widehat{\boldsymbol{\alpha}}) = p(\boldsymbol{\theta}|D,\widehat{\boldsymbol{\sigma}},\widehat{\boldsymbol{\alpha}})p(D|\widehat{\boldsymbol{\sigma}},\widehat{\boldsymbol{\alpha}})\,. \tag{3.37}$$

Substituting Eq. (3.37) into Eq. (3.36) one has

$$\hat{\sigma}_j^2 = \frac{\int_{\Theta} J_j(\boldsymbol{\theta})p(\boldsymbol{\theta}|D,\widehat{\boldsymbol{\sigma}},\widehat{\boldsymbol{\alpha}})p(D|\widehat{\boldsymbol{\sigma}},\widehat{\boldsymbol{\alpha}})d\boldsymbol{\theta}}{\int_{\Theta} p(\boldsymbol{\theta}|D,\widehat{\boldsymbol{\sigma}},\widehat{\boldsymbol{\alpha}})p(D|\widehat{\boldsymbol{\sigma}},\widehat{\boldsymbol{\alpha}})d\boldsymbol{\theta}}\,. \tag{3.38}$$

Noting that the factor $p(D|\widehat{\boldsymbol{\sigma}},\widehat{\boldsymbol{\alpha}})$ is independent of $\boldsymbol{\theta}$ and cancels out from both numerator and denominator, and also that $\int_{\Theta} p(\boldsymbol{\theta}|D,\widehat{\boldsymbol{\sigma}},\widehat{\boldsymbol{\alpha}})d\boldsymbol{\theta} = 1$, ones derives Eq. (3.19).

Using the prior PDF defined in Eq. (3.8) one has

$$\frac{\partial p(\boldsymbol{\theta}|\boldsymbol{\alpha})}{\partial \alpha_i} = \frac{\partial}{\partial \alpha_i}\left\{\frac{1}{(2\pi)^{\frac{N_\theta}{2}}}\prod_{n=1}^{N_\theta}\alpha_n^{\frac{1}{2}} exp\left[-\frac{1}{2}\sum_{n=1}^{N_\theta}\alpha_n\theta_n^2\right]\right\} \\ = p(\boldsymbol{\theta}|\boldsymbol{\alpha})\left[\frac{1}{2\alpha_i} - \frac{1}{2}\theta_i^2\right]. \tag{3.39}$$

Substituting Eq. (3.39) into the stationarity condition (3.18) we get

$$\int_{\Theta} p(D|\boldsymbol{\theta},\widehat{\boldsymbol{\sigma}})p(\boldsymbol{\theta}|\widehat{\boldsymbol{\alpha}})\left[\frac{1}{2\hat{\alpha}_i} - \frac{1}{2}\theta_i^2\right]d\boldsymbol{\theta} = 0\,. \tag{3.40}$$

Rearranging terms, one derives that

$$\hat{\alpha}_i = \frac{\int_{\Theta} p(D|\boldsymbol{\theta},\widehat{\boldsymbol{\sigma}})p(\boldsymbol{\theta}|\widehat{\boldsymbol{\alpha}})d\boldsymbol{\theta}}{\int_{\Theta}\theta_i^2 p(D|\boldsymbol{\theta},\widehat{\boldsymbol{\sigma}})p(\boldsymbol{\theta}|\widehat{\boldsymbol{\alpha}})d\boldsymbol{\theta}}\,. \tag{3.41}$$

Substituting Eq. (3.37) into Eq. (3.41) one has

$$\hat{\alpha}_i = \frac{\int_{\Theta} p(\boldsymbol{\theta}|D,\widehat{\boldsymbol{\sigma}},\widehat{\boldsymbol{\alpha}})p(D|\widehat{\boldsymbol{\sigma}},\widehat{\boldsymbol{\alpha}})d\boldsymbol{\theta}}{\int_{\Theta}\theta_i^2 p(\boldsymbol{\theta}|D,\widehat{\boldsymbol{\sigma}},\widehat{\boldsymbol{\alpha}})p(D|\widehat{\boldsymbol{\sigma}},\widehat{\boldsymbol{\alpha}})d\boldsymbol{\theta}}\,. \tag{3.42}$$

Noting that the factor $p(D|\widehat{\boldsymbol{\sigma}},\widehat{\boldsymbol{\alpha}})$ is independent of $\boldsymbol{\theta}$ and cancels out from both numerator and denominator, and also that $\int_{\Theta} p(\boldsymbol{\theta}|D,\widehat{\boldsymbol{\sigma}},\widehat{\boldsymbol{\alpha}})d\boldsymbol{\theta} = 1$, ones derives Eq. (3.20).

For the special case of $\sigma_j = \sigma,\ \forall j$ we follow the same procedure. In this case using the likelihood function (Eq. (3.6)) one gets

$$\frac{\partial p(D|\boldsymbol{\theta},\sigma)}{\partial \sigma} = \frac{\partial}{\partial \sigma}\left\{\frac{1}{\left(\sqrt{2\pi}\right)^{N_D N_o}\prod_{j=1}^{N_o}\hat{s}_j^{N_D}\,\sigma^{N_D N_o}}\exp\left\{-\frac{N_D N_o}{2\sigma^2}J(\boldsymbol{\theta})\right\}\right\} \\ = N_D p(D|\boldsymbol{\theta},\sigma)\left[-\frac{1}{\sigma} + \frac{1}{\sigma^3}\,J(\boldsymbol{\theta})\right]. \tag{3.43}$$

The stationarity condition (equivalent equation to Eq. (3.17)) for this special case is

$$\left.\frac{\partial p(D|\sigma,\boldsymbol{\alpha})}{\partial \sigma}\right|_{\substack{\sigma=\hat{\sigma}\\ \boldsymbol{\alpha}=\hat{\boldsymbol{\alpha}}}} = \left.\int_{\Theta} \frac{\partial p(D|\boldsymbol{\theta},\sigma)}{\partial \sigma} p(\boldsymbol{\theta}|\boldsymbol{\alpha}) d\boldsymbol{\theta}\right|_{\substack{\sigma=\hat{\sigma}\\ \boldsymbol{\alpha}=\hat{\boldsymbol{\alpha}}}} = 0 \tag{3.44}$$

and by substituting Eq. (3.43) into Eq. (3.44) one gets

$$\int_{\Theta} N_D p(D|\boldsymbol{\theta},\hat{\sigma}) \left[-\frac{1}{\hat{\sigma}} + \frac{1}{\hat{\sigma}^3} J(\boldsymbol{\theta})\right] p(\boldsymbol{\theta}|\hat{\boldsymbol{\alpha}}) d\boldsymbol{\theta} = 0\,. \tag{3.45}$$

Rearranging terms, one derives that

$$\hat{\sigma}^2 = \frac{\int_{\Theta} J(\boldsymbol{\theta}) p(D|\boldsymbol{\theta},\hat{\sigma}) p(\boldsymbol{\theta}|\hat{\boldsymbol{\alpha}}) d\boldsymbol{\theta}}{\int_{\Theta} p(D|\boldsymbol{\theta},\hat{\sigma}) p(\boldsymbol{\theta}|\hat{\boldsymbol{\alpha}}) d\boldsymbol{\theta}}\,. \tag{3.46}$$

Substituting Eq. (3.37) on Eq. (3.46) and noting that the factor $p(D|\hat{\sigma},\hat{\boldsymbol{\alpha}})$ cancels out from both numerator and denominator, one derives Eq. (3.23).

3.A.3 Equivalence of the Single-Objective and the Two-Step Optimization Problems

In this appendix we show that the solutions to the single-objective optimization problem (Eqs. (3.26) and (3.27)) and the two-step optimization problem are equivalent.

Starting from the iterative optimization problem, the solution to Eq. (3.12) satisfies:

$$\frac{\partial}{\partial\theta_n}\left[N_D N_o\left(\frac{1}{N_o}\sum_{j=1}^{N_o}\frac{1}{\sigma_j^2}J_j(\boldsymbol{\theta})\right)+\sum_{i=1}^{N_\theta}\alpha_i\theta_i^2\right]\Bigg|_{\boldsymbol{\theta}=\boldsymbol{\theta}^{(m)}}=0,\qquad n=1,\dots,N_\theta \tag{3.47}$$

which gives

$$\left[\sum_{j=1}^{N_o}\frac{N_D}{\sigma_j^2}\frac{\partial J_j(\boldsymbol{\theta})}{\partial\theta_n}+2\alpha_n\theta_n\right]\Bigg|_{\boldsymbol{\theta}=\boldsymbol{\theta}^{(m)}}=0,\qquad n=1,\dots,N_\theta. \tag{3.48}$$

For the optimal solution $\boldsymbol{\theta}^{(m)}=\widehat{\boldsymbol{\theta}}$, it holds that $\left(\sigma_j{}^{(m)}\right)^2=J_j\left(\boldsymbol{\theta}^{(m)}\right),\ j=1,\dots,N_o$ and $\alpha_i^{(m)}=\frac{1}{\left(\theta_i^{(m)}\right)^2},\ i=1,\dots,N_\theta$ and one gets

$$\sum_{j=1}^{N_o}\frac{N_D}{J_j\left(\widehat{\boldsymbol{\theta}}\right)}\frac{\partial J_j(\boldsymbol{\theta})}{\partial\theta_n}\Bigg|_{\boldsymbol{\theta}=\widehat{\boldsymbol{\theta}}}+2\frac{1}{\hat{\theta}_n}=0,\qquad n=1,\dots,N_\theta. \tag{3.49}$$

For the non-iterative optimization problem, the solution to Eq. (3.26) satisfies:

$$\frac{\partial}{\partial\theta_n}\left[N_D\sum_{j=1}^{N_o}ln\left(J_j(\boldsymbol{\theta})\right)+\sum_{i=1}^{N_\theta}ln(\theta_i^2)\right]\Bigg|_{\boldsymbol{\theta}=\widehat{\boldsymbol{\theta}}}=0,\qquad n=1,\dots,N_\theta \tag{3.50}$$

and after carrying out the derivatives with respect to θ_n one ends up with Eq. (3.49).

Thus the two solutions satisfy the same equation so they are equivalent.

For the special case of $\sigma_j=\sigma,\ \forall j$ we follow the same procedure. Starting from the iterative optimization problem, the solution to Eq. 3.12(3.14) satisfies:

$$\frac{\partial}{\partial\theta_n}\left[\frac{N_D N_o}{\sigma^2}J(\boldsymbol{\theta})+\sum_{i=1}^{N_\theta}\alpha_i\theta_i^2\right]\Bigg|_{\boldsymbol{\theta}=\boldsymbol{\theta}^{(m)}}=0,\qquad n=1,\dots,N_\theta \tag{3.51}$$

which gives

$$\left[\frac{N_D N_o}{\sigma^2}\frac{\partial J(\boldsymbol{\theta})}{\partial \theta_n} + 2\alpha_n \theta_n\right]\Bigg|_{\boldsymbol{\theta}=\boldsymbol{\theta}^{(m)}} = 0, \qquad n = 1, \dots, N_\theta. \tag{3.52}$$

For the optimal solution $\boldsymbol{\theta}^{(m)} = \widehat{\boldsymbol{\theta}}$, it holds that $\left(\sigma^{(m)}\right)^2 = J\left(\boldsymbol{\theta}^{(m)}\right)$ and $\alpha_i^{(m)} = \frac{1}{\left(\theta_i^{(m)}\right)^2}$, $i = 1, \dots, N_\theta$ and one gets

$$N_D N_o \frac{1}{J(\widehat{\boldsymbol{\theta}})}\frac{\partial J(\boldsymbol{\theta})}{\partial \theta_n}\Bigg|_{\boldsymbol{\theta}=\widehat{\boldsymbol{\theta}}} + 2\frac{1}{\hat{\theta}_n} = 0, \qquad n = 1, \dots, N_\theta. \tag{3.53}$$

For the non-iterative optimization problem, the solution to Eq. (3.27) satisfies:

$$\frac{\partial}{\partial \theta_n}\left[N_D N_o ln\big(J(\boldsymbol{\theta})\big) + \sum_{i=1}^{N_\theta} ln(\theta_i^2)\right]\Bigg|_{\boldsymbol{\theta}=\widehat{\boldsymbol{\theta}}} = 0, \qquad n = 1, \dots, N_\theta \tag{3.54}$$

and after carrying out the derivatives with respect to θ_n one ends up with Eq. (3.53).

Thus the two special case ($\sigma_j = \sigma,\ \forall j$) solutions satisfy the same equation so they are equivalent.

Chapter 4

GROUND-MOTION RESPONSE IN URBAN LOS ANGELES FROM THE 2019 RIDGECREST EARTHQUAKE SEQUENCE

This chapter presents a study of the ground-motion response that occurred in urban Los Angeles as a result of the two largest events of the July 2019 Ridgecrest, California earthquake sequence, the M7.1 main shock and M6.4 foreshock events. The city of Los Angeles is located about 200 km from the earthquake epicentral region and did not suffer structural damage; however, due to its underlying geology consisting of several deep sedimentary basins bounded by mountains, it experienced a wide range of ground motion amplitudes. Southern California is one of the most densely instrumented regions in the world, with numerous permanently installed strong motion networks present in the area. More specifically, the existence of the very dense Community Seismic Network (CSN) has led to unprecedented station numbers and density for the area of urban Los Angeles. The July 2019 Ridgecrest, California earthquake sequence provides a unique opportunity for a comprehensive study of the resulting ground motion response in urban Los Angeles. The collected data is extremely useful for investigating the correlation of earthquake data observations with site parameters, as well as for testing the effectiveness of methods for predicting ground motion intensity measures.

We make use of response pseudo-spectral acceleration intensity measures, also referred here as spectral accelerations, in order to address two main objectives. The first objective involves computing the spectral acceleration from the measured data. We study the ground-motion patterns in the computed spectral accelerations from seismic network recordings of the M7.1 and M6.4 earthquakes, and examine correlations with two site parameters: Vs30 (travel-time averaged shear-wave velocity in the top 30 m) and depth-to-basement. The second objective involves assessing the capabilities of different ways of predicting the spectral acceleration observed for the largest (M7.1) event. We study two commonly used methods for predicting the ground motion intensity

measures: 3D finite-difference simulations and Ground Motion Prediction Equations (GMPEs). We examine the performance of the two methods by studying their spectral acceleration predictions, as well as their residuals/errors when compared to the spectral accelerations calculated from the measurements.

Section 4.1 provides more details about the considered 2019 Ridgecrest earthquake sequence events, the recorded data, and the applied processing. Section 4.2 presents the details of calculating the spectral acceleration intensity measure, as well as the RotD50 and RotD100 intensity measures used in the study. Section 4.3 presents and discusses the resulting spectral accelerations calculated from the recorded data for a selection of periods of engineering significance, the correlation of the calculated spectral acceleration between the two considered events is examined together with the correlation of the calculated spectral accelerations with basement depth and Vs30. Section 4.4 displays and discusses the spectral acceleration predicted using 3D finite difference simulations. The differences in the performance between the two Southern California Earthquake Center (SCEC) 3D Community Velocity Models (CVM-S and CVM-H) are examined. Section 4.5 assesses the performance of the five 2014 Next Generation Attenuation (NGA) – West 2 Project GMPEs. In Section 4.6 we examine the performance of the simulation and GMPE predictions along a profile going through the Los Angeles Basin. Section 4.7 presents the main conclusions.

4.1 Data and Processing

The July 2019 Ridgecrest earthquake sequence occurred northeast of the town of Ridgecrest, CA (Figure 4.1A), along two major fault zones. The sequence consisted of seven moderate-to-strong events (magnitude greater than 5.0), and over a hundred events with magnitude greater than 4.0 (SCSN, 2019; Hauksson, et al., 2020). In this study, we consider the two largest events of the sequence – the M7.1 main shock and the M6.4 foreshock. The M7.1 main shock took place on July 6th, 2019 at 03:19 UTC (July 5th 20:19 local time) with a hypocenter of 35.770°N, 117.599°W and depth of about 8 km. The second strongest event of the sequence was the M6.4 earthquake that occurred approximately 34 hours before the M7.1 event, on July 4th, 2019 at 17:33 UTC (July 4th 10:33 local time). Its epicenter was located 11 km southeast of the main event's

epicenter (epicenter location: 35.705°N and 117.504°W), with a hypocentral depth of about 10 km. The shaking from the two events was widely felt throughout California and was well-recorded by the numerous seismic arrays operating in southern California. In particular, the city of Los Angeles, located about 200 km from the event epicenters (Figure 4.1A), experienced light-to-moderate ground shaking; however, the long-period shaking was strong enough that residents in the downtown high-rises reported experiencing vertigo (Los Angeles Times, 2019).

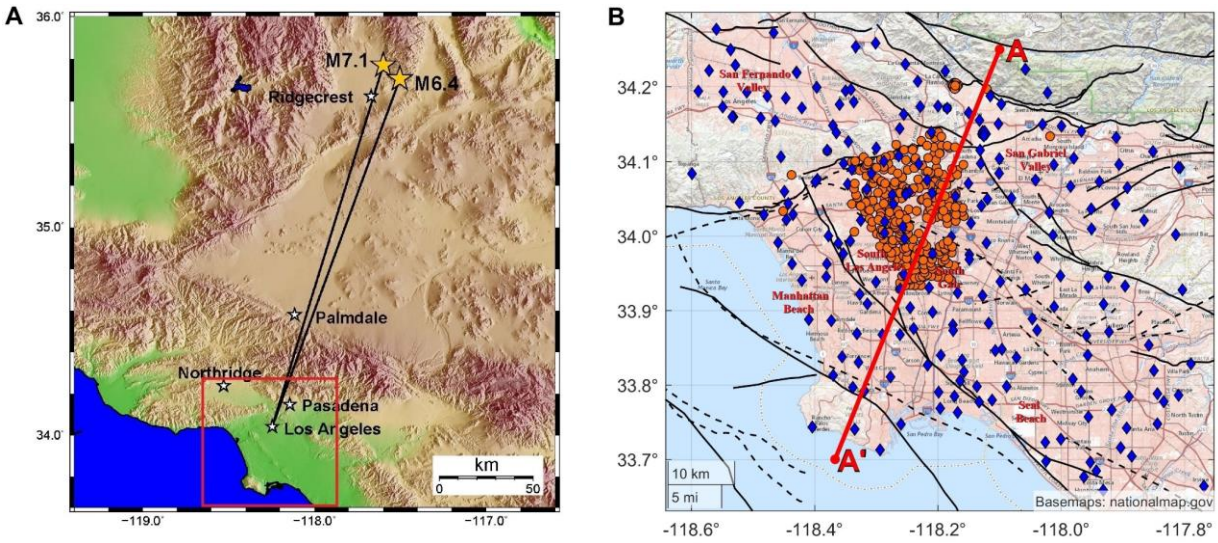

Figure 4.1. Maps of the region. (A) Earthquake epicenters and terrain. Red rectangle: the area of urban Los Angeles under consideration, magnified on the following figures. Black lines: the shortest source-to-receiver path corresponding to a distance of ~200 km. (B) Station and fault locations. Circles: CSN network. Diamonds: SCSN & CSMIP networks. Solid black lines: fault traces. Dashed black lines: blind fault surface projection. Profile A-A' is marked by the red line.

Acceleration time series from the two events form the basis of this study. We consider ground-level stations from the following three sources: 1) the Community Seismic Network (CSN); 2) the Southern California Seismic Network (SCSN); and 3) the California Strong Motion Instrumentation Program (CSMIP). The CSN provided data from 350 stations, and SCSN and CSMIP provided about 200 additional stations in our region of interest (Figure 4.1B). The links and archives for all data used in the study are provided in Appendix 4.A.7. The high station density visible in the northern part of the Los Angeles Basin is due to the CSN deployment which spans an approximately 30 km by 30 km area, with an average station spacing of about 0.5 km. The

SCSN and CSMIP stations are an order of magnitude more distant from one another with approximate station spacing of about 4 km.

The CSN and SCSN data were processed by applying a non-causal 4^{th}-order bandpass Butterworth filter for frequencies between 0.07 Hz and 23 Hz. The cutoff frequencies and order of the filter were selected to be similar to the ones applied to the already processed CSMIP V2 accelerograms. The overall data quality for all three networks for both events is high with good site-to-site coherence for neighboring stations in similar geological settings. The performance of the CSN MEMS-based sensors during the earthquakes was on par with the SCSN and CSMIP sensors. Figures 4.2 and 4.3 display a comparison of the recordings and the resulting pseudo-acceleration response spectra between a CSN accelerometer and a regional network accelerometer, for two example sites where the two sensors are placed close to one another. The first location is the 116th St. School in Los Angeles (Figure 4.2), the site geology is alluvium and the distance between the two sensors is about 70m. For the second location both sensors are located inside the Pasadena Art Center College of Design vault, which is a hard rock – granitic site (Figure 4.3). The performance of the CSN during the Ridgecrest events is also discussed by Clayton et al. (2019).

In Figure 4.4 we provide maps of the magnitudes of the peak ground acceleration (PGA) in the combined horizontal directions for the two events. The recordings have a maximum PGA of approximately 5.5 %g during the M7.1 event and of 4.5 %g during the M6.4. The higher PGAs were recorded in the San Fernando basin, as well as in the north-east and south-east Los Angeles basin. Among their other shortcomings (Shome, et al., 1998), PGA maps do not take into account the properties of a structure. In the following sections we will introduce the spectral amplification intensity measure which can take into account the structure's natural frequency and provide information regarding the possible amplification of specific frequencies and the vulnerability of infrastructure.

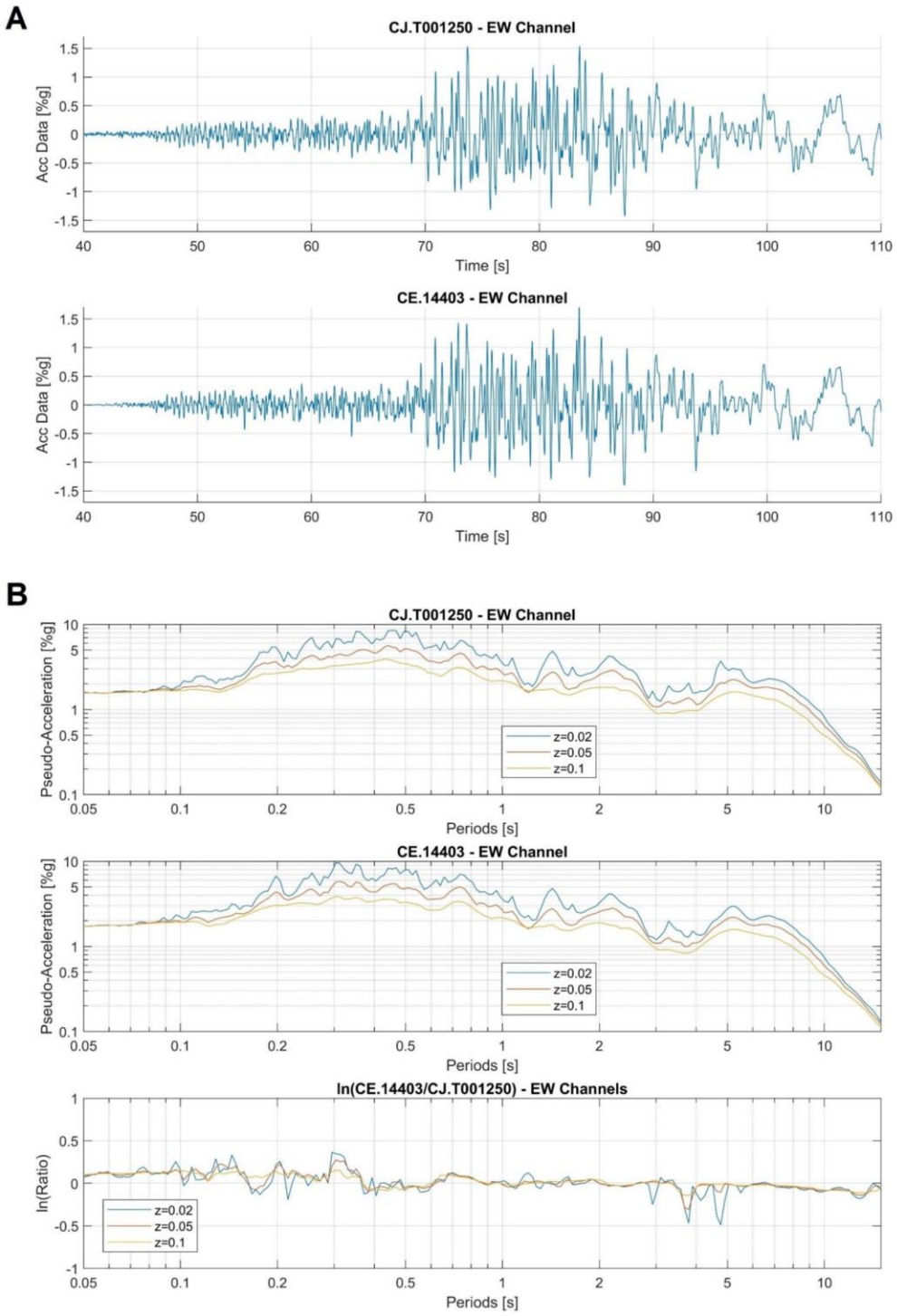

Figure 4.2. Los Angeles - 116th Street School sensor comparison for the M7.1 event (geological setting: alluvium). CSN network station: CJ.T001250, CE network station: CE.14403. East-West components. (A) Acceleration time histories. (B) Acceleration response spectra (2%, 5%, and 10% damping ratio) and residuals. The results are similar for all three components.

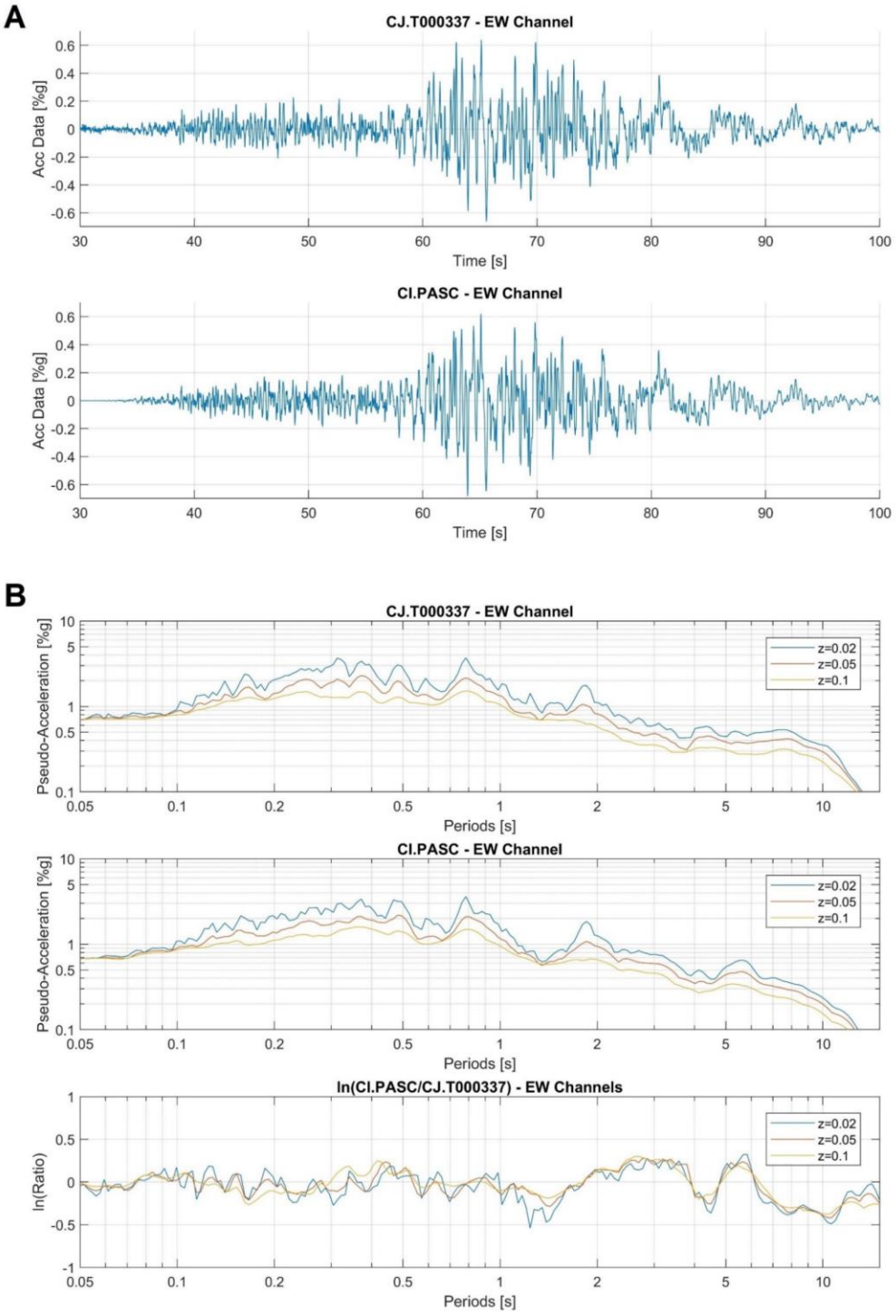

Figure 4.3. Pasadena Art Center College of Design Vault sensor comparison for the M7.1 event (geological setting: hard rock - granitic). CSN network station: CJ.T000337, CI network station: CI.PASC. East-West components. (A) Acceleration time histories. (B) Acceleration response spectra (2%, 5%, and 10% damping ratio) and residuals. The results are similar for all three components.

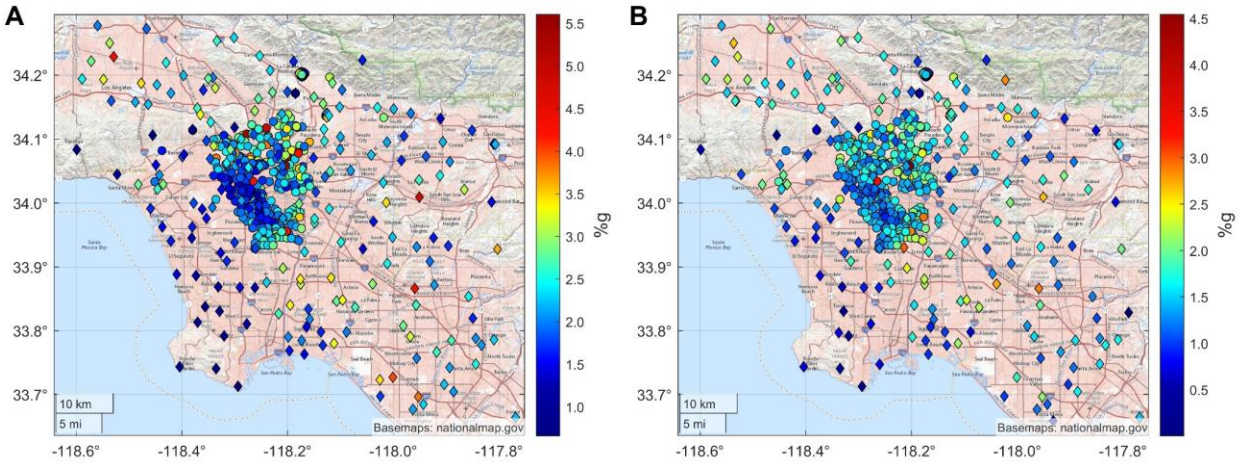

Figure 4.4. PGA maps. (A) M7.1 event. (B) M6.4 event. Circles: CSN stations, Diamonds: SCSN & CSMIP stations. Note varying colorbar amplitude scales.

4.2 Methodology

The calculation of the linear response spectral ordinates is well-established, with the concept being initiated with papers by Biot (1933) and Housner (1941). Here, we briefly discuss the calculation methodology to avoid any confusion.

We compute the response pseudo-spectral acceleration at each station by applying the recorded ground acceleration as input to a linear single-degree-of-freedom (SDoF) oscillator with natural period T and damping ratio ζ. The equation of motion for the linear SDoF oscillator is

$$\ddot{u}(t) + 2\zeta\omega\dot{u}(t) + \omega^2 u(t) = -\ddot{u}_g(t) \tag{4.1}$$

where $u(t)$ is the deformation response (relative displacement), $\dot{u}(t)$ is the relative velocity $\ddot{u}(t)$ is the relative acceleration of the system, $\ddot{u}_g(t)$ is the ground acceleration, and ω is the natural frequency of the SDoF oscillator ($\omega = 2\pi/T$).

Solving for the two available horizontal inputs (i.e. the ground accelerations in the geographical E-W and N-S directions) yields the oscillator displacements in the two horizontal directions: $u_x(t)$ and $u_y(t)$. The total horizontal displacement is

$$\boldsymbol{u}(t) = u_x(t)\boldsymbol{e_x} + u_y(t)\boldsymbol{e_y}. \tag{4.2}$$

The response pseudo-spectral acceleration intensity measure 'SA' is defined (Chopra, 2011) as

$$SA(T,\zeta) = \omega^2 \max_t\big(u(t)\big) \tag{4.3}$$

where the subscript t indicates that we are looking for the maximum with respect to time, and $u(t)$ is the Euclidean norm of the horizontal displacement, i.e.

$$u(t) = \big(u_x(t)^2 + u_y(t)^2\big)^{1/2}. \tag{4.4}$$

SA has units of acceleration and is related to the peak value of the base shear force (F_s), also referred to as the equivalent static force, by: $F_s = mA$. The response spectral "pseudo" acceleration measure tends to the "real" absolute acceleration response spectrum as the damping ratio of the SDoF system gets smaller. For damping value $\zeta = 0$, SA is equal to the absolute acceleration.

We also associate a geographical direction to this SA that is the direction of the vector $\boldsymbol{u}(t_m)$, i.e. the direction of the vector $\boldsymbol{u}(t)$ at time t_m when $u(t)$ attains its maximum value. Following Eq. (4.2) this direction can be defined by the angle

$$\varphi = arctan\left(\frac{u_y(t_m)}{u_x(t_m)}\right). \tag{4.5}$$

Two additional spectral acceleration intensity measures used in this study are RotD100 and RotD50. RotD100 is the maximum spectral acceleration over all rotation angles (Boore, 2010), defined in Appendix 4.A.1. In Appendix 4.A.2 we show that the previously defined SA is equivalent to RotD100. Furthermore, the direction of the SA (Eq. (4.5)) is equal to the rotation angle for which the maximum spectral acceleration occurs. Since Eq. (4.3) does not require an iteration over all (non-redundant) rotation angles, the calculation of SA is computationally more efficient. Moreover, since the recommended procedure for calculating RotD100 suggests 1-degree angle increments, calculating SA is more accurate.

RotD50 is the median spectral acceleration over all rotation angles (Boore, 2010), also defined in Appendix 4.A1. The GMPE offer RotD50 predictions rather than RotD100. Thus, for the model prediction sections (Sections 4.4, 4.5, and 4.6) the RotD50 intensity measure is calculated for both the data and the models, in order to enable comparisons between the measured and the GMPE predicted spectral accelerations.

4.3 Spectral Acceleration from Measured Data

Using the methodology presented in Section 4.2 we compute the SA from the data collected from all three seismic networks (CSN, SCSN, and CSMIP) in the Los Angeles basin region, during the M7.1 and M6.4 Ridgecrest earthquakes. The SA is computed at four natural periods T for the SDoF oscillator: 1, 3, 6, and 8 s. These four periods are representative of the fundamental periods of many of the structural systems present in the region, since the fundamental periods for low- and mid-rise buildings are close to 1 and 3 s, while for high-rises, large-diameter storage tanks, or long-span bridges, 6 and 8 s are more appropriate. A 5% damping ratio is used which allows for comparison with the GMPE predictions which also use 5% damping.

4.3.1 Spectral Acceleration Results and Discussion

Maps of the computed SA for periods T=1, 2, 3, and 8 s and 5% damping ratio are shown in Figure 4.5. Observing Figure 4.5 it is evident that the ground-motion response varies greatly across the Los Angeles region. Overall, the maximum computed SAs are the largest at T=1 s and the smallest at T=8 s. At T=1 s, the SA varies significantly over short distances with no pervasive patterns and with local maxima appearing in multiple locations. At T=3 s, more coherent behavior can be observed, with larger SA values appearing in the San Fernando Valley, the San Gabriel Valley, and in the central (e.g., South Gate) and southern (e.g., Long Beach) Los Angeles Basin. At the longer periods (T=6 s and 8 s), pervasive coherent behavior is now evident, with maxima in the San Fernando Valley, and in the west (e.g., Manhattan Beach), central (South Los Angeles), and south (e.g., near Seal Beach) Los Angeles Basin (the above locations are marked in Figure 4.1B).

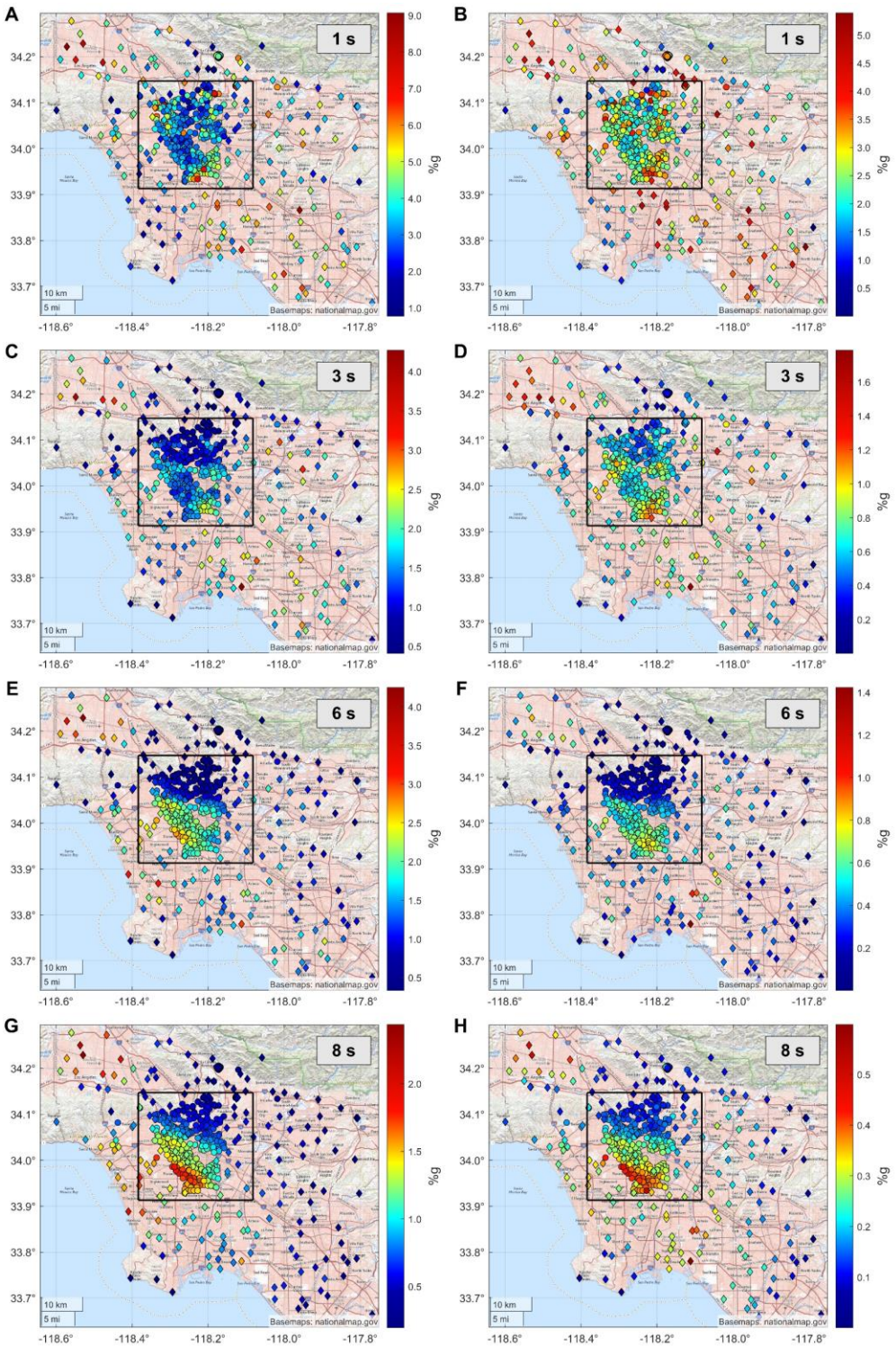

Figure 4.5. SA maps. Left column: M7.1 event. Right column: M6.4 event. (A-B) T=1 s. (C-D) T=3 s. (E-F) T=6 s. (G-H) T=8 s. Damping ratio ζ=5%. Circles: CSN stations, Diamonds: SCSN & CSMIP stations. Black rectangle: Area magnified in Figure 4.6. Note varying colorbar amplitude scales.

Figure 4.6 presents a detail of Figure 4.5 focused on the area with the denser CSN instrumentation. While for the longer periods coherent patterns are present throughout the region with the SA amplitude gradually varying, for shorter periods the spatial complexity of the SA patterns increases significantly. The agreement between the different networks is very good. The SA calculated for neighboring stations belonging in different networks is similar and the long period trends observed in all three (SCN, SCSN, and CSMIP) networks are the same. The dense CSN instrumentation allows us to see pockets of SA amplification, varying over length scales of 1-2 km, which might go undetected using only data from the sparser SCSN and CSMIP networks.

The SA results are for the most part reproducible between the two earthquakes. Even though, as expected, the SA values are generally smaller for the M6.4 event, the SA ratios between a site in the deeper Los Angeles Basin and a hard-rock site (e.g., in the San Rafael Hills or Mt. Wilson) are similar between the two events. At T=1, 3, and 8 s, the areas of the maximum SA are consistent between the two events (Figure 4.5A-H). The results for the two events are slightly different at T=6 s where for the Los Angeles Basin the maximum SAs appear towards the west coastline (e.g., Manhattan Beach and South Los Angeles) for the M7.1, but more to the east (e.g., South Gate), for the M6.4 event (Figure 4.5E,F).

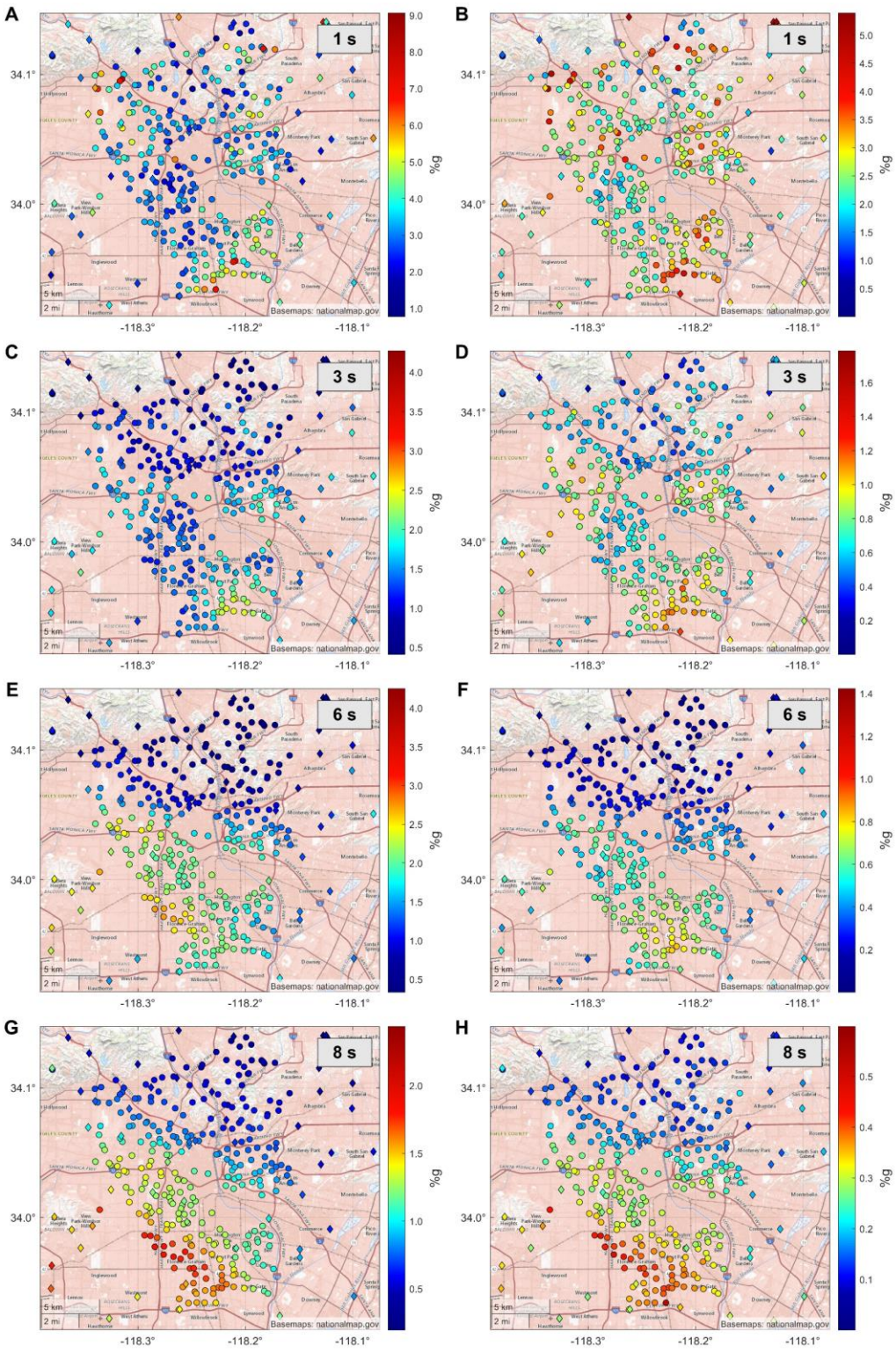

Figure 4.6. SA maps showing detail in the region marked by the black rectangle in Figure 4.5. Same format as Figure 4.5.

As another approach to quantifying the correlation between the two events, Figure 4.7 shows the SA values for all stations that recorded both events. It is apparent that an overall good correlation exists and that the observed SAs are consistent between the two events. To quantify the degree of correlation, two statistical measures are computed: Pearson's correlation coefficient (r) and the p-value (p) with the null hypothesis being that the slope of the least-squares (LS) regression line is zero (Lee, et al., 2000). We find r = 0.70, 0.80, 0.89, and 0.91 for T=1, 3, 6, and 8 s respectively. As the correlation coefficient approaches $+1$ the two variables have a stronger positive correlation. The SA correlation between the two events is stronger for longer periods, independent of the depth-to-basement at the station (shown by the color map in Figure 4.7). The p-values are $p < 0.001$ for all periods, an indication that the correlation is statistically significant.

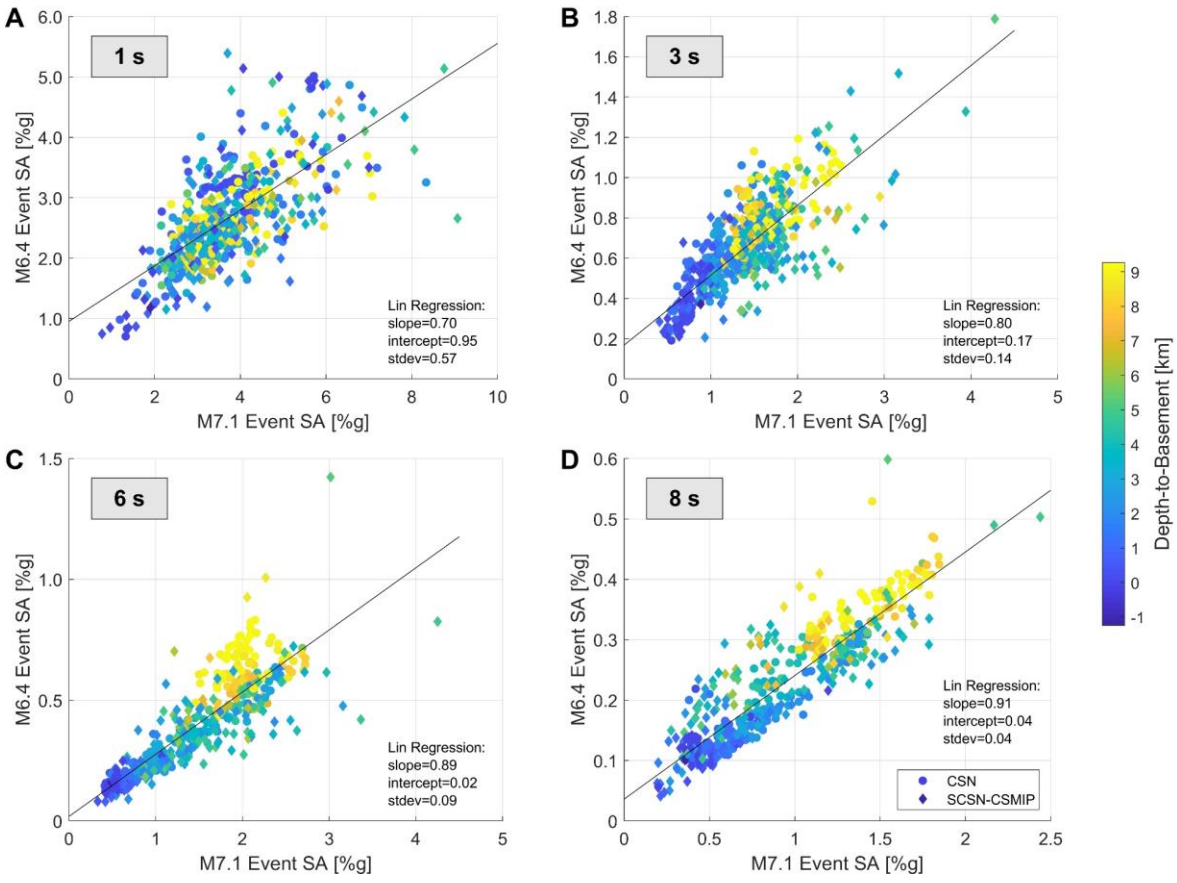

Figure 4.7. SA correlation between the two events. (A) T=1 s. (B) T=3 s. (C) T=6 s. (D) T=8 s. Damping ratio ζ=5%. Circles: CSN stations, Diamonds: SCSN & CSMIP stations. The colormap displays the depth-to-basement at each station. Line: LS regression fit. The slope and intercept of the LS regression line, and the standard deviation are provided in each subplot.

The directions associated with the maximum SA values are shown in Figure 4.8. The patterns in the directions further emphasize the observations of coherent behavior for the longer periods. At T=8 s, the SAs have coherent directions across the entire Los Angeles Basin. Considering waves with 8 s periods propagating at a shear-wave velocity of 2.5 km/s (and indeed the long period velocity for our events is close to that – Appendix 4.A.3), one gets a wavelength of about 20 km, while the wavelength goes down to only 2.5 km for a 1 s period. In reality, the wavelengths associated with the 1 s period energy are even shorter since they are more sensitive to the lower velocity, near-surface material. Taking into account this decrease in the wavelengths and the average station spacing it is not surprising that the coherence disappears at the shortest periods. For the longer periods the SAs are lot more coherent and the patterns that appear can be correlated to the larger scale basin structure and soil properties. For the shorter periods the motions are stronger and less spatial coherent, indicating a high-level of scattering at the kilometer length scale. High variability exists within just a few meters, stations belonging to the same surficial unit appear to have large variations in their ground response. Coherence in the directions can still be observed, for the shorter periods, but it appears over smaller length scales. This smaller length scale coherence is visible in specific areas (Figure 4.9) with the help of the denser CSN.

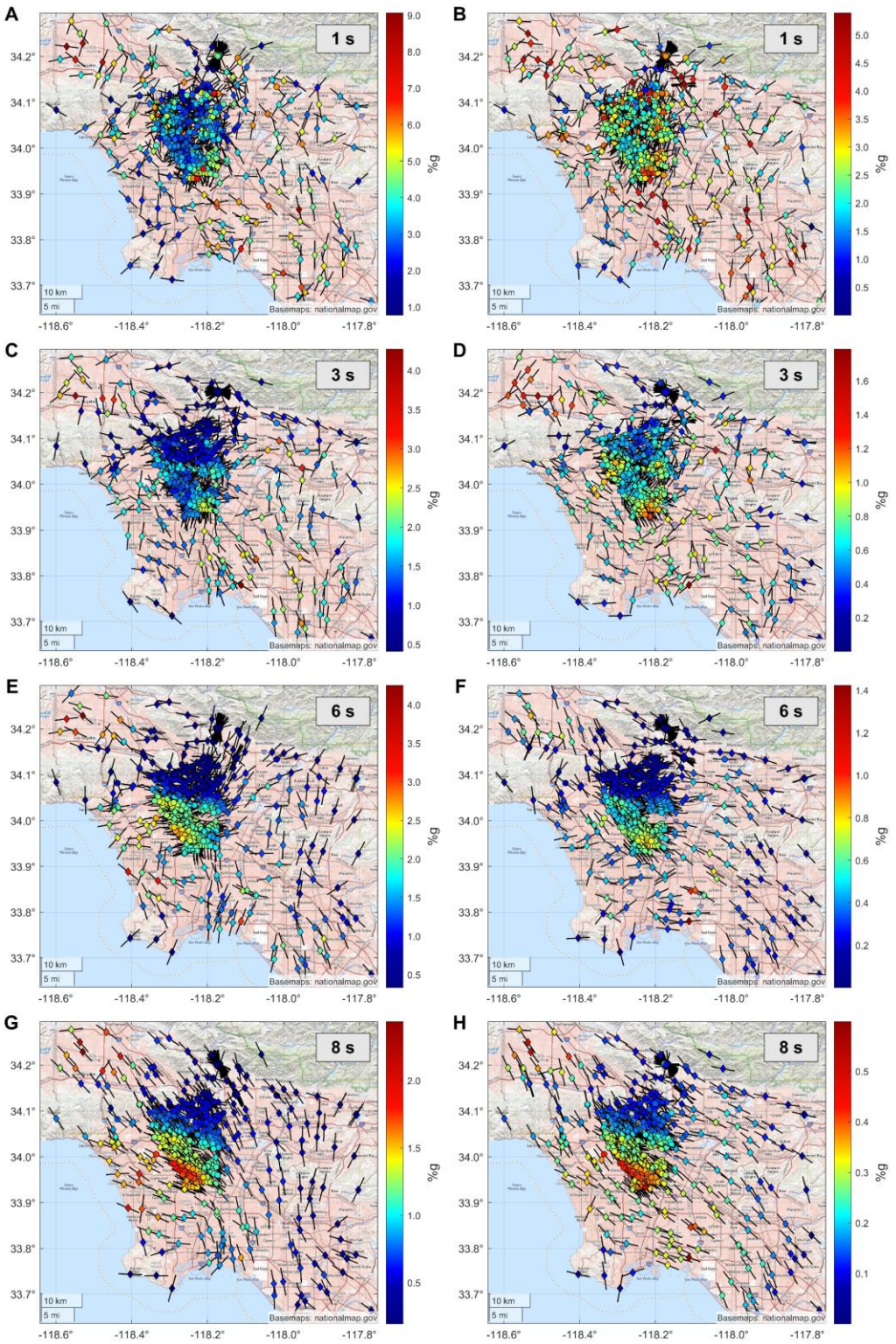

Figure 4.8. SA direction maps. Same format as Figure 4.5.

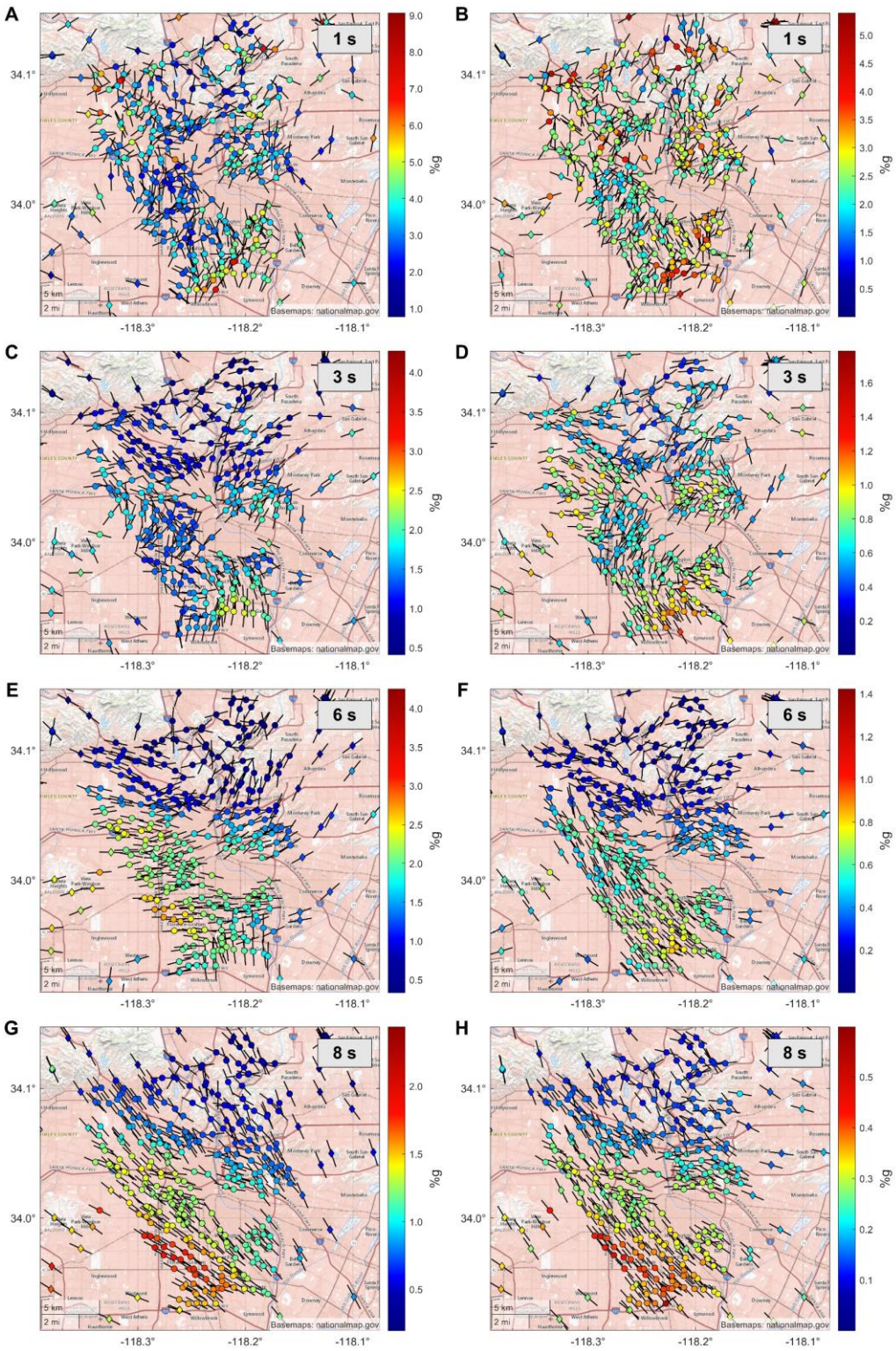

Figure 4.9. SA direction maps. Detail of Figure 4. Same format as Figure 4.5.

A good way to observe this smaller length scale coherence for the shorter periods is by studying the data from the CSN deployment in the campus of the Jet Propulsion Laboratory (JPL) in Pasadena. The campus is densely instrumented by the CSN, with average station spacing of about 50m. Figure 4.10 shows the SAs computed from the M7.1 event for 8 periods (T=0.1, 0.3, 0.5, 0.8, 1, 3, 6, and 8 s and damping ratio ζ=5%. Figure 4.11 is similar but for the M6.4 event. Here again the results are for the most part reproducible between the two earthquakes. Due to the high station density, coherent patterns in the SAs are visible even for the 0.5, 0.8, and 1 s, while the coherence disappears at the shorter periods (0.1 and 0.3 s).

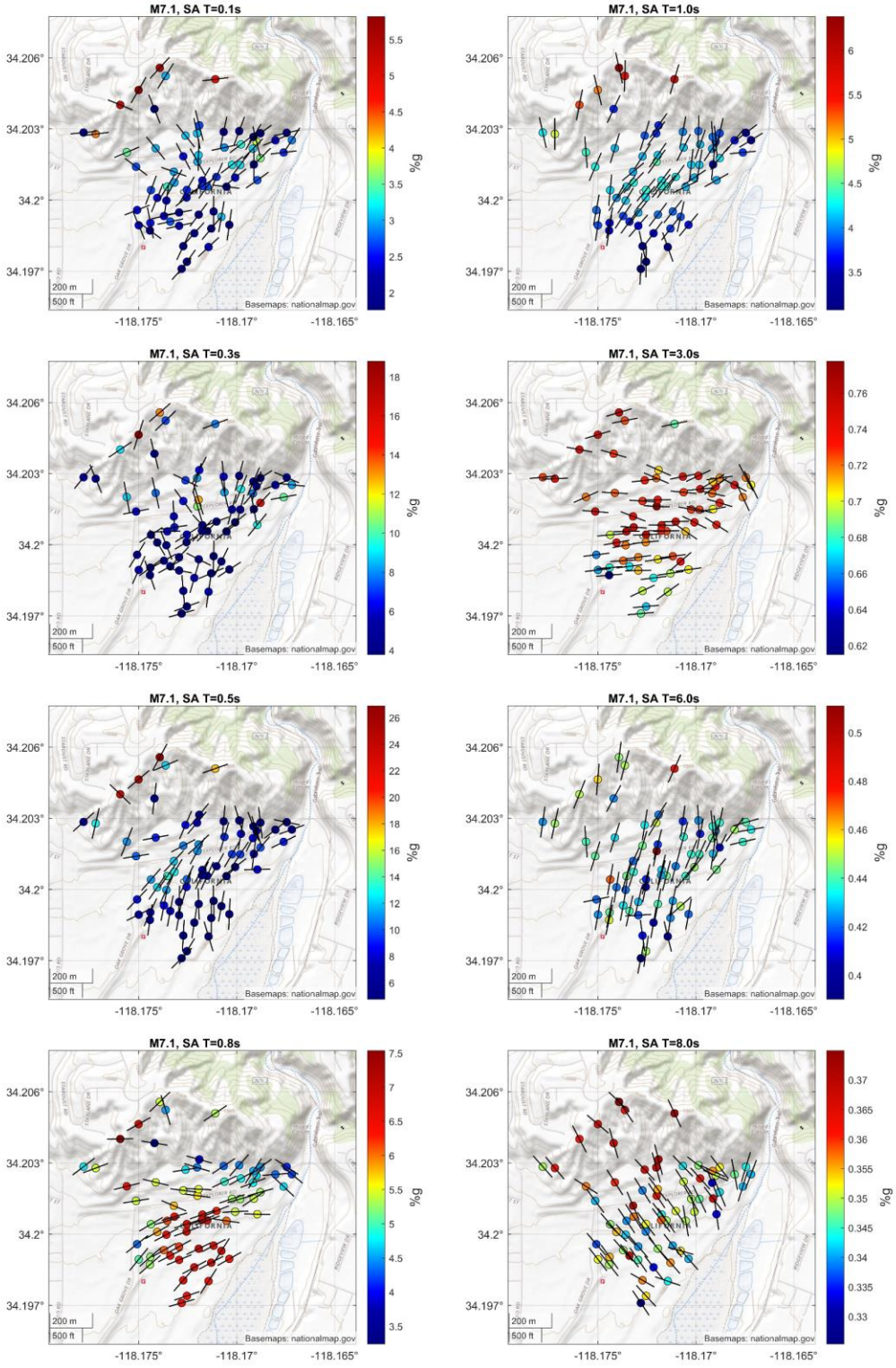

Figure 4.10. SA maps and directions for the JPL campus CSN deployment. M7.1 event. Right column periods: T=0.1, 0.3, 0.5, and 0.8 s. Left column periods: T=1, 3, 6, and 8 s. Damping ratio ζ=5%.

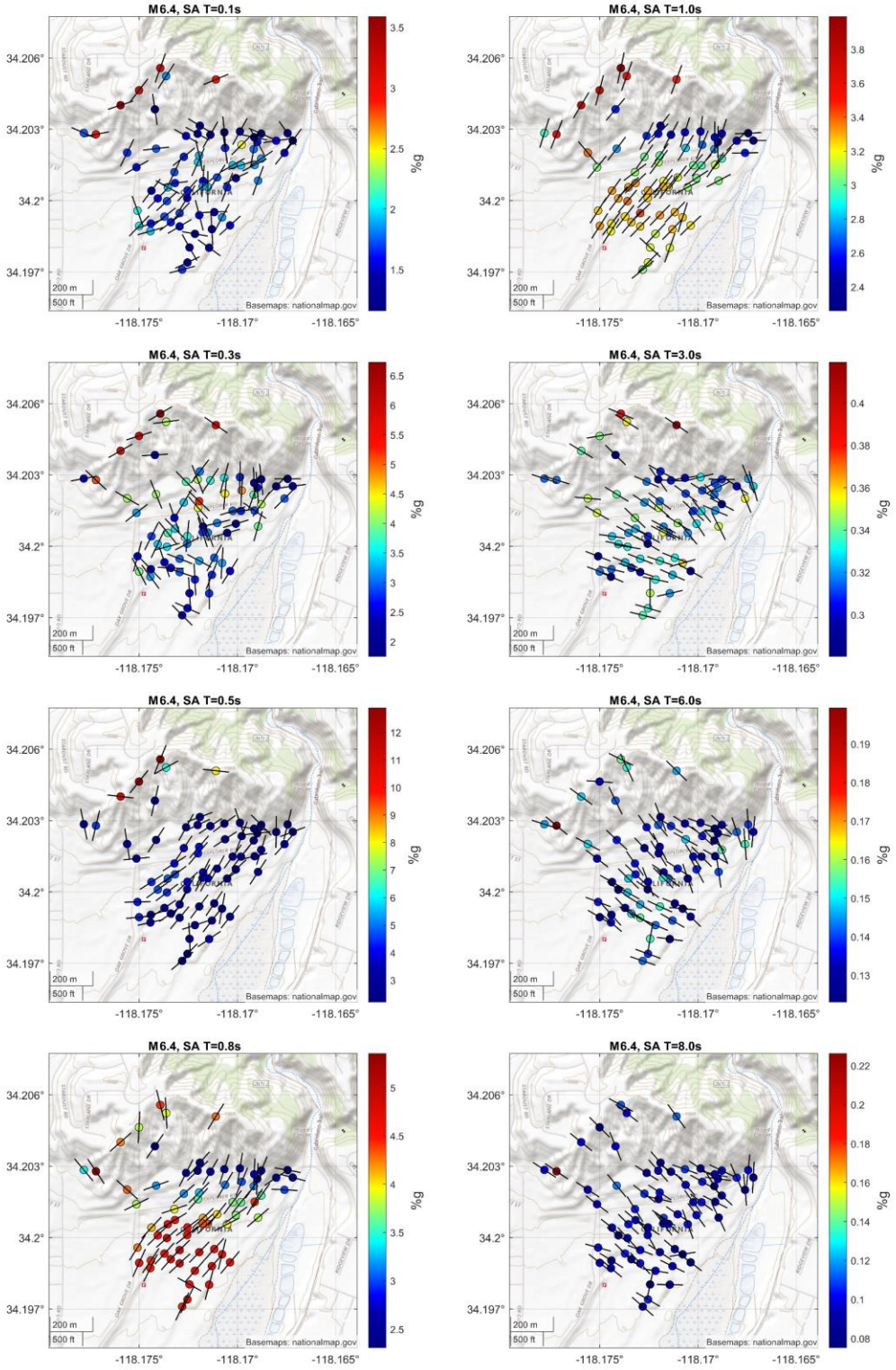

Figure 4.11. SA maps and directions for the JPL campus CSN deployment. M6.4 event. Right column periods: T=0.1, 0.3, 0.5, and 0.8 s. Left column periods: T=1, 3, 6, and 8 s. Damping ratio ζ=5%.

4.3.2 Maps of Similar Spectral Acceleration Intensity Measures

Another way to look at the above results is by dividing the SA amplitude of every station to the average SA amplitude of stations located on bedrock sites. These maps of "Relative SA" or "SA amplification" (since they express by how much the SA at a site is higher than the SA at the reference sites) allow for easy comparisons of the amplification of the response in the deeper basin relative to that of sites on bedrock. Three SCSN seismic stations in the mountains of the greater Los Angeles were selected. These three stations are: PASC located in the hills on the western boundary of the San Gabriel Valley, DJJ at Stone Canyon Reservoir in the eastern Santa Monica Mountains, and MWC at Mount Wilson Observatory in the San Gabriel Mountains. Maps of the SA amplification, equivalent to the above Figures 4.5 and 4.6 are presented in Figures 4.12 and 4.13. Looking at the SA amplification figures one can again very easily see the good correlation between the two events, with not only the patterns but the magnitudes also being very similar between the two events.

In the above presented results, a 5% damping ratio is used. However, a 2% damping ratio would be more appropriate for the longer ($\geq$ 6 s) periods. Strains are known to decay rapidly with increasing distance from the fault (Hays, 1984). Since the events were distant and the peak ground velocities recorded in the Los Angeles area were small, the response is expected to be in the linear regime. For a mid- or high-rise structural system linearly responding at its dominant mode, a 2% damping ratio is found to be a more suitable value (Cruz & Miranda, 2017). Appendix 4.A.4 contains maps using 2% damping ratio (Figures 4.29 and 4.30), similar to Figures 4.5 and 4.6.

Furthermore, as it was stated in Section 4.2, the RotD50 intensity measure will be used in subsequent sections (Sections 4.4, 4.5, and 4.6) for comparisons between the measurements and the model prediction. We provide the RotD50 maps calculated for 5% damping ratio in Appendix 4.A.5 (Figures 4.31 and 4.32).

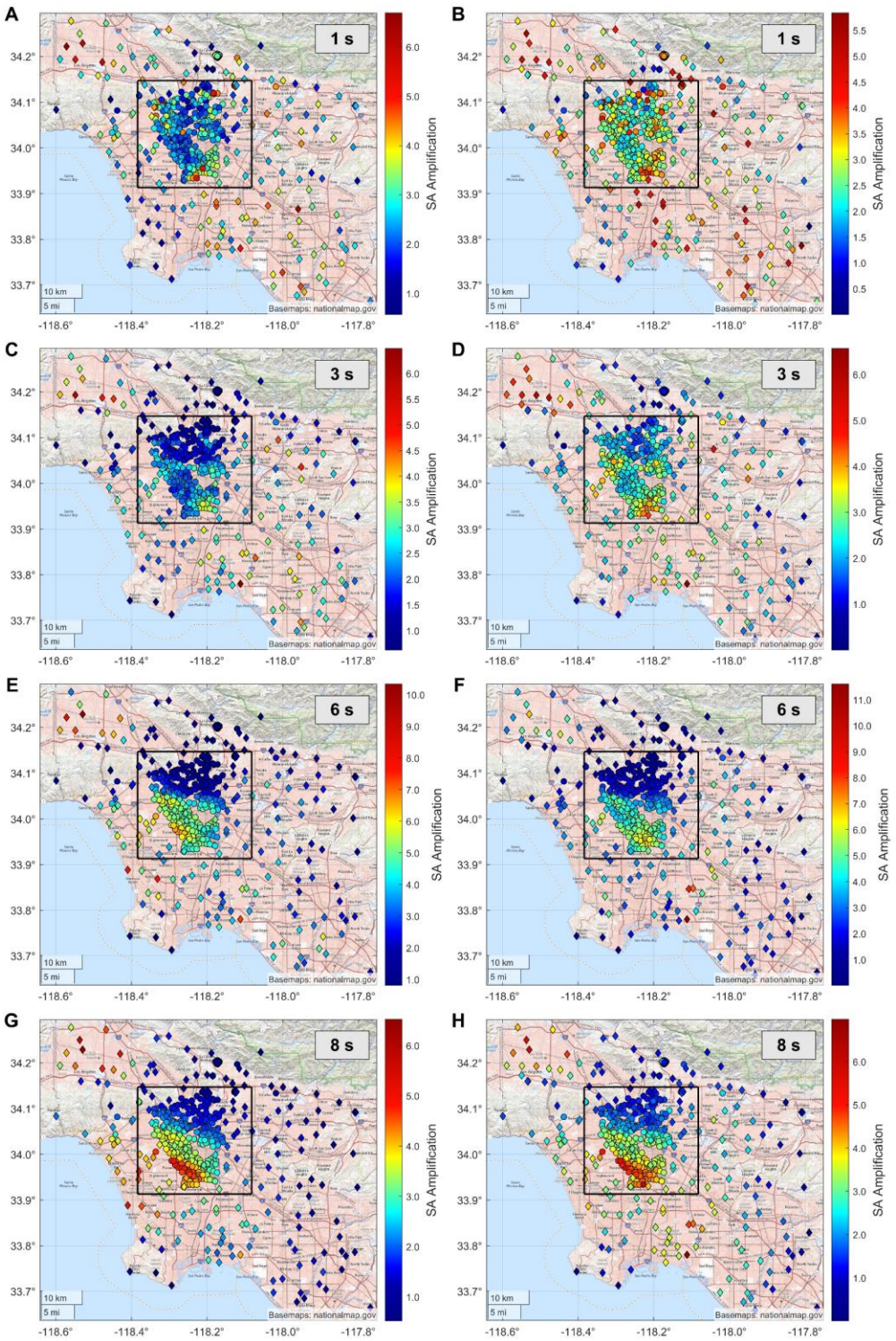

Figure 4.12. SA amplification maps. Left column: M7.1 event. Right column: M6.4 Event. (A-B) T=1 s. (C-D) T=3 s. (E-F) T=6 s. (G-H) T=8 s. Damping ratio ζ=5%. Circles: CSN stations, Diamonds: SCSN & CSMIP stations. Black rectangle: Area magnified in Figure 4.13. Note varying colorbar amplitude scales.

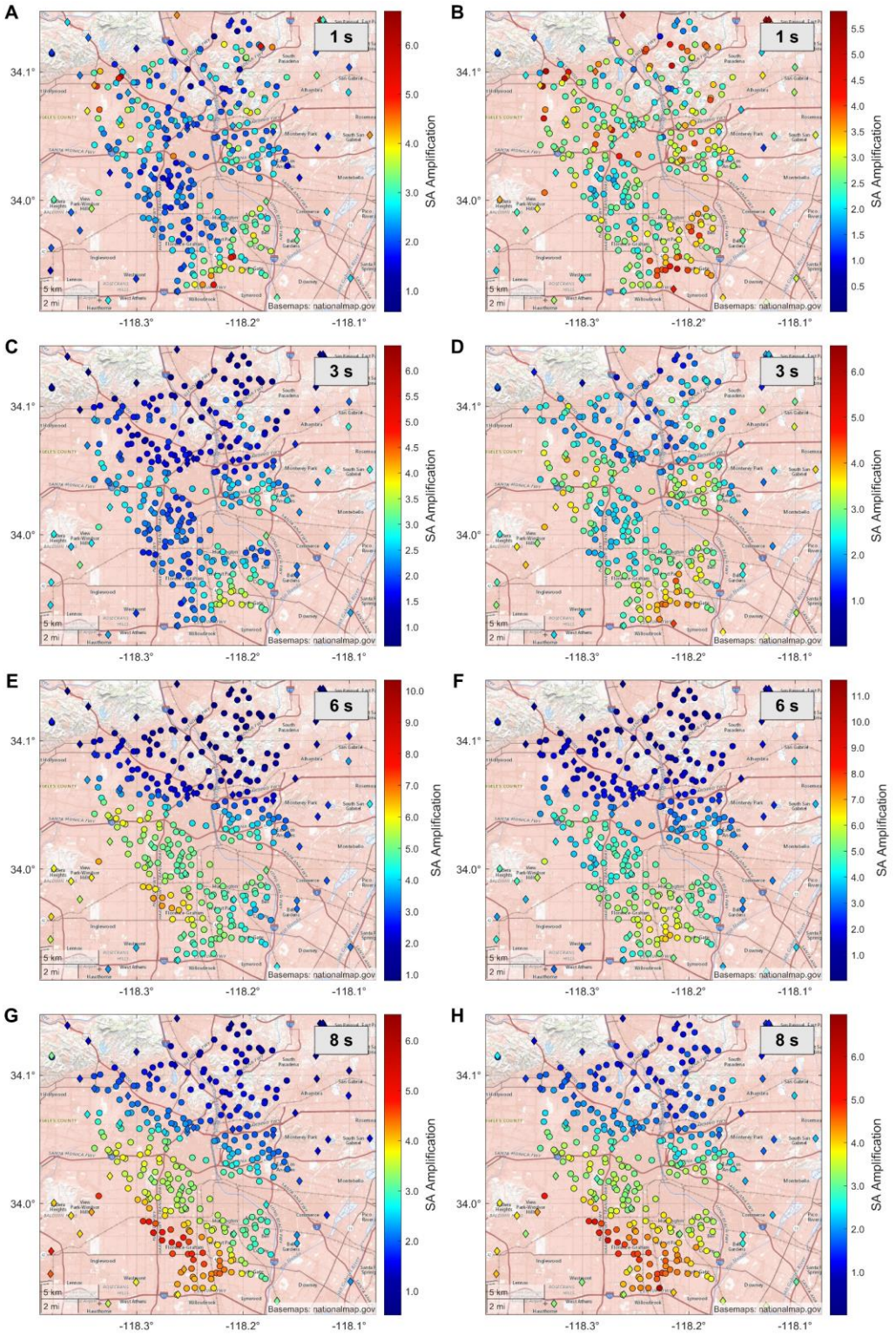

Figure 4.13. SA amplification maps detail. Detail of Figure 4.12. Same format as Figure 4.12.

Figure 4.14 displays maps of interpolated SA amplifications, for periods 1, 3, 6, and 8 s. Inverse Distance Weighting (IDW) (Shepard, 1968) was used for the interpolation. We split our area of interest with a uniform grid (200x200 grid points). The value at a grid point (interpolated value) is a linearly weighed combination of the values at the stations (measured values). As sample points we are using the 7 closest stations within a radius of 7.0km. An exponent of 3.0 is used so that the closest sampling points have a much bigger weight. If a grid point is collocated with a measured location the measured value at that point is used. The weighted distance average cannot be higher than the maximum or lower than the minimum measured value. Therefore, it cannot create extreme maxima and minima if such extremes do not already exist in the data. Following the IDW interpolation we bin the values in order to better capture some of the features of the amplifications. Seven bins are used: 0-1, 1-2, 2-3, 3-4, 4-5, 5-6, and 6+. IDW is reasonable to use in absence of any clear secondary information. Should any correlation with site parameters be understood and established Kriging with a trend could be a much more promising interpolation method.

The interpolation maps of Figure 4.14 contain and enhance the information presented in the previous figures. More specifically, the SA amplification in the San Fernando Valley basin is higher than the ones observed in the south for all periods considered. On the other hand, the SA amplifications in the San Gabriel Valley basin are low for all periods. In the Los Angeles basin, for the shorter periods (T=1 and 3 s) the maximum SA amplifications (worse site conditions) are in the east and south-east, while for the longer periods (T=6 and 8 s) the maximum SA amplifications are in the west. The interpolation of the data points over the area of interest provides an easy way to observe existing trends and the locations where the maxima occur. However, the quality of such interpolations depends on the station density and is expected to be better in the northern Los Angeles area due to the dense CSN instrumentation. For areas with few and distant station one should be aware that such interpolations may not be valid.

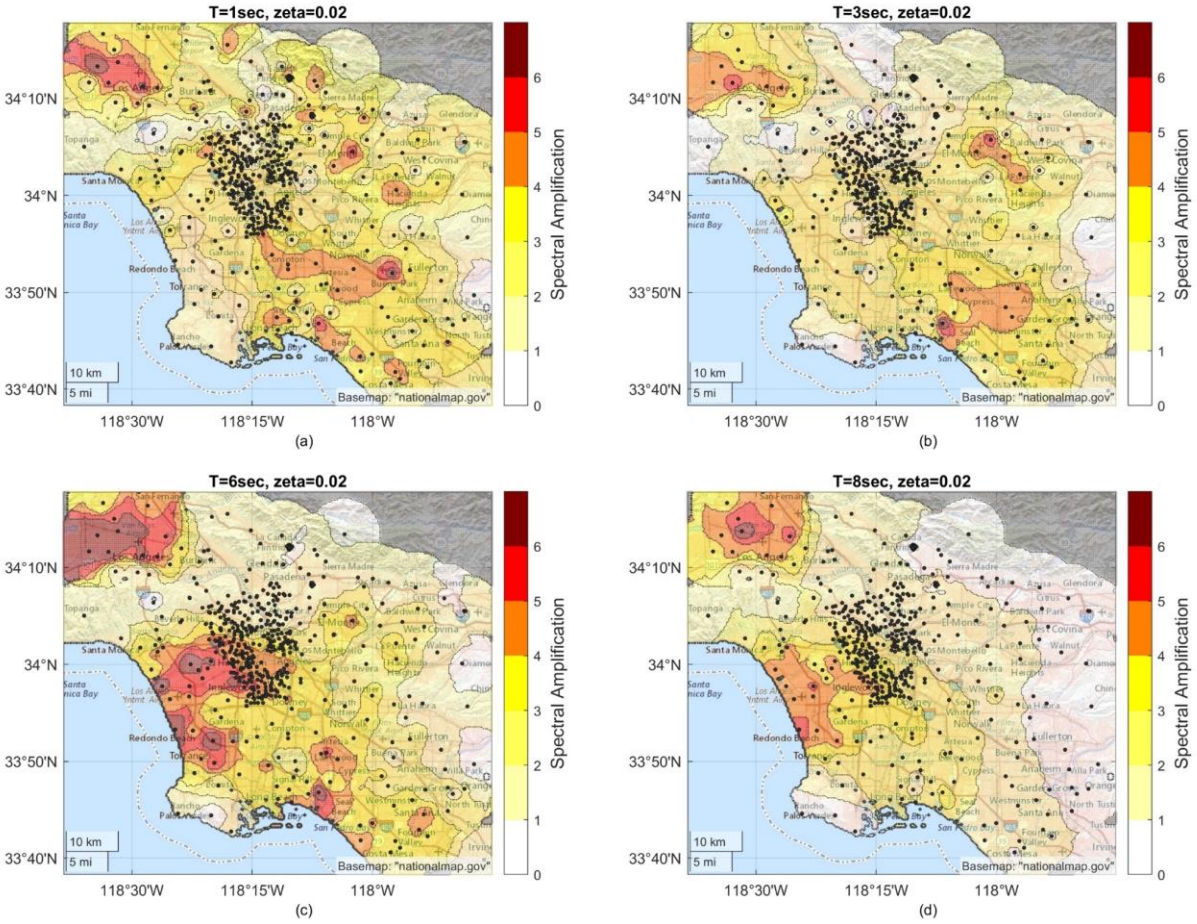

Figure 4.14. Contoured SA amplification maps, for the M7.1 event. (A) T=1 s. (B) T=3 s. (C) T=6 s. (D) T=8 s. The station locations are marked with black dots.

4.3.3 Correlation with site parameters

It is common practice in many engineering applications to estimate the ground motion response through empirical correlations with site parameters. Two of the most used site parameters are the depth-to-basement and Vs30. Ground motion amplification has been shown to increase at longer periods with increasing depth-to basement (e.g., Liu & Heaton, 1984), which is usually obtained by well penetration, seismic or gravity data (e.g., Shaw et al., 2015). Vs30 data, used as a proxy for different local soil properties, take into account site-specific measurements, as well as surface geology and topographic gradient (e.g., Thompson, et al., 2014; Thompson, 2018). In both cases, the resolution of these parameters is limited by the density and quality of the measurements.

We calculate the depth-to-basement and Vs30 for each site from grid values using a triangulation-based linear interpolation. The depth-to-basement grid values are from Shaw et al. (2015). A depth-to-basement value corresponds to the depth to crystalline rock / basement. Negative values correspond to surface outcrop (Figure 4.15A). The Vs30 grid values are from Thompson (2018) (Figure 4.15B) and account for constraints from multiple sources (site-specific measurements, surface geology, and topographic gradient). As discussed in Brown et al. (2002) there are a number of advantages to using slowness rather than velocity, hence in the following, we will be considering the shear-wave slowness in the top 30 meters, defined as Ss30 = 1/Vs30. This also allows us to better focus on the low Vs30 regions. We find the SA correlation with Ss30 to be stronger than the correlation with Vs30.

Figure 4.15C shows depth-to-basement plotted against Ss30 (and Vs30) at each station. A statistically significant correlation exists between the depth-to-basement and Ss30 values, with correlation coefficient r = 0.74 and the p-value $p < 0.001$ (between the depth-to-basement and Vs30 values these statistics are: r = -0.65 and $p < 0.001$). Sediments are highly correlated with basins and the Vs30 is affected by the existence of such sediments. The figure displays this built-in correlation between the Vs30 and the deeper structures. Another interesting feature of Figure 4.15C is the banded behavior of the Vs30 values. This is likely due to the fact that in the absence of site specific measurements, the Vs30 values account for surface geology and topographic gradient (Thompson, et al., 2014). The smoothness of the Vs30 dataset in combination with the high spatial density of the seismic networks, result in many stations having exactly the same Vs30 value even if their underlying soil conditions are not exactly the same.

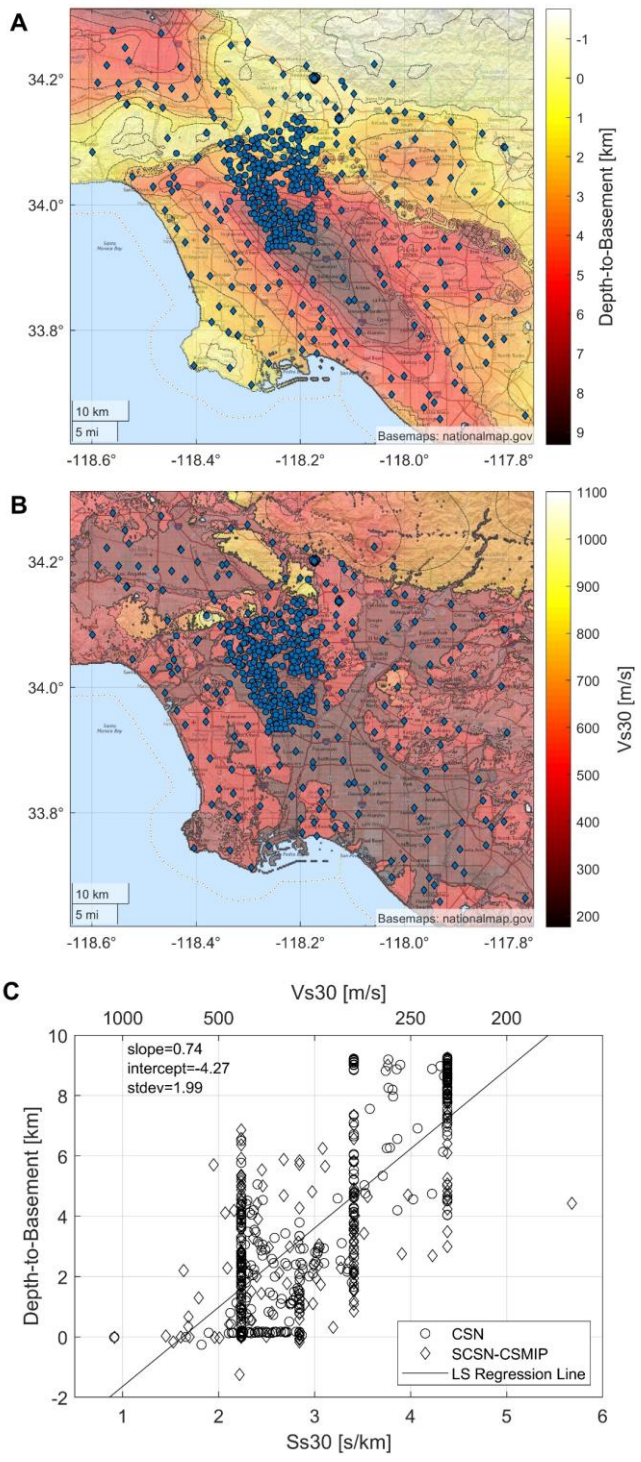

Figure 4.15. Site parameter plots. (A) Sensor locations plotted on top of contoured depth-to-basement. (B) Sensor locations plotted on top of contoured Vs30. (C) Scatter plot of the depth-to-basement plotted against Ss30 and Vs30 at the station locations. Circles: CSN stations, Diamonds: SCSN & CSMIP stations. Depth-to-Basement contours are marked at 1-km intervals. Vs30 contours are marked at 100-m/s intervals.

Figure 4.16 shows the correlation between every station's observed SA and its corresponding depth-to-basement. As before, to quantitatively assess the correlations, we calculate the correlation coefficients (r) and the p-values (p). We find r = 0.079, 0.61, 0.75, and 0.74 for T=1, 3, 6, and 8 s respectively. The p-values are p = 6.45e-2 for T=1 s and p < 0.001 for T=3, 6, and 8 s. For T=1 s there is no correlation between SA and the depth-to-basement. However, for longer periods a correlation appears and sites with larger depth-to-basement have on average larger SAs. The p-values confirm that the correlation is statistically significant for the longer periods. The correlation is the strongest at 6 s. As one can see in Figure 4.16 it is not always the case that the largest SAs correspond to the areas of the deepest basement depth.

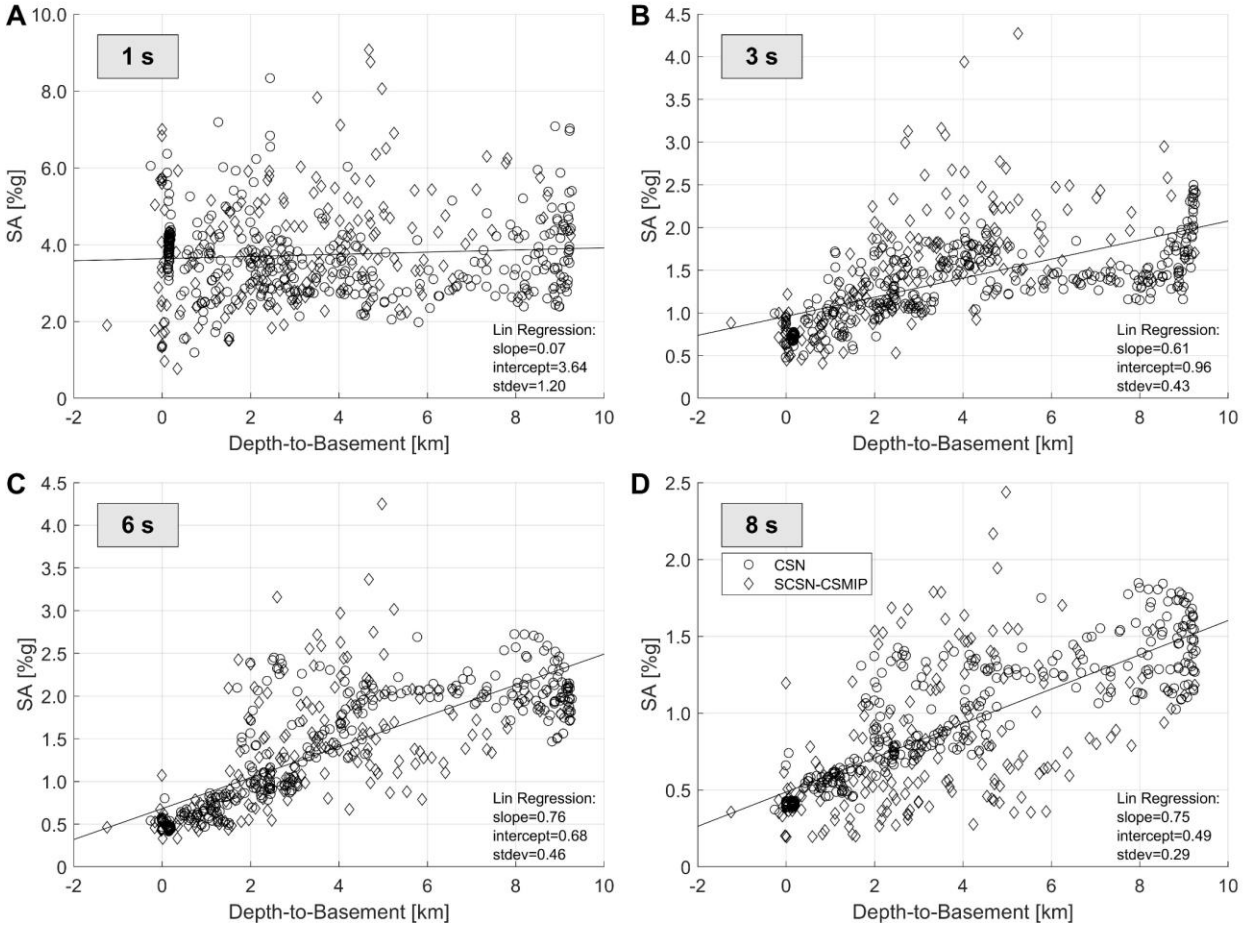

Figure 4.16. SA correlation with depth-to-basement, for the M7.1 event. (A) T=1 s. (B) T=3 s. (C) T=6 s. (D) T=8 s. Damping ratio ζ=5%. Circles: CSN stations, Diamonds: SCSN & CSMIP stations. The solid line shows the least-squares (LS) regression fit. The slope and intercept of the LS regression line, and the standard deviation are provided in each subplot.

Figure 4.17 displays the correlation between every station's observed SA and its corresponding Ss30. We find r = 0.12, 0.43, 0.52, and 0.49 for T=1, 3, 6, and 8 s respectively. The p-values are p = 3.22e-3 for T=1 s and p < 0.001 for T=3, 6, and 8 s. A main feature of Figure 4.17 is the banded pattern of the Ss30, discussed previously, due to the smoothness of the Vs30 grid. This pattern makes it difficult to visually observe any correlation between SA and Ss30 but the statistical measures r and p suggest that for T=3, 6, and 8 s, there exists a weak but statistically significant correlation. Again, for T=1 s there is almost no correlation, while the correlation is the strongest for T=6 s.

The correlation of the observations with Vs30 was perhaps expected to be stronger for the shorter periods. Vs30 and SA have been found to have a strong correlation at T=1 s in empirical ground-motion data sets, such as the NGA-W2 dataset (Ancheta, et al., 2014). The repeated Vs30 values and banded Vs30 behavior for the spatially dense CSN stations, also discussed in Figure 4.15C, likely obscures the Vs30 scaling at the shorter length-scales (i.e., shorter periods). The observed stronger correlation between SA and Vs30 for the longer periods might also come as a surprise, due to the fact that from its definition the Vs30 measure only accounts for the local, near surface conditions. These correlation trends likely result from the inherent correlation of Vs30 with basement depth in the Los Angeles region, as demonstrated in Figure 4.15C. At the longer periods, the correlation between SA and depth-to-basement is found to be stronger than the correlation between SA and Ss30. Another possible reason, however, could be the hybrid approach used to derive the Vs30 values, where apart from site-specific Vs30 measurements, surface geological units and topographic gradient are also taken into account (Thompson, et al., 2014). It is possible that these larger-scale features result in the correlation observed for the longer periods.

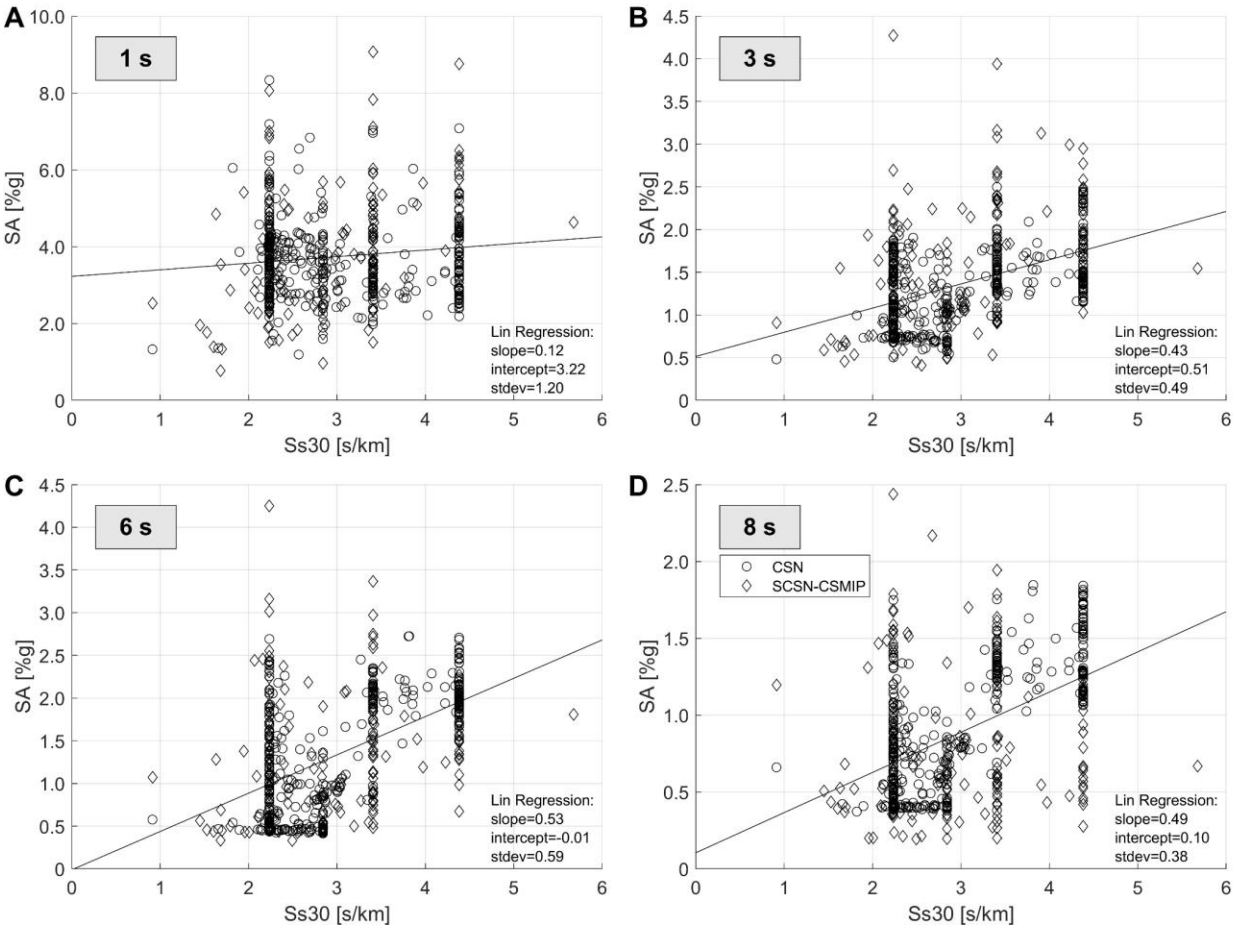

Figure 4.17. SA correlation with Ss30, for the M7.1 event. (A) T=1 s. (B) T=3 s. (C) T=6 s. (D) T=8 s. Damping ratio ζ=5%. Circles: CSN stations, Diamonds: SCSN & CSMIP stations. The solid line shows the least-squares (LS) regression fit. The slope and intercept of the LS regression line, and the standard deviation are provided in each subplot.

4.4 Spectral Acceleration Predicted by Ground Motion Simulations

Ground motion simulations for the M7.1 Ridgecrest event were performed using the 3D finite-difference method of Graves (1996). A suitable stochastic finite-fault rupture model was developed (Graves & Pitarka, 2020) using the Graves-Pitarka kinematic rupture generator method (Graves & Pitarka, 2016). The rupture model was constrained by the near-fault ground motion. The simulations use a minimum shear-wave velocity (V_S) of 500 m/s and 100 m grid spacing, which yield reliable results up to 1 Hz. We recognize that the basin has velocities lower than 500 m/s in the shallow near surface, however, these layers are relatively thin and generally impact frequencies

of 1Hz and higher. Anelastic attenuation Q is modeled using the relations $Q_S = 50V_S$ (for V_S in km/s) and $Q_P = 2Q_S$.

The simulations were run in both CVM-S and CVM-H. The specific versions of the velocity models used are CVM-S4.26.M01 (Lee, et al., 2014) ('CVM-S' hereafter) and CVM-H15.10.0 (Shaw, et al., 2015) ('CVM-H' hereafter). Due to differences in the approaches used to parameterize the models, the details of the Los Angeles Basin structure differ between the two models. In CVM-S, the initial basin structure follows a rule-based seismic velocity model, derived mainly from well log data, where seismic velocity is a function of sediment age and depth. In CVM-H, basin velocities are determined from sonic logs and seismic reflection profiles collected by the petroleum industry. The models are further refined using waveform tomography with a variety of data sets including earthquakes, ambient noise, seismic reflection and receiver functions. Both models utilize a high resolution geotechnical layer (GTL) based primarily on Vs30 values to represent the upper few hundred meters of the model; however, the implementation of the GTL is somewhat different in each model. Both CVMs are considered acceptable representations of the Southern California crustal structure, especially for periods longer than 5 s (Taborda, et al., 2016).

Figure 4.18 displays the shear-wave velocity cross sections for the two models along the profile A-A' (marked in Figure 4.1B). Compared to CVM-S, CVM-H contains a sharper definition of the general basin structure. In addition to that, CVM-H contains several lateral discontinuities including several fault-bounded velocity jumps not present in CVM-S. CVM-H has lower velocities in the upper 1-2 km of the basin compared to CVM-S, but higher velocities at 2-5 km depth. Below about 6 km depth, the velocities of the two models are similar.

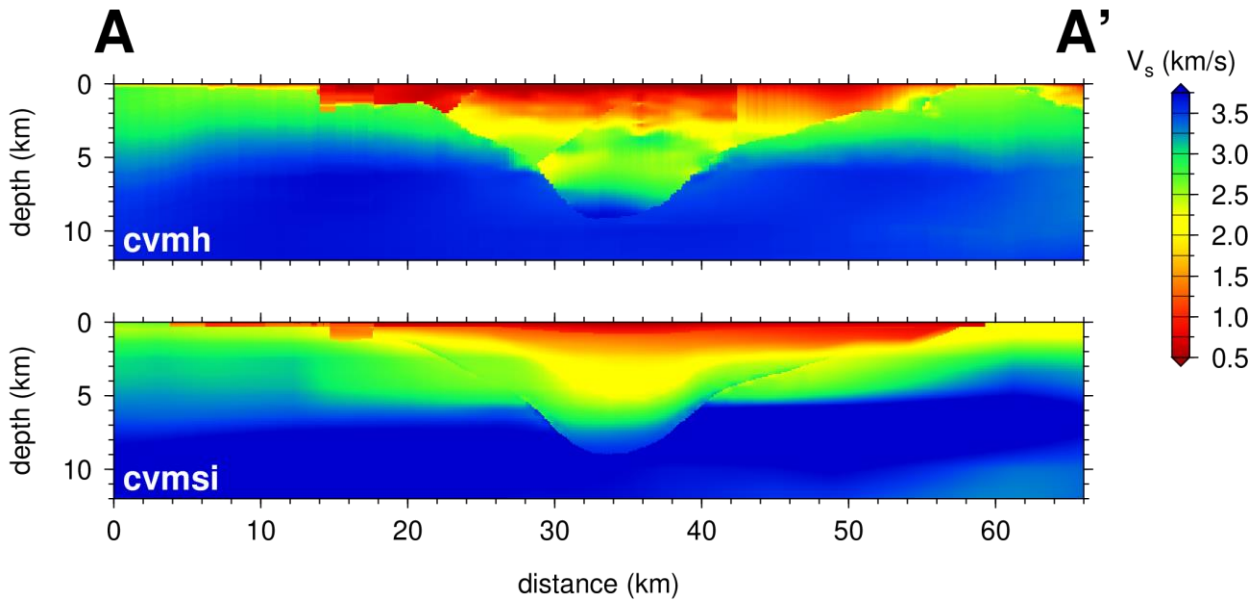

Figure 4.18. Shear-wave velocity cross sections for the two CVMs along profile A-A' (marked in Figure 4.19B) - image provided by Dr. R. Graves.

Since the NGA-West2 GMPEs (Bozorgnia, et al., 2014) offer RotD50 rather than SA predictions, we use the RotD50 intensity measure (Boore, 2010) for all comparisons between observations and model predictions. We calculate the model-predicted RotD50 from simulated waveforms low-pass filtered at 1 Hz using a 4th order, 2-pass Butterworth filter. Due to the bandwidth limitation, we only consider periods T=3, 6, and 8 s for the SDoF oscillator. As before, we use a damping ratio of 5%. Figure 4.20 displays maps of the model-predicted RotD50 for the two CVMs. The first column shows RotD50 maps calculated from the data (also available in Figure S4ACEG) for comparison. The different formulations of the two CVMs manifest themselves in the results. In the top few kms, the CVM-S model is overall smoother, while the CVM-H model contains sharp transitions and patches with large jumps in velocity (Figure 4.18). This is readily apparent in the results for T=3 s where the RotD50 pattern for CVM-H is much more spatially complex than the pattern seen for CVM-S. The impact of these differences decreases moving to longer periods as the longer wavelengths become more sensitive to the larger-scale structure of the basin. At 8 s period, the patterns are fairly similar for the two models, although the peak amplitudes for CVM-H occur near the central basin (e.g., Downey), whereas they occur towards the southern margin of the basin (e.g., Long Beach) in CVM-S. We suspect that this difference results from the sharper

vertical velocity gradient in CVM-H, which turns the waves more quickly towards the surface after they enter the basin from the northern margin.

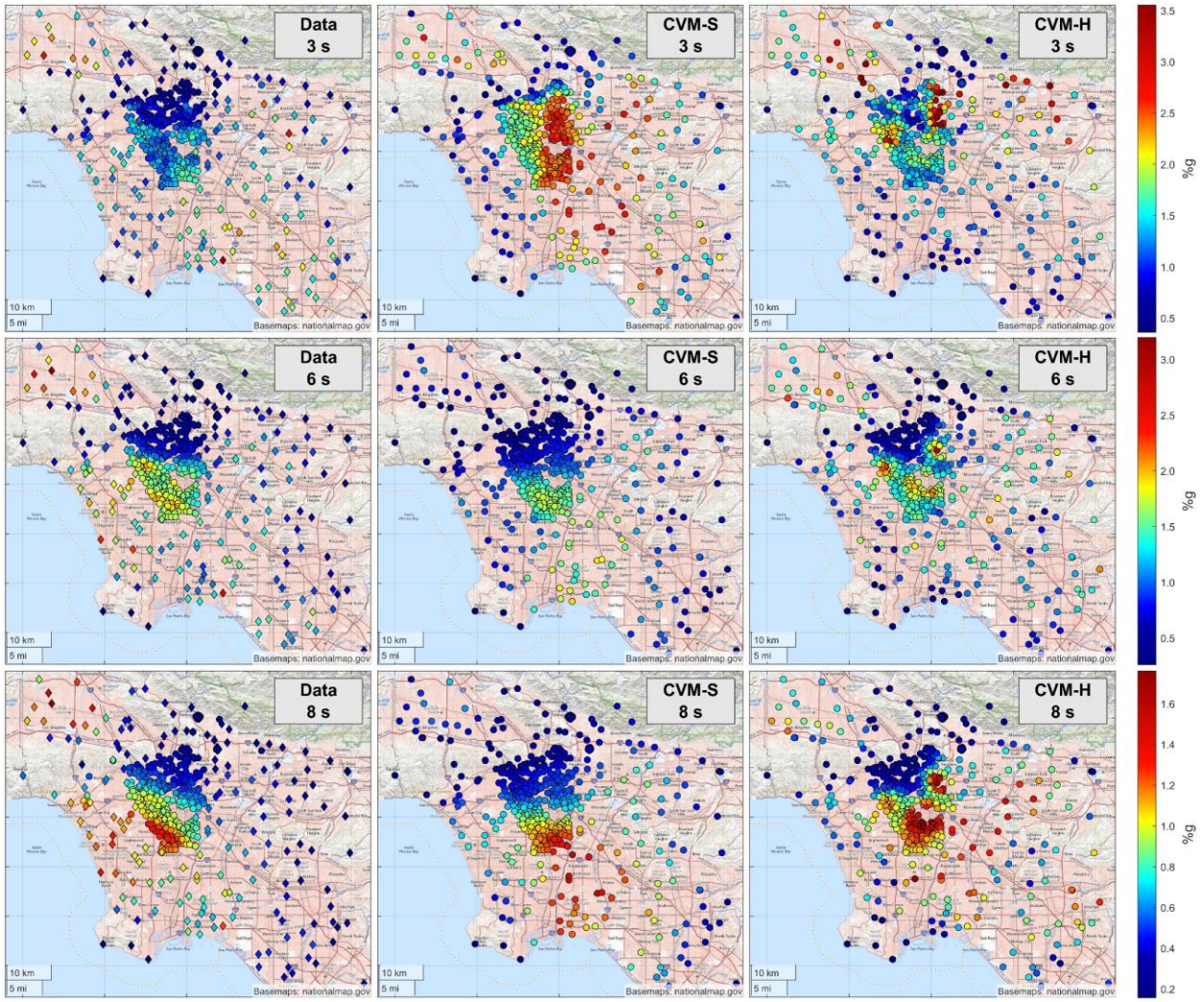

Figure 4.20. Data and model-predicted (simulations) RotD50 maps, for the M7.1 event. Column 1: Observations, Column 2: CVM-S model, Column 3: CVM-H model. Row 1: T=3 s, Row 2: T=6 s, Row 3: T=8 s. Damping ratio ζ=5%. Each row has a separate colorbar.

In order to provide a more quantitative measure of the models' performance, we compute the residuals for geographical site i, $i = 1, \dots, N$ given by (Abrahamson, et al., 1990)

$$r_i(T,\zeta) = ln\left(\frac{RotD50_{meas,i}(T,\zeta)}{RotD50_{pred,i}(T,\zeta)}\right) \tag{4.6}$$

where $RotD50_{meas,i}(T,\zeta)$ is the RotD50 computed from the data and $RotD50_{pred,i}(T,\zeta)$ is the RotD50 predicted by the model, for site i. The model bias is given by

$$B(T,\zeta) = \frac{1}{N}\sum_{i=1}^{N} r_i(T,\zeta) \tag{4.7}$$

and the standard deviation is given by

$$\sigma(T,\zeta) = \left[\frac{1}{N}\sum_{i=1}^{N}[r_i(T,\zeta) - B(T,\zeta)]^2\right]^{1/2}. \tag{4.8}$$

We also compute the absolute misfit (J) as a measure of the total mismatch between the simulation predictions and the data, found by

$$J(T,\zeta) = \frac{1}{N}\sum_{i=1}^{N}|r_i(T,\zeta)|. \tag{4.9}$$

The resulting model biases, standard deviations and absolute misfits are given in Tables 1-3. Figure 4.21 in the supplement displays maps of the residuals. Positive residuals indicate that the model under-predicts the data, while negative residuals indicate over-prediction. For both models, the total fit of the data is best (minimum J) at T=6 s and worst (maximum J) at T=3 s. For the shorter period (T=3 s) CVM-H has better performance (smaller J), while for the longer periods (T=6 and 8 s) the CVM-S performance is superior. Both models miss some areas where local maxima of RotD50 are observed (e.g., the San Fernando Valley and near Manhattan Beach for the longer periods).

The overall performance of the simulations is encouraging, with the average absolute misfit being about 0.35 for both models. For the longer periods (T=6 and 8 s) the range of the model-predicted SAs matches that of the observations. The drop in performance for 3 s is suspected to be due to the velocity structures not fitting well at these shorter periods. Developing the CVMs (e.g., waveform tomography information for the shorter periods, definition of the GTL, Vs30 values) and the various other components of the modeling (e.g., better inelastic attenuation factors, source modeling) are all potential paths for improvement.

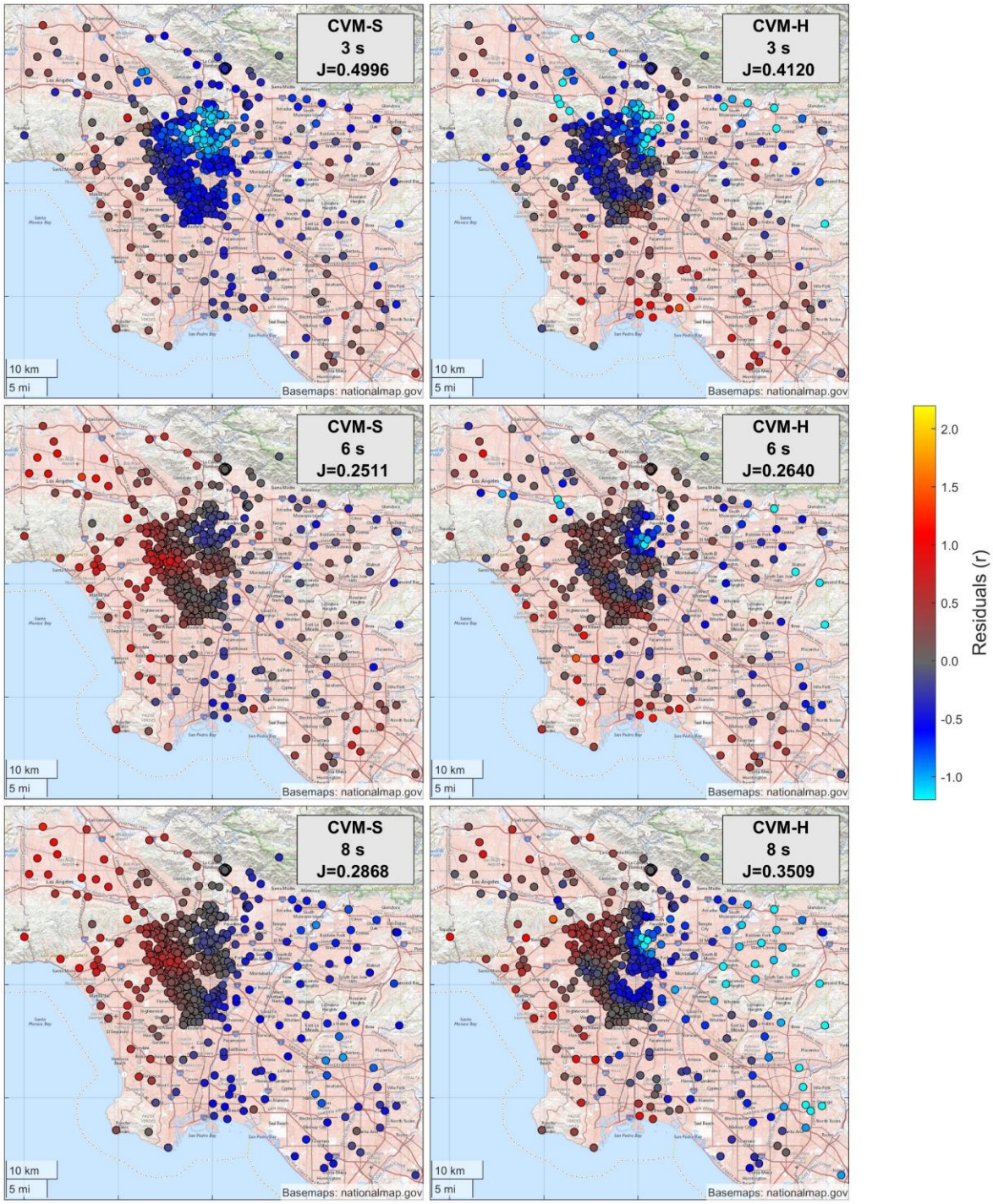

Figure 4.21. Maps of the residuals, calculated according to Eq. (4.6), between model-predicted (simulations) and data RotD50, for the M7.1 event. The selected models and periods are shown in the top right corner of each subplot. The resulting absolute misfit (J), calculated according to Eq. (4.6), is also indicated in the top right corner of each subplot. The colorbar is the same for all subplots and its range was limited to [-1.2, 2.2] in order to better capture the near-zero overprediction/underprediction variations.

Table 4.1. Model bias B(T, ζ = 0.05), calculated using Eq. (4.7), for the M7.1 event.

	T=1 s	T=3 s	T=6 s	T=8 s
CVM-S	-	-0.44	0.17	0.039
CVM-H	-	-0.26	0.026	-0.10
ASK14	-0.14	-0.016	0.62	0.40
BSSA14	0.16	0.10	0.65	0.55
CB14	0.14	0.25	0.95	0.81
CY14	0.048	-0.082	1.12	1.25

Table 4.2. Model standard deviation σ(T, ζ = 0.05), calculated using Eq. (4.8), for the M7.1 event.

	T=1 s	T=3 s	T=6 s	T=8 s
CVM-S	-	0.36	0.30	0.38
CVM-H	-	0.47	0.37	0.47
ASK14	0.41	0.31	0.38	0.40
BSSA14	0.41	0.36	0.39	0.43
CB14	0.40	0.35	0.43	0.42
CY14	0.39	0.34	0.36	0.39

Table 4.3. Model absolute misfit J(T, ζ = 0.05), calculated using Eq. (4.9), for the M7.1 event.

	T=1 s	T=3 s	T=6 s	T=8 s	Average
CVM-S	-	0.50	0.25	0.29	0.35
CVM-H	-	0.41	0.26	0.35	0.34
ASK14	0.36	0.25	0.63	0.47	0.43
BSSA14	0.36	0.30	0.69	0.62	0.49
CB14	0.35	0.34	0.95	0.82	0.61
CY14	0.32	0.28	1.12	1.25	0.74

4.5 Spectral Acceleration Predicted by GMPEs

GMPEs are frequently used in seismic hazard applications to provide spectral acceleration estimates as a function of predictor variables such as earthquake magnitude, site-to-source distance, and site parameters. In particular, the equations explicitly consider the Vs30 of the site, as well as sediment thickness, which is parameterized as depth to shear-wave velocity of 1.0 km/s (Z1.0) or 2.5 km/s (Z2.5). We consider four out of the five GMPEs developed as part of the NGA-West2 project (Bozorgnia, et al., 2014): ASK14 (Abrahamson, et al., 2014), BSSA14 (Boore, et al., 2014), CB14 (Campbell & Bozorgnia, 2014), and CY14 (Chiou & Youngs, 2014). The fifth GMPE (Idriss, 2014) is not applicable for the source-to-site distance and Vs30 ranges of our sites (Gregor, et al., 2014) and thus it is not considered. In the following results, the Vs30 for each site was calculated using linear interpolation of the grid values from Thompson (2018) and the Z1.0 and Z2.5 were found using the CVM-H model. Using Z1.0 and Z2.5 from the CVM-S model yields similar GMPE predictions. The effect of including the site Vs30 and Z1.0 or Z2.5 values in the GMPE inputs can be seen in Appendix 4.A.6. Figure 4.22 shows the GMPE-based RotD50 estimate (median prediction) maps for periods T=1, 3, 6, and 8 s and damping ratio 5%. Figure 4.23 shows the associated residual (Eq. (4.6)) maps and Tables 1-3 list the model biases, standard deviations and absolute misfits, calculated using Eqs. (4.7), (4.8), and (4.9).

The four GMPEs produce a wide range of spectral acceleration predictions. It is often the case that a GMPE performing well for one period does a poor job at a different period. For example, CY14 is the best performing GMPE (smallest J) at T=1 s but performs poorly at T=6 and 8 s. For the longer periods (T=6 and 8 s) all GMPEs suffer from under-predictions throughout the entire Los Angeles Basin. Weighting all four periods equally, ASK14 has the best average performance. Like the simulations, the GMPEs miss locations where the observed RotD50 maxima occur (e.g., the San Fernando Valley and west Los Angeles, for the longer periods). When compared with the performance of the simulations, the GMPEs perform better (smaller J) for the 3-s period, while for the longer periods (T=6 and 8 s) the simulations have better performance.

It is worth mentioning that the presented GMPE predictions have large standard deviations. The GMPEs considered here are average models that not always work well for a specific site and

earthquake. When using these models, there is often the assumption that the site-specific differences and geologic variations will be captured by the large variability in the predictions. GMPE predictions at the basin sites might improve as additional observations become available. However, the observed poor correlation between the ground-motion response and site parameters (e.g., Figures 4.16 and 4.17), especially for the shorter periods, suggest that the added ground motion data may not always offer improvement. Reconsidering the input site parameters and including new site parameters in the GMPEs may allow for further improvement, but at the expense of added complexity in GMPE implementation. Another alternative for improved performance is the use of non-ergodic ground motion models (e.g., Landwehr et al, 2016; Kuehn et al., 2019) and non-ergodic site response models (e.g., Stewart et al., 2017) that are specific to the Los Angeles basin region.

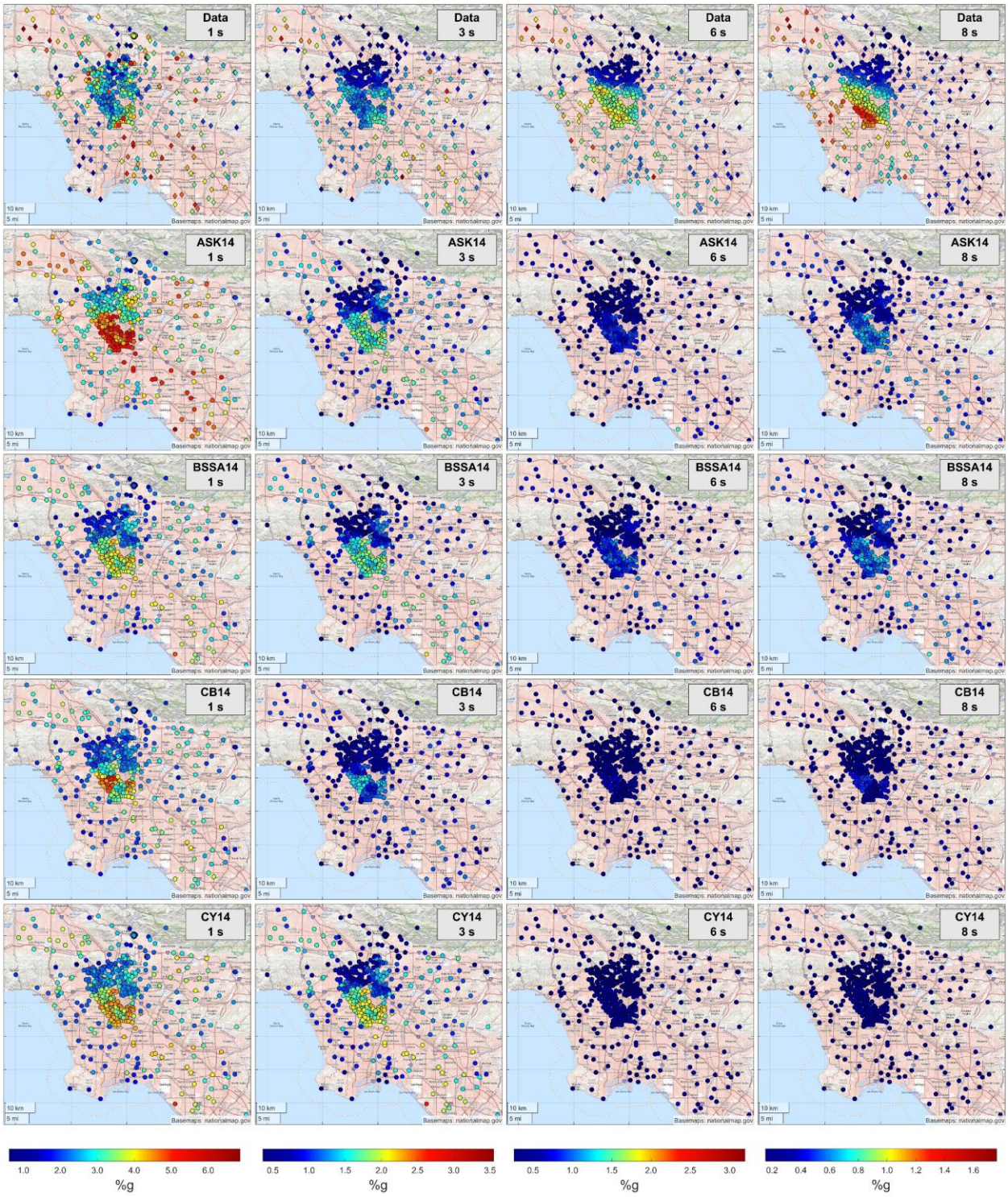

Figure 4.22. Data and model-predicted (GMPEs) RotD50 maps, for the M7.1 event. Column 1: T=1 s, Column 2: T=3 s, Column 3: T=6 s. Column 4: T=8 s. Row 1: Observations, Row 2: ASK14, Row 3: BSSA14, Row 4: CB14, Row 5: CY14. Damping ratio ζ=5%. Each column has a separate colorbar.

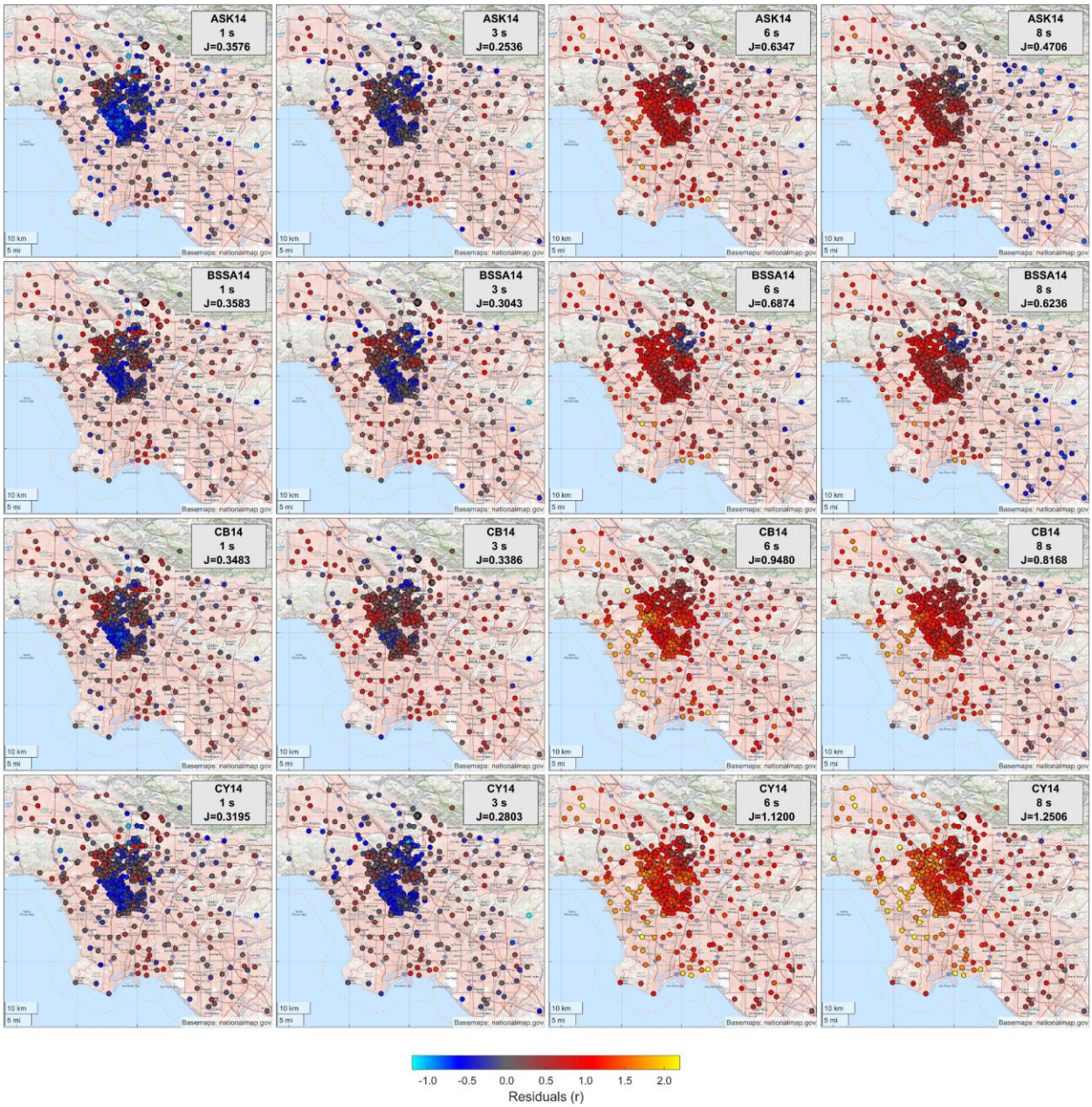

Figure 4.23. Maps of the residuals, calculated according to Eq. (4.6), between model-predicted (GMPEs) and data RotD50, for the M7.1 event. The selected GMPE names and periods are shown in the top right corner of each subplot. The resulting absolute misfit (J), calculated according to Eq. (6), is also indicated in the top right corner of each subplot. The colorbar is the same for all subplots and its range was limited to [-1.2, 2.2] in order to better capture the near-zero overprediction/underprediction variations.

4.6 Spectral Acceleration Prediction Performance Across Profile A-A'

In the previous sections we considered maps of the model predicted RotD50 (Figures 4.20 and 4.22) and the residuals throughout the Los Angeles Basin (Figures 4.21 and 4.23). These maps offer a good overview of the model performance and allow easy comparison for specific areas or stations. A different way of presenting the above results is by considering a profile A-A' going across the Los Angeles Basin. Figure 4.24 displays the observed and predicted RotD50 calculated for the 40 closest stations to this profile. We use only one GMPE here – ASK14, since it had the smallest average absolute misfit (J) in the four considered periods. Figure 4.24A and Figure 4.24B present the depth-to-basement and VS30 profiles along A-A'. The left column shows RotD50 values for periods T=1, 3, 6 and 8 s, and damping ratio 5%, and the right column shows the residuals (calculated from Eq. (4.6)). For the GMPE predictions the points mark the median predicted RotD50, and the error bars mark ±1 standard deviation.

Along our selected profile, the GMPE (ASK14) shows a reasonably good performance for the two shorter periods (T=1 and 3 s), however it mostly underpredicts the RotD50 in the deeper parts of the basin for the longer periods (T=6 and 8 s). For T=3 s the simulations overpredict the basin RotD50 at many stations and their performance is equivalent or worse than the GMPEs. However, for T=6 s the performance of both simulations is superior. For the longest period, T=8 s, the CVM-H simulations suffer from overpredictions, while CVM-S fits the data exceptionally well. Looking at the ±1 standard deviation error bars, one sees the large standard deviations that come with the GMPE predictions. For our data set it is often the case that the GMPE prediction is poor but the observed values fall within the ±1 standard deviation.

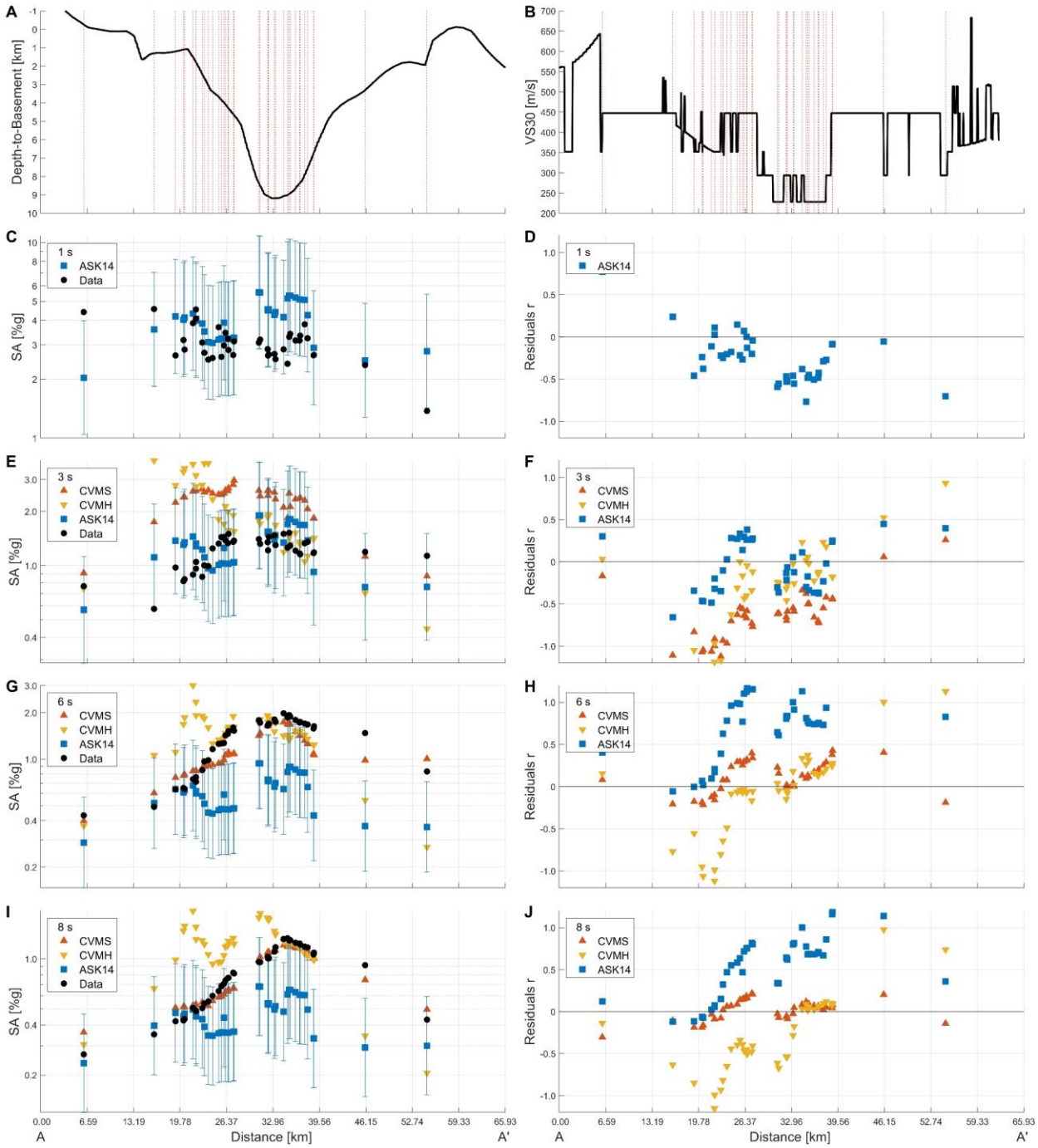

Figure 4.24. Performance along the profile A-A', for the M7.1 event. (A) Depth-to-basement along the profile. (B) Vs30 along the profile. (C-J) Left column: RotD50 values, Right column: Residuals (Eq. (4.6)). (C-D) T=1 s. (E-F) T=3 s. (G-H) T=6 s. (I-J) T=8 s. Damping ratio ζ=5%. Black circles: data, Red Triangles: CVM-S model simulations, Orange triangles (downward-pointing): CVM-H model simulations, Blue squares: ASK14 GMPE predictions. For the GMPE predictions the squares mark the median values and the error bars mark the ±1 standard deviation.

4.7 Conclusions

We constructed assessments of the geographical variability of long-period ground motions in the Los Angeles region during the two largest events of the 2019 Ridgecrest earthquake sequence (M7.1 and M6.4). These are presented in the form of spectral acceleration maps for periods of engineering significance (mainly T=1, 3, 6, and 8 s). Significant ground motion amplification is present in urban Los Angeles and appears to be reproducible between the two events. For the longer periods coherent SA patterns are present throughout the Los Angeles Basin, while for shorter periods the dense CSN instrumentation allows us to see the increased spatial complexity and the smaller length scale pockets of SA amplification. Considering the correlation of the observed ground motions with the site parameters of depth-to-basement and Ss30 (or Vs30), we find little to no correlation exists for the shortest examined period (T=1 s), while a correlation appears at 3 s and gets stronger for the longer periods. This lack of strong correlation suggests that other factors are influencing the response beyond what is captured considering the depth-to-basement and Vs30 parameters alone. These factors are likely related to the complex geologic structure within the basin such as lateral contrasts due to folding and faulting or variability in shallow geologic deposits connected with current and ancient watershed systems.

The SA maps produced from the Ridgecrest data (Figures 4.5 and 4.6) can be used as a simplified measure of the infrastructure response and are structure-type specific by accounting for different fundamental periods. For structures with long periods specifically, amplification of these long-period motions can be hazardous. In urban Los Angeles, the vulnerable long-period structures include high-rise buildings, large-diameter liquid storage tanks, and long-span bridges. The high-rises are mainly located in Downtown Los Angeles. In the Ridgecrest events the downtown area experienced SAs for T=6 and 8 s (Figure 4.5E-H) that were at least a factor of 2 higher than that of hard-rock sites to the north of the basin (e.g., in San Rafael Hills and Mt. Wilson). Large-diameter liquid storage tanks are known to have long fundamental periods due to fluid sloshing and are thus sensitive to these longer periods. For instance, a circular tank with a radius of 25 m and height of 20 m has a period of approximately 8 s (Housner, 1954). Liquid storage tanks are

very common in the Los Angeles Basin, especially in the southern part (near the Port of Los Angeles and oil refineries). During the Ridgecrest earthquakes, this area experienced large SA amplifications at T=8 s relative to the hard-rock sites to the north of the basin. In the case of a larger future event, such amplifications could be critical, possibly even causing severe damage and/or fire in oil storage tanks, similar to what occurred in the city of Tomakomai during the 2003 Tokachi-oki earthquake (Hatayama, 2008).

Several previous studies have also used earthquake records to create amplification maps for the Los Angeles region. Hartzell, et al. (1998) analyzed records from the 1971 San Fernando, 1987 Whittier Narrows, 1991 Sierra Madre, and 1994 Northridge earthquakes and reported Fourier spectra amplification factors relative to a hard-rock site in the Santa Monica Mountains for frequencies down to 1 Hz. Their lowest frequency band of 1-3 Hz (which is roughly comparable with our 1 s maps) shows amplification factors of 3-4 over the deepest portion of the central Los Angeles basin. These results are generally consistent with what we find for the Ridgecrest events.

More recently, Hatayama and Kalkan (2011) utilized recordings for the 2010 El Mayor-Cucapah earthquake to produce long period (4 s and longer) Fourier spectra amplification maps throughout the Los Angeles region. For their longest periods (8 and 10 s), they found a broad zone of strong amplification over the central Los Angeles basin with a maximum amplification of 5 relative to their reference hard-rock stations. At periods of 4 and 6 s the amplification patterns become more complex with several local maxima within the basin. The largest amplification factor they found was 10 at 6 s period in a region located along the western margin of the Los Angeles basin near (e.g., Manhattan Beach). They also compared the amplification patterns with depth to various isovelocity surfaces within CVM-H and found good correlation of increased amplification with large isovelocity surface depth for periods of 8 and 10 s, but much lower correlation at the shorter periods. Due to inherent differences in Fourier spectra and response spectral acceleration, it is difficult to directly compare our results to these. Nonetheless the general trends and observations are consistent with our findings, including the strong 6 s amplification found along the western margin of the LA basin, which shows little correlation with depth-to-basement in the current CVMs.

As data from new events become available and with the station density and numbers ever increasing, the resulting intensity measure maps will continue to evolve in accuracy and spatial resolution. It is important that maps constructed from observations are considered for pre-earthquake structure design and infrastructure planning, since there is not always a clear correlation between the measured intensities and the commonly-used site parameters.

In recent years there is a growing effort for site-specific seismic hazard analysis, with documents such the Alternative Analysis & Design Procedure guidelines published by the Los Angeles Tall Building Seismic Design Council (LATBSDC, 2008), and projects such as SCEC's Committee for Utilization of Ground Motions Simulations (UGMS) (e.g., Crouse, et al., 2018). We hope that this work will bring attention to the shortcomings of the currently used site parameters (Z1.0, Z2.5, and Vs30) and CVMs. The refinement of these parameters and models in light of new dense data is essential and will benefit greatly existing guidelines and projects.

In the second part of the study, we examined the performance of 2D ground-motion simulations using two different velocity models (CVM-S and CVM-H), as well as the performance of four NGA-West2 GMPEs, using the data collected from the M7.1 main shock. The agreement between the observations and the model predictions is generally good but there is room for improvement. Comparing the two velocity models we find that CVM-S is superior for the longer periods (T=6 and 8 s), while CVM-H performs better for T=3 s. The differences in the ground motion simulations can be associated with the different representations of the two velocity models for the Los Angeles Basin. The GMPEs suffer from underpredictions for the longer periods, while it is often the case that a GMPE performing well for one period does a poor job at a different period. Comparing the simulations with the GMPEs, one potential benefit of the simulations is that they produce full waveforms that can also be used for further studies and dynamic analyses (e.g., Krishnan, et al., 2006). For T=3 s, the GMPEs perform better, while for the longer periods (T=6 and 8 s), the simulations perform better than the GMPEs. While both simulations and GMPE estimates often reproduce the general amplitudes and trends of the ground-motion response, they have trouble capturing the finer-scale spatial variations of the observed response, as well as

matching the specific locations of the maximum amplifications. This stresses the need for caution and further validation when employing these methods in order to predict ground motion response.

4.A Appendices

4.A.1 Calculation of the RotD50 and RotD100 Intensity Measures

The RotD50 and RotD100 intensity measures as defined by Boore (2010) are computed as follows. Since the system is linear the oscillator displacements in the two horizontal directions ($u_x(t)$ and $u_y(t)$) are combined into a single time series corresponding to a rotation angle θ using the equation

$$u_{cmb}(t,\theta) = u_x(t)cos\theta + u_y(t)sin\theta. \tag{4.10}$$

The pseudo-spectral acceleration corresponding to the combined time series is

$$PSA_{cmb}(T,\zeta,\theta) = \omega^2 \max_t(|u_{cmb}(t,\theta)|)\,. \tag{4.11}$$

RotD50 is the median pseudo-spectral acceleration over all rotation angles

$$RotD50(T,\zeta) = \text{median}_\theta\{PSA_{cmb}(T,\zeta,\theta)\} \tag{4.12}$$

and RotD100 is the maximum pseudo-spectral acceleration over all rotation angles

$$RotD100(T,\zeta) = \max_\theta\{PSA_{cmb}(T,\zeta,\theta)\}\,. \tag{4.13}$$

4.A.2 Equivalence of the SA and RotD100 Intensity Measures

In the following we show that SA (Eq. (4.3)) and RotD100 (Eq. (4.13)) are equivalent intensity measures and that their orientation is the same. From Eqs. (10) and (7) we get

$$RotD100 \;=\; \omega^2\, max_\theta\left\{max_t\left\{\left|u_x(t)cos\theta + u_y(t)sin\theta\right|\right\}\right\} \tag{4.14}$$

$$=\; \omega^2\, max_t\left\{max_\theta\left\{\left|u_x(t)cos\theta + u_y(t)sin\theta\right|\right\}\right\}. \tag{4.15}$$

The non-redundant rotations involve $\theta \in [0, 180^o]$. Let $u_x(t) = r(t)cos\psi(t)$ and $u_y(t) = r(t)sin\psi(t)$. Then $r(t) = \left({u_x}^2(t) + u_y^2(t)\right)^{1/2}$ and $\psi(t) = arctan\left(\frac{u_y(t)}{u_x(t)}\right)$. Thus, we get

$$|u_x(t)cos\theta + u_y(t)sin\theta| = |r(t)(cos\psi(t)cos\theta + sin\psi(t)sin\theta)| \tag{4.16}$$

$$= r(t)\left|cos\left(\theta - \psi(t)\right)\right| \leq r(t)\,. \tag{4.17}$$

Since $\theta \in [0, 180^o]$, for each time t there exists a rotation angle $\theta(t)$ for which $|cos\left(\theta(t) - \psi(t)\right)| = 1$ which occurs for

$$\theta(t) = \psi(t) = arctan\left(\frac{u_y(t)}{u_x(t)}\right) \tag{4.18}$$

and gives

$$max_\theta|u_x(t)cos\theta(t) + u_y(t)sin\theta(t)| = r(t) = \left(u_x^2(t) + u_y^2(t)\right)^{\frac{1}{2}}. \tag{4.19}$$

Thus from Eq. (4.15) after maximizing with respect to θ we get

$$RotD100 = \omega^2\, max_t\left\{\left(u_x(t)^2 + u_y(t)^2\right)^{1/2}\right\} \tag{4.20}$$

which is exactly the same as the SA measure defined in Eq. (1). Furthermore, the time t_m at which this maximum occurs corresponds to rotation angle $\theta(t_m)$ given by Eq. (4.18) with t replaced by t_m and thus corresponds to the angle φ defined by Eq. (4.5) for the SA measure.

4.A.3 Long Period Ground Accelerations Along Two Profiles

The following figures present ground acceleration (NS components) along two profiles. After the usual processing (described in Section 4.1), the ground accelerations were further filtered by a band-pass Butterworth filter with cutoff frequencies 1/8 Hz and 1/4 Hz effectively keeping only the longer period ground motions.

The x’x profile goes from sites in the San Gabriel Hills to the dense instrumentation deeper in the basin. Figure 4.25A displays the profile and the selected stations. The 10 nearest stations to the x’x line segment were selected. Figure 4.25B displays the depth to basement along the profile, which is calculated using nearest neighbor interpolation of the grid points provided by Shaw, et al. (2015). The long period ground accelerations for the selected stations are shown in Figure 4.26.

The y’y profile goes across the JPL campus. The JPL campus densely instrumented by the CSN, with the average station spacing being about 50m. Figure 4.27A displays the profile and the selected stations. Figure 4.27B displays the depth to basement along the profile. The long period ground accelerations for the selected stations are shown in Figure 4.28.

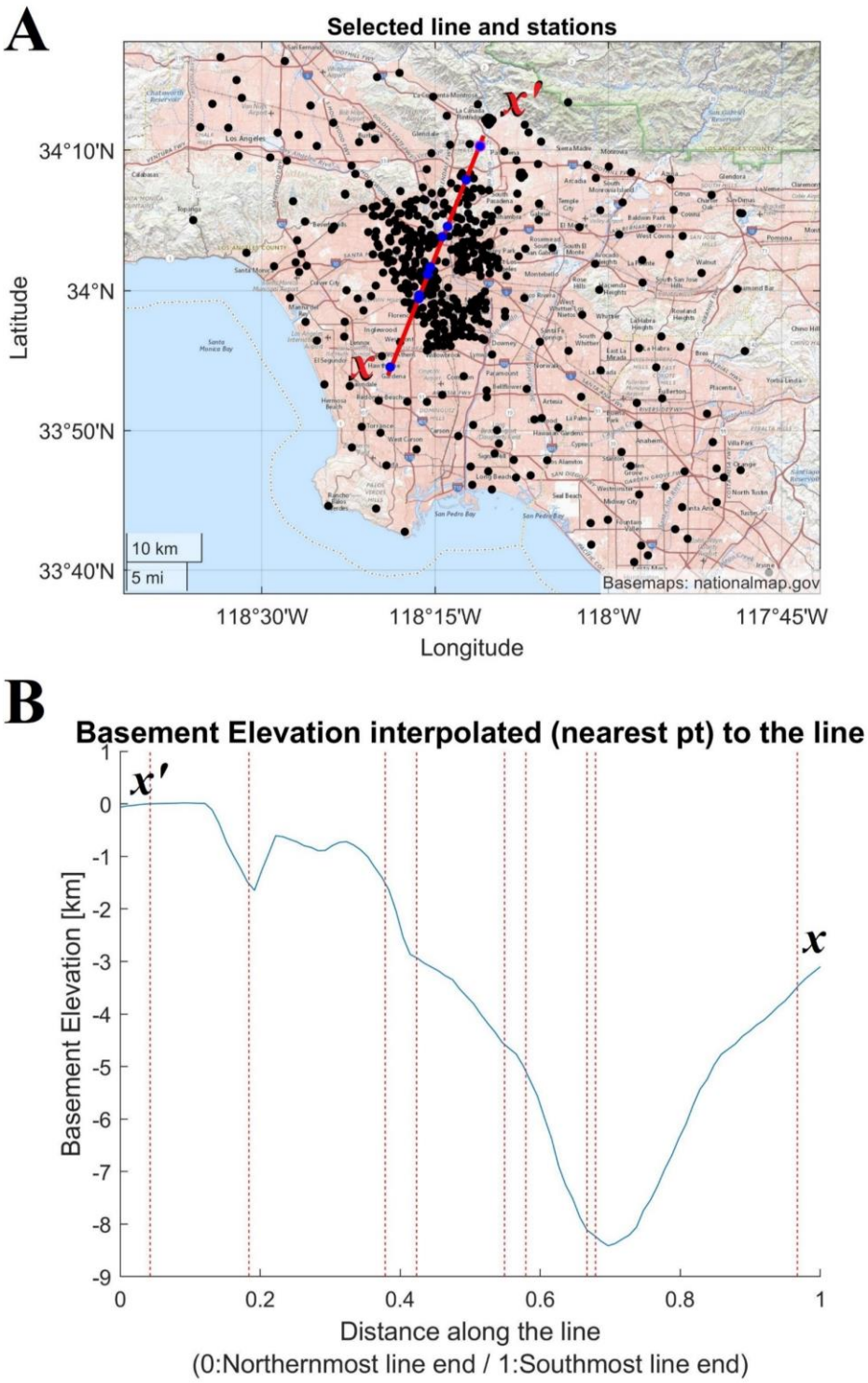

Figure 4.25. The selected x'x profile. (A) The profile and the selected stations. (B) The depth to basement along the profile. The red vertical lines denote the selected station location projections into the profile.

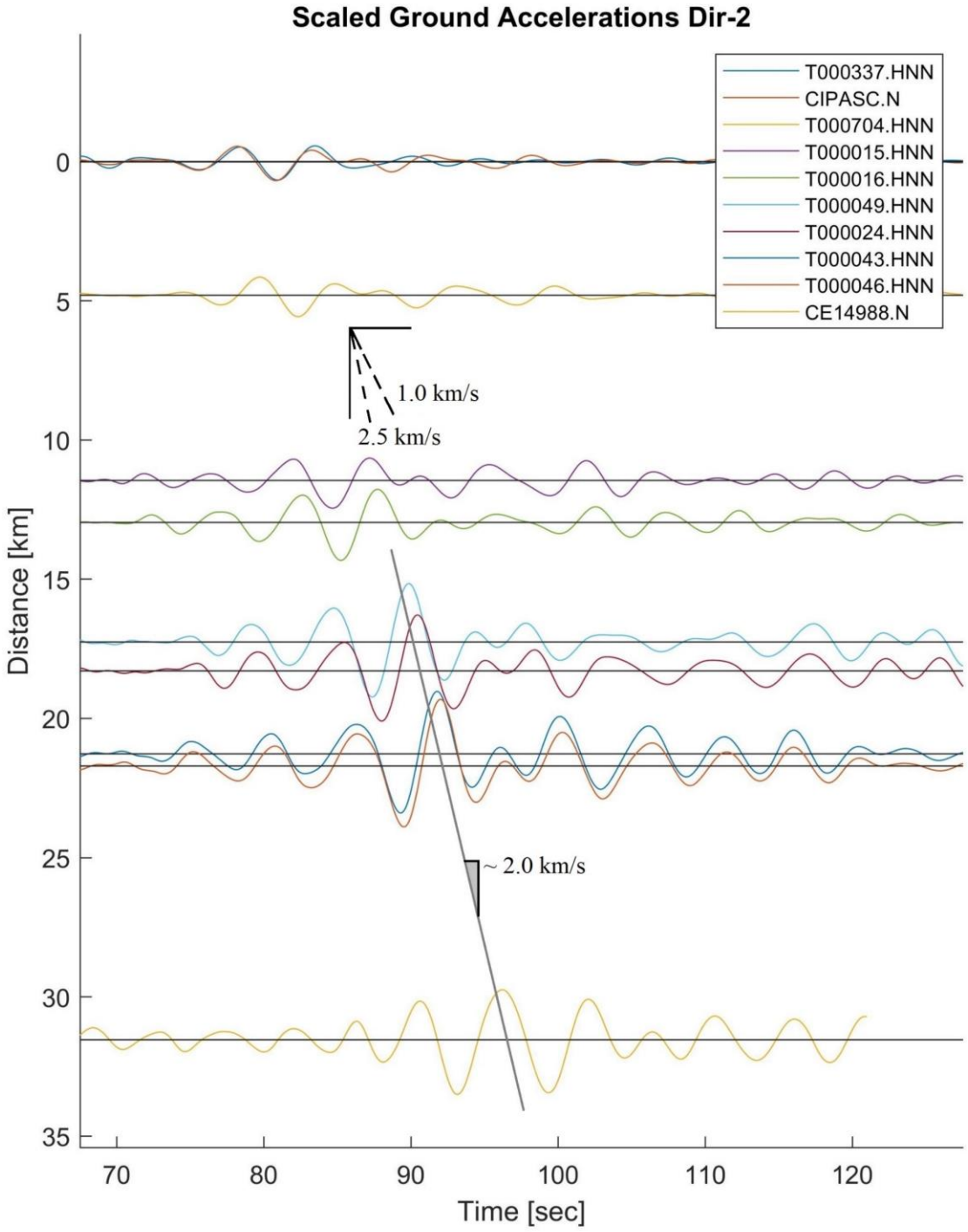

Figure 4.26. Long period ground accelerations along profile x'x. N-S components.

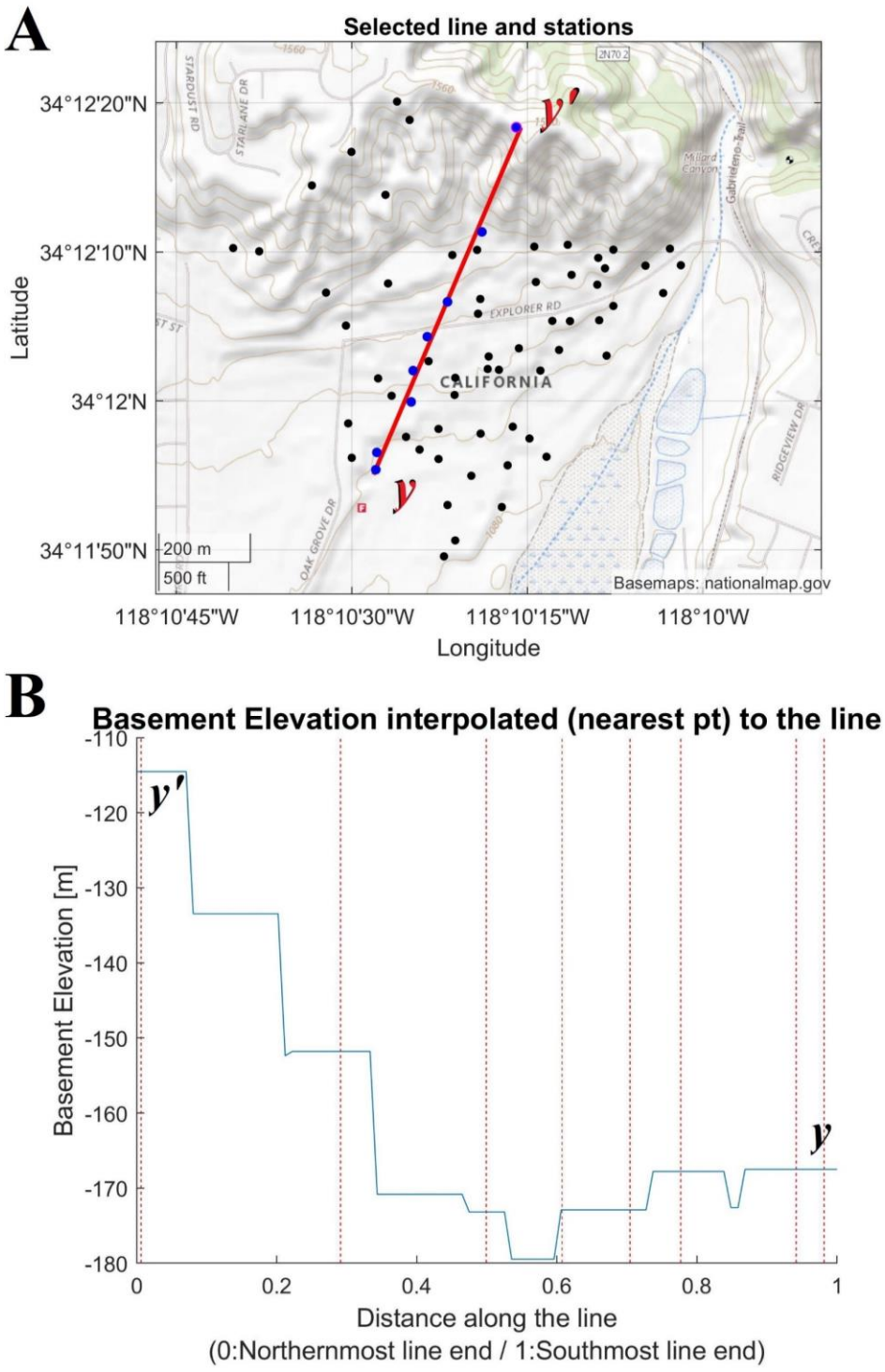

Figure 4.27. The selected y'y profile. (A) The profile and the selected stations. (B) The depth to basement along the profile. The red vertical lines denote the selected station location projections into the profile.

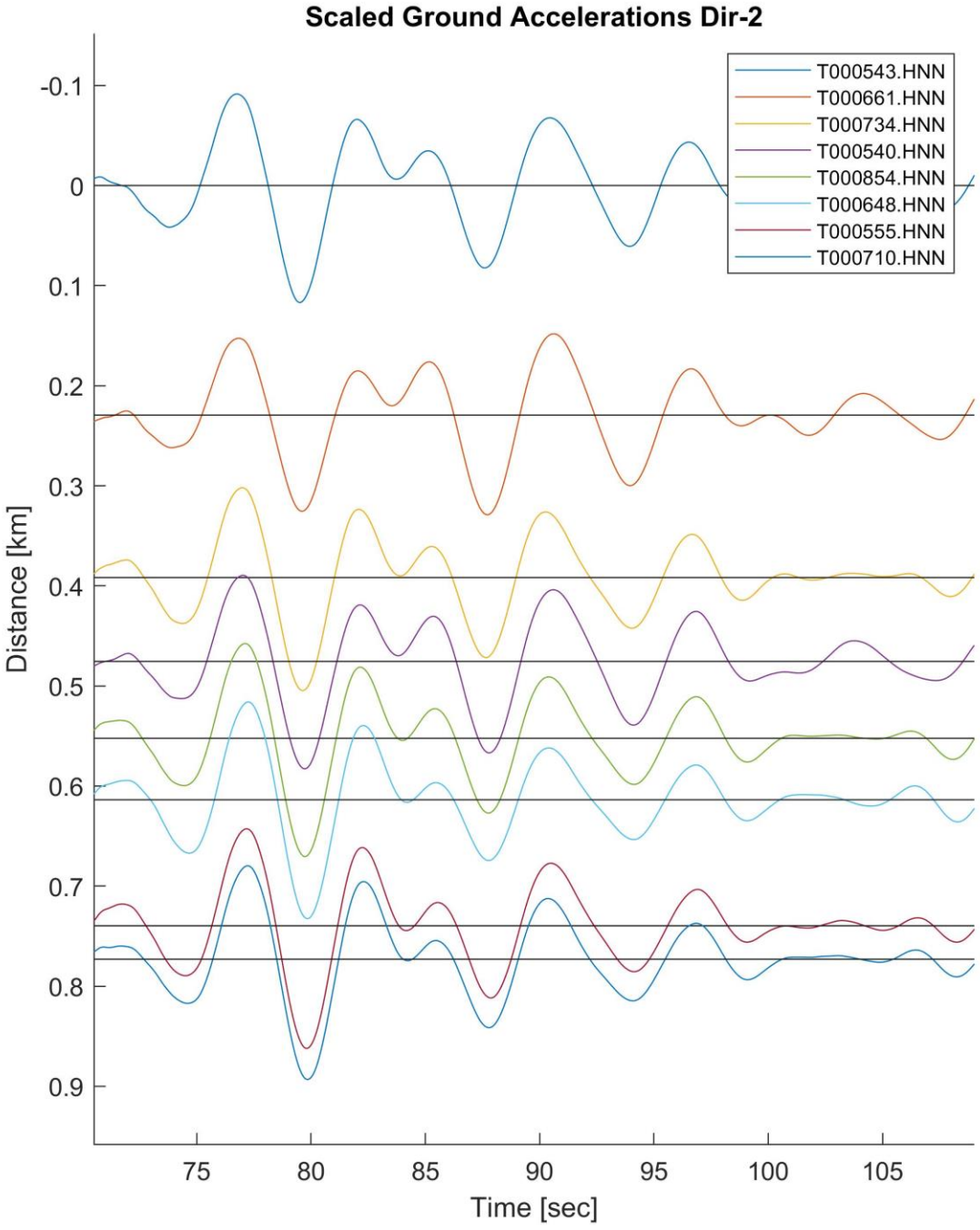

Figure 4.28. Long period ground accelerations along profile y'y. N-S components.

4.A.4 SA Maps for 2% Damping Ratio

A 2% damping ratio is more appropriate when the response of mid- or high-rise structural systems is of interest. For 2% damping the amplitudes are overall higher but the trends and behavior are similar to those observed and discussed for the 5% damping (Figures 4.5 and 4.6).

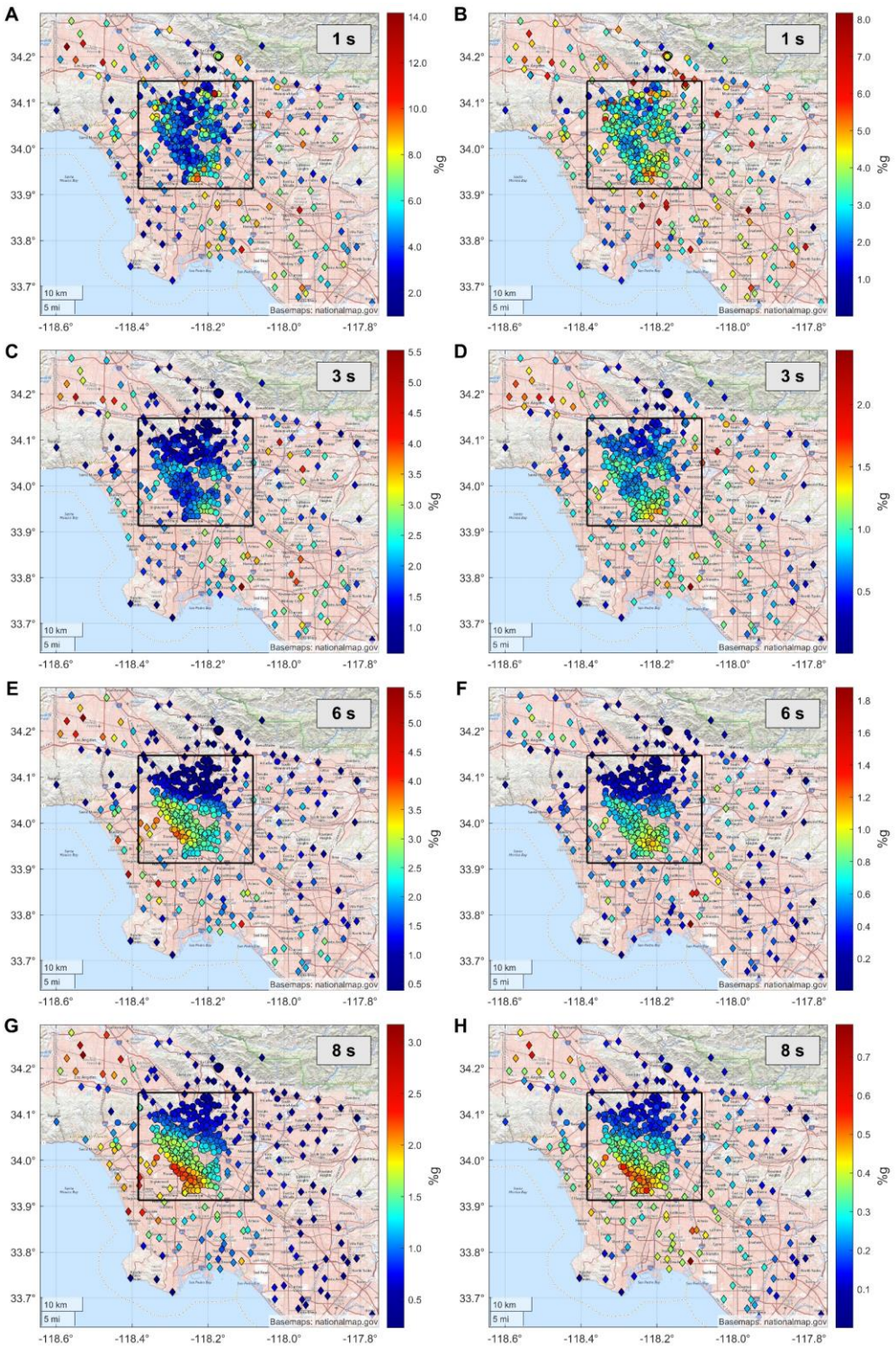

Figure 4.29. SA maps. Damping ratio ζ=2%. Left column: M7.1 Event. Right column: M6.4 Event. (A-B) T=1 s. (C-D) T=3 s. (E-F) T=6 s. (G-H) T=8 s. Circles: CSN stations, Diamonds: SCSN & CSMIP stations. The region inside the black rectangle is magnified in Figure 4.30. Note varying colorbar amplitude scales.

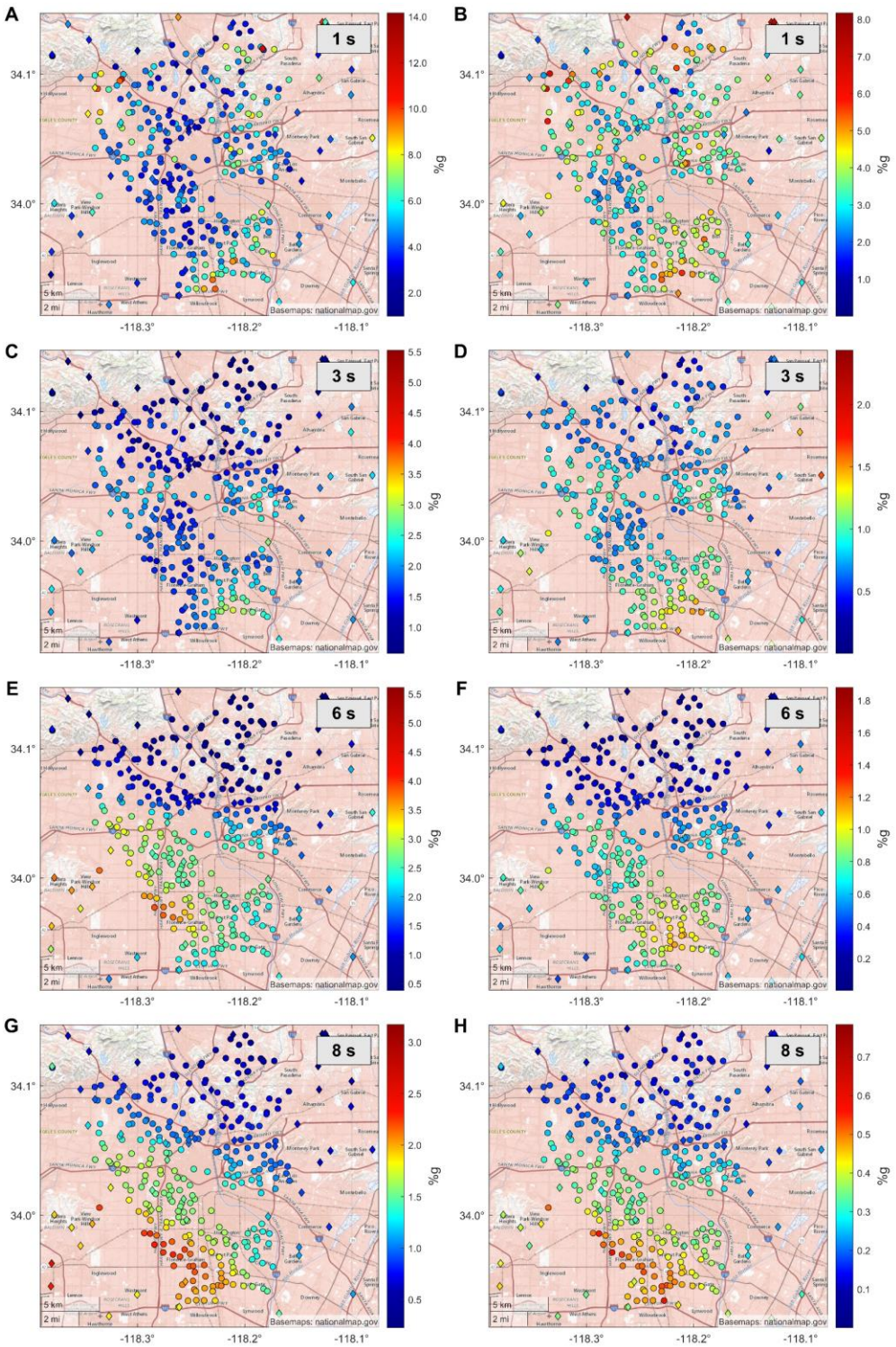

Figure 4.30. SA maps showing detail in the region marked by the black rectangle in Figure 4.29. Damping ratio ζ=2%. Same format as Figure 4.29.

4.A.5 RotD50 Maps for 5% Damping Ratio

Since RotD50 is the median pseudo-spectral acceleration over all rotation angles rather than the maximum the amplitudes are overall lower when compared with the 5% critical damping SA maps. However the trends and behavior are again similar to those observed and discussed for the 5% critical damping SA maps (Figures 4.5 and 4.6).

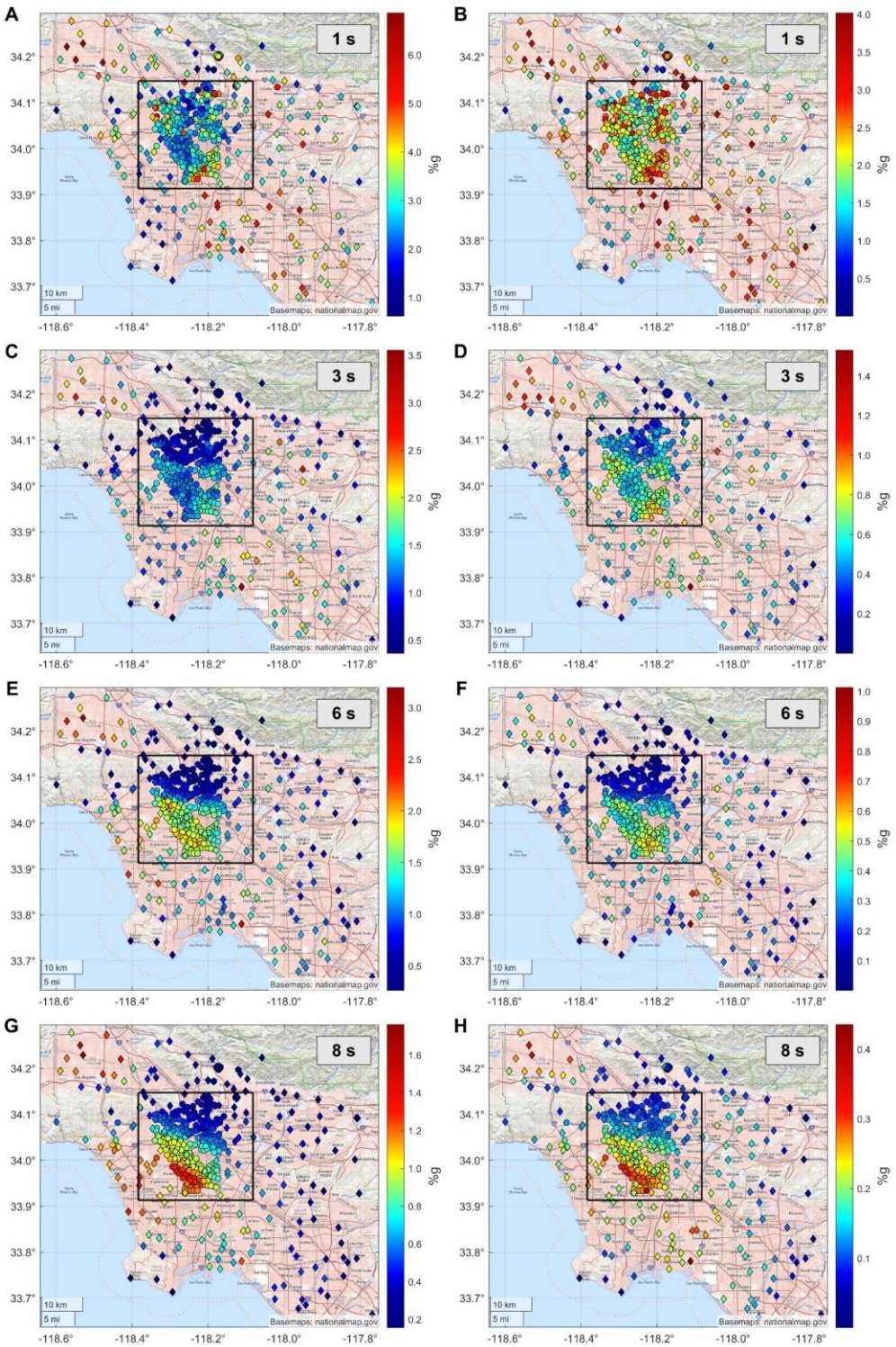

Figure 4.31. RotD50 maps. Damping ratio ζ=5%. Left column: M7.1 Event. Right column: M6.4 Event. (A-B) T=1 s. (C-D) T=3 s. (E-F) T=6 s. (G-H) T=8 s. Circles: CSN stations, Diamonds: SCSN & CSMIP stations. The region inside the black rectangle is magnified in Figure 4.32. Note varying colorbar amplitude scales.

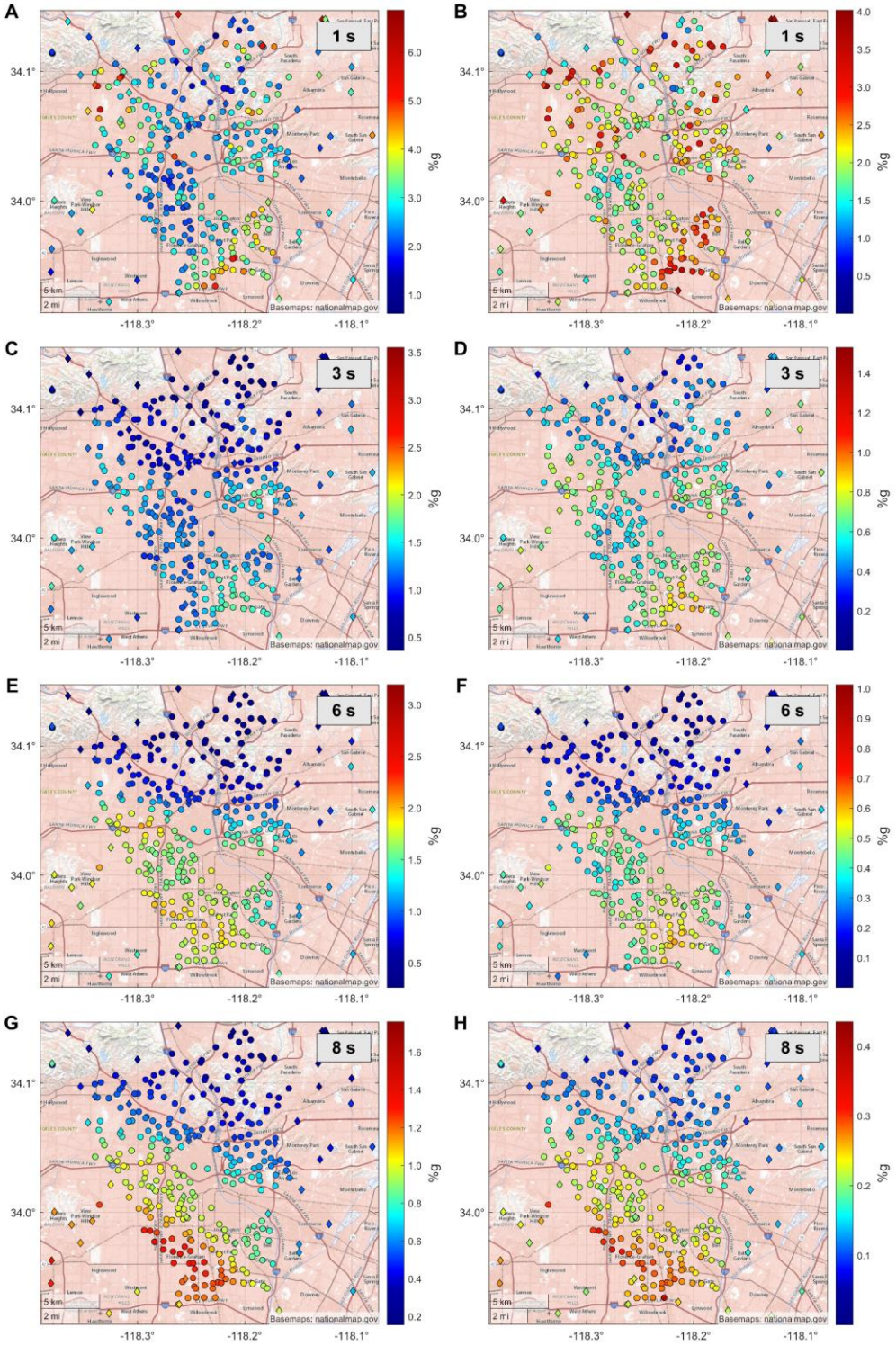

Figure 4.32. RotD50 maps showing detail in the region marked by the black rectangle in Figure 4.31. Damping ratio ζ=5%. Same format as Figure 4.31.

4.A.6 GMPE Predicted RotD50 Against Distance

In Figure 4.33 we present plots of the GMPE predicted RotD50 as a function of distance from the fault only (distance range: 1-350 km). A Vs30 equal to 300 m/s (representative of a soft soil site) and a right lateral strike slip was assumed. Here in contrast to what was done in Section 4.4 the Vs30 is constant for all points and the depths Z1.0 and Z2.5 are assumed unknown. The five lines correspond to the five NGA-West 2 GMPEs: ASK14 (Abrahamson, et al., 2014), BSSA14 (Boore, et al., 2014), CB14 (Campbell & Bozorgnia, 2014), and CY14 (Chiou & Youngs, 2014). The fifth GMPE (Idriss, 2014) is not plotted in the Section 4.5 maps, since it is not applicable for the source-to-site distance and Vs30 ranges of our sites (Gregor, et al., 2014).

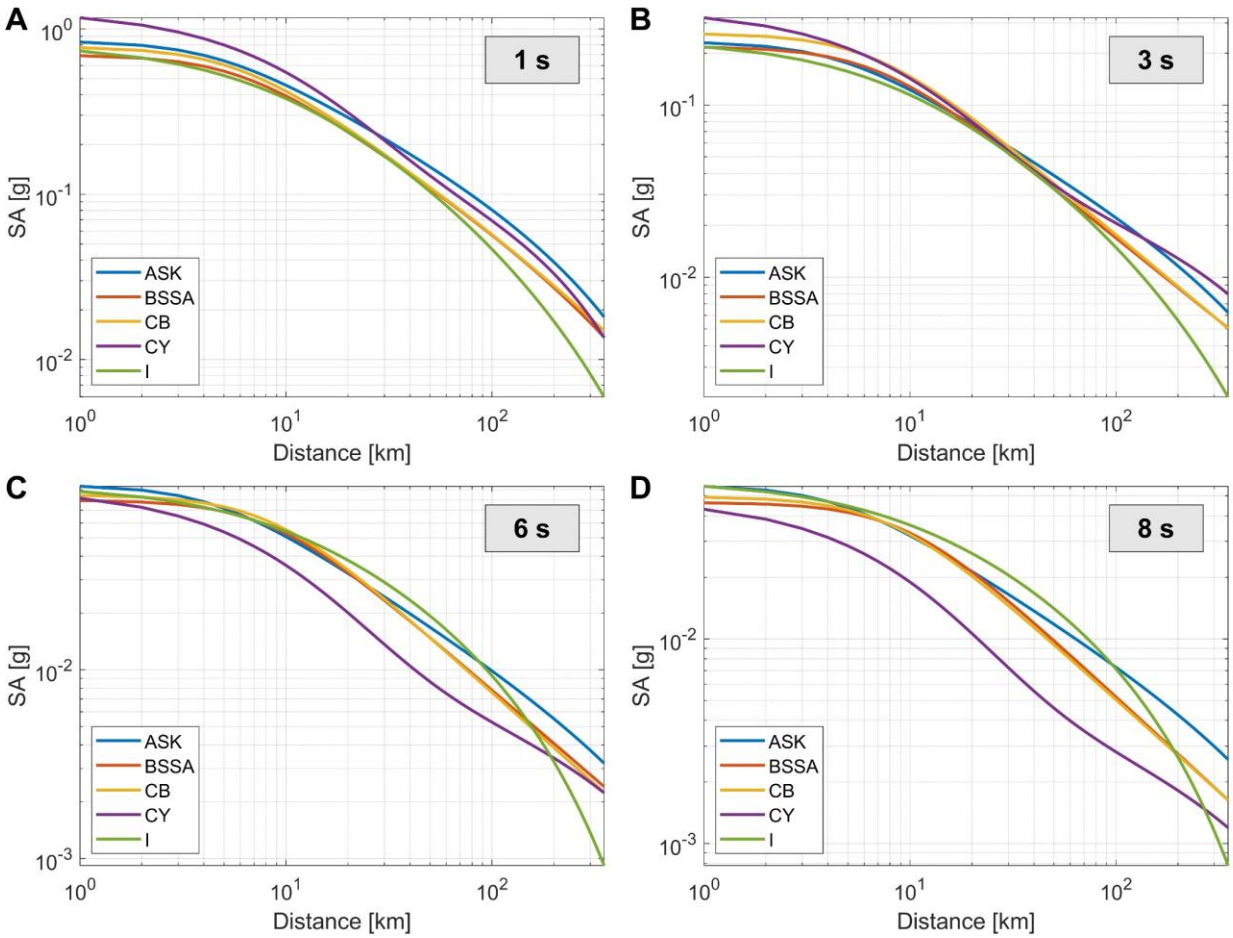

Figure 4.33. GMPE predicted RotD50 as a function of distance only for a soft soil site. M7.1 earthquake. Periods shown: (A) 1 s; (B) 3 s; (C) 6 s; and (D) 8 s.

In Figure 4.34 we present plots of the GMPE predicted RotD50 versus distance for the area of interest. Here, as it was done for Section 4.4, each point corresponds to a station and together with the distance from the station to the fault, the station's Vs30 (from Thompson, 2018) and its Z1.0 and Z2.5 (from the CVM-H velocity model) are also taken into account.

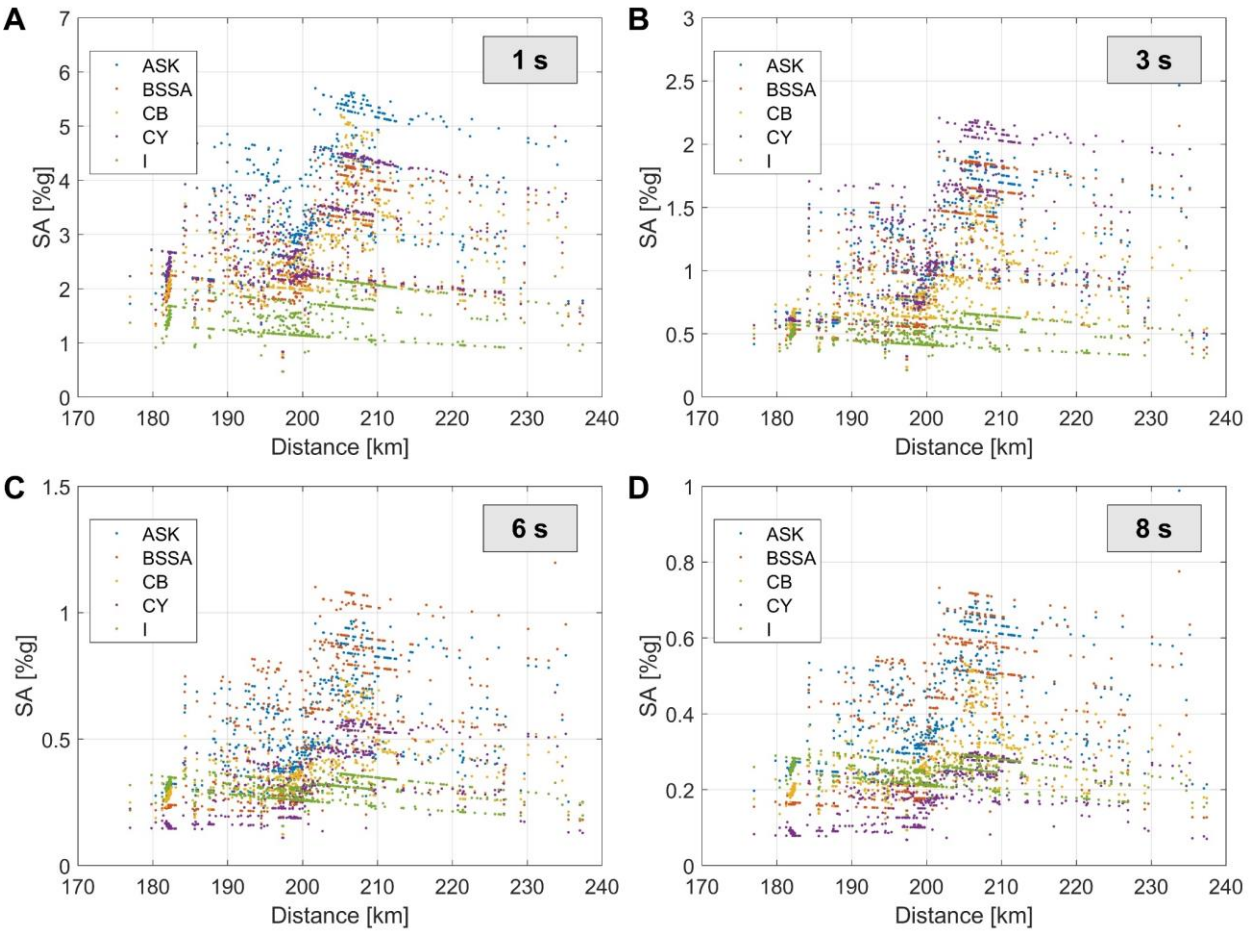

Figure 4.34. GMPE predicted RotD50 for the sites considered in the study. The site distance to the fault, Vs30 and Z1.0 or Z2.5 are considered. M7.1 earthquake. Periods shown: (A) 1 s; (B) 3 s; (C) 6 s; and (D) 8 s.

4.A.7 Data and Resources

The data from the Community Seismic Network (CSN) stations for the two Ridgecrest events is publicly available through the CSN website at http://csn.caltech.edu/data/. The Southern California Seismic Network (SCSN) data was accessed through the Southern California Earthquake Data Center (SCEDC) and are available at https://scedc.caltech.edu/. The California Strong Motion Instrumentation Program (CSMIP) data was accessed through the Center for Engineering Strong Motion Data (CESMD) and are available at https://strongmotioncenter.org/. All data used in this study from the three above sources is also archived on the SCEDC data center and can be accessed at https://scedc.caltech.edu/research-tools/ridgecrest-info.html. The topographic background base maps were made available by the U.S. Geological Survey's (USGS) National Geospatial Program and were accessed from https://basemap.nationalmap.gov/. The regional basement surface and major faults data are provided by Southern California Earthquake Center's (SCEC) Unified Structural Representation (USR) and are available at SCEC's GitHub repository https://github.com/SCECcode/. The Vs30 data are released by USGS and were accessed through https://www.sciencebase.gov/catalog/. The 3D seismic velocity models were accessed using the SCEC Unified Community Velocity Model (UCVM) software, version 19.4.0 (https://github.com/SCECcode/UCVMC/wiki/).

Chapter 5

CONCLUSIONS AND OUTLOOK

5.1 Conclusions

The thesis is organized in two parts. The first part deals with the development of structural identification algorithms based on finite element model updating, using response time histories recorded from dense sensor networks installed in buildings. Techniques are developed (a) for tracing the nonlinear characteristics of buildings by estimating the stiffness and damping ratios of equivalent linear finite element models using a moving time window approach, and (b) for identifying the location and extent of damage due to deterioration from cracks developed in one or more connections between floor beams and columns.

The second part of this thesis deals with a study of the recorded and model predicted ground motions in urban Los Angeles from the two largest events (M7.1 and M6.4) of the 2019 Ridgecrest earthquake sequence, using recordings from the very dense Community Sensor Network (CSN) as well as from multiple regional seismic networks. We produce maps of the response spectral accelerations for a selection of periods of engineering significance and study possible correlations of the computed response spectral accelerations with the geophysical parameters of basement depth and Vs30. Furthermore, we test the performance of methods for estimating the response spectral accelerations for the largest event (M7.1) of the Ridgecrest earthquake sequence, namely 3D finite difference simulations and ground motion prediction equations. We produce maps of the estimated response spectral accelerations and compare them with the observations.

The contributions of the first part of this work are summarized as follows.

- We introduced a deterministic structural identification approach in order to explore the possibility of estimating the condition of a steel frame structure and tracing possible nonlinear softening behavior, through the updating of the stiffness properties and modal damping ratios

of an equivalent linear finite element model over short segments of the recorded earthquake response using a moving time window approach. Results using simulated response time history data generated from different intensity scales of a seismic event demonstrate the promise of the presented approach and its limitations due to model error. Model error is introduced not only from the difference between the model and the actual system but also from the stiffness-related parameterization considered. To avoid ill-conditioning over the different segments in the moving time window approach, arising from the fact that the information in the data is inadequate to estimate all the model parameters, the number of stiffness-related parameters have to be kept small and the number of used modes has to be limited to the contributing ones. The proposed method can be seen as an alternative to the two-stage finite element model updating methods available in the literature.

- We developed a Sparse Bayesian Learning (SBL) technique for damage identification in buildings, integrating nonlinear models of buildings with response time history data recorded from a dense sensor network installed on buildings, similar to the ones deployed by the CSN. The SBL method is based on the premise that damage is sparse, manifested in a small number of elements in a structure or small number of floors in a high-rise building. The proposed method extends existing SBL techniques which, since they rely on processing measurements related to modal properties, are limited to linear models for describing the damage through changes in stiffness properties. We have shown that the two-step iterative optimization algorithm, arising in the SBL technique for estimating iteratively the optimal values of the model parameters in the first step and the optimal values of the hyperparameters in the second step, is equivalent to a single-objective optimization with respect to the model parameters. The developed SBL technique is generally applicable to other civil and mechanical structures with damages that are described by parameterized linear and nonlinear models and undergo sparse damage.

- The parameters in our proposed method are related to nonlinear properties of the finite element model of the structure. Specifically, the nonlinearities in this study are associated with the

stiffness in tension of fiber elements and are introduced in order to allow for more realistic modeling of the damage due to weld cracking. The effectiveness of the SBL technique was successfully tested in a virtual environment by applying it to simulated data generated from an OpenSEES nonlinear finite element model of a 15-story, three-dimensional, steel-frame building. The nonlinearities are introduced at the floor beam corner elements of the building. The SBL algorithm was shown to be very promising in identifying the location and extent of damage for various sparse damage scenarios associated with cracks and under the presence of significant model error. The systematic study carried out revealed the strengths of the proposed method to successfully identify the location of damage, as well as the extent of damage, for small to moderate model errors. For large model errors the identification of the location of damage was in most cases successful with a number of false alarms manifested in undamaged locations. The extent of damage identified in the locations where damage was introduced was close to the inflicted damage, while the discrepancy between the identified and inflicted magnitude of damage depends on the size of the model error considered. It is also found that one or two biaxial sensors per floor are sufficient to identify the damage in a floor and even the damaged side in a floor, but floor measurements alone do not seem to be adequate to pinpoint the beam end that may be damaged. The identified location and size of damages due to developed cracks can be incorporated into nonlinear finite element models to update predictions of important structural response quantities of interest, such as stresses and interstory drifts.

The contributions of the second part are summarized below.

- We constructed assessments of the geographical variability of long-period ground motions in the Los Angeles region during the two largest events of the 2019 Ridgecrest earthquake sequence in the form of response spectral acceleration maps. The produced maps can be used as a simplified measure of the infrastructure response and are structure-type specific by accounting for different fundamental periods. The maps reveal significant ground motion amplification present in urban Los Angeles. For structures with longer periods (e.g., high rise

building or large diameter liquid storage tanks) such amplifications could be hazardous, and the maps reveal areas where the existence of such structures would be dangerous. Our findings regarding the observed spectral amplification patterns agree with the site amplification patterns observed in previous studies of the ground response urban Los Angeles, as it was discussed in more detail in Section 4.7. Nonetheless, the extremely high spatial resolution of the maps, attributable to the CSN, is unprecedented for the area of urban Los Angeles. A correlation between the observed spectral accelerations from two events exists for all examined periods (T=1, 3, 6, and 8 s) and the correlation gets stronger for the longer periods. For the longer periods coherent patterns which appear to be correlated to the larger scale basin structure and soil properties are visible throughout the whole Los Angeles Basin. For the shorter periods the motions are stronger and less spatial coherent; however, the high spatial density, due to CSN, is able to capture a smaller scale coherence. Furthermore, we examined possible correlations of the computed SA with two common geophysical parameters: basement depth and Vs30, and found no significant correlation for the 1 s period, while a correlation appears and gets stronger for longer periods.

- We tested the performance of two state-of-the-art methods for estimating ground motions for the largest event (M7.1) of the 2019 Ridgecrest earthquake sequence, namely 3D finite difference simulations and ground motion prediction equations. The agreement between the observations and the model predictions is generally good but there is room for improvement. For the simulations, we were interested in the performance of the two Southern California Earthquake Center 3D Community Velocity Models (CVM-S and CVM-H). Comparing the two velocity models we find that CVM-S performs better for the longer periods (T=6 and 8 s), while CVM-H performs better for T=3 s. The differences in the ground motion simulations can be associated with the different representations of the two velocity models for the Los Angeles Basin. For the Ground Motion Prediction Equations, we considered four of the 2014 Next Generation Attenuation-West2 Project equations. The GMPEs produce a wide range of estimates. It is often the case that a GMPE performing well for one period does a poor job at a different period. For the longer periods (T=6 and 8 s) all GMPEs suffer from under-predictions throughout the entire Los Angeles Basin.

5.2 Outlook

Related to structural damage identification studies carried out in this thesis, several extensions of this work are possible.

- The findings in Chapter 3 may motivate field studies on actual buildings as well as systematic studies in controlled laboratory environment on small-scale buildings to verify the effectiveness of the proposed method with real data. The dense instrumentation in selected high-rise building in the Los Angeles area, provided from the CSN network, could offer this opportunity in the future, provided damage occurs during strong ground motion. The availability of such data will actually test the performance of the method under actual model and measurement errors and not the artificial model and measurement errors induced in this thesis. This will really be a challenging task since other type of model errors include also the variabilities arising from environmental effects (e.g. temperature), as well as mass distribution in the building which may not remain constant over time. Moreover, laboratory experiments on small-scale building or other structures with inflicted cracks can be performed on shaking tables to verify the effectiveness of the proposed SBL technique. The advantage of the small-scale experiments is that one can control the inflicted damage in a laboratory setting, study different damage scenarios, and inflict different model errors by mass distributions. Such systematic studies using actual structures and data, and not under a virtual environment, will be invaluable to test the effectiveness of the proposed algorithms, their limitations and the conditions under which damage can be identified.

- In light of the difficulties for damage identification due to large model error, it is expected that the simultaneous processing of the damage identification information from multiple low intensity seismic aftershocks may provide more robust estimates of the damage locations. For this, a possible future direction is to extend the SBL method to handle the processing of multiple low intensity earthquake datasets.

- Another possible direction is the extension of the SBL algorithm developed in Chapter 3 to identify damage during strong ground motion which activates the nonlinear hysteretic characteristics of the material used in buildings. This requires a model that includes the hysteretic nonlinearities activated during strong motion. Once such models are incorporated into the algorithm, the application of SBL is straightforward. Along the direction of investigating the capabilities and the limits of the SBL algorithm for structural damage identification one can apply the algorithm to handle different material degradation mechanisms that may be activated at localized locations and involve more than one parameters per damage location. However, due to activation of the extra hysteretic nonlinearities in a large number of beam and columns, the computational time required to perform one model simulation is expected to substantially increase and therefore the time-to-solution provided by the SBL will drastically increase. To tackle the excessive computational effort, one should further investigate parallelizing the processes involved in the SBL algorithm (using parallel computing servers instead of a personal computer).

- The results in this study suggest that increasing the number of sensors per building floor does not necessarily improve damage identification capabilities for the specific type of damage considered. This may also suggest that it might not be necessary to instrument all floors of a building, depending always on the type of analysis that needs to be performed. A systematic study that will also be useful in a cost-effective design of dense sensor network to be installed in civil infrastructure components (e.g. building, bridges, offshore structures), like the future expansion of the CSN to cover additional civil infrastructure, is the optimization of the sensor network in terms of the number and location of sensors in the structure. Optimal design of the sensor network is useful for cost-effective reliable monitoring of the structure for identifying the location and extent of damage. It is believed that such a design will depend on the type of the infrastructure component, the type of damage expected during a seismic event, and the excitation characteristics.

Related to the ground motion response studies using the dense seismic networks installed in urban Los Angeles the following ideas can be further pursued.

- While our study of the ground response in urban Los Angeles did involve investigating the amplification of the spectral acceleration of a site relative to the average spectral acceleration of several bedrock site, we did not explore site amplifications per se. The computed amplification of the spectral acceleration apart from site effects also includes the effects of the source, as well as the effects of the wave propagation across the basement/sediment interface and through the deep sediments of the basin. When the earthquake source is distant, like for our case, the different effects of source, path, and site are known to be more easy to separate (Rogers, et al., 1984). Separating the site effects is possible through the use of one or more site estimation techniques. Some example site estimation techniques include the reference-site spectral ratio method (Borcherdt, 1970; Borcherdt & Gibbs, 1976) and the source-site spectral inversion method (Andrews, 1986; Hartzell, 1992). A comparison of various site-response estimation techniques is also provided by Field and Jacob (1995). This could be considered as a follow up study (using the data collected from the two events but also from smaller events of the Ridgecrest sequence) and could possibly give a clear (and high spatial resolution) picture of the site amplification in urban Los Angeles, directly comparable with past site amplification studies (e.g., Rogers, et al., 1985; Harmsen, 1997; Hartzell, et al., 1998).

- In Section 4.3.1 we presented maps of the observed spectral acceleration recorded by the CSN deployment in the campus of the Jet Propulsion Laboratory (JPL) for a selection of periods between 0.1 and 8 s. The dense CSN instrumentation allowed the observation of a smaller length scale coherence over the 0.5, 0.8, and 1 s periods. To the north the JPL campus extends to the top of Gould mesa. The largest spectral acceleration is occurring at the top of the mesa. The spectral accelerations decrease at the bottom/edge of the mesa, increase south of the mesa and decrease again. The above observations are found to be similar for both events (M7.1 and M6.4) of the 2019 Ridgecrest earthquake sequence that we studied. It would be very interesting to see if such behavior can be related to morphological features of the geology underlying the

JPL campus. One- and two-dimensional simulations could shed light to the observed spectral acceleration amplifications. Similar recent studies include those by Asimaki & Mohammadi (2018) and Asimaki, et al. (2020). The small JPL campus size in combination with the presence of interesting geologic features and the dense spatial density of the collected data from multiple events make this an interesting possible future study.

REFERENCES

Abrahamson, N. A., Silva, W. J., & Kamai, R. (2014). Summary of the ASK14 ground motion relation for active crustal regions. *Earthquake Spectra, 30(3), pp.1025-1055*.

Abrahamson, N. A., Somerville, P. G., & A., C. C. (1990). Uncertainty in numerical strong motion predictions. *Proc. of the Fourth U.S. National Conference on Earthquake Engineering, Vol. 1, 407- 416*.

An, Y., Chatzi, E., Sim, S. H., Laflamme, S., Blachowski, B., & Ou, J. (2019). Recent progress and future trends on damage identification methods for bridge structures. *Structural Control and Health Monitoring, 26(10), p.e2416*.

Ancheta, T. D., Darragh, R. B., Stewart, J. P., Seyhan, E., Silva, J., W., . . . Kishida, T. (2014). NGA-West2 Database. *Earthquake Spectra, 30(3), pp.989-1005*.

Andrews, D. J. (1986). Objective determination of source parameters and similarity of earthquakes of different size. *Earthquake source mechanics, 37, pp.259-267*.

Antsaklis, P. J., & Michel, A. N. (2007). *A Linear Systems Primer*. Birkhauser.

Asimaki, D., & Mohammadi, K. (2018). On the complexity of seismic waves trapped in irregular topographies. *Soil Dynamics and Earthquake Engineering, 114, pp.424-437*.

Asimaki, D., Mohammadi, K., Ayoubi, P., Mayoral, J. M., & Montalva, G. (2020). Investigating the spatial variability of ground motions during the 2017 Mw 7.1 Puebla-Mexico City earthquake via idealized simulations of basin effects. *Soil Dynamics and Earthquake Engineering, 132, p.106073*.

Beck, J. L. (1979). Determining models of structures from earthquake records. *California Institute of Technology, Pasadena. Doctoral Dissertation*.

Beck, J. L. (1989). Statistical system identification of structures. *In Proceedings of international conference on structural safety and reliability (pp. 1395-1402). ASCE*.

Beck, J. L. (2010). Bayesian system identification based on probability logic. *Structural Control and Health Monitoring, 17(7), pp.825-847*.

Beck, J. L., & Jennings, P. C. (1980). Structural identification using linear models and earthquake records. *Earthquake engineering & structural dynamics 8, no. 2* , 145-160.

Beck, J. L., & Katafygiotis, L. S. (1998). Updating models and their uncertainties. I: Bayesian statistical framework. *Journal of Engineering Mechanics, 124(4), pp.455-461*.

Beck, J. L., & Yuen, K. V. (2004). Model selection using response measurements: Bayesian probabilistic approach. *Journal of Engineering Mechanics, 130(2), pp.192-203*.

Biot, M. (1933). Theory of elastic systems vibrating under transient impulse with an application to earthquake-proof buildings. *Proceedings of the National Academy of Sciences of the United States of America, 19(2),* 262-268.

Bishop, C. M. (2006). *Pattern recognition and machine learning.* Springer.

Bjornsson, A. B. (2014). A Retrofitting Framework for Pre-Northridge Steel Moment-Frame Buildings. *California Institute of Technology, Pasadena. Doctoral Dissertation*.

Boore, D. M. (2010). Orientation-independent, nongeometric-mean measures of seismic intensity from two horizontal components of motion. *Bulletin of the Seismological Society of America, 100(4), pp.1830-1835*.

Boore, D. M., Stewart, J. P., Seyhan, E., & Atkinson, G. M. (2014). NGA-West2 equations for predicting PGA, PGV, and 5% damped PSA for shallow crustal earthquakes. *Earthquake Spectra, 30(3), pp.1057-1085*.

Borcherdt, R. D. (1970). Effects of local geology on ground motion near San Francisco Bay. *Bulletin of the Seismological Society of America, 60(1), pp.29-61*.

Borcherdt, R. D., & Gibbs, J. F. (1976). Effects of local geological conditions in the San Francisco Bay region on ground motions and the intensities of the 1906 earthquake. *Bulletin of the Seismological Society of America, 66(2), pp.467-500*.

Bozorgnia, Y., Abrahamson, N. A., Atik, L. A., Ancheta, T. D., Atkinson, G. M., Baker, J. W., . . . Darragh, R. (2014). NGA-West2 research project. *Earthquake Spectra, 30(3), pp.973-987*.

Brown, L. T., Boore, D. M., & Stokoe, K. H. (2002). Comparison of shear-wave slowness profiles at 10 strong-motion sites from noninvasive SASW measurements and measurements made in boreholes. *Bulletin of the Seismological Society of America, 92(8), pp.3116-3133*.

Broyden, C. G. (1970). The convergence of a class of double-rank minimization algorithms 1. general considerations. *IMA Journal of Applied Mathematics, 6(1), pp.76-90*.

Buyco, K. J. (2018). Improving Seismic Collapse Risk Assessments of Steel. *California Institute of Technology, Pasadena. Doctoral Dissertation*.

Byrd, R. H., Gilbert, J. C., & Nocedal, J. (2000). A trust region method based on interior point techniques for nonlinear programming. *Mathematical programming, 89(1), pp.149-185*.

Caltech. (1926). Southern California Seismic Network. *International Federation of Digital Seismograph Networks. Other/Seismic Network. doi:10.7914/SN/CI*.

Campbell, K. W. (1976). A note on the distribution of earthquake damage in Long Beach, 1933. *Bulletin of the Seismological Society of America, 66(3),* pp. 1001-1005.

Campbell, K. W., & Bozorgnia, Y. (2014). NGA-West2 ground motion model for the average horizontal components of PGA, PGV, and 5% damped linear acceleration response spectra. *Earthquake Spectra, 30(3), pp.1087-1115*.

Carden, E. P., & Fanning, P. (2004). Vibration based condition monitoring: a review. *Structural health monitoring, 3(4), pp.355-377*.

Caughey, T. K., & O'Kelly, M. E. (1965). Classical normal modes in damped linear dynamic systems. *Journal of Applied Mechanics, 32(3), p.583*.

Challa, V. R. (1992). Nonlinear seismic behavior of steel planar moment-resisting frames. *California Institute of Technology, Pasadena. Doctoral Dissertation*.

Challa, V. R., & Hall, J. F. (1994). Earthquake Collapse Analysis of Steel Frames. *Earthquake Engineering & Structural Dynamics. 23: 1199–1218*.

Ching, J., & Chen, Y. C. (2007). Transitional Markov chain Monte Carlo method for Bayesian model updating, model class selection, and model averaging. *Journal of engineering mechanics, 133(7), pp.816-832*.

Chiou, B. J., & Youngs, R. R. (2014). Update of the Chiou and Youngs NGA model for the average horizontal component of peak ground motion and response spectra. *Earthquake Spectra, 30(3), pp.1117-1153*.

Chopra, A. K. (2011). *Dynamics of Structures: Theory and Applications to Earthquake Engineering, 4th edition.* Upper Saddle River, NJ: Pearson Prentice Hall.

Clayton, R. W., Heaton, T. H., Chandy, K. M., Krause, A., Kohler, M. D., Bunn, J. J., . . . Strand, L. (2011). Community seismic network. *Annals of Geophysics, 54(6), pp.738-747*.

Clayton, R. W., Heaton, T. H., Kohler, M. D., Chandy, K. M., Guy, R. G., & Bunn, J. J. (2015). Community seismic network: A dense array to sense earthquake strong motion. *Seismological Research Letters, 86(5)*, 1354-1363.

Clayton, R. W., Kohler, M. D., Guy, R. G., Bunn, J. J., Heaton, T. H., & Chandy, K. M. (2019). CSN-LAUSD Network: A Dense Accelerometer Network in Los Angeles Schools. *Seismological Research Letters*.

Cox, R. T. (1946). Probability, frequency and reasonable expectation. *American journal of physics, 14(1), pp.1-13*.

Cruz, C., & Miranda, E. (2017). Evaluation of damping ratios for the seismic analysis of tall buildings. *Journal of structural engineering, 143(1).*

CSI. (1999). SAP2000, Integrated finite element analysis and design of structures. *Computers and Structures*.

Doebling, S. W., Farrar, C. R., Prime, M. B., & Shevitz, D. W. (1996). Damage identification and health monitoring of structural and mechanical systems from changes in their vibration characteristics: a literature review (No. LA-13070-MS). *Los Alamos National Lab., NM, USA.*

Ebrahimian, H., Astroza, R., Conte, J. P., & de Callafon, R. A. (2017). Nonlinear finite element model updating for damage identification of civil structures using batch Bayesian estimation. *Mechanical Systems and Signal Processing, 84, pp.194-222*.

Fan, W., & Qiao, P. (2011). Vibration-based damage identification methods: a review and comparative study. *Structural health monitoring, 10(1), pp.83-111*.

Faul, A. C., & Tipping, M. E. (2002). Analysis of sparse Bayesian learning. *Advances in neural information processing systems (pp. 383-389)*.

Field, E. H., & Jacob, K. H. (1995). A comparison and test of various site-response estimation techniques, including three that are not reference-site dependent. *Bulletin of the seismological society of America, 85(4), pp.1127-1143*.

Friedland, B. (2012). *Control system design: an introduction to state-space methods.* Courier Corporation.

Friswell, M. I., & Mottershead, J. E. (1995). *Finite element model updating in structural dynamics.* Kluwer Academic Publishers, Boston, USA.

Gao, S., Liu, H., Davis, P. M., & Knopoff, L. (1996). Localized amplification of seismic waves and correlation with damage due to the Northridge earthquake: evidence for focusing in Santa Monica. *Bulletin of the Seismological Society of America, 86(1B), pp.S209-S230*.

Graves, R. W. (1996). Simulating seismic wave propagation in 3D elastic media using staggered-grid finite differences. *Bulletin of the Seismological Society of America, 86(4), pp.1091-1106*.

Graves, R. W., & Pitarka, A. (2016). Kinematic ground-motion simulations on rough faults including effects of 3D stochastic velocity perturbations. *Bulletin of the Seismological Society of America, 106(5), pp.2136-2153*.

Graves, R. W., & Pitarka, A. (2020). 3D Ground Motion Simulations for Events in the 2019 Ridgecrest Sequence. 17th World Conference on Earthquake Engineering, 17WCEE, Sendai, Japan - September 13th to 18th 2020.

Graves, R. W., Pitarka, A., & Somerville, P. G. (1998). . Ground-motion amplification in the Santa Monica area: Effects of shallow basin-edge structure. *Bulletin of the Seismological Society of America, 88(5), pp.1224-1242*.

Green, P. L., Cross, E. J., & Worden, K. (2015). Bayesian system identification of dynamical systems using highly informative training data. *Mechanical systems and signal processing, 56, pp.109-122*.

Gregor, N., Abrahamson, N. A., Atkinson, G. M., Boore, D. M., Bozorgnia, Y., Campbell, K. W., . . . Silva, W. (2014). Comparison of NGA-West2 GMPEs. *Earthquake Spectra, 30(3), pp.1179-1197*.

Gull, S. F. (1988). Bayesian inductive inference and maximum entropy. *In Maximum-entropy and Bayesian methods in science and engineering (pp. 53-74). Springer, Dordrecht*.

Hall, J. F. (1995). Parameter study of the response of moment-resisting steel frame buildings to near-source ground motions. *95-08. California Institute of Technology, Pasadena, CA.: Earthquake Engineering Research Laboratory*.

Hall, J. F. (1998). Seismic response of steel frame buildings to near-source ground motions. *Earthquake engineering & structural dynamics, 27(12)*, 1445-1464.

Hall, J. F., & Challa, V. M. (1995). Beam-column modeling. *Journal of engineering mechanics, 121(12), pp.1284-1291*.

Hansen, P. C. (1998). *Rank-deficient and discrete ill-posed problems: numerical aspects of linear inversion.* Society for Industrial and Applied Mathematics.

Harmsen, S. C. (1997). Determination of site amplification in the Los Angeles urban area from inversion of strong-motion records. *Bulletin of the Seismological Society of America, 87(4),* 866-887.

Harmsen, S. C. (1997). Determination of site amplification in the Los Angeles urban area from inversion of strong-motion records. *Bulletin of the Seismological Society of America, 87(4), pp.866-887*.

Hartzell, S. H. (1992). Site response estimation from earthquake data. *Bulletin of the Seismological Society of America, 82(6), pp.2308-2327*.

Hartzell, S., Harmsen, S., Frankel, A., Carver, D., Cranswick, E., Meremonte, M., & Michael, J. (1998). First-generation site-response maps for the Los Angeles region based on earthquake ground motions. *Bulletin of the Seismological Society of America, 88(2)*, pp. 463-472.

Hartzell, S., Leeds, A., Frankel, A., & Michael, J. (1996). Site response for urban Los Angeles using aftershocks of the Northridge earthquake. *Bulletin of the Seismological Society of America, 86(1B)*, pp. S168-S192.

Hatayama, K. (2008). Lessons from the 2003 Tokachi-oki, Japan, earthquake for prediction of long-period strong ground motions and sloshing damage to oil storage tanks. *Journal of seismology*, *12(2)*, 255-263.

Hatayama, K., & Kalkan, E. (2011). Long-period (3 to 10 s) ground motions in and around the Los Angeles basin during the Mw 7.2 El-Mayor Cucapah Earthquake of April 4, 2010. *Proc. of the 4th IASPEI/IAEE International Symposium*, 23-26.

Hauksson, E., Yoon, C., Yu, E., Andrews, J. R., Alvarez, M., Bhadha, R., & Thomas, V. (2020). Caltech/USGS Southern California Seismic Network (SCSN) and Southern California Earthquake Data Center (SCEDC): Data Availability for the 2019 Ridgecrest Sequence. *Seismological Research Letters*.

Hays, W. W. (1984). Technical problems in the construction of a map to zone the earthquake ground-shaking hazard in the United States. *Engineering geology*, *20(1-2)*, 13-23.

Hou, R., Wang, X., Xia, Q., & Xia, Y. (2020). Sparse Bayesian learning for structural damage detection under varying temperature conditions. *Mechanical Systems and Signal Processing, 145, p.106965*.

Hou, R., Xia, Y., Zhou, X., & Huang, Y. (2019). Sparse Bayesian learning for structural damage detection using expectation–maximization technique. *Structural Control and Health Monitoring, 26(5), p.e2343*.

Housner, G. W. (1941). Calculating the response of an oscillator to arbitrary ground motion. *Bulletin of the seismological Society of America, 31(2)*, 143-149.

Housner, G. W. (1954). Earthquake pressures on fluid containers. *California Institute of Technology, Pasadena (1954)*.

Huang, Y., & Beck, J. L. (2015). Hierarchical sparse Bayesian learning for structural health monitoring with incomplete modal data. *International Journal for Uncertainty Quantification, 5(2)*.

Huang, Y., & Beck, J. L. (2018). Full Gibbs sampling procedure for Bayesian system identification incorporating sparse Bayesian learning with automatic relevance determination. *Computer-Aided Civil and Infrastructure Engineering, 33(9), pp.712-730*.

Huang, Y., Beck, J. L., & Li, H. (2017a). Hierarchical sparse Bayesian learning for structural damage detection: theory, computation and application. *Structural Safety, 64, pp.37-53*.

Huang, Y., Beck, J. L., & Li, H. (2017b). Bayesian system identification based on hierarchical sparse Bayesian learning and Gibbs sampling with application to structural damage assessment. *Computer Methods in Applied Mechanics and Engineering, 318, pp.382-411*.

Huang, Y., Beck, J. L., & Li, H. (2019a). Multitask sparse Bayesian learning with applications in structural health monitoring. *Computer-Aided Civil and Infrastructure Engineering, 34(9), pp.732-754*.

Huang, Y., Shao, C., Wu, B., Beck, J. L., & Li, H. (2019b). State-of-the-art review on Bayesian inference in structural system identification and damage assessment. *Advances in Structural Engineering, 22(6), pp.1329-1351*.

Hutton, K., Woessner, J., & Hauksson, E. (2010). Earthquake monitoring in southern California for seventy-seven years (1932–2008). *Bulletin of the Seismological Society of America, 100(2), pp.423-446*.

Idriss, I. M. (2014). An NGA-West2 empirical model for estimating the horizontal spectral values generated by shallow crustal earthquakes. *Earthquake Spectra, 30(3), pp.1155-1177*.

Jaynes, E. T. (1983). Papers on probability, statistics and statistical physics. *R. D. Rosenkrantz, ed., Reidel, Dordrecht, The Netherlands. Reprint, 1989, Kluwer Academic Publishers Group, Boston, Mass*.

Jaynes, E. T. (2003). Probability theory: The logic of science. *Cambridge university press*.

Jefferys, W. H., & Berger, J. O. (1992). Ockham's razor and Bayesian analysis. *American Scientist, 80(1), pp.64-72*.

Jeffreys, H. (1939). *Theory of probability.* Oxford Univ. Press.

Katafygiotis, L. S., & Beck, J. L. (1998). Updating models and their uncertainties. II: Model identifiability. *Journal of Engineering Mechanics, 124(4), pp.463-467*.

Kohler, M. D., Magistrale, H., & Clayton, R. W. (2003). Mantle heterogeneities and the SCEC reference three-dimensional seismic velocity model version 3. *Bulletin of the Seismological Society of America, 93(2), pp.757-774*.

Komatitsch, D., Liu, Q., Tromp, J., Suss, P., Stidham, C., & Shaw, J. H. (2004). Simulations of ground motion in the Los Angeles basin based upon the spectral-element method. *Bulletin of the Seismological Society of America, 94(1), pp.187-206*.

Kuehn, N. M., Abrahamson, N. A., & Walling, M. A. (2019). Incorporating nonergodic path effects into the NGA-West2 ground-motion prediction equations. *Bulletin of the Seismological Society of America, 109(2), pp.575-585*.

Kuok, S. C., & Yuen, K. V. (2012). Structural health monitoring of Canton Tower using Bayesian framework. *Smart Structures and Systems, 10(4-5), pp.375-391*.

LADBS. (2017). Structural Monitoring Equipment in Buildings Designed with Nonlinear Response History Procedure. *Information Bulletin / Public - Building Code. Reference No.: LABC 1613.10.2. City of Los Angeles Department of Building and Safety.*

Landwehr, N., Kuehn, N. M., Scheffer, T., & Abrahamson, N. (2016). A nonergodic ground-motion model for California with spatially varying coefficients. *Bulletin of the Seismological Society of America, 106(6), pp.2574-2583*.

LATBSDC. (2008). An alternative procedure for seismic analysis and design of tall buildings located in the Los Angeles region. *Los Angeles Tall Buildings Structural Design Council*.

Lee, C. F., Lee, J. C., & Lee, A. C. (2000). *Statistics for business and financial economics* (3rd ed.). Singapore: World Scientific.

Lee, E. J., Chen, P., & Jordan, T. H. (2014). Testing waveform predictions of 3D velocity models against two recent Los Angeles earthquakes. *Seismological Research Letters, 85(6), pp.1275-1284*.

Lee, E. J., Chen, P., Jordan, T. H., Maechling, P. B., Denolle, M. A., & Beroza, G. C. (2014). Full-3-D tomography for crustal structure in southern California based on the scattering-integral and the adjoint-wavefield methods. *Journal of Geophysical Research: Solid Earth, 119(8), pp.6421-6451*.

Liu, H. L., & Heaton, T. H. (1984). Array analysis of the ground velocities and accelerations from the 1971 San Fernando, California, earthquake. *Bulletin of the Seismological Society of America, 74(5)*, pp. 1951-1968.

Los Angeles Times. (2019). *"Earthquake shook L.A. skyscrapers so hard some got vertigo", by Rong-Gong Lin II. Available at https://www.latimes.com/california/story/2019-08-14/ridgecrest-earthquake-produced-minutes-of-shaking-new-story (Last Accessed April 2020).*

MacKay, D. J. (1992). Bayesian interpolation. *Neural computation, 4(3), pp.415-447*.

MacKay, D. J. (1996). Bayesian methods for backpropagation networks. *Models of neural networks III (pp. 211-254). Springer, New York, NY*.

Magistrale, H., Day, S., Clayton, R. W., & Graves, R. W. (2000). The SCEC southern California reference three-dimensional seismic velocity model version 2. *Bulletin of the Seismological Society of America, 90(6B), pp.S65-S76*.

MATLAB. (2019). MATLAB Optimization Toolbox, User's Guide, Release 2019a. *The MathWorks, Natick, MA, USA*.

Mazzoni, S., McKenna, F., Scott, M. H., & Fenves, G. L. (2006). OpenSees command language manual. *Pacific Earthquake Engineering Research (PEER) Center, 264*.

Miller, D. K. (1998). Lessons learned from the Northridge earthquake. *Engineering structures, 20(4-6), pp.249-260*.

Moaveni, B. (2007). System and Damage Identification of Civil Structures. *Department of Structural Engineering, University of California, San Diego. Doctoral Dissertation*.

Moaveni, B., He, X., Conte, J. P., & Restrepo, J. I. (2010). Damage identification study of a seven-story full-scale building slice tested on the UCSD-NEES shake table. *Structural Safety, 32(5), pp.347-356*.

Moaveni, B., He, X., Conte, J., Restrepo, J. I., & Panagiotou, M. (2011). System identification study of a 7-story full-scale building slice tested on the UCSD-NEES shake table. *Journal of Structural Engineering, 137(6), pp.705-717*.

Mottershead, J. E., & Friswell, M. I. (1993). Model updating in structural dynamics: A survey . *Journal of sound and vibration, 167(2), pp. 347-375*.

Neumaier, A. (1998). Solving ill-conditioned and singular linear systems: A tutorial on regularization. *SIAM review, 40(3), pp.636-666*.

Olsen, K. B., Archuleta, R. J., & Matarese, J. R. (1995). Three-dimensional simulation of a magnitude 7.75 earthquake on the San Andreas fault. *Science, 270(5242), pp.1628-1632*.

Olsen, K. B., Day, S. M., & Bradley, C. R. (2003). Estimation of Q for long-period (> 2 sec) waves in the Los Angeles basin. *Bulletin of the Seismological Society of America, 93(2), pp.627-638*.

Petersen, M. D., Frankel, A. D., Harmsen, S. C., Mueller, C. S., Haller, K. M., Wheeler, R. L., . . . Luco, N. (2008). Documentation for the 2008 update of the United States national seismic hazard maps (No. 2008-1128). *Geological Survey (US)*.

Rodgers, A. J., Pitarka, A., Petersson, N. A., Sjögreen, B., & McCallen, D. B. (2018). Broadband (0–4 Hz) ground motions for a magnitude 7.0 Hayward fault earthquake with three-dimensional structure and topography. *Geophysical Research Letters, 45(2), pp.739-747*.

Roeder, C. W. (2000). State of the art report on connection performance. FEMA 355d. *Washington DC: Federal Emergency Management Agency*.

Rogers, A. M., Borcherdt, R. D., Covington, P. A., & Perkins, D. M. (1984). A comparative ground response study near Los Angeles using recordings of Nevada nuclear tests and the 1971 San Fernando earthquake. *Bulletin of the Seismological Society of America, 74(5)*, pp. 1925-1949.

Rogers, A. M., Tinsley, J. C., & Borcherdt, R. D. (1985). Predicting relative ground response. *US Geol. Surv. Profess. Pap, 1360*, pp. 221-248.

Rogers, A. M., Tinsley, J. C., & Borcherdt, R. D. (1985). Predicting relative ground response. *US Geol. Surv. Profess. Pap, 1360, pp.221-248*.

Rogers, A. M., Tinsley, J. C., Hays, W. W., & King, K. W. (1979). Evaluation of the relation between near-surface geological units and ground response in the vicinity of Long Beach, California. *Bulletin of the Seismological Society of America, 69(5)*, pp. 1603-1622.

Roten, D., Olsen, K. B., Day, S. M., & Cui, Y. (2017). Quantification of fault-zone plasticity effects with spontaneous rupture simulations. *Pure and Applied Geophysics, 174(9), pp.3369-3391*.

Rytter, A. (1993). Vibrational Based Inspection of Civil Engineering Structures. *Dept. of Building Technology and Structural Engineering, Aalborg University. Doctoral Dissertation*.

Saikia, C. K., Dreger, D. S., & Helmberger, D. V. (1994). Modeling of energy amplification recorded within greater Los Angeles using irregular structure. *Bulletin of the Seismological Society of America, 84(1), pp.47-61*.

SCSN. (2019). *"07/2019, Ridgecrest Sequence: M6.4 and M7.1", by Jennifer Andrews. Available at https://www.scsn.org/index.php/2019/07/04/07-2019-ridgecrest-sequence/index.html (Last Accessed April 2020)*.

Shaw, J. H., Plesch, A., Tape, C., Suess, M. P., Jordan, T. H., Ely, G., . . . Olsen, K. (2015). Unified structural representation of the southern California crust and upper mantle. *Earth and Planetary Science Letters, 415, pp.1-15*.

Shepard, D. (1968). A two-dimensional interpolation function for irregularly-spaced data. *Proceedings of the 1968 23rd ACM national conference*, 517-524.

Shi, Z., & Day, S. M. (2013). Rupture dynamics and ground motion from 3-D rough-fault simulations. *Journal of Geophysical Research: Solid Earth, 118(3), pp.1122-1141*.

Shome, N., Cornell, C., Bazzurro, P., & Carballo, J. (1998). Earthquakes, records, and nonlinear responses. *Earthquake Spectra, 14(3)*, 469-500.

Simoen, E., DeRoeck, G., & and Lombaert, G. (2015). Dealing with uncertainty in model updating for damage assessment: A review. *Mechanical Systems and Signal Processing, 56-57*, 123-149.

Sohn, H., Farrar, C. R., Hemez, F. M., Shunk, D. D., Stinemates, D. W., Nadler, B. R., & Czarnecki, J. J. (2003). A review of structural health monitoring literature: 1996–2001 (No. LA-13976-MS). *Los Alamos National Lab., NM, USA*.

Stewart, J. P., Afshari, K., & Goulet, C. A. (2017). Non-ergodic site response in seismic hazard analysis. *Earthquake Spectra, 33(4), pp.1385-1414*.

Süss, M. P., & Shaw, J. H. (2003). P wave seismic velocity structure derived from sonic logs and industry reflection data in the Los Angeles basin, California. *Journal of Geophysical Research: Solid Earth, 108(B3)*.

Taborda, R., & Bielak, J. (2013). Ground-motion simulation and validation of the 2008 Chino Hills, California, earthquake. *Bulletin of the Seismological Society of America, 103(1), pp.131-156*.

Taborda, R., & Bielak, J. (2014). Ground-motion simulation and validation of the 2008 Chino Hills, California, earthquake using different velocity models. *Bulletin of the Seismological Society of America, 104(4), pp.1876-1898*.

Taborda, R., Azizzadeh-Roodpish, S., Khoshnevis, N., & Cheng, K. (2016). Evaluation of the southern California seismic velocity models through simulation of recorded events. *Geophysical Journal International, 205(3), pp.1342-1364*.

Taucer, F., Spacone, E., & Filippou, F. C. (1991). A fiber beam-column element for seismic response analysis of reinforced concrete structures (Vol. 91, No. 17). *Berkekey, California: Earthquake Engineering Research Center, College of Engineering, University of California*.

Thompson, E. M. (2018). *An Updated Vs30 Map for California with Geologic and Topographic Constraints: U.S. Geological Survey data release. Available at https://doi.org/10.5066/F7JQ108S*.

Thompson, E. M., Wald, D. J., & Worden, C. B. (2014). A VS30 map for California with geologic and topographic constraints. *Bulletin of the Seismological Society of America, 104(5), pp.2313-2321*.

Tipping, M. E. (2001). Sparse Bayesian learning and the relevance vector machine. *Journal of Machine Learning Research, 1(Jun), pp.211-244*.

Titurus, B., & Friswell, M. I. (2008). Regularization in model updating. *International Journal for numerical methods in engineering, 75(4), pp.440-478*.

Vanik, M. W., Beck, J. L., & Au, S. K. (2000). Bayesian probabilistic approach to structural health monitoring. *Journal of Engineering Mechanics, 126(7)*, 738-745.

Vidale, J. E., & Helmberger, D. V. (1988). Elastic finite-difference modeling of the 1971 San Fernando, California earthquake. *Bulletin of the Seismological Society of America, 78(1), pp.122-141*.

Wald, D. J., & Graves, R. W. (1998). The seismic response of the Los Angeles basin, California. *Bulletin of the Seismological Society of America, 88(2)*, 337-356.

Withers, K. B., Olsen, K. B., & Day, S. M. (2015). Memory-efficient simulation of frequency-dependent Q. *Bulletin of the Seismological Society of America, 105(6), pp.3129-3142*.

Withers, K. B., Olsen, K. B., Day, S. M., & Shi, Z. (2019). Ground Motion and Intraevent Variability from 3D Deterministic Broadband (0–7.5 Hz) Simulations along a Nonplanar Strike-Slip Fault. *Bulletin of the Seismological Society of America, 109(1), pp.229-250*.

Wollherr, S., Gabriel, A. A., & Uphoff, C. (2018). Off-fault plasticity in three-dimensional dynamic rupture simulations using a modal Discontinuous Galerkin method on unstructured meshes: implementation, verification and application. *Geophysical Journal International, 214(3), pp.1556-1584*.

Yuen, K. V. (2010). *Bayesian methods for structural dynamics and civil engineering.* John Wiley & Sons.